Nonlinear Modeling and Control of Magnetic Bearings

A Dissertation

Presented to

the faculty of the School of Engineering and Applied Science

University of Virginia

in partial fulfillment

of the requirements for the degree

Doctor of Philosophy

by

Ali Gerami

May

2015

APPROVAL SHEET

The dissertation

is submitted in partial fulfillment of the requirements

for the degree of

Doctor of Philosophy

____
AUTHOR

The dissertation has been read and approved by the examining committee:

Carl Knospe
____
Advisor

Roger Fittro (Co-Advisor)
____

Houston Wood (Chairman)
____

Gavin Garner
____

Gang Tao
____

____

Accepted for the School of Engineering and Applied Science:

Dean, School of Engineering and Applied Science

May
2015

ABSTRACT

In this Dissertation a nonlinear modeling and control method for magnetic bearings is proposed, considering the core material nonlinear high flux behavior for the first time. A combination of the generalized Lur'e method and linear matrix inequalities is used during the modeling and control design process. The nonlinear modeling makes it possible to operate an existing industrial AMB system with larger electric currents and thus achieve a larger maximum load capacity than existing AMB modeling and control practices allow. As a result, existing industrial AMB's can be tuned to become more resilient in dealing with external disturbances. In addition, smaller and lighter AMBs can be designed by using the proposed method, which enables achievement of the same maximum force requirement of present-day larger AMB systems.

The proposed control method is verified by experimental data drawn from a balance beam test rig designed for this project and very good correlation was obtained between the experimental data and theoretical predictions. In comparison to classical control design, a significantly improved transient response and a significantly higher dynamic load capacity was achieved through the use of the proposed modeling and control design.

The control synthesis based on the nonlinear model with a generalized sector condition offered little or no performance improvement over the control synthesis based on the nonlinear model with a regular sector condition for the problem considered. Despite this fact, using the generalized sector condition was proven to be necessary to guarantee a less conservative design compared to classical control design.

The uncertainty descriptions developed in this work were appropriate and because of the use of the generalized sector condition, guaranteed not to be overly conservative.

While the nonlinear behavior of the magnetic bearings due to the material magnetization has been studied and modeled previously, the extra load capability within the nonlinear region has not been optimally used in the control strategies. A combined approach for modeling and control of magnetic bearing that counts on the extra load capability within the nonlinear magnetization region is proposed in this work. Various optimized controllers with different objectives are designed using the extra load capability for the first time on this dissertation.

1 Table of Contents

List of Figures

List of Tables

Nomenclature

A	Cross sectional area of the coil
A	System matrix
A_{Beam}	Cross sectional area of the beam
A_g	Pole face area
A_{wire}	Cross sectional area of each wire
a	Relative permeability constant 1
B	Saturation input matrix
B	Magnetic flux density
B_1	Magnetic flux in the magnetic actuator
B_2	Magnetic flux in the target lamination
B_g	Magnetic flux in the airgap
B_{Knee}	Flux density at the end of the linear range
B_{Sat}	Saturation flux density
B_u	Input matrix
B_w	Disturbance matrix
b	Relative permeability constant 2
C	Output matrix
D	Balance beam's friction coefficient
d	Wire diameter
E	Disturbance Input Matrix
F	Electromagnet force
F_I	Nonlinear force assuming zero displacement
F_L	Total force linearized w.r.t displacement
F_w	Amplitude of the external disturbance
f_1	First bending frequency
f_2	Second bending frequency
f_3	Third bending frequency
f_{cut}	Cutoff frequency
f_{pole}	The frequency of the unstable pole
f_w	Frequency of the external disturbance
dF/dt	Slew rate
$dF/dt_{Disturbance}$	The required slew rate to balance the beam under an external disturbance
dF/dt_{Weight}	The required slew rate to balance the beam under it's off-centered weight
G	State constraint matrix
G(s)	Balance beam transfer function
g	Airgap
g_0	Nominal Airgap
H	Magnetic flux
H_1	Magnetic field in the magnetic actuator
H_2	Magnetic field in the target lamination
H_g	Magnetic field in the airgap
H_s	Magnetic field in the magnetic material

h	Thickness of the balance beam
I_b	Bias current
I_{Beam}	Area moment of inertia of the beam
I_c	Control Current
$I_{c\max}$	Maximum control current
I_{knee}	Current that produce the knee flux density
$I_{\max}$	Current corresponding to the end of the nonlinear range
I	Electrical current
dI_c / dt	Current slew rate
J	Balance beam's mass moment of inertia
J_{coil}	Current density of the coil
$J_{\max}$	Maximum current density
k_{1i}	Slope of segment I of the first sector bound
k_{2i}	Slope of segment I of the second sector bound
k_d	Derivative gain
k_p	Proportional gain
K_a	Actuator gain
K_I	Current coefficient of the force
K_s	Sensor gain
K_X	Displacement coefficient of the force
L	Inductance of each electromagnet with two coils
L_1	Length of the magnetic circuit in the magnetic actuator
L_2	Length of the magnetic circuit in the target lamination
L_a	Distance between the pivot and the electromagnet at each end
L_{Beam}	Total length of the beam
L_g	Distance between the beam's center of gravity and pivot
$L_{\max}$	Maximum tolerable inductance of the amplifier
L_s	Distance the flux travels inside the magnetic material
L_{se}	Distance between the sensor and the pivot
L_w	Distance between the external force and the pivot
M_p	Overshoot
N	Number of turns
NI	Magneto-motive force
P	Variable matrix
Q	Variable matrix inverse
q	Control input
r	Distance from the center of the flywheel
T	Total balance beam torque
T_p	Peak time
T_r	Rise time
T_s	Settling time
u	Input vector
V	Lyaponov function
V_c	Amplifier voltage
W	Weigh of the beam

w	Disturbance vector
w_d	Damped natural frequency
w_n	Natural frequency
x	Vertical displacement of the beam at the actuator location
α	Disturbance signal energy index
β	Transient response speed index
ζ	Damping ratio
η	Ellipsoid size index
Θ	Normalized angle from horizon
θ	Angular displacement of the beam with respect to the horizon
$\theta_{\max}$	Maximum angular displacement of the beam with respect to the horizon
λ	Normalized control current
μ_0	The permeability of free space
μ_r	Relative permeability of the magnetic material.
η	Packing density
ρ	Density
ρ	Ellipsoid radius index
ϕ	Magnetic flux
ψ	Nonlinear input function
ψ_1	First sector bound
ψ_2	Second sector bound
ω	Rotational velocity

1 Introduction

1.1 Motivation

In industrial AMB practice, the capability of generating larger force is highly desirable. Magnetic bearings are usually operated in the linear region of the magnetic core's magnetization curve. Figure 1 shows that even after the linear region, there is still a significant capacity for producing larger flux densities (B) and, therefore, larger forces. Current AMB practice using linear control does not take advantage of this. In addition, magnetic bearings are normally designed to be able to handle the worst-case scenario of external disturbances. Therefore a safety factor is applied in AMB designs. As a result AMB's are generally significantly overdesigned, which increases their cost and limits their implementation.

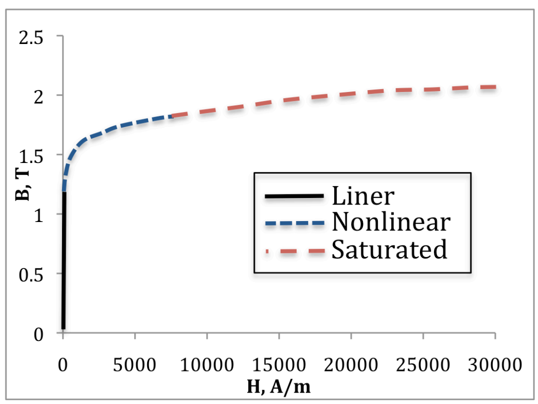

Figure 1-1 Magnetic Core Magnetization

In this thesis, a nonlinear model is introduced that enables the control engineer to potentially utilize that extra magnetization capacity.

When designing new AMB's, the proposed nonlinear model can potentially reduce the size and cost of the bearings. The bearing can be designed to operate in the linear region for standard operation and in the case of an extreme load condition; the bearing can be operated in the nonlinear magnetic region in order to balance the system. In the case of existing AMBs, the extra amplifier and AMB capacity is normally already available, and therefore with a change of control software only, the suggested modeling and control method can be used to improve the performance of the system.

1.2 Energy Storage Incentive

A long-term goal and future work for this project is to develop a new software modification, modeling, and magnetic bearing control algorithm that would enable increased energy density of energy storage flywheels. This software modification could be implemented on existing flywheel systems and make them safer and more efficient. Based on our theoretical work, the new software would potentially allow up to 2 times more energy to be stored in existing flywheel systems. As a result, energy storage costs would be significantly reduced, saving hundreds of millions of dollars in the United States alone.

1.3 An Introduction to Flywheels

A flywheel is a mechanical device that stores energy in the form of kinetic energy, such that it can be converted to another form of energy for future use. The first flywheels in use were pottery wheels. After the industrial revolution, flywheels found a wider variety of use in steam and internal combustion engines. In recent years, the use of flywheels as mechanical batteries for different applications has gained momentum.

The main goal of a flywheel's mechanical design is to maximize the kinetic energy stored in the system. The kinetic energy of a disk with moment of inertia J that is rotating with rotational velocity ω can be calculated as:

$$K.E. = \frac{1}{2} J\omega^2 \tag{1-1}$$

Therefore to increase the energy stored either J, ω or both should be increased. J is related to the mass of the system and it's distance from the axis of rotation ($J = \int r^2 dm$). Therefore flywheels usually have a disk-like shape with the most mass on the outmost part. The other way to increase the stored energy is to increase the rotational speed. The challenge here is the bearings. In fluid film or ball bearings, increasing the speed yields very large friction losses. Therefore for high-speed flywheels the natural choice is the magnetic bearing. Magnetic bearings are friction-free and are therefore highly suitable for high-speed operation.

1.4 Recent Developments in Flywheel Energy Storage systems

In 2011, the first grid-size energy storage flywheel unit (20 MW capacity) was installed in the United States. Since then, flywheels have become an increasingly popular way to store energy. Even though predictions indicate that flywheels will account for just 2% of the energy storage market in the near future, the flywheel's long life, low environmental impact, and novelty make it very attractive. In 2011, 15% of the smart grid grants in the US were invested in flywheels. In this thesis a method is proposed to safely increase the rotational speed and therefore the energy storage capacity of flywheel energy storage systems.

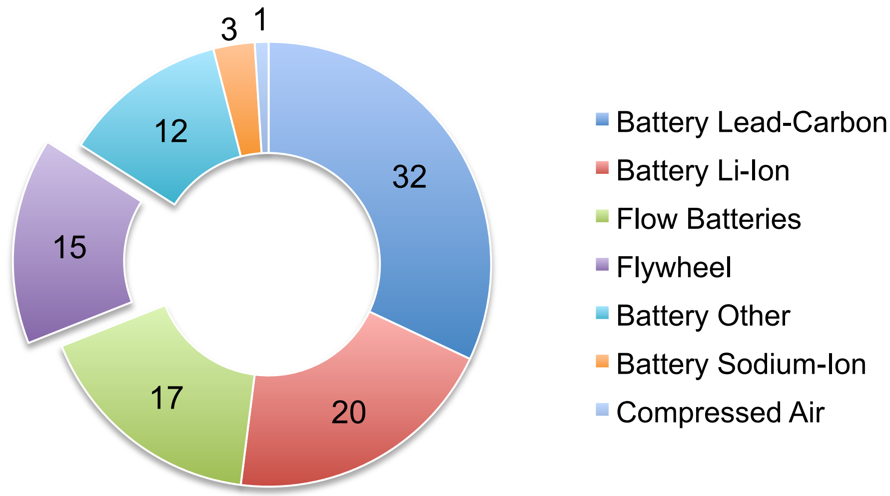

Figure 1-2 Department of Energy Smart Grid Demonstration Grants (Total $184.8m)

Even though investors and grants have supported the development of flywheels, a lack of familiarity with the technology poses challenges to the growth of this market. A significant gap exists between the current safety and cost of energy storage flywheels and the requirements needed by the energy industry to make the technology more economical and competitive.

In the past, the limiting factor in flywheel design has been the rotor material's yielding stress. Even though more energy can be stored in the flywheel by spinning it faster, this increase in speed subjects the material to immense centrifugal forces. Recently, new rotor materials, such as carbon fiber, have been used to increase the material yield stress and therefore increase the maximum allowable rotational speed of the shaft. These design modifications increase the energy storage density of the unit and thereby reduce the overall cost of energy storage. However, during this same period of time, no major advancement has been made to improve the load density of magnetic bearings. Therefore, in many cases, the magnetic bearing has become the performance limiter in the overall flywheel energy storage design. The force exerted on the radial magnetic bearings inside flywheel energy storage systems, is caused by small unbalanced weights:

$$F = mr\omega^2 \qquad (1-2)$$

Since the unbalanced weight (m) and distance from the center of the flywheel (r) does not change over time, increasing the magnetic bearing's load capacity enables the flywheel to tolerate higher rotational speeds.

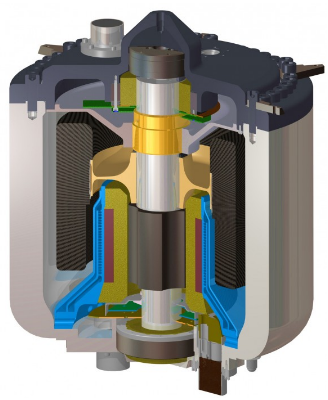

Figure 1-3 Energy Storage Flywheel (archthings 2010)

Based on Equations (1-1) and (1-2), it is estimated that the flywheels could achieve up to two times higher load capacity by implementing magnetic bearing systems capable of operating into the nonlinear magnetization region. Today's state-of-the-art magnetic bearing systems operate based on linear magnetization models and can therefore use only about half of the available load capacity. The main reasons for the shortcoming are:

1-Current magnetic bearings operate in the low end of the linear magnetic region, the majority of the linear region is reserved for safety considerations and the nonlinear region is left completely unused.

2- Previously available modeling and control strategies (absolute stability theory) were not accurate enough to be of practical advantage. To compensate for the inaccuracy, the nonlinear control design was overly conservative and would not allow a significant increase in the load capacity.

The modeling and control method proposed in this thesis will significantly increase the performance and capacity of flywheels by more fully utilizing the magnetic bearing's load capability. The following plan was followed:

1-A comprehensive analytical study of the nonlinear behavior, modeling, and control of the magnetic bearings, as an important part of the flywheel system was carried out. In this work, the extra magnetization capability lying in the nonlinear region of the magnetization curve was explored and utilized. Due to some recent developments in nonlinear modeling, the practical use of this extra capacity has become feasible. This development enables standard operation in the mid-linear magnetization region while reserving the upper-linear and nonlinear magnetization regions as a factor of safety.

2-The new nonlinear modeling and control strategy is then used to operate a test rig to validate the proposed method. For this phase, a balance beam (see Fig. 4) was built as a simple experimental test rig to capture the fundamental magnetic bearing dynamics. These dynamics are directly related to the requirements for their use on a flywheel energy storage system. The experiments act as an initial proof of concept of the theory, models and simulations developed in step 1.

3-As future work, based on the experimental proof of concept results in step 2, the design can be refined and optimized for a flywheel storage application. A full flywheel system simulation should be developed in order to predict performance capabilities, compare results to the present state-of-the-art, and pave the way toward applying these methods to a full-scale flywheel system in the future.

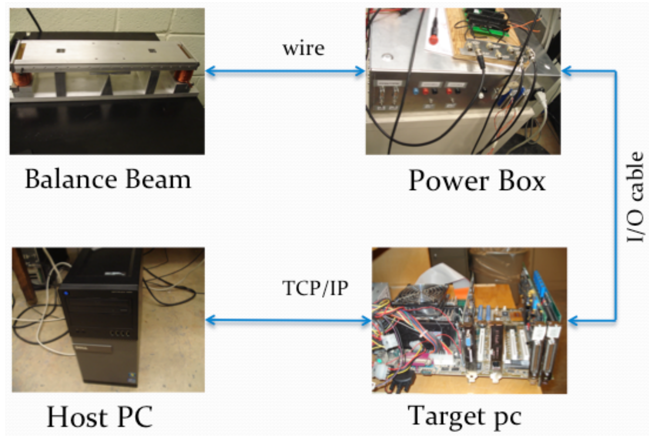

Figure 1-4 The Balance Beam Test Rig

This breakthrough AMB control technique could be used to either increase the load capacity of the existing magnetic bearing by adding a module to the controller or to design smaller new magnetic bearings (about 20% smaller in outer diameter). The proposed design will make flywheel systems more efficient in the following ways:

1-Increase the energy density of existing stationary flywheel systems

2-Increase the safety of existing mobile and stationary flywheel systems

3-Decrease the size of new flywheel designs

4-Reduce the maintenance costs of new and currently operational flywheel systems

1.5 Economic outcomes and external validation

The annual global demand for grid-scale energy storage will reach an astounding 185.4 gigawatt-hours (GWh) by 2017 and represent a $113.5 billion incremental revenue. In the grid-scale sector alone, an average year-on-year demand growth of 231% from 2012 through 2015 and 43% per year for 2016 and 2017 is predicted [John Petersen, Lux Research, 2012]. The US will account for about 23% of this market. Flywheels will retain at least 2% of the grid scale energy storage market in 2017 and will continue to grow.

This prediction makes the flywheel energy storage a 0.5 billion-dollar market in the U.S. alone. Other industries including trains, motor sports, etc. make the global flywheel energy storage larger than a $**2 billon market** by 2017. Since the technology is relatively new, the main concerns about the flywheel system are its safety and high cost. Our proposed upgrade and design strategy could impact the market with regards to both of these areas in the following ways:

Cost per kWh

Based on current flywheel technology, which uses stronger and lighter materials, such as carbon fiber, magnetic bearings are rapidly becoming one of the key limiting factors in total energy storage capacity. Our modeling and control strategy allows 50% more magnetic flux which subsequently increases the magnetic bearing’s force capacity by a factor of two. As a result, the flywheel can support faster rotational speeds, which results in a higher energy storage capacity. This increase in energy storage capacity results in an increase in energy density, which in turn results in energy storage cost reduction, saving hundreds of millions of dollars in United States alone.

Safety

Failure in flywheels occur due to three primary factors:

1-Manufacturing defects: The total failure rate of flywheels from manufacturing defects is about 1%.

2-Wear and Tear: Given the average operation expectancy for the installed flywheel capacity in power grids, one would expect up to 0.6% of flywheels to fail each year, or up to 12% over the plant's expected 20 year lifetime [Tom Konard, Altenergystocks, 2011].

3-Unexpected dynamic load: This failure can happen to flywheels in transportation systems.

Based on this information, an estimate of the likely failure rate of flywheels over a plant's 20 year planned life is between 4% and 13% in stationary systems. A significant percentage of these failures can be prevented by a combination of predictive maintenance and our proposed modeling and control strategy. By enabling operation in the nonlinear magnetic region, **the safety factor can potentially be increased up to 2 times by the inclusion of software upgrades** alone. This can save tens of millions of dollars in maintenance costs.

Size and Weight

The use of the proposed concept could result in a reduction of the magnetic bearing outer diameter by 20% and the weight by 35%. In some applications, such as satellites and space stations, this upgrade would be critical (considering that it currently costs $10,000 to send one pound of material into space).

1.6 Significance of the envisioned commercial product, market size and competitors

The U.S. grid scale energy storage industry, with an estimated size of $25 billion, is the primary market for the proposed technology. For flywheel frequency regulation, the new technology can lead to savings of hundreds of millions of dollars in investments and operational costs. Data centers and metro systems are two other emerging markets for the flywheels systems and therefore the proposed technology. The currently available high-end flywheel systems are, and are therefore not exploiting the full potential of the magnetic material. Based on the results of this study, a 2x performance improvement of flywheel systems is envisioned via the implementation of the proposed modeling and control strategy.

1.7 Literature Review

Extensive research has been done to take into account some AMB nonlinearities. These studies can be divided into categories based on the nonlinearity that is modeled, the modeling method and the control method used.

1-Modeled Nonlinearity: The force created by an electromagnet is proportional to the square of the current intensity and inversely proportional to the air-gap between the rotor and the stator. The model of an AMB is thus nonlinear, and leads to many complexities in control synthesis. Much work has been devoted to the synthesis of such control laws. The majority of the research in nonlinear AMB's has considered this nonlinearity. Yin [1], Inoue [2], Abdelfatah [3], Hong [4], Smith [5] are just a few out of the many references. The force, displacement, and current relationship have usually been studied with single-DOF systems. Also quite a few studies have been performed on two or more DOF systems in order to model geometric coupling and gyroscopic effects. Walsh [6] considered the geometric coupling of a 2-DOF AMB and studied the changes in stiffness and the resulting bifurcation. Abdelfatah [3] studied the nonlinear oscillations caused by the gyroscopic effect. He [7] and Huang [8] modeled and controlled 5 and 6-DOF systems. Other researchers have considered geometric nonlinearity Hu [9], amplifier nonlinearities Inoue [2], hysteresis Wang [10] and control system delays Tsuyoshi [2,11], Zheng [12,13]. More recently, self-sensing magnetic bearings Noh [14] and contact between rotor and auxiliary bearing Foiles [15] have been studied.

2-Modeling Method: AMB nonlinearities have been modeled with different methods ranging from ordinary differential equations and state dependant parameters Truong [16] to neural network methods Jeng [17] and fuzzy modeling methods Lee [18], Xu [19], Yu [20] and Hong[4]. Feedback linearization has also been used to introduce auxiliary nonlinear feedback, [5,21,22,23] such that the system can be treated as linear for control design purposes.

3-Control strategy: Extensive studies have been carried out on suitable strategies for the control of nonlinear AMB's, ranging from state-space and transfer function approaches to H_∞ control Matsumura [24], and sliding mode control Tian [25] and Cho [26]. Fuzzy control techniques have been applied [8,12,27], as well as optimal control approaches such as discrete dynamic programming Steffani [28]. To reduce power losses, Two Flatness-based designs; Constant Current Sum (CCS) by Löwis [29] and Current Almost Complementary (CAC) by Grochmal [30] were introduced for low-bias and zero-bias control of active magnetic bearings.

1.8 Overview of the thesis

In this work, the Lur'e problem is considered for AMB modeling. It consists of a nonlinear feedback analysis problem. It evaluates the stability of a linear dynamical system that has a nonlinear feedback component, which satisfies a sector condition. New conditions for global asymptotic stability and absolute stability in Lur'e systems have been investigated and derived by various research groups. However, while using Lur'e systems are common in the subject of chaotic synchronization, have been used to model the AMB core material magnetization for the first time in this thesis.

A combination of absolute stability with the generalized sector condition of a Lur'e system and linear matrix inequalities was used during the modeling and control process. While the generalized sector condition allows for more flexible modeling of nonlinear feedback in Lur'e systems; formulating the conditions in terms of linear matrix inequalities (LMIs) makes the optimization-based evaluation easier. Magnetic bearing control with the new method demonstrates a larger domain of attraction than that achieved using present industrial practices as well as the Popov or circle criterion methods. The proposed nonlinear modeling makes it possible to operate the existing industrial AMBs with larger electric currents and therefore achieve larger load capacity.

The modeling results were verified by experiments on a single-degree-of-freedom test rig. The test rig used in this thesis consisted of a beam that pivots around a central fulcrum and electro-magnets on each side. The rigid beam rotates freely around the pivot and the electro-magnets produce the required force to achieve stabilization. The beam balancing test rig acts mimic to the behavior of a single axis active thrust magnetic bearing.

This chapter has explained the motivation for the research and gives a brief introduction to flywheel energy storage systems. In Chapter 2, the test rig design is described in detail. The system dynamics and nonlinear modeling is explained in Chapter 3. This chapter also includes the constraints and a brief introduction to the generalized sector condition. The proposed control strategy and design process is presented in Chapter 4. Three optimization approaches for maximizing the domain of attraction, improving the transient response and operation with exogenous disturbances are addressed, both for traditional and generalized sector conditions. Experimental verification is presented in Chapter 5. And Chapter 6 summarizes the thesis and makes suggestions for future work.

2 Test Rig Design

The main goal of the experimental test rig was to design a system that is simple enough for testing a new nonlinear material modeling and control synthesis methodology, yet also capable of capturing all of the important aspects of a magnetic bearing system. This chapter provides a detailed description of the mechanical, electromagnetic, and electronic parts of the test rig, as well as the specifications influencing the design.

2.1 Problem Statement

Since the modeling and control method in this thesis is nonlinear, a balance beam test rig with the capability of nonlinear operation was chosen. For the core material a magnetic material commonly used in industry (M-19 silicon iron) was chosen. The M-19 silicon iron B-H curve exhibits typical nonlinear behavior for flux densities greater than 1.2T. And for flux densities greater than 1.6T, the material is fully saturated. Therefore the test rig should be able to provide flux densities up to 1.6T. The corresponding operating currents can be estimated from the equation:

$$B = \frac{\mu_0 NI}{2g_0 + \frac{L_s}{\mu_r}} \qquad (2-1)$$

Here, B is the flux density, NI is the magneto-motive force, g_0 is the nominal airgap, L_s is the distance the flux travels inside the magnetic material, μ_0 is the permeability of free space, and μ_r is the relative permeability of the magnetic material. A balance beam test rig was already available in the University of Virginia Rotor Machinery and Control (ROMAC) lab, however it had to be modified in order to meet the design requirements of this work. The coil currents required to operate the existing balance beam were calculated to be between 4.13A and 8.49A. In order to reach these current levels, both the coils and the amplifiers must have the ability to generate the necessary electric current.

The maximum current density $\left(J_{\max}\right)$ is a limit commonly employed to avoid problems associated with coil overheating such as wire insulation breakdown.

$$J_{\max} = \frac{\left(NI\right)_{\max}}{A} \qquad (2-2)$$

Here, A is the total coil cross sectional area and NI is the magneto-motive force. The maximum current density is primarily dependent on the cooling method (forced vs. natural convection), wire material, and wire type (flat or traditional wire). For the case of the existing balance beam, a suitable value for $J_{\max}$ was determined to be 6 A/mm^2 and the coil cross sectional area was $A = 13mm \times 5mm = 65mm^2$. Therefore, the maximum magneto-motive force was calculated to be 390 A.turns and the maximum allowable flux density was calculated to be 0.3T based on Equation 2-1. This value is significantly bellow the nonlinear region. In order to solve this problem, the following solutions were investigated:

1-Increase the Magneto-Motive Force (MMF):

There is an empty space between the coils, which can be used for additional coil windings. This space is approximately 5 millimeters meaning that, the coil cross sectional area could be increased by 50%

$$A_{\max} = 13mm \times 7.5mm = 97.5mm$$

Therefore, the resulting maximum magneto-motive force would be equal to,

$$(NI)_{\max} = J_{\max} A_{\max} = 6 \times 97.5 = 585 A.Turn$$

And the corresponding maximum possible flux density would only be 0.45T, which is still not adequate.

2- Reduce the Magnetic Material:

As another solution, some magnetic laminations of the core material could be removed in order to make the system saturate with a smaller current. If the laminations were reduced evenly there would be no change in the flux density (See Eq. 2-1). The system could be made to saturate by reducing the laminations in some parts of the core and leaving the laminations as they are in other parts of the core. However this was not considered to be a good solution because the resulting test rig would not be a representative model of existing industrial AMB's that have the same lamination cross sectional area throughout the entire bearing. In order to have an accurate AMB model, the cross sectional area should be consistent everywhere in the magnetic circuit, and in that case, Equation (2-1) shows that reducing the magnetic material will not affect the flux density generated by the coils.

3-Reduce the airgap:

A reduction in the airgap could potentially make the system saturate. In order to achieve saturation, the already small airgap (20 mils) would have to be reduced to 6 mils. This small airgap is very difficult to work with in practice, and it is also much smaller than the airgaps used in practical applications. Therefore, it was decided not to pursue this method.

4-Designe a new test rig with nonlinear operation capabilities:

With the previous alternatives eliminated, this was the only option available. In order to meet all the design specifications, the test rig described in the next section was developed.

2.2 System overview

The experimental test rig is composed of a rigid beam free to rotate around a pivot, two electromagnets (actuators), two eddy current displacement sensors, several other structural parts to support the beam, and other electrical components including two amplifiers, power supplies, one data acquisition card capable of both analog to digital and digital to analog conversion, and a computer with a Linux operating system and real time application interface (RTAI) which enables real time control. Figure 2-1 shows a block diagram of the system.

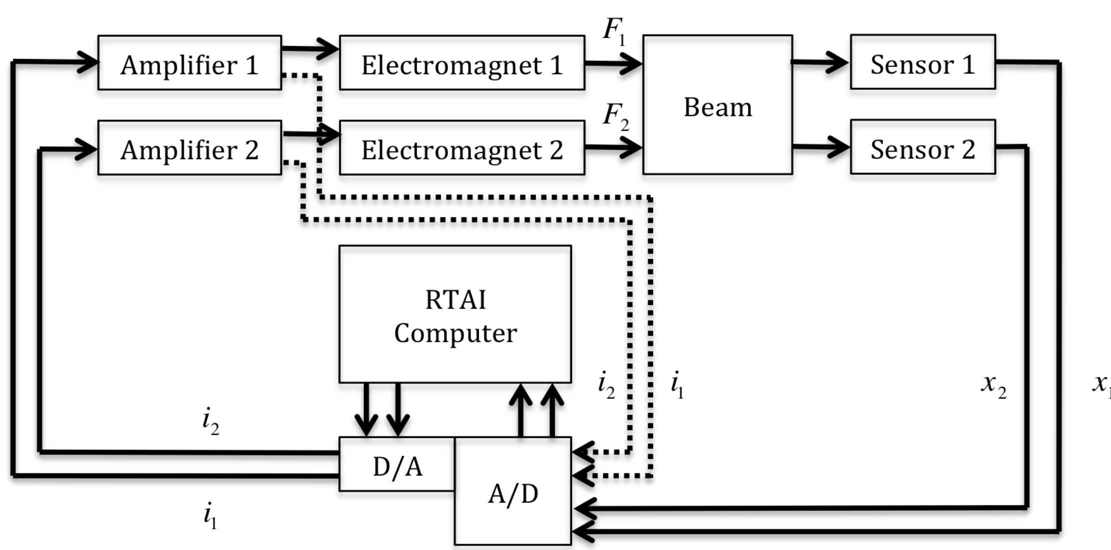

Figure 2-1 Balance Beam System Block Diagram

The displacement, measured as an electric voltage, is sampled by the data acquisition card's A/D convertor and thereby transferred to the computer. The control algorithm in turn calculates the appropriate control effort, which is sent out of the D/A ports of the data acquisition card. This output voltage is sent to the pulse wide modulation (PWM) power amplifiers, which subsequently transform this command to an electrical current, which drives the electromagnets. Finally, the electromagnets exert a restoring force on the beam to keep it balanced. To monitor the electromagnets' currents, the current monitors from the amplifiers are also wired to the A/D card. A detailed view of the mechanical system is provided in Figure 2-2 and detailed drawings of all of the parts can be found in Appendix B. The balance beam has three magnetic actuators. The inner two are for balancing the beam and the one on the right end is for producing an external disturbance.

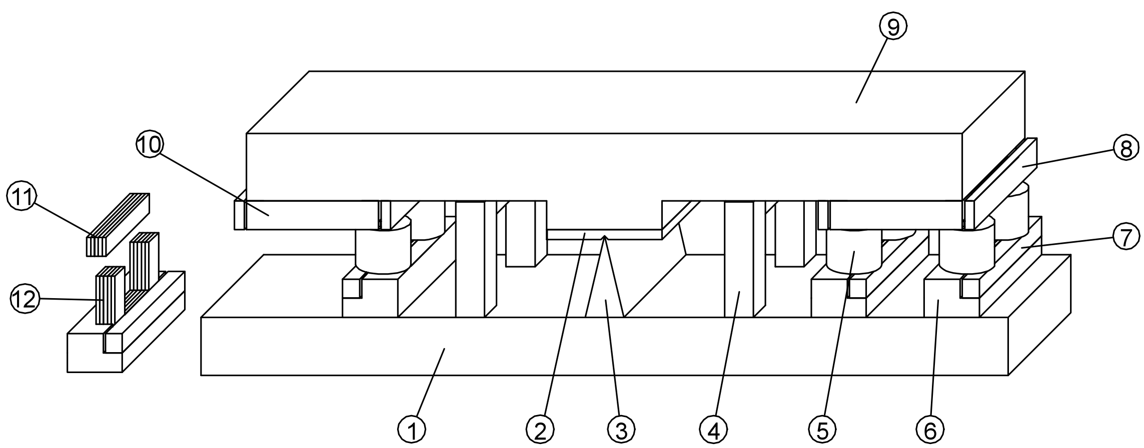

1	Base Plate	7	Core Lamination Clamp
2	Pivot Plate	8	Target Lamination Clamp
3	Pivot	9	Beam
4	Sensor Stand/ backup Bearing	10	Target Lamination Holder
5	Coil	11	Target lamination
6	Electromagnet Stand	12	Core lamination

Figure 2-2 Balance Beam Overview and Part Names

The test rig design process consisted of several steps. First the actuator related parts were designed. Then the actuator parameters were used to design the mechanical and electrical portions of the system. Finally, a system-level analysis was conducted to ensure that the overall system level performance requirements were met.

2.3 Electromagnets

Airgap

The nominal airgap is one of the most important design factors. Changing the airgap, changes the system's stiffness, unstable pole, the maximum required electrical current, and the design bias current. In the design process, a value for the airgap was assumed within the range of common industrial practice. The electromagnets were designed based on the assumed value of the airgap and the constraints imposed on them. Then the balance beam was designed based on the airgap, the designed electromagnets and the constraints on the vibration response of the beam. If the design did not meet the frequency response constraints another value for the airgap was chosen and the entire process was repeated until a satisfactory design was reached. Table 2-3 shows the effect of the airgap on the bias and maximum current of the electromagnets and the frequency response of the beam.

Coil Design

Each electromagnet has two driving coils (one on each leg of the actuator). Each coil consists of 110 turns of 14 AWG copper magnet wire with an electrical resistance of 0.11 Ω at room temperature. A proper wire choice with an appropriate number of turns enables an adequate magnetic force without overheating. Therefore, a proper coil should satisfy the following four constraints:

<u>Flux Density (Constraint 1)</u>

The purpose of the new balance beam design is to make sure the system can generate flux densities up to 1.6T ($B_{sat} = 1.6T$), which means:

$$NI > \frac{B_{sat}\left(2g_0 + \frac{L_s}{\mu_r(1.6)}\right)}{\mu_0} = NI_{\min} \qquad (2-3)$$

Here the relative permeability is dependent on the flux density (see Chapter 3 for more details). $\mu_r(1.6)$ is the relative permeability at 1.6T. N is the number of coil turns In each electromagnet. Since there are two coils in each electromagnet, N is twice the turns in each coil. The minimum requirement for the magneto-motive force (NI) is listed in Table 2-1.

Table 2-1 BALANCE BEAM DESIGN REQUIREMENTS

Parameter	Value	Unit	Parameter	Value	Unit
$NI_{\min}$	1210	Aturn	$dF/dt_{Disturbance}$	6,906	N/s
$A_{\min}$	201	mm^2	$L_{\max}$	40	mH
dF/dt_{Weight}	110	N/s			

<u>Current Density (constraint 2)</u>

As was mentioned before, the maximum allowable current density ($J_{\max}$) is a constraint that prevents problems associated with coil overheating including insulation breakdown. This limit varies from 4 to 10 A/mm^2 [35]. The lower end is acceptable for totally enclosed systems and the higher end is acceptable for systems with forced air-cooling. This limit also depends on the wire material and type (flat/traditional). The $J_{\max}$ for traditional copper wire under natural convective cooling was assumed to be 6 A/mm^2 [36]. In order to satisfy the maximum current density limit the following condition must be satisfied:

$$0.5NI = J_{\max} A_{\min} < J_{\max} A \qquad (2-4)$$

Here, A is the cross sectional area of each coil. To obtain the number of turns in each coil, N is divided by 2. The minimum requirement for the coil cross sectional area is listed in Table 2-1. The designed coil has a cross sectional area of $280 \ mm^2$ which satisfies this constraint.

<u>Ampacity (constraint 3)</u>

National Electrical Safety Codes define ampacity (Amper capacity) as the maximum amount of electrical current that a conductor can carry without immediate or progressive deterioration. The value for ampacity can be found in American Wire Gauge (AWG) tables. The current in the wire should not exceed the wire ampacity,

$$I_{\max} < Ampacity \qquad (2-5)$$

The ampacity of various AWG wires is listed in Table 2-2. There are three values of ampacity for each wire size, which express the current at which it is safe to operate the wire with different temperature limits. These temperatures in Celsius are listed in the Ampacity column header.

Table 2-2 Suitable AWG wires (Est. stands for estimated)

AWG	Diameter (mm)	Ampacity 60/75/90	Est. Turns (Each Coil)	Est. Max Current (A)	Inductance (mH)
1	7.348	110 / 130 / 150	6	200.40	0.019
2	6.544	95 / 115 / 130	8	158.94	0.030
3	5.827	85 / 100 / 110	10	126.02	0.048
4	5.189	70 / 85 / 95	12	99.94	0.077
5	4.621		15	79.25	0.122
6	4.115	55 / 65 / 75	19	62.85	0.194
7	3.665		24	49.85	0.308
8	3.264	40 / 50 / 55	30	39.54	0.490
9	2.906		38	31.34	0.779
10	2.588	30 / 35 / 40	48	24.86	1.239
11	2.305		61	19.72	1.969
12	2.053	25 / 25 / 30	77	15.64	3.129
13	1.828		97	12.40	4.978
14	1.628	20 / 20 / 25	122	9.84	7.912
15	1.45		154	7.80	12.573
16	1.291	— / — / 18	194	6.19	20.009
17	1.15		244	4.91	31.779
18	1.024	— / — / 14	308	3.89	50.551
19	0.912		389	3.09	80.343
20	0.812		490	2.45	127.851
21	0.723		619	1.94	203.411
22	0.644		780	1.54	323.135
23	0.573		985	1.22	515.595

<u>Slew Rate Needed for The Beam's Vibration Without External Disturbance (Constraint 4)</u>

Using large a number of turns leads to smaller currents and in turn a smaller amplifier to maintain the same flux density. On the other hand, this amplifier should provide the system with an adequate slew rate, which can be calculated as:

$$\frac{dF}{dt} = \frac{dF}{dI_c}\frac{dI_c}{dt} = K_I \frac{V_c}{L} \qquad (2-6)$$

Here, K_I is a force coefficient and can be found in Section 3-2, V_c is the amplifier voltage. As can be seen, using higher amplifier voltages yields higher slew rates and therefore a more responsive system. Based on the available amplifiers the voltage (V_c) was chosen to be 80V. L is the inductance of the coil:

$$L = \frac{\mu_0 A_g N^2}{2g_0} \tag{2-7}$$

Plugging the inductance into Equation (2-6) yields:

$$\frac{dI_c}{dt} = \frac{V_c}{L} = \frac{2g_0 V_c}{\mu_0 A_g N^2} \tag{2-8}$$

$$\frac{dF}{dt} = K_I \frac{dI_c}{dIt} = \frac{\mu_0 N^2 A_g I_b}{g_0^2} \frac{2g_0 V_c}{\mu_0 A_g N^2} = \frac{2V_c I_b}{g_0} \tag{2-9}$$

Here, A_g is the pole face area and I_b is the bias current. The pole face area design can be found under the magnetic core in this Section. The bias current is designed to provide a flux density in the mid range of the linear region of the magnetization curve. For the material used in the balance beam (M19 silicon steel), the end of the linear region of the B-H curve is at a flux density of 1.2T ($B_{Knee} = 1.2T$), therefore the bias current is the current that can generate a flux density of 0.6T. Based on the Eq. (2-9) it is interesting to note that even though the time rate of change of current is heavily dependent on the number of turns (N), the time rate of change of force (slew rate) is not dependant on N. Generally, the external forces dictate the required force slew rate, but the slew rate should also be adequate to balance the beam when the unstable pole is excited. In that case, the vibration frequency of the beam is f_{Pole} and the torque acting on the beam is a result of the off-centered weight, and the actuator should cancel this torque:

$$\dot{T}_{Actuator} = \dot{T}_{Weight} \Rightarrow L_a \frac{dF}{dt}_{Weight} = L_g W f_{Pole} \Rightarrow \frac{dF}{dt}_{Weight} = f_{pole} W \frac{L_g}{L_a} \qquad (2-10)$$

Here, dF/dt_{Weight} is the required slew rate to balance the beam under it's off-centered weight (see Table 2-1), W is the weight of the beam, L_a is distance between the pivot and the electromagnet at each end, and L_g is the distance between the beam's center of gravity and pivot. The unstable pole frequency can be approximated using the system's dynamic equation:

$$J\ddot{\theta} = -D\dot{\theta} + L_a F, \quad F = K_I I_c + K_X x, \quad x = L_a \theta \qquad (2-11)$$

Here, J is the beam's mass moment of inertia, θ is the angular displacement of the beam with respect to the horizon, and K_I and K_X are the force coefficients that can be found in Section 3-2. The transfer function can be calculated as:

$$G(s) = \frac{\theta(s)}{I_c(s)} = \frac{L_a K_I}{Js^2 + Ds - L_a^2 K_X} \qquad (2-12)$$

For the test rig used in this work, the friction coefficient (D) is negligible. Therefore, the unstable pole can be calculated as follows:

$$S = f_{pole} = \sqrt{\frac{L_a^2 K_x}{J}} = \sqrt{\frac{L_a^2 \mu_0 N^2 A_g I_b^2}{J g_0^3}} \qquad (2-13)$$

Here, f_{pole} is the frequency of the unstable pole. The value for the f_{pole} can be found in Table 2-4.

Slew Rate needed for the external dynamic force (constraint 5)

The test rig will be tested with an external force of up to 600N (the maximum force that can be generated using the nonlinear approach), but with low frequencies (frequencies smaller than 50Hz) to resemble scenarios like the effect of earthquake on an energy storage flywheel, a storm on a wind turbine, etc. The actuator should have a large enough slew rate to deal with the external dynamic force. Basically the time rate of change of the actuator torque should be at least equal to the time rate of change of the torque generated by the disturbance forces.

$$\dot{T}_{Actuator} = \dot{T}_{Disturbance} \Rightarrow L_a \frac{dF}{dt}_{Disturbance} = L_w F_w f_w \Rightarrow \frac{dF}{dt}_{Disturbance} = f_w F_w \frac{L_w}{L_a} \qquad (2-14)$$

Here, $dF/dt_{Disturbance}$ is the required slew rate to balance the beam under an external disturbance, while f_w and F_w are the frequency and the amplitude of the external disturbance. L_w is the distance between the external force and the pivot. The required dynamic slew rate value can be found in Table 2-1.

Coil inductance (constraint 6)

Since there is a limit on the amplifier's switching frequency, the time rate of change of the control current is limited:

$$\frac{dI_c}{dt} = \frac{V_c}{L} < \text{Switching Frequency} \qquad (2\text{-}15)$$

Therefore, there is a limitation on the actuator's inductance and subsequently the number of turns:

$$L = \frac{\mu_0 A_g (N)^2}{2g_0} < L_{\max} \;\; \Rightarrow \;\; N < \sqrt{\frac{2g_0 L_{\max}}{\mu_0 A_g}} \qquad (2-16)$$

Since there are two coils in each electromagnet the number of turns is multiplied by 2. In the amplifier's data-sheet there is usually a guide for calibrating the amplifier for different inductances of the load. For the amplifier used in this work (Copley 315), the highest inductance listed for calibration ($L_{\max}$) is 40mH. Therefore the coil inductance should not exceed this value. The coil inductance for different AWG wires is listed in Table 2-2.

<u>Wire size and number of turns</u>

Constraints 1 and 2 determine the maximum required magneto-motive force and the coil cross sectional area. In order to apply the constraints, one needs to know the approximate number of turns and the operating current for each wire size. The number of coil turns that can fit into the coil area can be approximated as follow:

$$NA_{wire} = \eta A \qquad (2-17)$$

Here, A_{wire} is the cross sectional area of each wire, A the coil cross sectional area that can be found using Constraint 2, and η is the fraction of the coil area that is filled by the wires (packing density). The value of η depends on the packing shape of the wire. This value ranges from $\pi/4 \approx 0.79$ for square packing to $\sqrt{3}\pi/6 \approx 0.91$ for hexagonal packing [37]. Tight coils are hexagonally packed; therefore Equation (2-17) can be rewritten as:

$$N \approx \frac{2\sqrt{3}}{3}\frac{A}{d^2} \qquad (2-18)$$

Here, d is the wire diameter. This approximation is more accurate for a higher number of turns but a coil with very few turns needs a huge current supply and is not suitable anyway from an amplifier selection prospective. Now that the number of turns is estimated, Constraint 1 can be used to approximate the maximum current:

$$I_{\max} = \frac{B_{sat}\left(2g_0 + \dfrac{L_s}{\mu_r}\right)}{N\mu_0} \qquad (2-19)$$

In the test rig used for this work, there are two coils per actuator. In addition, when the beam is at its maximum angle the airgap is twice the nominal airgap. Therefore N and g should be multiplied by two and Equation (2-19) should be modified to the following:

$$I_{\max} = \frac{B_{sat}\left(4g_0 + \dfrac{L_s}{\mu_r}\right)}{2N\mu_0} \qquad (2-20)$$

The value of μ_r for different flux densities can be calculated as (see Section 3-3):

$$\mu_r = aB + b \qquad (2-21)$$

Here a and b are constants obtained from the silicon iron B-H curve with (a=-9434.9, b=15650). For each wire size, the ampacity, slew rate, and inductance are listed in Table 2-2. Using this information, constraints 3-6 can be applied. Table 2-2 indicates that wires with large diameter (AWG8 or less) are not appropriate due to the ampacity constraint (Constraint 3), and also because the current that is needed is very large and amplifiers with such large currents are not available or extremely expensive. The available amplifier has a maximum continuous operating current of 15A and peak current of 30A, therefore AWG9-12 wires are not appropriate either. Wires with very small diameters (AWG18 or higher) do not satisfy the actuator inductance constraint (constraint 6). Between the remaining choices AWG14 has a small inductance and its maximum operating current is within the amplifier’s operating range and was therefore chosen.

Magnetic Core

The iron core and target pieces were built from M-19 Silicon steel laminations. Silicon steel is probably the most commonly used magnetic material in motion control products. Even though it’s a bit more expensive compared to other common materials, the performance and low-loss characteristics justify this expense. This material has different grades, which is related to the core losses. M19 offers nearly the lowest core loss in this class of material, with only a small cost increase. The pole faces of the core and target pieces are polished for a more accurate airgap. The sharp corners on the lamination stack are lightly rounded in order to prevent damage to the coils. The cross sectional area of the core has a direct effect on the force generated by the electromagnets. Large cross sectional areas create large forces which means other parts of the test rig should be designed accordingly to deal with the large force. Therefore a large cross sectional area is not desirable. On the other hand the cross sectional area should be large enough for the coil to be wrapped around it. The cross sectional area was designed to be

$A = 0.5in \times 0.5in$ for the test rig. The magnetic material is laminated to minimize the generation of eddy currents. Each lamination has a thickness of 0.018 inch (0.45 mm). Under normal operating conditions the electromagnets should operate without saturation; however, for larger currents the entire magnetic circuit should saturate uniformly. If only a part of the material saturates, the entire electromagnet will not operate properly. Therefore the magnetic material that is not saturated is not benefiting the system. Target lamination stacks (bar-shaped lamination stacks) have the same cross sectional area as that of the core lamination stacks (U-shaped lamination stacks) to maximize the use of the magnetic material and have nearly all of it saturate at the same coil current level.

2.4 Mechanical components

<u>Beam Bending Modes</u>

High frequency external disturbances can potentially excite the beam's first few bending modes; therefore the beam's bending mode frequencies should be calculated to insure rigid body motion. The beam is centered on a pivot with forces exerted by two electromagnets at both ends. Due to symmetry, the angle of rotation and the displacement in the center of the beam is zero. As a result, the beam's bending modes are the same as that of a cantilever half beam (see Fig. 2-3).

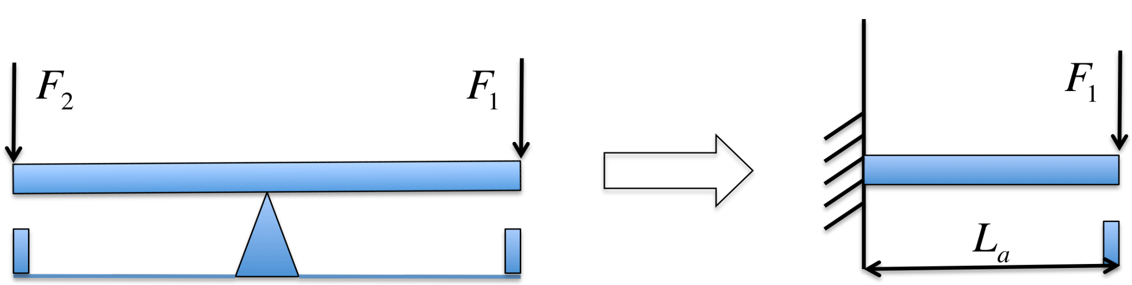

Figure 2-3 The Balance Beam Bending Mode Model

The first two bending mode frequencies are listed below [38] (Thomson & Dahleh, 1997):

$$f_1 = \frac{1}{2\pi}\frac{3.5156}{L_{beam}^2}\sqrt{\frac{EI_{beam}}{\rho A_{beam}}} \qquad (2-22)$$

$$f_2 = 6.268 f_1 \qquad (2-23)$$

Here, E is Young modulus of elasticity and ρ is the density of aluminum. I_{beam} is the area moment of inertia of the beam, and A_{beam} is the cross sectional area of the beam. Table 2-4 shows the calculated values for these parameters. It's of importance to note that the half-beam models just the symmetric mode shapes. The beam's first bending mode is symmetric; therefore f_1 is the first bending frequency. The beam's second mode shape is not symmetric; therefore f_2 is the frequency of the third mode shape of the beam, which is symmetric. The second bending frequency is between f_1 and f_2. The experiment in this work will be conducted assuming a rigid beam. Therefore even the first bending mode should be far away from the unstable pole frequency and accurate calculation of the second and third bending modes are not of concern. As a rule of thumb f_1 should be at least 5 time larger than f_{Pole}. The following table shows how a change in the airgap and beam thickness affects the unstable pole frequency and the bending modes.

Table 2-3 BALANCE BEAM DESIGN PARAMETERS

$g_0(mils)$	$h(in)$	$J(gm^2)$	$I_b(A)$	$I_{max}(A)$	$f_{Pole}(Hz)$	$f_1(Hz)$
15	0.75	94.495	1.74	6.26	163	70
30	0.75	94.495	3.40	10.67	58	70
45	0.75	94.495	5.05	15.08	31	70
15	1.75	153.335	1.74	6.26	128	162
30	**1.75**	**153.335**	**3.40**	**10.67**	**45**	**162**
45	1.75	153.335	5.05	15.08	25	162
15	2.75	221.678	1.74	6.26	106	255
30	2.75	221.678	3.40	10.67	38	255
45	2.75	221.678	5.05	15.08	20	255

Beam Design

The beam was designed to be long enough to house the target pieces and thick enough to have acceptable bending modes. The beam has an overall length of 18.625 inches (473 mm), a depth of 1.75 inches (44 mm), and a width of 3.25 inches (83 mm). It is machined from aluminum with a relative permeability of 9. Each side of the beam has 19 evenly space threaded holes to allow for the addition of balancing weights or an external source of excitation (for instance an electric motor with a half-disk mounted on it's rotor can be used for sinusoidal external excitation). The mass of the beam including the target laminations, the target lamination holders and the end caps is 13.519 lb (6.132 Kg).

It is very important for the beam to have its center of gravity at the pivot point (see Fig. 2-2). To verify this, a single mass of 20g was moved along the beam until it was perfectly balanced. The distance between the balancing mass and the pivot was then measured and used to measure the center of gravity. The center of gravity was calculated to be just 1.03 mm from the pivot point, which is good enough for the testing purposes of this work. If required for final balancing, small balancing weights can be added to the beam to fine tune the center of gravity.

Table 2-4 BALANCE BEAM DESIGN PARAMETERS

Parameter	Value	Unit	Parameter	Value	Unit
I_b	3.3967	A	dI_c / dt	6214	A/s
V_c	80	V	dF / dt	713,281	N/s
E_{Aluminum}	69	GPa	f_{Pole}	45	Hz
ρ_{Aluminum}	2700	kg / m^3	f_1	162	Hz
K_I	115	N/A	f_2	1017	Hz
K_X	511704	N/m			

Pivot design

To allow rotational freedom a pivot was needed. Here a knife-edge and a thin notch is used as the pivot assembly. This method is chosen because of its simplicity and low friction. The pivot assembly is composed of the pivot that is screwed to the base plate and the balance plate, which is screwed to the beam. The balance plate has a notch depth of 0.094 inch (2.39 mm) and notch width of 0.188 inch (4.77 mm). The pivot length was chosen to provide the system with the designed nominal airgap of 0.03 inch (0.762 mm).

Base Plate

The base plate is a 1.5-inch (38.1 mm) thick plate made of aluminum and weighs 13.312 lb (6.038 kg) including the electromagnets, sensor stands, and the pivot. It is designed to be large enough to hold everything together and thick enough to provide adequate rigidity.

Electromagnet and target piece stands

Each electromagnet is held firmly in its place by an electromagnet stand and a clamp that bolts into it. The target laminations are fixed at each end of the electromagnet holders by clamps. The target lamination holders are in turn bolted to the beam. The test rig has three electromagnets (two for controls and one for disturbance), therefore there are three target laminations. In order to keep the symmetry, a dummy weight is clamped to the left side of the left target lamination holder (see Figure 2-2). The dummy weight was chosen such that it eliminates the beam's small unbalance due to machining tolerances.

Sensor stands/ Auxiliary bearings

Eddy current sensors are used to sense the position of the balance beam. Each eddy current sensor is housed inside a sensor stand that is designed to protect the sensor from impact with the beam, while holding it in place. Each stand has a notched area in the middle. The sensors are mounted in this area to ensure the sensor is never closer than 0.06 inch (0.13 mm) to the beam. These stands also act as auxiliary stops to prevent the beam from contacting and damaging the pole faces of the electromagnets.

Mechanical assembly

The beam's length has a direct relationship to its angle of rotation (with a fixed airgap, a longer beam means a smaller angle of rotation) and plays an important role in system modeling and control. Calibration of precise airgaps between each electromagnet and the target lamination is extremely important. The sensor stands, the electromagnet holders, and the pivot can be shimmed to adjust the airgap. Shims are positioned under the pivot plate to adjust the overall airgap. The airgap for each individual electromagnet can be adjusted by placing a shim under the holder. In order to restrict the angular motion of the beam, shims can be placed under the sensor stands. The nominal airgap is designed to be 30 mils (0.762 mm). There is a 3 mils offset provided by the sensor stands to prevent the beam from contacting the electromagnets. Therefore the total airgap range is 3-27 mils for each electromagnet. The length from the center of the electromagnet to the pivot is 6.125 inch (155 mm). The disturbance electromagnets are placed at 9.0625 inch (230 mm) from the center pivot with an airgap of 30 mils. This distance gives the disturbance electromagnet a long enough lever arm to produce the same torque as the control electromagnets while operating in the linear region. In other words the torque produced by the disturbance electromagnet at 1.2T (end of the linear region) equals the torque produced by the control electromagnet at 1.6T (end of the nonlinear region).

2.5 Electrical and electronic components

<u>Power amplifier</u>

Table 2-2 indicates that the amplifiers should provide at least 80 volts and 9.61 amperes. Based on the Apex amplifier table (see appendix A) a SA12 PWM amplifier was initially chosen. SA12 has a very high switching frequency (200 kHz) and can provide a wide range of voltages (16-200V) and currents (0-15A continuous). However, two Copley Corporation Model 315 amplifiers were available from another test rig. These amplifiers can provide voltages in the range of 24-160V and a continuous current of 15A. They are PWM amplifiers with a switching frequency of 24 kHz. This type of amplifier is capable of operating in both current and voltage mode. Typically in magnetic bearing systems current mode is used. This mode maintains the current at a desired level by pulse width modulation. In voltage mode operation, the amplifier maintains a constant voltage, which can be useful for some other control strategies. Current mode operation was chosen for this work.

<u>Eddy current displacement sensors</u>

The airgap and consequently the beam angle are measured by multiNCDT 100 model DT110(40)-S-U1(29)-A,C4,5 Sensors produced by Micro-Epsilon. The sensor has a nominal range of 40 mils (1 mm), displacement sensitivity of 265 mV/mil, and bandwidth of 10 kHz. The output of the sensor is fed to the system's module that contains the circuitry for linearizing the output. The beam angle can be calculated from the sensor measurements, which in turn is used by the control algorithm.

Data Acquisition Card

For analog to digital (A/D) conversion, a PCI-DAS6034 card, produced by Measurement Computing is used. The board provides up to 16 analog inputs. Each input can be individually configured as single ended or differential. The board's input ranges are bipolar only and the software can choose any of the four bipolar ranges of ±10V, ±5V, ±500mV, or ±50mV. The card has a 16-bit resolution.

For digital to analog (D/A) conversion, a PCI-DDA08/12 card, produced by Measurement Computing is used. The board provides up to 8 analog outputs. The D/A converters can be independently configured for either bipolar or unipolar. Bipolar ranges are ±10V, ±5V, and ±2.5V. Unipolar ranges are 0 to 10V, 0 to 5V, and 0 to 2.5V. The card has a 12-bit resolution and a minimum of 5,000,000 V/s slew rate on the analog output, which is more than adequate.

RTAI and Linux

Control algorithms are executed in the real time application interface (RTAI) environment. Matlab's xPCTarget was also considered as an option but RTAI proved to be easier to use and since it is an open source product operating in Linux, it is also free. Control algorithms are developed in Scicos, which is an environment similar to Matlab's Simulink.

2.6 System specifications summary

This chapter has described the reason for developing the test rig as well as the design details, calibration, and specifications of different parts of the experimental test rig. Table 2-5 presents various system specifications and design dimensions.

Table 2-5 BALANCE BEAM DIMENSIONS

Symbol	Specification	Value	Unit
J	Moment of inertia of the beam	153.33	gm^2
D	Friction coefficient in the pivot	0	Ns/m
L_g	Distance between the pivot and center of gravity	1.04	mm
L_a	Distance between the pivot and the control electromagnets	0.1556	m
L_{se}	Distance between the pivot and the sensors	0.0889	m
L_w	Distance between the pivot and the disturbance electromagnets	0.2302	m
L_{beam}	Total length of the beam	0.4731	m
g_0	Airgap between the core and target lamination	0.762	mm
A_g	Pole face area of the core lamination	161.3	mm^2
L_s	Length in which the flux travels inside the silicon iron	0.178	m
W	Weight of the beam including the target laminations	60.134	N
$\theta_{\max}$	Maximum angle of rotation of the beam	0.0048	Rad
N	Number of turns in each electromagnet with two coils	220	$turns$
I_b	Bias current	3.40	A
I_{Knee}	The current that produces the knee flux density	6.78	A
$I_{\max}$	Maximum operating current of the electromagnets	10.67	A
$I_{c\max}$	Maximum control current	7.27	A
L	Inductance of each electromagnet with two coils	6.4	mH

3 Nonlinear Model

In this chapter a nonlinear model for magnetic bearings is proposed to reach the objective of operation in a high flux mode. The nonlinear model includes the nonlinear material magnetization behavior for the silicon iron. In the first section, a brief background for magnetic circuit modeling is included in which the material magnetization nonlinearity is taken into account. In Section 2 the conventional linear force model is summarized. A nonlinear force model is proposed in Section 3. In Section 4, the test rig used for all experimental work is discussed. Section 5 contains the linear test rig model that is used as a benchmark. In Section 6, the nonlinear model for the test rig is developed and finally, in Section 7 the physical constraints on the test rig are explained.

3.1 Nonlinear Magnetic Circuit Analysis

In this section a magnetic circuit analysis is conducted for a thrust magnetic bearing.
A magnetic circuit is made up of a closed loop containing the magnetic flux. The flux is generated by electromagnets (coils) and sometimes by a combination of permanent and electromagnets. The coils are wrapped around the magnetic cores consisting of ferromagnetic materials such as silicon iron. There may also be air gaps or other materials in the loop as well (see Fig. 3-1).

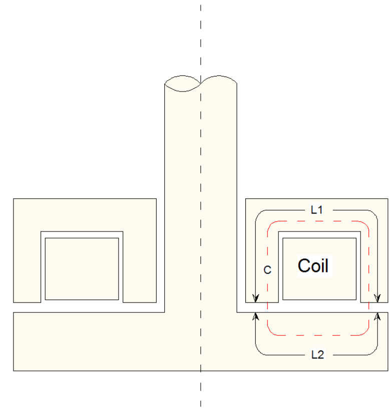

Figure 3-1 Magnetic Circuit of a Thrust AMB

In order to analyze magnetic circuits, two basic laws (Ampere's integral law and flux continuity law) are used. Ampere's integral law applies to a contour such as C_1 , which is shown in Figure 3-1. It states that, the integral of magnetic field over a contour is equal to the net magneto-motive force (MMF).

$$\oint_{C_1} H.ds = \int_{S_1} J_{coil}.dA \qquad (3-1)$$

Here, H is the magnetic field, J_{coil} is the current density and S_1 is the area of the contour C_1. Ampere's integral law plays a role similar to Kirchhoff's voltage law in electric circuits. The flux continuity law is similar to Kirchhoff's current law. The continuity law states that through a closed surface or a node, the net magnetic flux (ϕ) is zero.

$$\sum \phi = 0 \qquad (3-2)$$

A thrust magnetic bearing consists of a magnetic actuator that is mounted on the stator and a disk mounted on the rotor that the magnetic actuator acts upon (see Fig 3-1). For magnetic circuit analysis, the following notations are introduced. H_1 is the magnetic field in the magnetic actuator (upper part of the magnetic circuit), L_1 is the length of the magnetic circuit in the magnetic actuator and A_1 is the cross-sectional area (pole face area) of the magnetic actuator. Similarly H_2, L_2, and A_2 are the corresponding parameters in the disk (lower part of the magnetic circuit) and H_g, L_g, and A_g are the corresponding parameters in the airgap. Applying Ampere's law yields:

$$H_1L_1 + H_2L_2 + 2H_g g = NI \qquad (3-3)$$

Here, N and I are the number of turns and the electric current in the coil. The magnetic flux density (B_g) and the magnetic field (H_g) in the airgap are linearly related as follows,

$$B_g = \mu_0 H_g \qquad (3-4)$$

Here, μ_0 is the permeability of free space. Unlike in the airgap, the flux density (B) and magnetic field (H) in the magnetic material are related nonlinearly. Magnetization tables can be used to find one from the other.

$$B_1 = f(H_1), \quad B_2 = f(H_2) \qquad (3-5)$$

Here, B_1 and B_2 are the magnetic flux density in the magnetic actuator and the disk respectively. The flux continuity law (Eq. 3-2) implies that the net flux through each section of the circuit is the same, which results in,

$$\phi = B_1 A_1 = B_2 A_2 = B_g A_g \tag{3-6}$$

In order to use the magnetic material effectively, magnetic bearings are designed in a way such that in the case of high electric currents, all the lamination material saturates at approximately the same time; therefore, the flux density is approximately the same everywhere. To achieve the same flux density, an equal cross sectional area is required around the entire circuit (see Eq. (3-7)).

$$\left.\begin{array}{ll} \text{AMB Design} & \Rightarrow A_1 = A_2 = A_g = A_g \\ \text{Continuity Law} & \Rightarrow \phi = B_1 A_1 = B_2 A_2 = B_g A_g \end{array}\right\} B_1 = B_2 = B_g = B_g \tag{3-7}$$

In addition, since the flux density is the same, the magnetic field should be the same everywhere in the magnetic material (see Eq. (3-8)).

$$\left.\begin{array}{l} B_1 = B_2 \\ \text{Same Magnetization Properties} \end{array}\right\} H_1 = H_2 = H_s \tag{3-8}$$

Here, (H_s) is the magnetic field in the magnetic material. Substituting Eqs. 3-4,3-5,3-7 and, 3-8 into the magnetic circuit laws (Eqs. 3-3 and 3-6) results in:

$$\left.\begin{array}{l} \dfrac{\phi}{A_g} = B_1 = B_g \Rightarrow f(H_1) = \mu_0 H_g \\ H_s(L_1 + L_2) + 2H_g g = NI \end{array}\right\} H_s(L_1 + L_2) + 2\frac{f(H_s)}{\mu_0} g = NI \tag{3-9}$$

The goal here is to find the magnetic circuit flux density as a function of the current. The magnetic flux density and the magnetic field in the magnetic material are assumed to be related via a variable relative permeability (μ_r).

$$f(H_s) = \mu_0 \mu_r(B) H_s \tag{3-10}$$

By using Eq. (3-10), Eq. (3-9) simplifies to,

$$H_s L_s + 2\mu_r H_s g = NI \quad \Rightarrow \quad H_s = \frac{NI}{L_s + 2\mu_r g} \tag{3-11}$$

$$B = \mu_0 \mu_r H_s = \frac{NI}{\dfrac{L_s}{\mu_0 \mu_r(B)} + \dfrac{2g}{\mu_0}} \tag{3-12}$$

Where, $L_s = L_1 + L_2$. The flux density is found as a function of the electric current, but still needs to be determined from the nonlinear magnetization curve. An approximation for is provided in the next section. The flux is calculated as:

$$\phi = BA_g = \frac{NI}{\dfrac{L_s}{\mu_0 \mu_r(B) A_g} + \dfrac{2g}{\mu_0 A_g}} \tag{3-13}$$

The first term in the denominator is the reluctance of the silicon iron and the second term is the reluctance of the airgap.

3.2 Linear Force Model

Traditionally the magnetic bearing force is calculated by the following equations:

$$F = \frac{A_g}{\mu_0} B^2 \tag{3-14}$$

$$B = \left(\frac{\mu_0 N I}{2 g_0} \right) \tag{3-15}$$

Equations (3-14) and (3-15) assume that the reluctance of the magnetic material is negligible as compared to the reluctance of the airgap. Substituting Eq. (3-15) into Eq. (3-14) yields the electromagnet force equation:

$$F = \frac{\mu_0 A_g N^2 I^2}{4 g_0^2} \tag{3-16}$$

Where the magnetic material is neglected. Electromagnetic force is always attractive; therefore, in order to have a stable system, the electromagnets in magnetic bearings operate in pairs (Fig. 3-2).

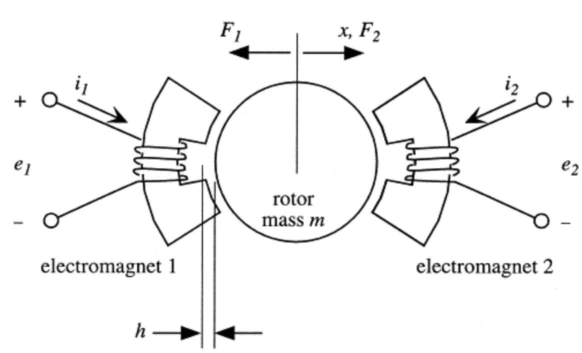

Figure 3-2 A Pair of Electromagnets

The electromagnetic force is highly nonlinear with respect to the input current and the airgap. In order to linearize the force equation, the current at each electromagnet is typically separated into bias and control components. The left electromagnet current is $I_1 = I_b + I_c$ and the right electromagnet's current is: $I_2 = I_b - I_c$ Therefore, the force equation for each actuator can be written as:

$$F_1 = \frac{A\mu_0 N^2 (I_b + I_c)^2}{4(g_0 + x)^2} \qquad (3-17)$$

$$F_2 = \frac{A\mu_0 N^2 (I_b - I_c)^2}{4(g_0 - x)^2} \qquad (3-18)$$

Here, F_1 and F_2 are the forces of the left and right electromagnets respectively, I_b is the biased current, I_c is the control current and x is the rotor's displacement. The net force on the rotor is,

$$F = F_1 - F_2 \qquad (3-19)$$

Substituting Eqs. (3-17) and (3-18) into Eq. (3-19), results in the following force equation,

$$F = \frac{\mu_0 N^2 A_g}{4}\left(\frac{(I_b + I_c)^2}{(g_0 - x)^2} - \frac{(I_b - I_c)^2}{(g_0 + x)^2}\right) \qquad (3-20)$$

Using Taylor series expansion, Eqn. (3-20) can be simplified to:

$$F = \frac{\mu_0 N^2 A_g I_b^2}{g_0^{\ 3}} x + \frac{\mu_0 N^2 A_g I_b}{g_0^{\ 2}} I_c + H.O.T$$

$$F \approx K_X x + K_I I_c \qquad K_X = \frac{\mu_0 N^2 A_g I_b^2}{g_0^3} \qquad K_I = \frac{\mu_0 N^2 A_g I_b}{g_0^2} \tag{3-21}$$

Eq. (3-21) is linear with respect to both the displacement and the control current.

3.3 Proposed Nonlinear Force Model

In the standard linear formulation, it is assumed that the magnetic reluctance of silicon iron is negligible compared to the magnetic reluctance of the airgap (these two reluctances can be seen in Eq. (3-13)). However, for a large magnetic flux, the magnetic reluctance of the silicon iron is significant. This makes the system highly nonlinear. By modeling this nonlinearity, the nonlinear flux density was obtained in Eq. (3-12).

In conventional AMB models it is assumed that the relative permeability is a constant till the magnetic flux reaches a knee value (B_{knee}) and then the material saturates. In order to get to higher load capacity, a more precise flux model is needed. In this Thesis, silicon iron behavior is studied more accurately and therefore the magnetization curve is divided into 3 different regions:

1. Linear region: The reluctance of the magnetic material is not significant (less than 5% of the airgap reluctance) and Eq. (3-15) can be used for the flux density.
2. Nonlinear region: The magnetic reluctance of the magnetic material should be taken into account Eq. (3-12) and increasing the current yields a significant increase in the electromagnet's force.
3. Nearly saturated region: The magnetic reluctance of the magnetic material is very significant and even a significant increase in the electric current won't increase the force appreciably.

In order to determine these regions, the test rig's electric current, force, and the reluctance ratio should be found for a fixed flux density.

The magnetization curve and relative permeability of M19 silicon iron are shown in the following Figures.

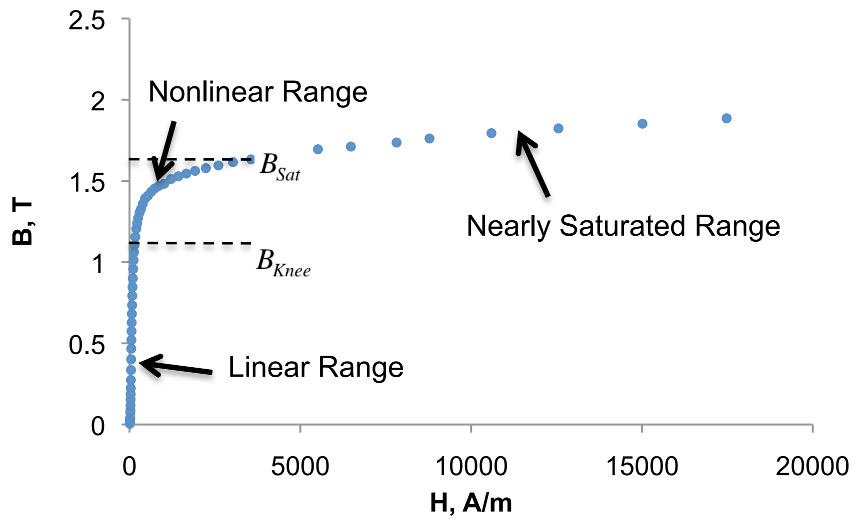

Figure 3-3 M19 Magnetization Curve

As can be seen, the material is very responsive to the change in magnetic field for smaller values of H but at higher values of H (above the knee point in the curve), it becomes less responsive and finally saturates.

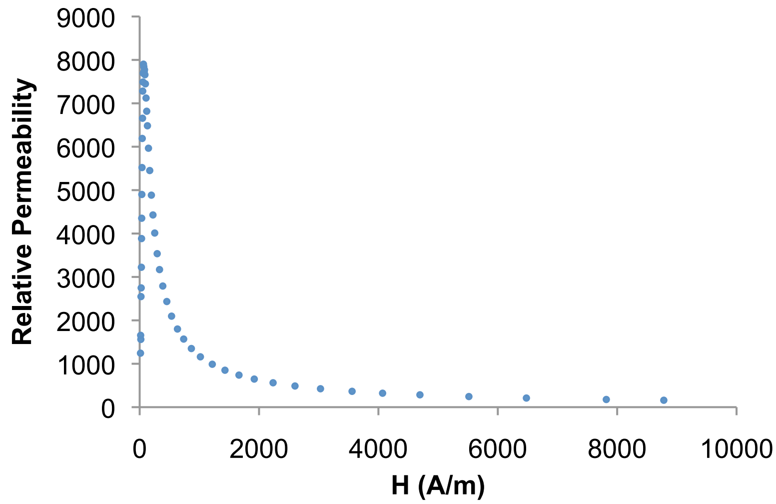

Figure 3-4 M19 Relative Permeability

The relative permeability is very large for smaller values of B and H and usually it is considered as a constant.

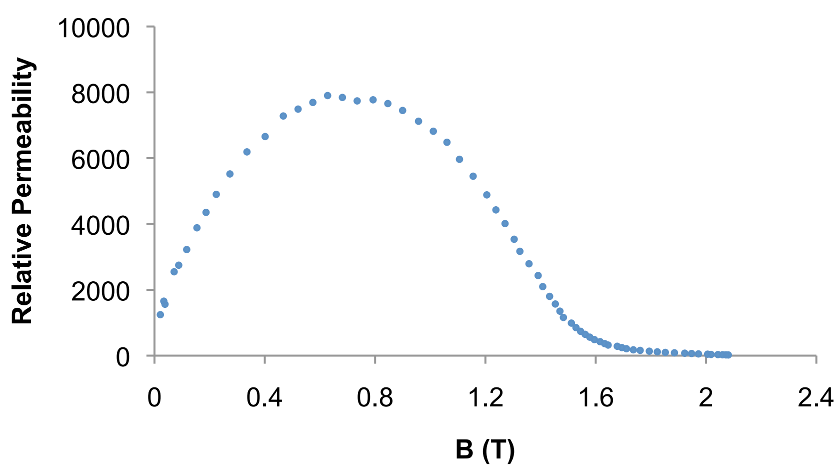

Figure 3-5 M19 Relative Permeability

When μ_r is large the reluctance of the silicon iron ($\frac{L_s}{\mu_0 \mu_r A_g}$) is negligible compared to the reluctance of the airgap ($\frac{2g}{\mu_0 A_g}$) and Eq. (3-12) simplifies to Eq. (3-15). For large values of magnetic flux density, the relative permeability decreases significantly, therefore the reluctance of the silicon iron gains more significance compared to the airgap and should not be neglected. In order to provide an example for the importance of the silicon iron's reluctance, the specifications of the balance beam test rig (Table 2-3) are used. The test rig is explained in more detail in Section 3-4 and Chapter 2. Figure (3-6) shows the ratio of the reluctance of the silicon iron to the reluctance of the airgap in the balance beam test rig.

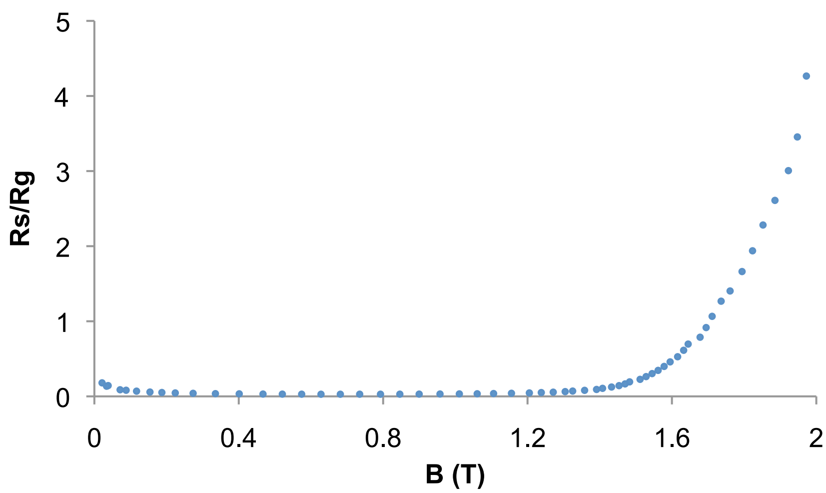

Figure 3-6 Magnetic Circuit Reluctance Comparison

As was mentioned before, Ampere's law (Eq. (3-3)) can be simplified to,

$$H_s L_s + 2 H_g g_0 = NI \tag{3-22}$$

When the flux density (B) is known, H_s is obtained from the silicon iron magnetization table and H_g is obtained as $H_g = B/\mu_0$, Therefore the electric current is calculated as,

$$I = \frac{H_s(table)L_s + 2g_0 B/\mu_0}{N} \qquad (3-23)$$

The magnetic force is calculated using Eq. (3-14). In Table 3-1 the electric current, the nonlinear magnetic force, the estimated linear force, and the reluctance ratio, corresponding to a known flux density are tabulated.

Table 3-1 Test rig's force, electric current and (M19-si-Fe) reluctance ratio

B (T)	Hs (A/M)	I (A)	Force (N)	Force (linear prediction) (N)	Force Error (%)	Reluctance Ratio
0.1	29	0.3	3.5	4	14	0.07
0.2	36	0.5	13	14	9	0.05
0.3	43	0.8	29	31	7	0.04
0.4	48	0.9	41	44	7	0.03
0.5	55	1.2	70	74	6	0.03
0.6	63	1.5	101	107	6	0.03
0.7	69	1.6	119	126	6	0.03
0.8	81	1.9	161	171	6	0.03
0.9	96	2.1	208	220	6	0.03
1.0	118	2.4	262	280	7	0.03
1.1	147	2.6	314	338	8	0.04
1.2	196	2.9	373	408	9	0.05
1.3	293	3.2	437	494	13	0.06
1.4	534	3.6	509	623	22	0.11
1.5	1216	4.3	587	883	50	0.23
1.6	2602	5.4	653	1,391	113	0.46
1.7	5516	7.5	737	2,707	267	0.92
1.8	10595	11.0	826	5,857	609	1.7
1.9	17480	15.7	913	11,890	1,203	2.6
2.0	36064	28.0	1033	37,940	3,574	5.1
2.1	79973	56.8	1132	155,490	13,635	10.8

As can be seen in Table 3-1, the reluctance ratio is significant for flux densities larger than 1.2T (knee point) and we need to use the nonlinear force model. At a flux density of slightly larger than 1.7T the silicon iron reluctance becomes larger than the airgap reluctance and the silicon iron magnetization behavior plays a larger role in the flux density of the magnetic circuit than the airgap. After 1.6T, the coil current needs to be significantly increased in order to increase the force; therefore, at this point the material is considered to be fully saturated. By using Eq. (3-23) the electric current was calculated assuming the flux density is known. However, for AMB systems, the input is the electric current, therefore flux density and force should be found as a function of the electric current. In order to achieve this, the relative permeably as a function of magnetic flux is required.

Using the data from Figure (3-5), a linear curve fit is used to estimate the silicon iron relative permeability for flux densities above B_{knee} (Fig. 3-7). Quadratic and cubic curve fits for the relative permeably were also considered. Even though a higher order equation is more accurate, it increases the complexity of the model and in this case, it decreases the quadratic error by less than 1 percent. Therefore a linear fit was deemed to be accurate enough for this work.

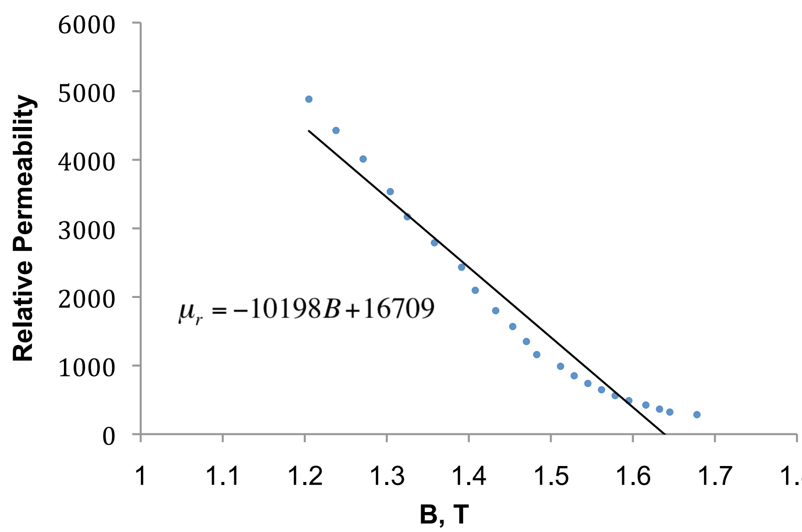

Figure 3-7 M19 Relative Permeability (1.2T<B<1.6T)

The relative permeability is estimated as,

$$\mu_r = aB + b, \qquad a = -10198, \qquad b = 16709 \tag{3-24}$$

By substituting Eq. (3-24) into Eq. (3-12), the nonlinear flux density equation is obtained as:

$$2gaB^2 + (2gb + L_s - a)B - NI\mu_0 b = 0 \tag{3-25}$$

Solving Eq. (3-25) and substituting it into the force equation (Eq. (3-14)) yields the nonlinear force equation for the right and left actuators in Figure 3-2.

$$F_1 = \frac{1}{g_0^2\left(1 + \frac{2x}{g_0}\right)}\left[c_1 I_1^2 + c_2 x + c_3 + (c_4 I_1 + c_5 x + c_6)\sqrt{c_7 I_1^2 + c_8 I_1 x + c_{10} x + c_{11}}\right] \tag{3-26}$$

$$F_2 = \frac{1}{g_0^2\left(1 - \frac{2x}{g_0}\right)}\left[c_1 I_2^2 - c_2 x + c_3 + (c_4 I_2 - c_5 x + c_6)\sqrt{c_7 I_2^2 - c_8 I_2 x - c_{10} x + c_{11}}\right] \tag{3-27}$$

Here I_1 and I_2 are the electric currents in the left and right actuators, g_0 is the nominal airgap (the airgap when the rotor is centered), $g = g_0 \pm x$, and $c_1, c_2, ..., c_{11}$ are constants that are dependent on the system parameters.

$$\begin{aligned}
&c_1 = \frac{A\mu_0}{8N^2}, \qquad c_2 = \frac{a(L_1 + L_2)A + 2a^2 A g_0}{2\mu_0 b^2} \\
&c_3 = \frac{A(L_1 + L_2)^2 + 4a(L_1 + L_2)A g_0 + 4a^2 A g_0}{8\mu_0 b^2} \\
&c_4 = \frac{AN}{2}, c_5 = \frac{aA}{b\mu_0}, c_6 = \frac{A(L_1 + L_2) + 4Aag_0}{4b\mu_0} \\
&c_7 = \frac{\mu_0^2}{16N^2}, \qquad c_8 = \frac{\mu_0 N(2ag_0 - L_1 - L_2)}{8b} \\
&c_9 = \frac{\mu_0 Na}{4b}, \qquad c_{10} = \frac{a(L_1 + L_2) + 2a^2 g_0}{4b^2} \\
&c_{11} = \frac{(L_1 + L_2)^2 + 4a(L_1 + L_2)g_0 + 4a^2 g_0^2}{16b^2}
\end{aligned} \tag{3-28}$$

3.4 Balance Beam

In this thesis a balance beam test rig is used for experiments (see Fig. 3-8 and Chapter 2 for more details). The dynamic portion of the rig consists of a beam mounted on a single DOF pivot with one electromagnet at each end. The beam rotates on the mechanical sharp edge pivot and the electromagnets produce the necessary force for stabilizing the beam. The test rig's dynamics are simple however it contains all of the important fundamental features of a magnetic bearing system. Dynamics of the rig are modeled by the following differential equations,

$$J\ddot{\theta} = -D\dot{\theta} + T_2 - T_1 = -D\dot{\theta} + L_a\left(F_2 - F_1\right) \qquad (3-29)$$

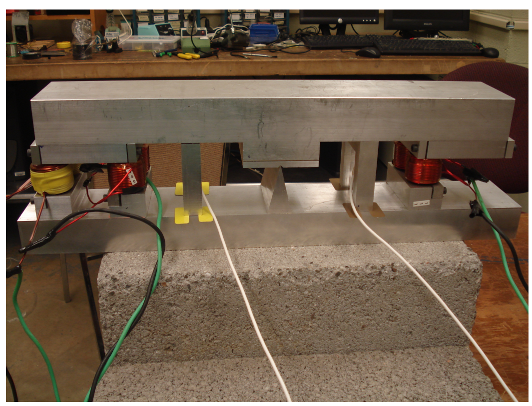

Figure 3-8 The Balance Beam

Here, θ is the angle between the beam and the horizontal axis. D is the system damping due to the pivot and air friction. T_1 and T_2 are the left and right torques provided by the two electromagnets, F_1 and F_2 are the left and right electromagnetic forces and L_a is the distance between the electromagnets and the central pivot.

3.5 Linear Balance Beam Model

In the case of a linear model, Eq. (3-16) is used to calculate the force at each end. The airgap at each side is calculated by:

$$g_1 = g_0 - L_a\theta, \qquad g_2 = g_0 + L_a\theta \tag{3-30}$$

Substituting Eqs. (3-16) and (3-30) into the system's dynamic equation yields:

$$J\ddot{\theta} = -D\dot{\theta} + \frac{L_a\mu_0 AN^2}{4}\left(\frac{I_1^2}{(g_0 - L_a\theta)^2} - \frac{I_2^2}{(g_0 + L_a\theta)^2}\right) \tag{3-31}$$

Applying the bias current and linearizing the system around its equilibrium point yields the following equation,

$$\begin{bmatrix}\dot{\theta}\\ \ddot{\theta}\end{bmatrix} = \begin{bmatrix}0 & 1\\ \dfrac{4c_t L_a I_b^2}{J g_0} & -\dfrac{D}{J}\end{bmatrix}\begin{bmatrix}\theta\\ \dot{\theta}\end{bmatrix} + \begin{bmatrix}0\\ -\dfrac{4c_t I_b}{J}\end{bmatrix} I_c \tag{3-32}$$

The constant $c_t = \dfrac{\mu_0 L_a AN^2}{4g_0^2}$ is introduced for simplification [34]. This linearized model is used as a benchmark for measuring the effectiveness of the proposed nonlinear model.

3.6 Nonlinear balance beam Model using Lur'e Method

In the linear model, a bias current (I_b) was used to linearize the system, which means that both of the electromagnets work at the same time even when the beam's angle of rotation is zero, therefore some energy is always lost. In the nonlinear model a bias current is still used but not for linearizing the system. The bias current provides the system with an acceptable slew rate. A single electromagnet's nonlinear force plot is shown in Figure (3-9).

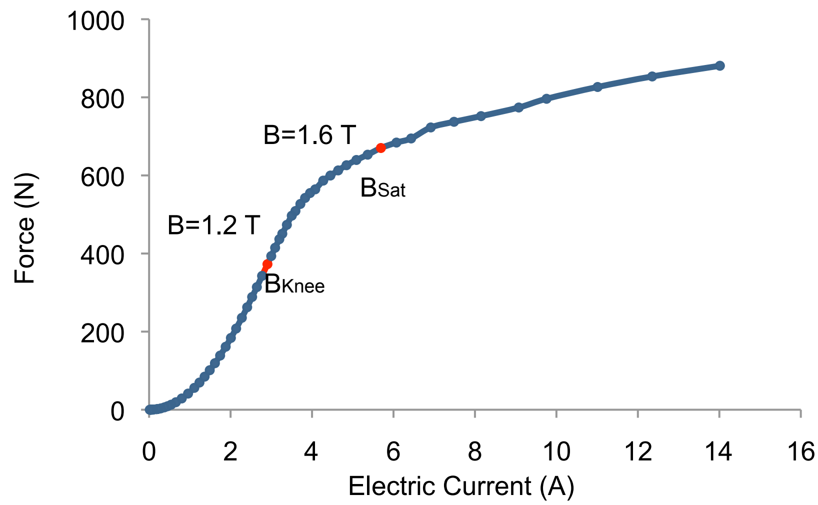

Figure 3-9 The Nonlinear Force

As can be seen, for small currents the curve's slope is close to zero. The slope of the curve in Figure (3-9) is the rate of change of force with respect to the current, which is directly related to the force slew rate (see Section 2-3). When the slew rate is small, the system needs a long reaction time to produce a significant force, which is not desirable from a stability prespective. Figure (3-10) shows the effective force on the balance beam for a dual acting actuator with a bias current.

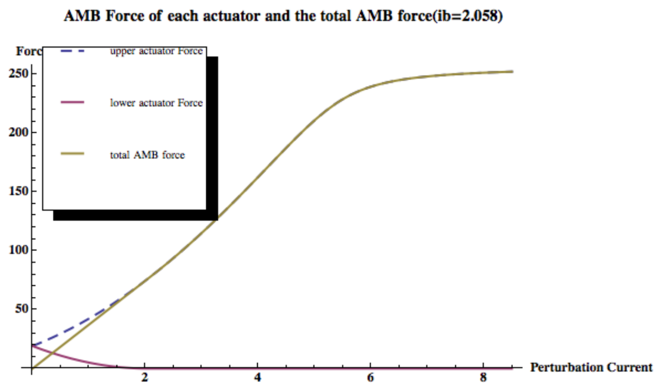

Figure 3-10 Nonlinear Force With Bias Current

Using the bias current provides the system with a much better slew rate for small control currents. When the control current is small, both electromagnets work together. When increasing the control current, I_1 increases and I_2 decreases. Consequently when the control current is equal to the bias current, I_2 becomes zero. The control strategy does not allow negative I_1 or I_2; therefore, for control currents larger than the bias current, one electromagnet is off and the other operates in the nonlinear region. For this work, the bias current was chosen to be half of the current corresponding to the flux density B_{knee} (1.2T). This choice of I_b makes the second electromagnet turn off at the end of the linear region. For flux densities greater than 1.2T (B_{knee}), the nonlinear force is calculated by using Eqs. (3-12) and (3-14). In the linear region the relative permeability is assumed to be a constant ($\mu_r = a + bB\big|_{B=1.2\ \text{Tesla}} = a + 1.2b$). And the two actuator forces are calculated as:

$$\left.\begin{aligned} F_1(\text{Linear}) &= A\mu_0\left(\frac{N(I_b+I_c)}{\frac{L_s}{\mu_r}+2(g_0+x)}\right)^2 \\ F_2(\text{Linear}) &= A\mu_0\left(\frac{N(I_b-I_c)}{\frac{L_s}{\mu_r}+2(g_0-x)}\right)^2 \end{aligned}\right] \qquad (3-33)$$

Here $F_1(\text{Linear})$ and $F_2(\text{Linear})$ are the forces of the left and right electromagnets in the linear region. For flux densities between 1.2T and 1.6T, the nonlinear force is calculated by using Eqs. (3-26) and (3-27),

$$F_1(\text{Nonlinear}) = \frac{1}{g_0^2\left(1+\frac{2x}{g_0}\right)}\left[\begin{aligned} &c_1(I_b+I_c)^2 + c_2x + c_3 \\ &+(c_4(I_b+I_c)+c_5x+c_6)\sqrt{c_7(I_b+I_c)^2+c_8(I_b+I_c)^2x+c_{10}x+c_{11}} \end{aligned}\right] \qquad (3-34)$$

$$F_2(\text{Nonlinear}) = \frac{1}{g_0^2\left(1-\frac{2x}{g_0}\right)}\left[\begin{aligned} &c_1(I_b-I_c)^2 - c_2x + c_3 \\ &+(c_4(I_b-I_c)-c_5x+c_6)\sqrt{c_7(I_b-I_c)^2+c_8(I_b-I_c)^2x-c_{10}x+c_{11}} \end{aligned}\right] \qquad (3-35)$$

Here $F_1(\text{Nonlinear})$ and $F_2(\text{Nonlinear})$ are the forces of the left and right electromagnets in the nonlinear region. Since the electric current should not be negative, the force equation needs to be modified. The effective electromagnetic force on the beam is shown below,

$$F_1 = \begin{cases} 0 & I_c < I_b \\ F_1(\text{Linear}) & -I_b < I_c < I_b \\ F_1(\text{Nonlinear}) & I_b < I_c \end{cases} \qquad (3-36)$$

$$F_2 = \begin{cases} 0 & I_b < I_c \\ F_2(\text{Linear}) & -I_b < I_c < I_b \\ F_2(\text{Nonlinear}) & I_c < -I_b \end{cases} \qquad (3-37)$$

These equations are highly nonlinear and can't be written in state space form directly; therefore the Lur'e method is used to model the balance beam nonlinearly [39]. The control problems described by the Lur'e method have a forward path that is linear and time-invariant, and a feedback path that contains a memory-less, possibly time-varying nonlinearity (ψ) (see Fig. 3-11).

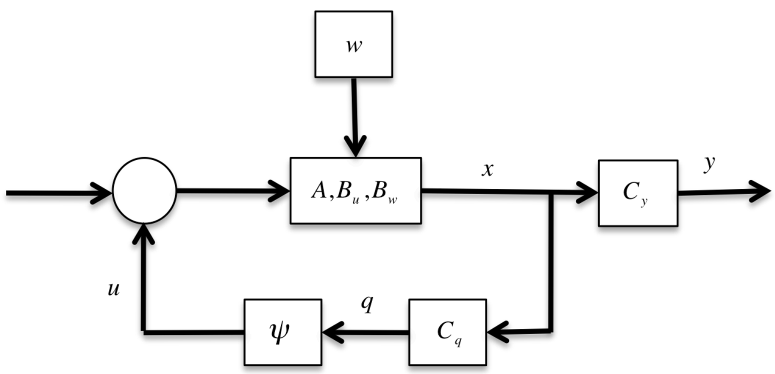

Figure 3-11 The Lur'e Problem

The Lur'e system can be described by the following equations,

$$\begin{aligned} &\dot{x} = Ax + B_u u + B_w w, && q = C_q x \\ &y = C_y x, && u(t) \in R^m,\ x \in R^n \\ &u_i(t) = \psi_i(q_i(t)) && i = 1,\ldots,m \end{aligned} \qquad (3-39)$$

Here, x is the state vector, A is the system matrix, B_u is the input matrix, u is the input vector, B_w is the disturbance matrix, w is the disturbance vector, C_q is the control matrix, q_i's are the control outputs (in this case the electric current). y is the output, C_y is the output matrix, i is the number of inputs (our system is single input, single output, therefore $i=1$), u_i's are the different elements of the input vector (magnetic actuator force), and ψ_i's are nonlinear input functions (nonlinear force equation). The functions ψ_i should satisfy the following sector condition (see Fig. 3-12),

$$k_{1i}\sigma^2 \le \sigma\psi_i(\sigma) \le k_{2i}\sigma^2 \quad \text{for all } \sigma \in R \tag{3-40}$$

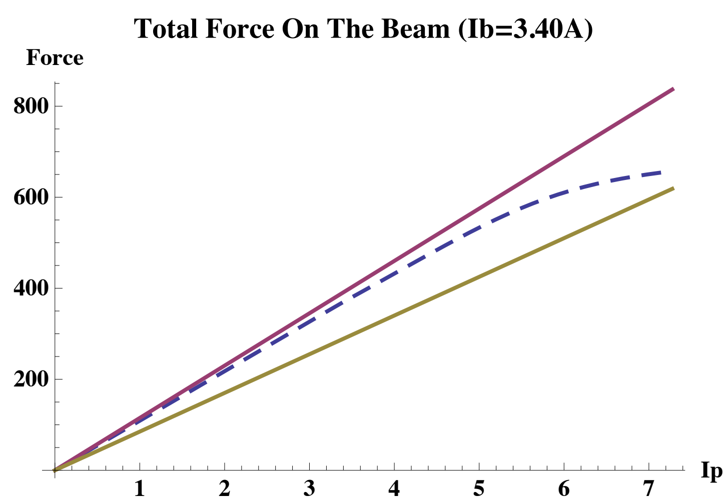

Figure 3-12 The Sector Condition

Equations (3-36) and (3-37) are both nonlinear with respect to current and displacement. In this thesis, the magnetization nonlinearity, which depends on the electric current, is modeled. Therefore the force equation is linearized with respect to the displacement, but it remains nonlinear with respect to the electric current,

$$F_L(x, I_c) = \left.\frac{\partial F}{\partial x}\right|_{x=0,\ I_c=0} x + F(x=0, I_c) = K_X x + F_I \qquad (3-41)$$

Here, F_L is obtained by linearizing the net force on the balance beam with respect to displacement. By substituting F_L into the balance beam dynamic equation, the balance beam is modeled into the Lur'e system form as follows,

$$J\ddot{\theta} = -D\dot{\theta} + L_a(F_1 - F_2) = -D\dot{\theta} + L_a^2 K_X \theta + L_a F_I \qquad (3-42)$$

In state space form Eq. (3-42) can be written as:

$$\begin{bmatrix} \dot{\theta} \\ \ddot{\theta} \end{bmatrix} = \begin{bmatrix} 0 & 1 \\ \dfrac{L_a^2 K_X}{J} & -\dfrac{D}{J} \end{bmatrix} \begin{bmatrix} \theta \\ \dot{\theta} \end{bmatrix} + \begin{bmatrix} 0 \\ \dfrac{L_a}{J} \end{bmatrix} F_I(I_c) \qquad (3-43)$$

Here, K_X is obtained by linearizing the beam around its equilibrium point and $F_I(I_c)$ is the nonlinear force assuming no displacement. This system has a forward path that is linear and time-invariant, and a feedback path that contains the nonlinearity F_I (see Fig. 3-13).

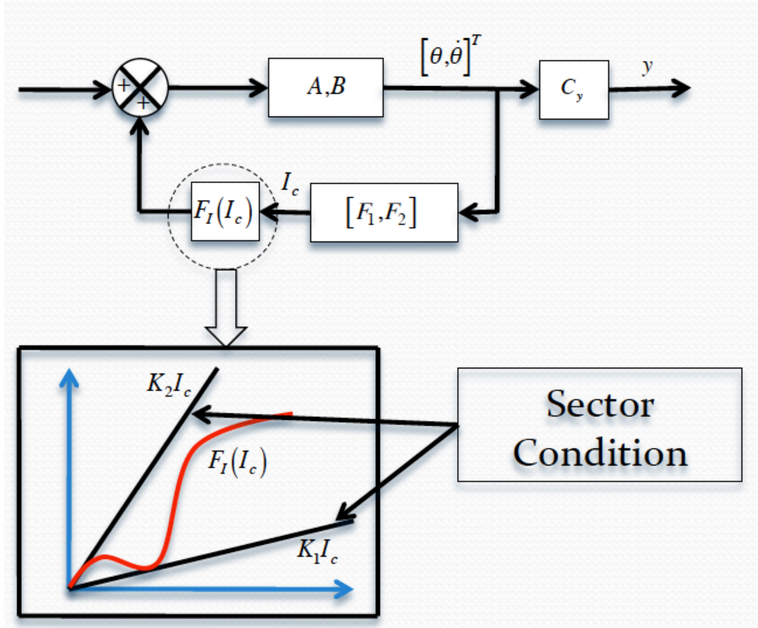

Figure 3-13 The Sector Condition

<u>Validity of the sector bound</u>

In conventional models, the magnetic bearing force is linearized with respect to both current and displacement:

$$F(x,I_c) = K_X x + K_I(I_c) + H.O.T \approx K_X x + K_I(I_c) \qquad (3-44)$$

In this process, the higher order terms are assumed to be negligible for small displacements and currents. In the nonlinear model proposed in this thesis, the force is linearized with respect to displacement, but it remains nonlinear with respect to the control current:

$$F(x,I_c) = K_X x + \underbrace{F(x=0,I_c)}_{F_I} + H.O.T \approx K_X x + F_I \qquad (3-45)$$

The nonlinear part of the force $(F_I + H.O.T)$ should satisfy the Lur'e system's sector condition (see Eq. 3-40). For small displacements the higher order terms are negligible and the sector bound can be found for the force equation at zero displacement (F_I) (see Fig. 3-12).

During the AMB operation, the displacement can grow larger and make the eliminated higher order terms significant, which in turn can cloud the validity of the chosen sector bounds. Therefore the validity of the sector bound should be investigated for large displacements. The following equation shows the nonlinear portion of the force:

$$F_I + H.O.T = F(x, I_c) - K_X x \qquad (3-46)$$

Which is sketched in the following graph (Fig. 3-14)

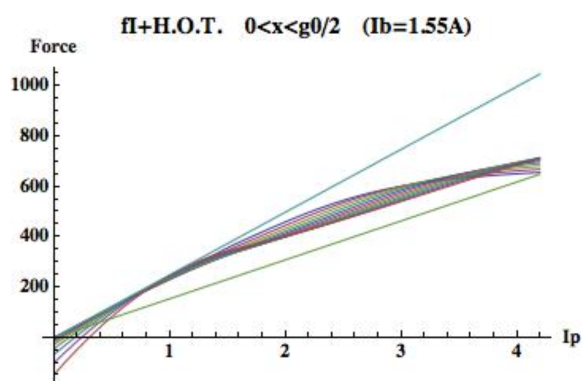

Figure 3-14 Nonlinear Force With Large Displacements (0<x<g0/2)

As can be seen, the sector bounds that were found for (F_I) are acceptable even in the presence of relatively large displacements. As expected, for small control currents, the higher order terms are more significant compared to (F_I). In the large displacement case, the control strategy dictates a large control current which allows us to neglect the portions of the graph that are out of the sector bound. In other words, a combination of a small I_c and a large x will not happen in the actual closed loop control system. The following graph (Fig. 3-15) shows results for displacements smaller than 25% of the airgap. Even in the presence of a small control current, the value of $F_I + H.O.T$ is predominantly inside the sector bound.

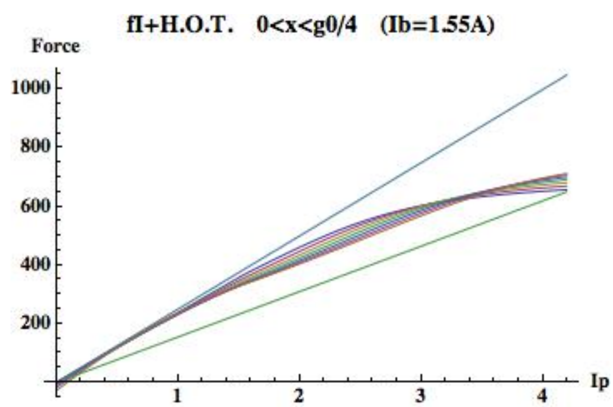

Figure 3-15 Nonlinear Force With Large Displacements (0<x<g0/4)

The force graphs for the nonlinear force and the force lineralized with respect to displacement are shown in Figs. 3-16 and 3-17.

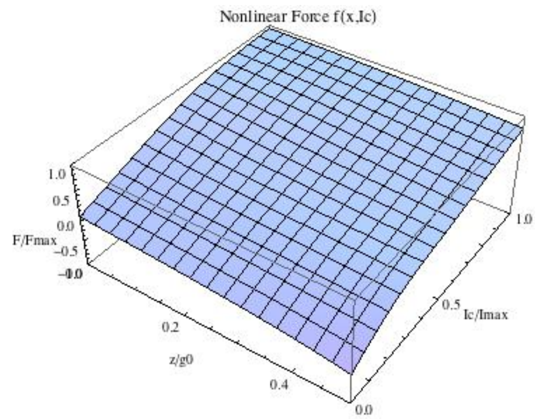

Figure 3-16 The Nonlinear Force

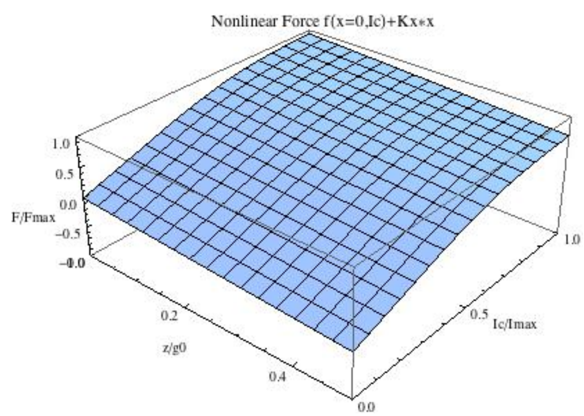

Figure 3-17 The Nonlinear Force Linearized W.R.T. Displacement

In both graphs, the control current, displacement, and the force are normalized with respect to the maximum control current, the airgap, and the maximum force. Figure 3-18 shows the error generated by linearizing the force with respect to displacement:

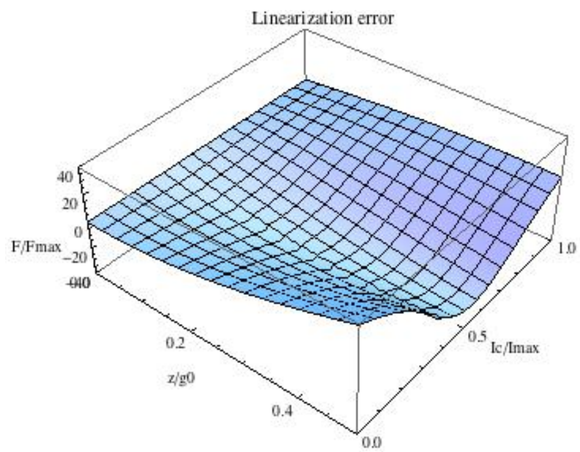

Figure 3-18 The Linearization Error

The error is large in the presence of a large displacement and a small current, but as was discussed before, the control strategy will prevent this situation from happening. In other areas of the graph, the error is relatively small (<10%).

Switching compensation

In the proposed force model, it is assumed that the relative permeability is a constant before reaching the nonlinear portion of the B-H curve. Based on the material property graph (Fig (3-3)) the nonlinear part of the B-H curve starts at the knee point of 1.2T. The bias current is chosen to produce half of this flux density; therefore, when the control current equals the bias current, the flux density reaches the nonlinear region. On the other hand, a variation in the displacement alters the flux density that is generated. Therefore, due to larger airgap reluctance, the flux density produced in the presence of a nonzero displacement and a control current equal to the bias current is less than 1.2T (see Fig. 3-19).

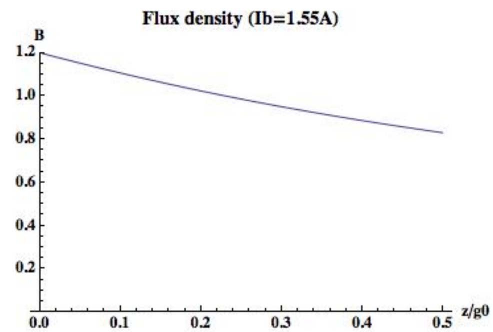

Figure 3-19 The Flux Density for Ib=Ic With Variable Displacement

The force calculated for the nonlinear portion of the B-H curve is valid for 1.2<B<1.6, while the force calculated for the linear region is valid for $0 < I_c < I_b$ which translates to $0 < B < B(I_c = I_b)$. According to Figure 3-19, $B(I_c = I_b)$ is less than 1.2T for a nonzero z. Therefore a small discontinuity can exist when the control current reaches the bias current (when the force switches between the linear and nonlinear operating regions) (see Fig. 3-20).

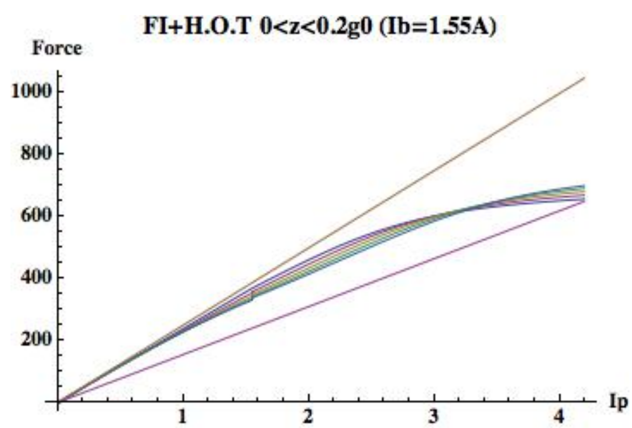

Figure 3-20 The Nonlinear Force Without Switching Compensation

This occurs because the constant relative permeability in the linear B-H region is assumed to be:

$$\mu_r = aB_{knee} + b \quad or \quad \mu_r = 1.2a + b \tag{3-47}$$

But for nonzero values of displacement the switching between the linear and nonlinear regions occurs before B=1.2. In order to compensate for this, the flux density for different displacements with a control current equal to the bias current must be calculated. The relative permeability in the linear portion of the B-H curve is calculated as follows,

$$\mu_r = aB\left(I_c = I_p\right) + b \tag{3-48}$$

By using this relative permeability in the linear force region, the discontinuity disappears and the switching will be smooth (see Fig. 3-15).

4 Control Synthesis

In this chapter, the tools necessary for a control design based on the proposed nonlinear model are developed. These tools facilitate the control design for a Lur'e system with a sector bounded nonlinear feedback, and input and state constraints. This chapter is organized into the following sections. In the first section the Linear Matrix Inequalities (LMI's) are introduced. In the second section, the control design objectives are explained. The third section defines the constraints. In the fourth and fifth sections some optimization problems are proposed to maximize the stability region (domain of attraction) and the system's dynamic performance. Finally, in this chapter the issue of disturbance tolerance/rejection is addressed.

4.1 LMI Introduction

In this section, LMIs and their basic properties are introduced. A Linear Matrix Inequality (LMI) is a convex constraint. Therefore optimization problems with a convex objective function and LMI constraints can be solved efficiently by commercial software. A linear matrix Inequality has the form:

$$F(x) = F_0 + \sum_{i=1}^{m} x_i F_i > 0, \quad x \in R^m, \quad F_i \in R^{n \times n} \qquad (4-1)$$

Here, F_i's are constant symmetric matrices, $x_i's$ are the independent variables and x is the variable vector. The inequality means that F(x) is a positive definite matrix which means that it must satisfy the following condition:

$$z^T F(x) z > 0, \quad \forall z = 0, \quad z \in R^n \qquad (4-2)$$

As mentioned before, an important property of the LMI's is that the set $\{x | F(x) > 0\}$ is a convex constraint on x. Therefore a combination of LMI constraints and a convex objective function, results in a convex optimization problem that can be solved in a straight forward manner.

Stability is one of the most basic requirements for any closed loop system. The Lyapunov method for analyzing stability describes the stability problem in the form of an LMI. The basic idea is to find a positive definite function of the state, for which it's time derivative is negative. As an example, a necessary and sufficient condition for the system $\dot{x} = Ax$ to be stable is the existence of a Lyapunov function $V(x) = x^T P(x)x$ where P(x) is a positive definite Matrix and $\dot{V}(x)$ is negative definite. This can be formulated as follows:

$$V(x) = x^T P(x)x > 0 \;\; \Rightarrow \;\; P(x) > 0 \qquad (4-3)$$

$$\dot{V}(x) = \dot{x}^T P(x)x + x^T P(x)\dot{x} < 0 \;\; \Rightarrow \;\; A^T P + PA < 0 \qquad (4-4)$$

This is an LMI with a variable matrix (P(x)), instead of a variable vector (x) as in Eq. (4-1). It can be proven that variable matrix and variable vector LMI's are interchangeable [39]. There is a large variety of constraints that can be described in LMI form by using procedures including: Schur complement, s-procedure, max singular value, etc. In this thesis, all the constraints are converted to LMIs by using one of the previously mentioned methods. The conversion process is not explained in detail in this thesis, but can be found in LMI textbooks and the papers listed in the references.

4.2 Problem Statement

The objective in this chapter is to design a feedback law such that the closed-loop system possesses a larger stability region, a better transient response, and an improved disturbance tolerance/rejection capability compared to conventional methods. Specifically, this work is interested in the control of a system with actuator saturation and a sector-bounded feedback nonlinearity. It is important to note that while the research referenced in this work only deal with actuator saturation as a nonlinearity, the model used in this work considers two different nonlinearities (actuator saturation and material magnetization). These two nonlinearities are illustrated schematically in Figure 4-1.

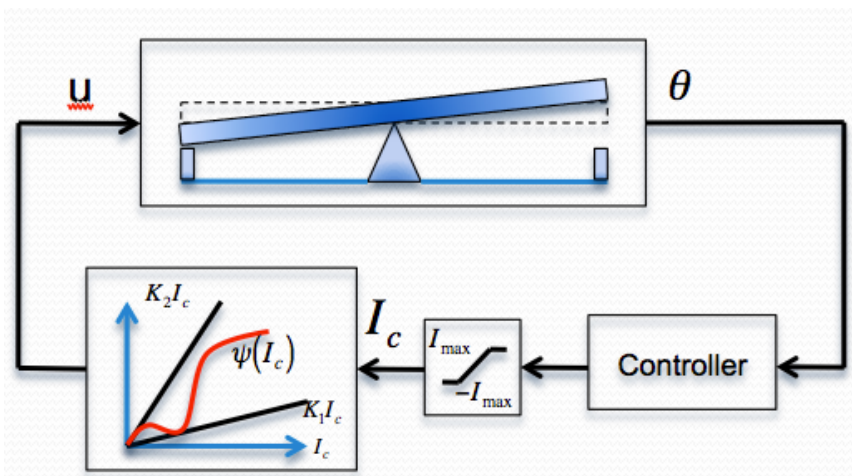

Figure 4-1 The Modeling Nonlinearities

This system can be formulated in equation form as follows:

$$\begin{aligned} \dot{x} &= Ax + Bu, \\ u &= \psi(\sigma) \qquad \Rightarrow \qquad \dot{x} = Ax + B\psi(sat(Fx)) \\ \sigma &= sat(Fx) \end{aligned} \tag{4-5}$$

The nonlinearity is bounded by two sectors (see Fig. (4-2)):

$$K_1\sigma^2 \le \sigma\psi(\sigma) \le K_2\sigma^2 \qquad (4-6)$$

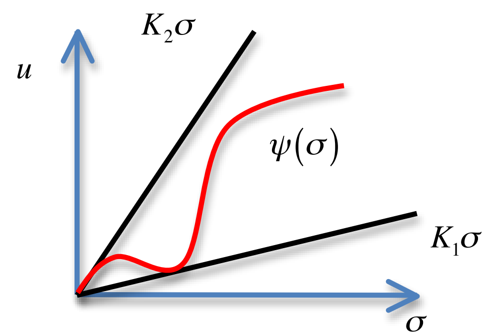

Figure 4-2 The Sector Bounds for a Nonlinear Feedback

By defining a Lyapunov function candidate as $V(x) = x^T P(x)x$, the system is stable if a function P(x)>0 can be found that satisfies the following condition:

$$\dot{V}(x) = 2x^T P(x)\left[Ax + B\psi(Fx)\right] \le 0 \qquad (4-7)$$

Finding a P(x)>0 that satisfies the previous condition guarantees the stability of the system.

While analytical characterization of the domain of attraction (stability region) is difficult, most literature focuses on enlarging an invariant set inside the domain of attraction by appropriately designing a feedback gain. Clearly when an ellipsoid is invariant, it is inside the domain of attraction.

Therefore, designing a feedback law such that the closed-loop system has a large stability region, requires that an invariant set (usually an invariant ellipsoid) be placed inside the stability region and it's area maximized. It is important to note that an ellipsoid is associated with any positive definite matrix P(x) and can be defined as:

$$\varepsilon(P,\rho) = \left\{\zeta \in R^n \middle| \zeta^T P \zeta \le \rho\right\} \tag{4-8}$$

Here, $\varepsilon(P,\rho)$ is an ellipsoid centered at the origin and P(x) is a positive definite matrix. The ellipsoid is invariant if for every trajectory x of the system, $x(t_0) \in \varepsilon(P,\rho)$ implies $x(t) \in \varepsilon(P,\rho)$ for all $t \ge t_0$.

The stability condition of Eq. (4-7) is a sufficient condition, and for single input systems it can be proven to be a necessary condition as well. Therefore, the largest invariant ellipsoid can be defined exactly [40].

If the condition of Eq. (4-7) is satisfied, the system is stable and all trajectories starting inside the ellipsoid of Eq. (4-8) will remain inside it. However in some cases ψ is very complicated and therefore it is beneficial to bound it within simpler functions ψ_1 and ψ_2. Also, there are always uncertainties associated with the nonlinear function and it is necessary to study the invariance of the ellipsoid for a class of nonlinear functions that are within a certain bound (ψ_1 and ψ_2). In other words:

$$\psi \in co\{\psi_1, \psi_2\} \tag{4-9}$$

Here, $co\{\psi_1, \psi_2\}$ is the convex hull of ψ_1 and ψ_2 expressed as:

$$co\{x_1, x_2, \cdots, x_N\} := \left\{\sum_{i=1}^{N} \lambda_i x_i : \sum_{i=1}^{N} \lambda_i = 1, \lambda_i \geq 0\right\} \tag{4-10}$$

In absolute stability problems, ψ_1 and ψ_2 are usually two lines:

$$\psi_1(\sigma) = k_1 \sigma, \qquad \psi_2(\sigma) = k_2 \sigma \tag{4-11}$$

It can be proven that the system is stable if and only if Eq. (4-7) is satisfied on both sector bounds [41]. Therefore both of the following conditions should be satisfied for the system of Eq. (4-5) with sector bounds expressed in Eq. (4-11) to be stable and the ellipsoid of Eq. (4-8) to be invariant.

$$\dot{V}(x) = 2x^T P\left[Ax + Bk_1 Fx\right] \leq 0 \tag{4-12}$$

$$\dot{V}(x) = 2x^T P\left[Ax + Bk_2 Fx\right] \leq 0 \tag{4-13}$$

In order to simplify the mathematical manipulation, the parameter $Q = (P/\rho)^{-1}$ is introduced and the constraints (4-12) and (4-13) are modified to the followings:

$$Q(A + k_1 BF)^T + (A + k_1 BF)Q < 0 \tag{4-14}$$

$$Q(A + k_2 BF)^T + (A + k_2 BF)Q < 0 \tag{4-15}$$

In order to make sure $|Fx|$ is no larger than the maximum tolerable current in the coil ($I_{\max}$), an additional constraint needs to be added to the system. This new constraints is explained in detail in Section 4.3 of this Chapter. An improved transient response can also be achieved by using LMI's with the following form in place of Eq. (4-7) [42].

$$\dot{V}(x) = 2x^T P(x)\left[Ax + B\psi(Fx)\right] \le -\beta x^T P(x) x \qquad (4-16)$$

Here, β is a positive number that can be an indicator of the convergence rate of the trajectories. For a β>0 the trajectories starting inside the ellipsoid will converge to the origin. A larger value of β usually means a faster convergence rate, a faster transient response and, a lower overshoot.

In 2004, Hu et al. [43] introduced a less conservative sector condition for the Lur'e problem. In their method, lines with multiple bends were used to bound the nonlinearity. This generalized condition allowed the sector bounds to be more flexible and more accurately approximate the nonlinear feedback function. The generalized sector condition was defined as,

$$\psi(u,t) \in co\left\{\psi_1(u), \psi_2(u)\right\} \qquad \text{for all} \qquad u,t \in R \qquad (4-17)$$

In this thesis, ψ_1 and ψ_2 are piecewise continuous concave or convex functions and in Equation (4-17), $co\left\{\psi_1(u), \psi_2(u)\right\}$ is the convex Hull of ψ_1 and ψ_2 which are defined as follows:

$$\psi_1(\sigma) = \begin{cases} k_{01}\sigma & 0 < u < b_{11} \\ k_{11}\sigma + c_{11} & b_{11} < u < b_{21} \\ \vdots & \\ k_{N_1 1}\sigma + c_{N_1 1} & b_{N_1 1} < u < \infty \end{cases} \qquad (4-18)$$

$$\psi_2(\sigma)=\begin{cases} k_{02}\sigma & 0<u<b_{12} \\ k_{12}\sigma+c_{12} & b_{12}<u<b_{22} \\ \vdots & \\ k_{N_2 2}\sigma+c_{N_2 2} & b_{N_2 2}<u<\infty \end{cases} \qquad (4-19)$$

Here, k_{im} is defined as the slope of different segments of the sector bound and c_{im} is the y-intercept of these segments. For example k_{31} is the slope of the fourth segment of the first sector bound and c_{12} is the y-intercept of the second segment of the second sector bound. For the first segment, $i=0$ and since it passes through the origin, the y-intercept is zero. Figure (4-3) illustrates the generalized sector condition.

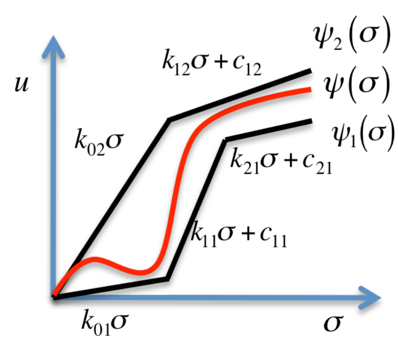

Figure 4-3 The Generalized Sector Condition

For the system of Eq. (4-5), an ellipsoid $\varepsilon(P,\rho)$ is contractively invariant on ψ_1 if and only if:

$$(A+k_{01}BF)^T P+P(A+k_{01}BF)<0 \qquad (4-20)$$

and there exists $H_i \in R^{1\times n}$, $i\in I[1,N_1]$ such that:

$$(A+BH_{i1})^T P + P(A+BH_{i1}) < 0, \qquad i \in I[1,N_1] \qquad (4-21)$$

$$\varepsilon(P,\rho) \subset \bigcap_{i=1}^{N} L\left(\frac{H_{i1}-k_{i1}F}{c_{i1}}\right) \qquad (4-22)$$

By defining the following new parameters:

$$Q = \left(\frac{P}{\rho}\right)^{-1}, \qquad Y_{i1} = H_{i1}Q$$

The invariance condition can be transformed into the following LMI:

$$a)\ \ Q(A+k_{01}BF)^T + (A+k_{01}BF)Q < 0$$

$$b)\ \ QA^T + AQ + Y_{i1}B^T + BY_{i1} < 0 \qquad (4-23)$$

$$c)\ \ \begin{bmatrix} 1 & \dfrac{Y_{i1}-k_{i1}FQ}{c_{i1}} \\ \dfrac{Y_{i1}^T - k_{i1}QF^T}{c_{i1}} & Q \end{bmatrix}$$

Similarly, for invariance on the second sector bound, (ψ_2) the following LMI should hold:

$$
\begin{aligned}
&a)\ \ Q\left(A+k_{02}BF\right)^T+\left(A+k_{02}BF\right)Q<0 \\
&b)\ \ QA^T+AQ+Y_{i2}B^T+BY_{i2}<0 \\
&c)\ \begin{bmatrix} 1 & \dfrac{Y_{i2}-k_{i2}FQ}{c_{i1}} \\ \dfrac{Y_{i2}^T-k_{i2}QF^T}{c_{i2}} & Q \end{bmatrix}
\end{aligned}
\qquad (4-24)
$$

Here $Y_{i2}=H_{i2}Q$. When the generalized sector condition is used instead of the normal sector conditions, Eq's (4-20), (4-21), and (4-22) replace Eq's (4-12) and (4-13) in the optimization problem.

In this thesis various controllers are designed to address different control objectives. These objectives are categorized into the following three control designs:

Design 1 (largest invariant ellipsoid (largest domain of attraction))

To find the largest invariant ellipsoid, usually a set of initial points ($X_0 \in R^n$) is provided which determine the shape of the invariant ellipsoid. A feedback matrix F should be found such that $\varepsilon(P,\rho)$ is invariant and α in $\alpha X_0 \subset \varepsilon(P,\rho)$ is maximized.

Design 2 (transient response performance)

In order to achieve the best transient response, the stability problem is defined as in Eq. (4-16) and a feedback matrix F is found such that $\varepsilon(P,\rho)$ is invariant and β is maximized.

Design 3 (disturbance rejection with a guaranteed domain of attraction)

In order to guarantee the desired domain of attraction a set of initial states is given. The goal is to design a controller that can start from the set of initial states while also maximizing the tolerable disturbance energy $\alpha_{\max} = \int_0^\infty w^T(t)w(t)dt$.

4.3 Constraints

In this section, the input saturation and state constraints are addressed. In this work, the input to the nonlinear feedback (σ) is defined as the electric current (I_c), which must be less than a maximum value $(I_{\max})$. Since the control current (I_c) can be larger than the bias current (I_b), a saturation function is added to the controller to ensure that the current in left and right electromagnets (I_1 and I_2) maintain a positive value (see Fig. (4-4)). Therefore when control currents larger than the bias current are required, one electromagnet turns off and the other is supplied by a combination of bias and control currents.

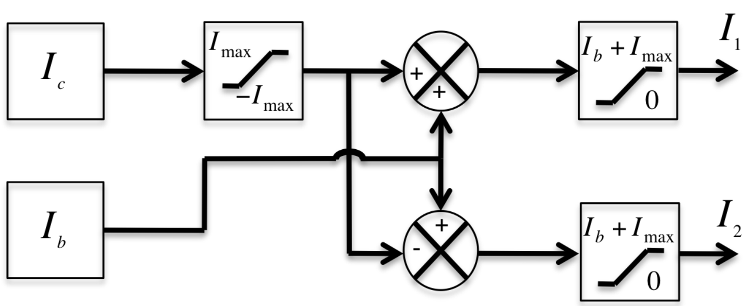

Figure 4-4 Input Electric Current to Each Electromagnet

The displacement is also restricted; if θ exceeds $\theta_{\max}$, the beam will hit the back-up bearing. Furthermore, in the Lur'e problem, the nonlinear feedback should be within the sector bounds. Since the bounds can be freely chosen, this is not technically a constraint, but it is a condition that must be satisfied. All these constraints and conditions are summarized as follows,

$$\left|I_c\right| \le I_{\max} \qquad (4-25)$$

$$I_1, I_2 > 0 \qquad (4-26)$$

$$\left|\theta\right| \le \theta_{\max} \qquad (4-27)$$

$$F_I\left(I_c\right) \in co\left\{\psi_1, \psi_2\right\} \qquad (4-28)$$

To enable easier mathematical manipulation, the following notation is used. The input constraint (Eq. (4-25)) becomes,

$$L\left(F / I_{\max}\right) = \left\{x \in R^n : \left|F_i x / I_{\max}\right| \le 1, i = 1,2,...,p\right\} \qquad (4-29)$$

Where, F_i is the i^{th} row of F. Similarly; the state constraint are formulated as,

$$L\left(G\right) = \left\{x \in R^n : \left|G_i x\right| \le 1, i = 1,2,...,p\right\} \qquad (4-30)$$

Since for this work there is only one input and one state constraint in both cases p=1 and G and F have just one row. G can be defines as:

$$G = \left[\frac{1}{\theta_{\max}},\ 0\right], \qquad (4-31)$$

4.4 Design 1: Largest Invariant Ellipsoid

Here, the goal is to design a controller that maximizes the stability region while also satisfying all the system constraints. The stability region can be measured by the size of the invariant ellipsoid. The shape of the invariant ellipsoid can be decided by a set of reference points (X_0) and its size can be measured by a number α, that satisfies $\alpha \in \varepsilon(P,\rho)$. To enlarge the invariant ellipsoid, α should be maximized. The following optimization problem finds a feedback law (F) that maximizes α:

$$
\begin{aligned}
&\sup_{P>0,F} \alpha \\
&(a)\ \alpha x_i \in \varepsilon(P,\rho),\ i=1,2,\cdots,l\ \ and\ \ x_i \in X_0 \\
&(b)\ \text{Either inequalities } (4-12) \text{ and } (4-13) \\
&\quad\ \text{or } (4-20),\ (4-21)\ \text{ and } (4-22) \\
&(c)\ \varepsilon(P,\rho) \subset L(F/I_{\max}) \\
&(d)\ \varepsilon(P,\rho) \subset L(G)
\end{aligned}
\qquad (4-32)
$$

Constraint (a) defines the shape of the ellipsoid. Constraints (b) guarantee that the ellipsoid is invariant either within the regular or the generalized sector bounds. Constraints (c) and (d) consider the state and input constraints. The optimization problem is transformed into an LMI problem and solved by interior-point methods. In order to change the optimization problem into a convex LMI, the following variables were introduced $Q = P^{-1}, H = FQ, \gamma = \frac{1}{\alpha^2}$, and the LMI is then described as,

$$
\begin{aligned}
&\sup_{Q>0,H} \gamma \\
&(a)\ \begin{bmatrix} \gamma & x_i^T \\ x_i & Q \end{bmatrix} \geq 0,\ i = 1,2,\cdots,l \ \ and \ \ x_i \in X_0 \\
&(b)\ \text{Either inequalities } (4-14) \text{ and } (4-15) \\
&\quad \text{or } (4-23) \text{ and } (4-24) \qquad\qquad\qquad (4-33) \\
&(c)\ \begin{bmatrix} 1 & h_j / I_{\max} \\ h_j^T / I_{\max} & Q \end{bmatrix} \geq 0,\ \ j = 1,2,\cdots,m \\
&(d)\ \ g_k Q g_k^T \leq 1,\ k = 1,2,\cdots,p
\end{aligned}
$$

Here, h_j is the j^{th} row of H and g_k is the k^{th} row of G. For easier manipulation, condition (c) is replaced with the following condition in the optimization process:

$$
\begin{bmatrix} I_{\max}^2 & h_j \\ h_j^T & Q \end{bmatrix} \geq 0
$$

4.5 Design 2: Best Transient Response

The Design 1 controller can result in a slow transient response. For many applications the controller design should have better transient response while maintaining an acceptable stability region. As was mentioned previously, the ellipsoid invariance constraint can be described by (4-13). In this equation, a bigger value for β indicates a better transient response. Therefore, in order to obtain the best transient response, the objective is to find the largest β that satisfies all of the required constraints. In other words, to get the best transient response, β is maximized in the following optimization problem:

$$
\begin{aligned}
&\sup_{P>0,F} \; \beta \\
&(a) \;\; x_i \in \varepsilon(P,\rho), \; i = 1,2,\cdots,l \;\; and \;\; x_i \in X_0 \\
&(b) \;\; \text{Either inequalities } (4-12) \text{ and } (4-13) \text{ with } \beta \text{ on the R.H.S. instead of } 0 \\
&\quad\;\; \text{or } (4-20), (4-21) \text{ with } \beta \text{ on the R.H.S. instead of } 0 \text{ and condition } (4-22) \\
&(c) \;\; \varepsilon(P,\rho) \subset L(F/I_{\max}) \\
&(d) \;\; \varepsilon(P,\rho) \subset L(G)
\end{aligned}
\qquad (4-34)
$$

The corresponding optimization problem is described by the following LMI,

$$
\begin{aligned}
&\sup_{Q>0,H} \; \beta \\
&(a) \begin{bmatrix} 1 & x_i^T \\ x_i & Q \end{bmatrix} \geq 0, \; i = 1,2,\cdots,l \;\; and \;\; x_i \in X_0 \\
&(b) \;\; \text{Either inequalities } (4-14) \text{ and } (4-15) \text{ with } \beta \text{ on the R.H.S. instead of } 0 \\
&\quad\;\; \text{or } (4-23) \text{ and } (4-24) \text{ with } \beta \text{ on the R.H.S. of parts a and b instead of } 0 \\
&(c) \begin{bmatrix} I_{\max}^2 & h_j \\ h_j^T & Q \end{bmatrix} \geq 0, \;\; j = 1,2,\cdots,m \\
&(d) \;\; g_k Q g_k^T \leq 1, \; k = 1,2,\cdots,p
\end{aligned}
\qquad (4-35)
$$

4.6 Design 3: Disturbance rejection

As previously mentioned, the proposed nonlinear method enables the system to respond with an increased force capability. Both of the previous designs are good uses of this extra capability. However the main advantage of the proposed nonlinear model is in dealing with external disturbances. This means that the additional force can be used to aid the system in tolerating significantly larger disturbances than achievable based on a linear model.

The disturbances that have been studied in the literature can be divided into input-additive and non-input-additive. In the first case, the disturbance is dependent on the bounded input, andt in the second case, the disturbances enter the system independently from the bounded control inputs. The work done by Polyak [43] (Polyak, Nazin, Topunov, & Nazin, 2006) is an example of the input additive case. However in most physical systems, the disturbance is independent from the input; therefore, this thesis studies non-input-additive disturbances.

In the first case, the disturbance rejection is easier to achieve. In the second case, with no boundedness assumption on the magnitude of the disturbances and in presence of a nonzero initial condition, the best that can be expected is a certain degree of disturbance tolerance for the closed loop system.

The system's maximum disturbance tolerance/rejection can be measured based on the magnitude or the energy of the disturbance it can withstand. In this work, the maximum tolerable disturbance energy is estimated. Using a similar method, the maximum tolerable magnitude of the disturbance can also be determined. Hu reported an example in which the disturbance is assumed to be bounded by magnitude [44] (Tingshu Hu, Lin, & Chen, 2002). This section presents a control design for the balance beam in the presence of L2-disturbances and other constraints that were introduced previously. The system studied in this thesis has the following form:

$$\begin{aligned} &\dot{x} = Ax + B\psi\big(sat(Fx)\big) + Ew \qquad x \in R^n \qquad u \in R^m \qquad w \in R^q \\ &z = Cx \end{aligned} \qquad (4-36)$$

The energy of the disturbance can be estimated as follows:

$$\alpha = \int_0^\infty w^T(t)w(t)dt \qquad (4-37)$$

A condition is used in this dissertation that guarantees that trajectories starting from an ellipsoid remain inside a second outer ellipsoid. The existence of these two ellipsoids under a disturbance with a specified energy (α) means that the system is capable of tolerating the disturbance. In other words, the disturbance tolerance can be measured by finding the maximum energy $(\alpha_{\max})$ under which the two ellipsoids exist. The size and difference between these two ellipsoids are the indicators of the disturbance rejection capability of the closed loop system under the designed feedback law.

For disturbances bounded by magnitude, an invariant ellipsoid can be used to bound the state trajectory [41] (Tingshu Hu et al., 2002)[Theorem 2]. However, for disturbances bounded by the energy, there exists no bounded invariant set. Therefore this thesis uses two nested-ellipsoids such that all trajectories starting from the inner ellipsoid remain inside the outer ellipsoid for all disturbances with an energy less than α. This is explained in the following theorem in [45] (Fang, Lin, & Hu, 2004):

Theorem. Consider the system:

$$\begin{aligned} &\dot{x} = Ax + Bsat(u) + Ew \qquad x \in R^{n} \qquad u \in R^{m} \qquad w \in R^{q} \\ &z = Cx \end{aligned} \tag{4-38}$$

Assume that the feedback law $u = Fx$ and a positive matrix P(x) are given. If there exists an $H \in R^{m\times n}$ and a positive number η such that,

$$\begin{aligned} &a)\ \left(A + B\left(D_i F + D_i^- H\right)\right)^T P + P\left(A + B\left(D_i F + D_i^- H\right)\right) + \frac{1}{\eta} PEE^T P \le 0 \quad i \in \left[1, 2^m\right] \\ &b)\ \varepsilon\left(P, 1 + \alpha\eta\right) \subset L(H) \end{aligned} \tag{4-39}$$

then every trajectory of the closed loop system that starts inside of $\varepsilon(P,1)$ remains inside of $\varepsilon(P,1+\alpha\eta)$. Every trajectory of the closed loop system that starts from the origin remains inside $\varepsilon(P,\alpha\eta)$ as long as condition (a) holds and $\varepsilon(P,1+\alpha\eta)\subset L(H)$.

Here, D is a set of $m\times m$ diagonal matrices whose diagonal elements are either 1 or 0. There are 2^m elements in D. D_i is an element of D and its complement is defined as follows:

$$D_i^- = I - D_i \qquad i = 1,2^m \tag{4-40}$$

The balance beam is a single input system $(m=1)$, and therefore $i=1,2$ and:

$$D_1 = [1] \;\; D_1^- = [0] \;\; D_2 = [0] \;\; D_2^- = [1] \tag{4-41}$$

For a single input system, Condition (4-39) can be simplified to:

$$\begin{aligned}
&a1)\;\; (A+BF)^T P + P(A+BF) + \frac{1}{\eta} PEE^T P \le 0 \qquad i=1 \\
&a2)\;\; (A+BH)^T P + P(A+BH) + \frac{1}{\eta} PEE^T P \le 0 \qquad i=2 \\
&b)\;\; \varepsilon(P,1+\alpha\eta)\subset L(H)
\end{aligned} \tag{4-42}$$

In the theorem, it is assumed that the feedback law (F), η which is related to the size of the ellipsoid, and the disturbance energy α are given. If conditions (a2) and (b) hold, it means that a feedback law (h) exists that guarantees the trajectories remain inside the outer ellipsoid without saturating. If condition (a1) holds alongside conditions (a2) and (b), for the given feedback law (F), the trajectories remain inside the outer ellipsoid.

These conditions are defined for the system of Equations (4-38) with a saturation type nonlinearity. However, the nonlinearity in the proposed model (ψ) is not a saturation-type nonlinearity (see Eq.4-36). And since the optimization problem is solved for control synthesis purposes, the feedback is an unknown variable that needs to be optimized. The conditions of Eq.(4-42) can be altered for the proposed nonlinear model as follows:

$$\begin{aligned}
&a)\ \left(A + k_1 BF\right)^T P + P\left(A + k_1 BF\right) + \frac{1}{\eta} PEE^T P \le 0 \\
&b)\ \left(A + k_2 BF\right)^T P + P\left(A + k_2 BF\right) + \frac{1}{\eta} PEE^T P \le 0
\end{aligned} \qquad \left(4-43\right)$$

Therefore, an optimization problem that finds the maximum tolerance disturbance energy with nonzero initial conditions (initial conditions inside $\varepsilon\left(S,1\right)$) is defined as follows:

$$\begin{aligned}
&a)\ \varepsilon\left(S,1\right) \subset \varepsilon\left(P,1\right) \\
&b)\ \mathrm{E}q.\ \left(4-43\right) \\
&c)\ \varepsilon\left(P,1+\alpha\eta\right) \subset L\left(H\right)
\end{aligned} \qquad \left(4-44\right)$$

Next, an optimization problem that finds the feedback law that maximizes the tolerable disturbance energy is defined. For consistency with previous designs, it is assumed that the trajectories start from initial points X_0 inside the inner ellipsoid and not from $\varepsilon\left(S,1\right)$. The system also needs to satisfy the input and state constraints. The resulting optimization problem can be expressed as:

$$\sup_{P>0,F} \alpha$$

$$
\begin{aligned}
&(a)\ x_i \in \varepsilon(P,1), i=1,2,\cdots,l \ \ and \ \ x_i \in X_0 \\
&b1)\ (A+k_1BF)^T P + P(A+k_1BF) + \frac{1}{\eta} PEE^T P \le 0 \\
&b2)\ (A+k_2BF)^T P + P(A+k_2BF) + \frac{1}{\eta} PEE^T P \le 0 \\
&(c)\ \varepsilon(P,1+\alpha\eta) \subset L(F/I_{\max}) \\
&(d)\ \varepsilon(P,1+\alpha\eta) \subset L(G)
\end{aligned}
\qquad (4-45)
$$

Conditions (b1) and (b2) are the disturbance tolerance with respect to normal sector lines. And this optimization problem can be expressed with the following LMI:

$$Sup_{Q>0,F,\mu(0,1)} \ \overline{\alpha}$$

$$
\begin{aligned}
&a)\ \begin{bmatrix} 1 & x_i^T \\ x_i & Q \end{bmatrix} \ge 0, \qquad i=1,2,\cdots,l \qquad and \qquad x_i \in X_0 \\
&b1)\ \begin{bmatrix} Q(A+k_1BY)^T + (A+k_1BY)Q & \overline{\alpha}E \\ \overline{\alpha}E^T & \frac{\mu-1}{\mu} I \end{bmatrix} \le 0 \\
&b1)\ \begin{bmatrix} Q(A+k_2BY)^T + (A+k_2BY)Q & \overline{\alpha}E \\ \overline{\alpha}E^T & \frac{\mu-1}{\mu} I \end{bmatrix} \le 0 \\
&c)\ \begin{bmatrix} I_{\max}^2\mu & Y \\ Y^T & Q \end{bmatrix} \ge 0 \\
&(d)\ g_k Q g_k^T \le 1, \ k=1,2,\cdots,p
\end{aligned}
\qquad (4-46)
$$

Here Y=FQ, $\mu = \frac{1}{1+\alpha\eta}$, $\mu \in (1,0)$, $\overline{\alpha} = \sqrt{\alpha}$. The above optimization problem is designed to find the maximum tolerable energy, for each fixed $\mu \in (0,1)$. Therefore, the optimization problem should be solved by varying μ between 0 and 1. The algorithm for finding the maximum tolerable energy is illustrated with the following flowchart (see Fig. (4-5)).

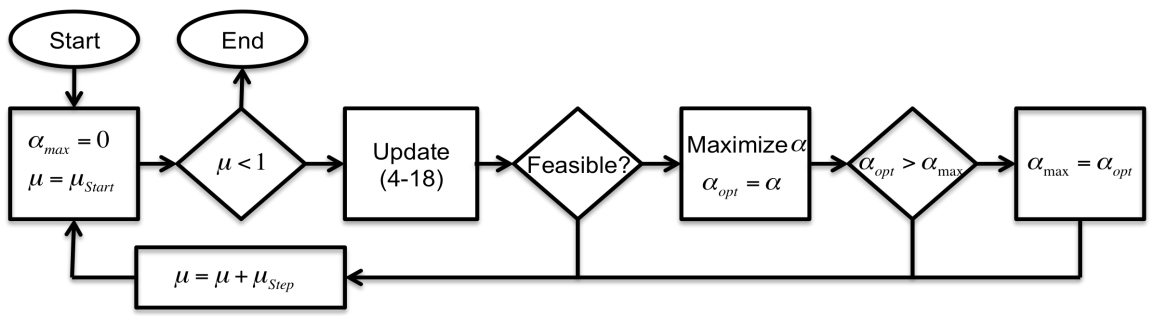

Figure 4-5 Optimization Flowchart for Disturbance Rejection

In the case of magnetic bearings, the outer ellipsoid should be set such that the closed loop trajectories will not exceed 50% of the airgap since this the usual location of the backup bearings and backup bearing contact should be avoided. This condition can be corporated into the state constraint and the optimization problem can be solved to find the maximum tolerable disturbance energy. Clearly the optimization problem can be set up to find the smallest outer ellipsoid in a similar fashion.

5 Simulation and experiment

In this chapter simulation and experimental results are presented. Controllers for the largest domain of attraction, best transient response, and best disturbance rejection were designed in Sections 5-2,5-3, and 5-4. The controllers were designed based on the balance beam specifications and the available M-19 silicon iron magnetization curve and the system's response was simulated in each case. Section 5-6 examines each component model more closely, using experimental data to make necessary adjustments to the system. Section 5-7 describes the procedure of designing a simple PID controller for preliminary testing of the system components. Section 5-8 is dedicated to the low pass filter design. The electromagnets' calibration process is reported in Section 5-9 and the final 2 sections compare the experimental data and the simulation for transient response and disturbance rejection.

5.1 Introduction

In this chapter, various controllers were designed to examine the significance of the modeled nonlinearity. The model based on the proposed nonlinear method with regular and generalized sector conditions, is compared with the linear model. A schematic view of these different models is shown in Figure 5-1.

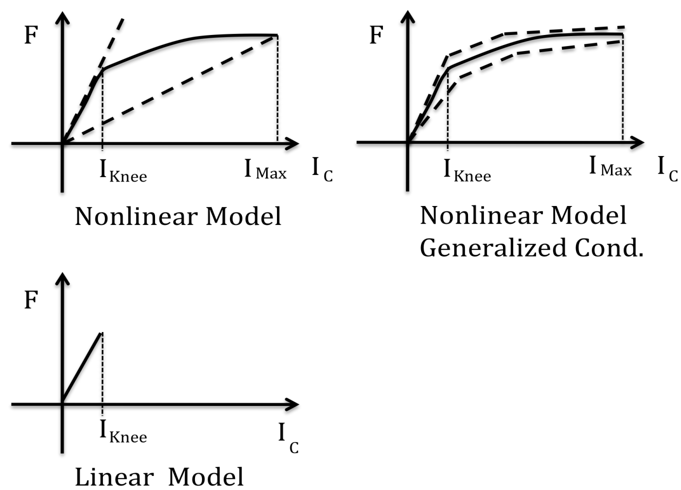

Figure 5-1 A Schematic View of The Modeling Methods

As can be seen while the linear model can be operated to the maximum current of I_{knee}, the nonlinear models can be operated with a much higher current of $I_{\max}$. The values of I_{knee} and $I_{\max}$ can be found in Table 2-5. The following dimensionless variables are used in the simulation.

$$\Theta = \frac{\theta}{\theta_{\max}} \tag{5-1}$$

$$\lambda = \frac{I}{I_{\max}} \tag{5-2}$$

5.2 Largest Invariant Ellipsoid

The method discussed in Section 4-4 was used to design a controller, which can achieve the largest initial angle in the domain of attraction. In other words, a controller is designed which can start from the largest possible initial angle (θ_0) as an initial condition and still remain stable. The choice of $X_0 = (g_0 / L_a, 0)$ makes the optimization solely focus on maximizing the initial angle (θ_0) and not the initial angular velocity (because the second term in the vector is zero). Results listed in Table 5-1 show that the linear controller can stabilize the system from an initial normalized angle of $\Theta_0 = 0.8$, while the nonlinear controllers are able to stabilize the system from the largest possible initial angle $(\Theta_0 = 1)$. The domain of attraction and the constraints are shown in Figure 5-2. The sloped lines represent the constraint imposed by the maximum possible electric current (amplifier constraint). Using the nonlinear model makes these constraints less restrictive and therefore allows for a larger domain of attraction.

Table 5-1 LARGEST CONTROLEABLE STARTING ANGLE

Model	Θ_0
Linear	0.801
Nonlinear (reg. sce)	1.000
Nonlinear (gen. sec.)	1.000

The nonlinear models improve both the maximum stabilizable initial angle as well as the maximum initial angular velocity that the beam can start from and remain stable. In this case the generalized sector condition has little to no improvement over the regular sector condition and the corresponding ellipsoids and amplifier constraints are nearly identical. The improvement enabled by the use of the generalized sector condition will be seen more clearly in the following sections.

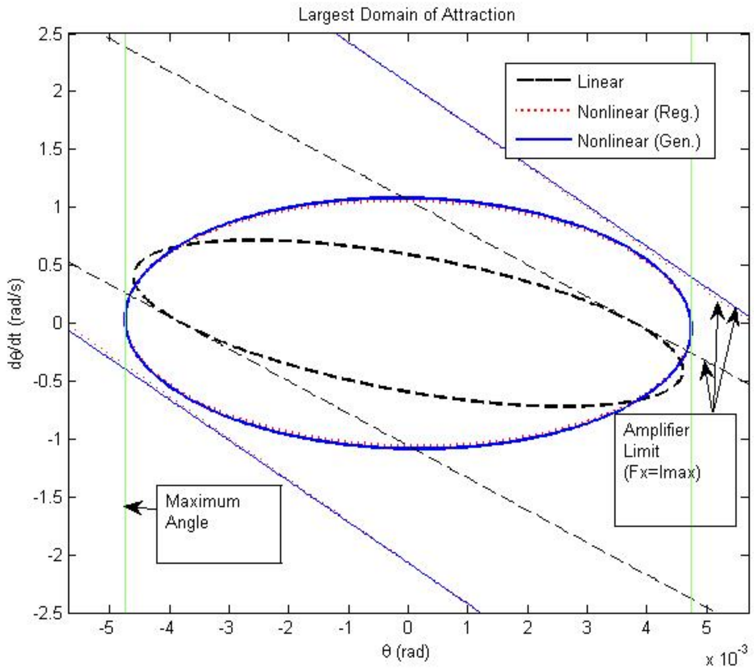

Figure 5-2 Domain of Attraction for Linear and Nonlinear Models

5.3 Best Transient Response

Section 4-5 of Chapter 4 presented the design method for a controller that can provide the best transient response while also maintaining an acceptable domain of attraction. The β values were calculated for various normalized starting angles (Θ_0), and the results are reported in Table 5-2 for the different models, where the transient response speed index is the value of β in the stability equation (Eq. 4-16).

Table 5-2 BEST TRANSIENT RESPONCE

Θ_0 max	β (Transient Response speed Index)		
	Linear	Nonlinear (Reg.)	Nonlinear (Gen.)
0	3000	3000	3000
0.1	1092	1447	1573
0.2	795.8	1041	1128
0.3	668.6	864.4	934.3
0.4	577.4	761.2	820.4
0.5	448.9	681.5	737.7
0.6	297.3	577.7	639.9
0.7	181.8	461.6	526.6
0.8	94.83	342.2	402.8
0.9	26.28	216.9	264.1
1.0	-----	----	----

Table 5-2 shows that using the nonlinear model can significantly improve the transient response of the system. It is also necessary to know the importance of using the generalized sector condition. In Table 5-2 both nonlinear models have improved the transient response, however there can be situations where using the nonlinear model with the regular sector condition does not result in an improvement over the linear model results. This can be explained more clearly by the results presented in Table 5-3.

Table 5-3 BEST TRANSIENT RESPONSE FOR DIFFERENT AIRGAPS

Airgap (mm)	Θ_0 max	β (Transient Response speed Index)		
		Lin.	Regular Sec.	Generalized Sec.
0.001	1	87	72	298
0.0025	0.8	638	1443	1962
0.005	0.99	17	266	354
0.01	0.97	5	235	1556

As a case study, here the airgap in the balance beam is modified and corresponding changes to other factors in the model are also made. As can be seen in Table 5-3, for the airgap of 0.001 mm even though the linear model has a smaller maximum current, it produces a better transient response. The reason for this result is that the regular sector condition in the nonlinear model is very conservative and in some cases can even be more restrictive than the linear model. This shortcoming can be eliminated completely by using the generalized sector condition. Using the nonlinear model with the generalized sector condition guarantees a significantly better transient response compared to traditional linear models as well as outperforming the regular sector condition results.

Figure 5-3 depicts the transient response of system with a nonzero initial position for linear and nonlinear models. As can be seen, controllers that are designed using the nonlinear model have a better transient response. The nonlinear controllers' settling time are approximately 30% smaller than the linear controller's settling time. The PD control parameters of the linear, nonlinear with regular sector, and nonlinear with generalized sector models are [2274 6.393], [4080 9.655], and [3944 8.897] respectively. The transient response speed index (β) for these three controllers is 552, 846, and 917 respectively.

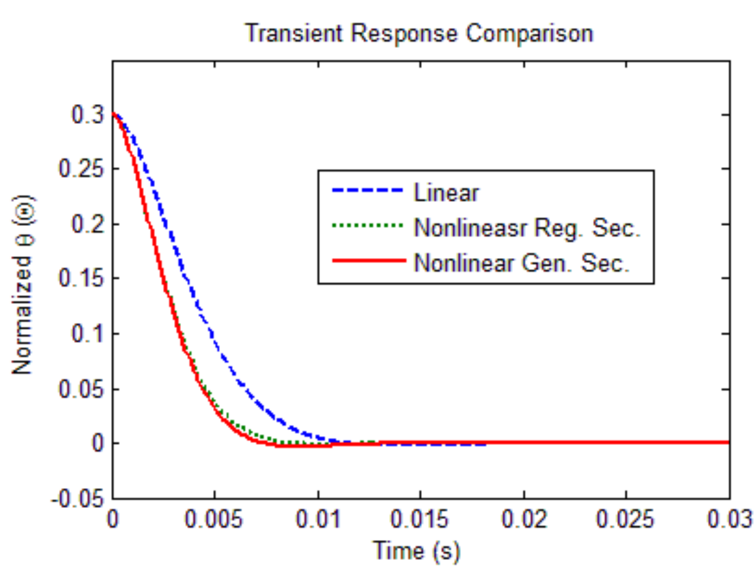

Figure 5-3 The Transient Response With Nonzero Initial Conditions

5.4 Disturbance Rejection

One of the most appealing advantages of using the nonlinear model is to increase the disturbance rejection potential. By using the proposed nonlinear model, the system can operate safely even when a significant increased load is applied due to a worst case operating condition (such as a storm on a wind turbine, turbulence on an offshore drilling rig, etc.). In this section a controller is developed based on the method presented in Sec. (4-6).

Table 5-4 DISTURBANCE REJECTION

Θ_0 max	α (Maximum Energy Index) Nonlinear	Linear
0	719	157
0.1	707	147
0.2	673	124
0.3	623	94.6
0.4	560	64.9
0.5	489	38.8
0.6	408	18.2
0.7	321	4.86
0.8	223	0.002
0.9	114	Not Feasible
1.0	Not Feasible	Not Feasible

The maximum tolerable disturbance energies for different models are shown in Table 5-4. It can be seen that by using the nonlinear model, the disturbance rejection capability of the test rig is significantly improved. As a more tangible example, assume that the balance beam represents a thrust magnetic bearing system with a backup bearing located at 50% of the airgap. The system has an initial position of 30% of the airgap. While the system is operating, a pulse-like disturbance upsets the system. The corresponding simulation results for this example case are shown in figures 5-4 and 5-5. In both figures, the top graph is a comparison of the time response of the system with a linear model as well as the proposed nonlinear model. The bottom graph in both figures shows the total control torque exerted on the beam in the linear and nonlinear models alongside the disturbance force.

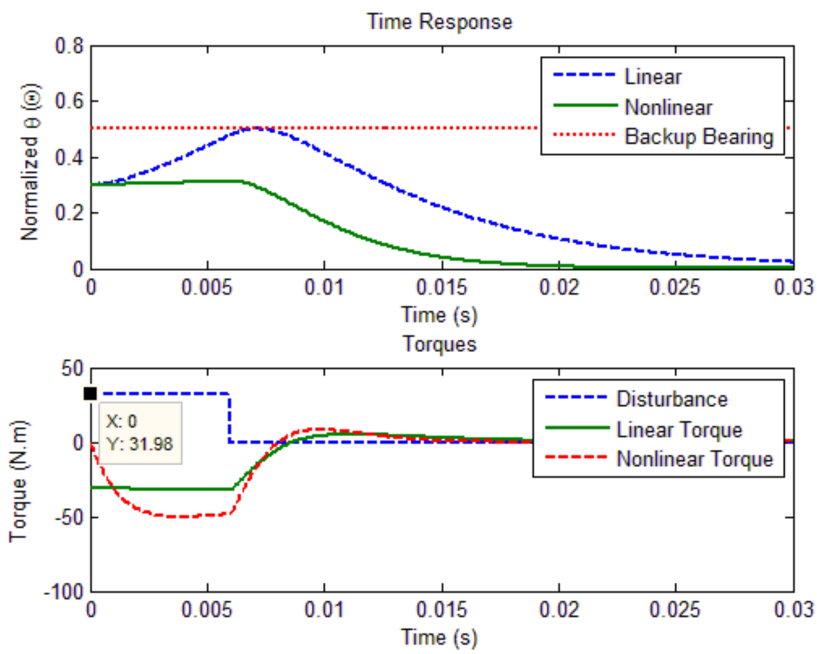

Figure 5-4 Time Response Comparison (Disturbance energy 261)

Figure 5-4 depicts transient response results associated with the maximum tolerable disturbance torque achievable by the linear model. The linear control parameters are $[F_1 \;\; F_2] = [1262 \;\; 5.202]$ and the nonlinear control parameters are $[F_1 \;\; F_2] = [2070 \;\; 6.920]$. With a disturbance torque amplitude of 32N.m and a time duration of 0.006(s), the linear system nearly makes contact with the backup bearing (exactly how the disturbance is applied is explained in sections 5-10). Applying the same disturbance force on the system that benefits from the controller designed by using the nonlinear model results in significantly smaller vibration amplitude and almost no overshoot. Here, a disturbance with a signal energy index (α) of 261 almost drives the linear system into contact with the backup bearing. However the predicted value for guaranteed tolerable disturbance energy is 85. It's important to note that the controller guarantees the stability of the system for all disturbances with a maximum energy index of $\alpha_{\max}$. Individual signals can have a larger energy index and still not destabilize the system. In case of Figure 5-4, a signal energy index of 261 does not destabilize the linear system.

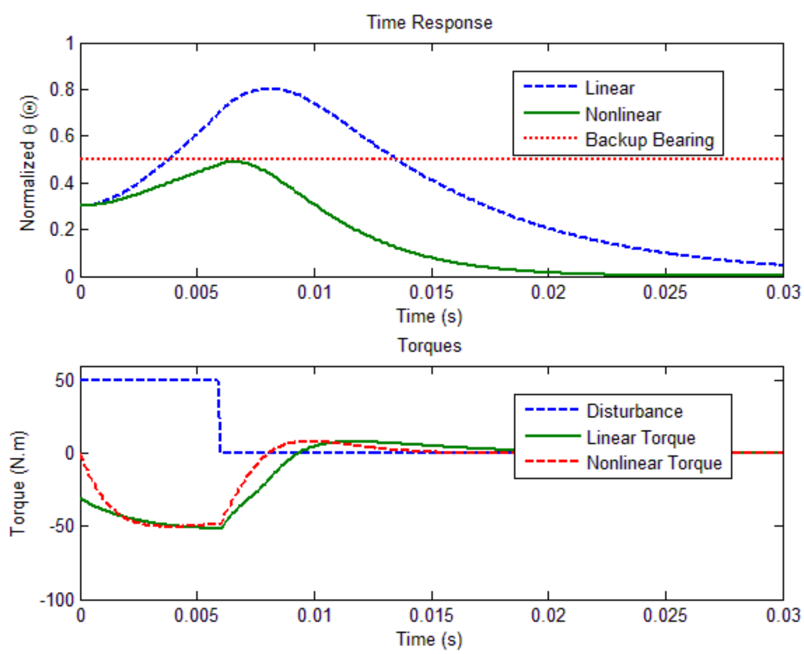

Figure 5-5 Time Response Comparison (Disturbance Energy 634)

Figure 5-5 depicts results associated with the maximum tolerable disturbance by the system with the nonlinear controller. While the nonlinear design tolerates torques as large as 50N.m and a time duration of 0.006s, the linear system with this same disturbance results in contact with the backup bearing. The torque graph shows how the extra torque capability helps stabilizing the system. The energy index (α) of this individual signal is 634 and the predicted guaranteed tolerable energy index is 450 in this case.

In this example, the disturbance response results demonstrate that for an existing AMB system, the system could tolerate a 56% larger disturbance torque and therefore 2.4 times the disturbance energy by just making adjustments to the controller.

The controllers designed for rejecting disturbances with energy of $\alpha_{\max}$ are capable of stabilizing the system under any disturbance with energy less than or equal to $\alpha_{\max}$. Disturbances with the same energy but different amplitudes and durations were imposed on the simulated system to examine the system's stability. These disturbance signals are depicted in Figure 5-6. In this simulation the controller is designed to stabilize the system from an initial normalized angle of 0.5 and therefore the energy of the disturbance signals are designed to be 489 (see Table 5-4)

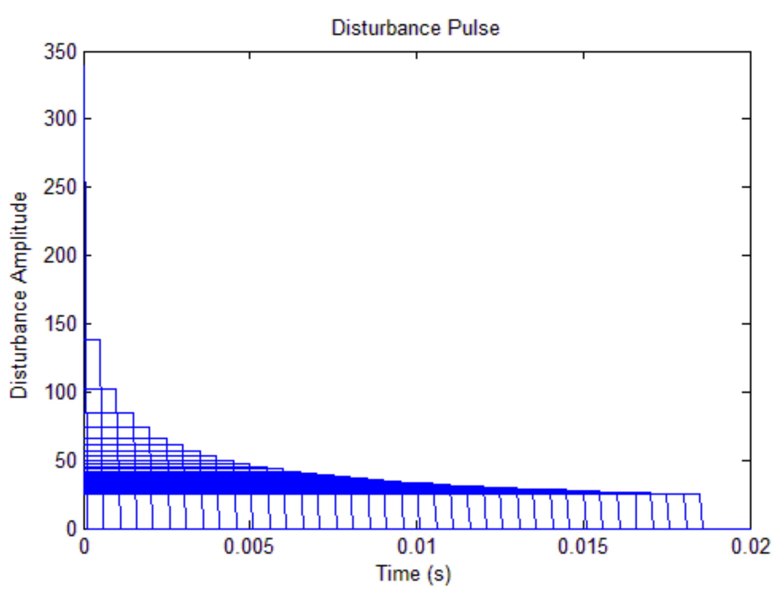

Figure 5-6 Various Disturbances With The Same Energy

The system with the controller designed based on the nonlinear model remains stable for all disturbances depicted in Figure 5-6. Figure 5-7 is a plot of the state trajectories for this system. The states starting inside the inner ellipsoid will remain inside the outer ellipsoid. The points inside the outer ellipsoid represent the states that satisfy all the constraints imposed on the system. The vertical straight lines represent the state constraint and the two inclined lines represent the input (amplifier) constraint. The outer ellipsoid should be inside these straight lines to satisfy the input and state constraints. All trajectories start from $(\Theta_0, \dot{\Theta}_0) = (0.5, 0)$. As can be seen, all state trajectories stay bounded and inside the outer ellipsoid and therefore there is no contact with the beam and the electromagnets. Figure 5-8 is the time response of the system subjected disturbance pulses depicted in Fig. (5-6).

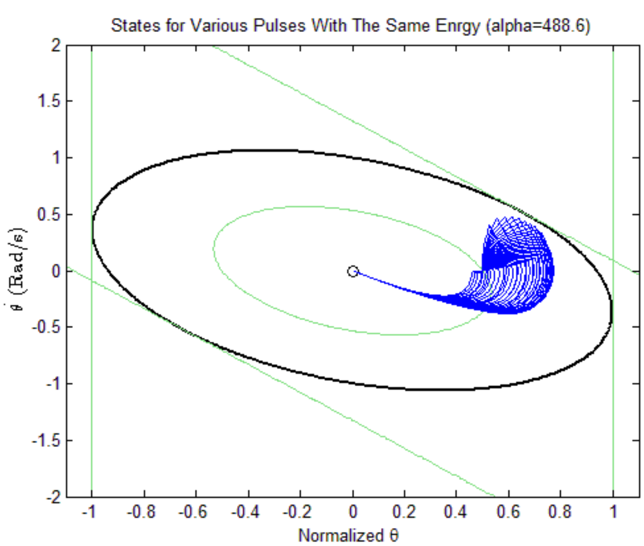

Figure 5-7 State Trajectories Under Disturbance (Nonlinear Model)

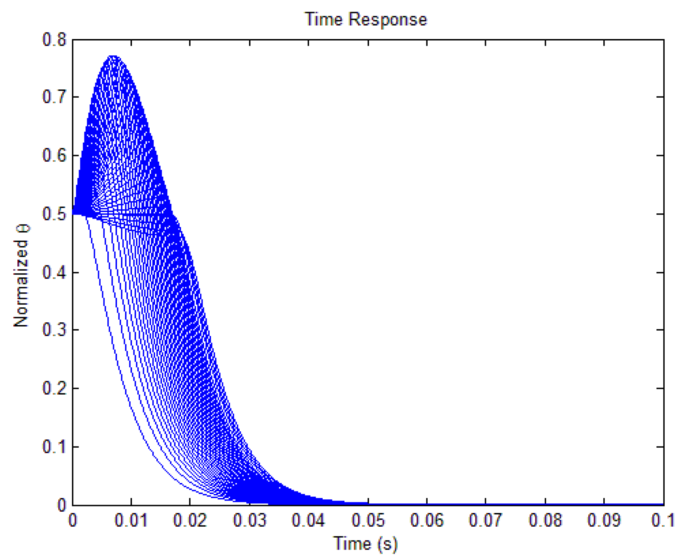

Figure 5-8 Time Response Under Disturbance (Nonlinear Model)

Figures 5-9 and 5-10 are the state trajectory and time response of the system with the controller designed based on the linear model. The system is subjected to the disturbances of Figure 5-6. While the external disturbances are exactly the same for linear and nonlinear controllers, the system response is extremely different and in case of the linear controller, contact is made between the beam and the electromagnets.

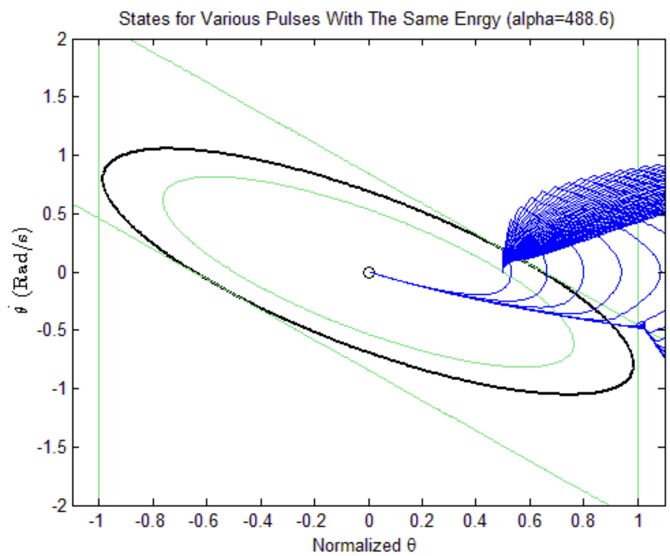

Figure 5-9 State Trajectories Under Disturbance (Linear Model)

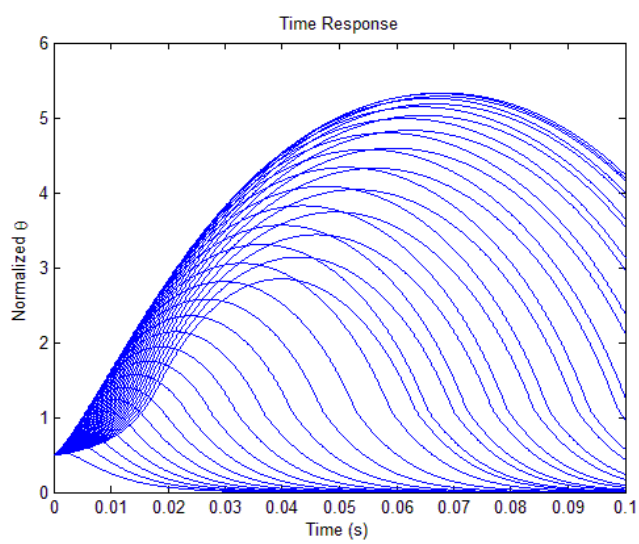

Figure 5-10 Time Response Under Disturbance (Linear Model)

5.5 Testing Individual components

For proper operation of the test rig, all components need to be modeled accurately. The test rig consists of the beam, the amplifiers, the sensors, the A/D and D/A cards, and the controller. Each individual component's model can be verified experimentally as follows:

1-The beam

The natural frequencies of the beam were found by modeling. In order to measure the first bending frequency a Rap test should be conducted. The Rap test consists of mounting an accelerometer on the beam, hitting the beam with an instrumental hammer and monitoring the frequency spectrum. The sensor should be placed such that the bending mode is observable and the hammer should hit a place that is controllable to excite the bending mode. Therefore the sensor should be placed close to the end of the beam and the hammer should impact the beam close to the end as well. Since the pivot is in the middle and the beam is not stable by itself, this test is not very easy to conduct with out some modifications. In order to stabilize the beam, one can either add two loose wires to each end to keep the beam from dropping to one side. Then the beam can momentarily be balanced by hand, released and hit by the hammer very quickly. As an alternative, two wires can be tightened very close to the pivot in order to prevent its movement while also having a low impact on the beam's first bending mode boundary conditions (position and angle in the middle is zero).

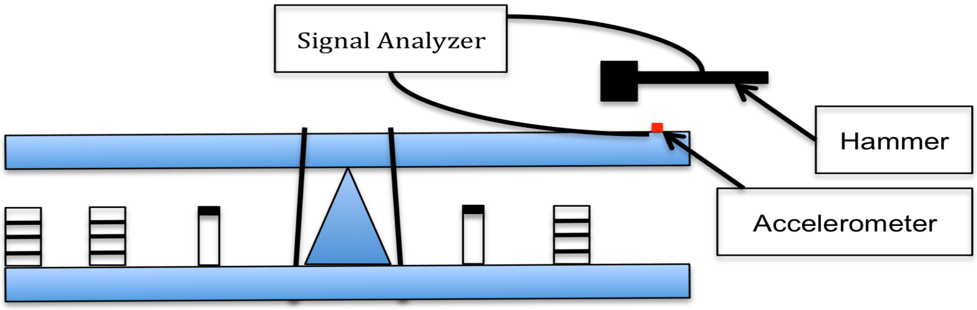

Figure 5-11 Beam's Natural Frequency Test

2-The amplifiers

The amplifier's bandwidth can be found by a sine swept test. The sine swept test consists of providing the system with a sine wave input and sweeping the frequency of the input sine wave over a wide range of frequencies. The output of the system is then compared to the input to obtain the frequency spectrum and transfer function of the system. In the case of the amplifier, the sine waves should be provided to the control input of the amplifier. The amplitude of the sine waves should not be very large in order to prevent the amplifier from saturating or exhibiting any other nonlinear behavior. The output of the amplifier is the current monitor. This output can be compared to the input to obtain the amplifier's bandwidth and cutoff frequency.

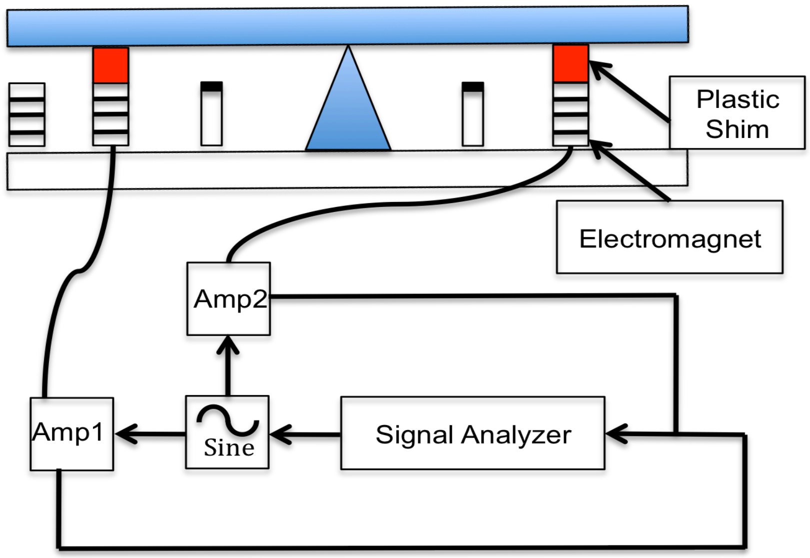

Figure 5-12 Amplifier Bandwidth Test

Figure 5-12 displays the test setup for the sine swept testing of the amplifier with the beam shimmed to maintain a fixed nominal airgap. Since the current monitor has a gain of 0.2 V/A, the DC output to input ratio is predicted to be -7.9588 dB:

$$\text{Output/Input} = \text{Amplifier Gain} \times \text{Current Monitor Gain} = 2 \times 0.2 = 0.4$$

$$20\text{Log}(\text{Output/Input}) = 20\text{Log}(0.4) = -7.9588$$

Using the above procedure, the amplifier's cutoff frequency was determined to be approximately 920Hz. Figure 5-14 demonstrates the amplifier's frequency response for frequencies smaller than 500Hz. This figure shows the amplifier's behavior more precisely. The amplitude is normalized and is not logarithmic. The amplifier maintains very good precision even for frequencies as high as 500Hz.

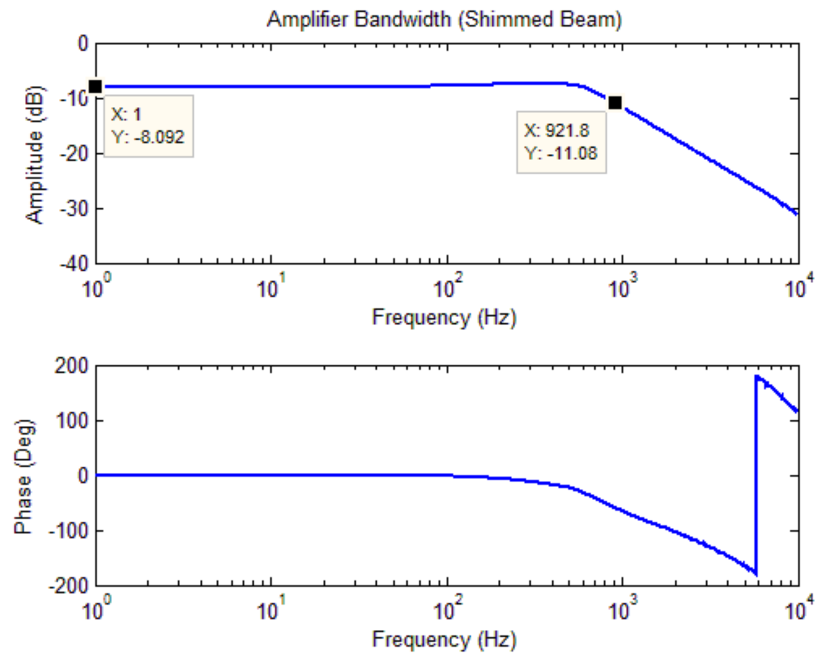

Figure 5-13 The Amplifier Logarithmic Swept Sine (Shimmed Beam)

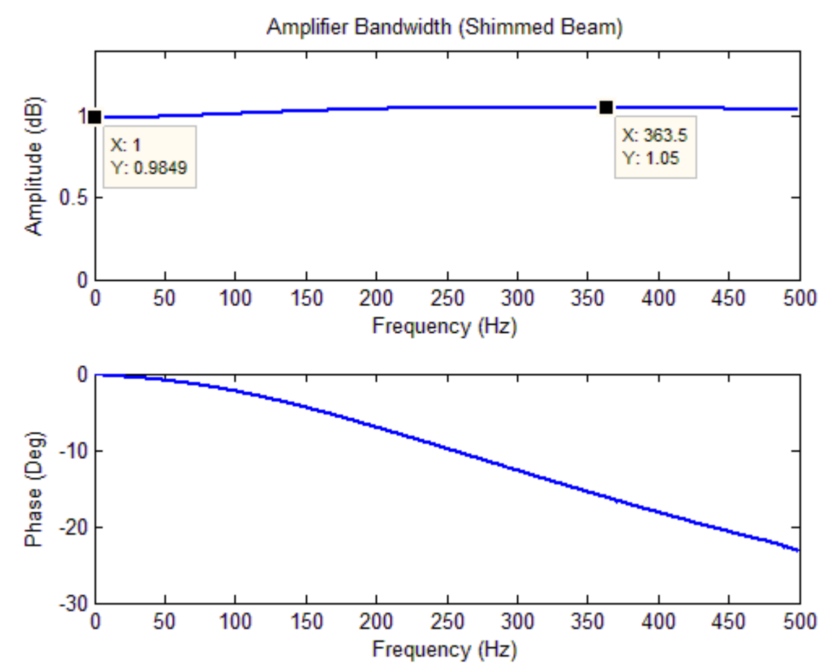

Figure 5-14 The Amplifier Swept Sine (Shimmed Beam)

3-Sensors

Dynamic testing of the sensors requires a more sensitive sensor that can measure the distance and compare it with the system's sensors, which was determined to be impractical and unnecessary for this work. Therefore the sensors were not dynamically tested. The sensor bandwidth stated by the manufacturer is much higher than the actuator bandwidths and therefore precise dynamic modeling is not necessary. However the sensors were statically tested and calibrated in order to accurately model the sensors' DC gain. In addition to DC gain sensor noise was analyzed. To measure the noise level in the sensors, the following test was conducted. The electromagnets were shimmed at the nominal airgap with plastic shims and the sensor signal fed into a signal analyzer (Fig 5.15). In order to capture the effect of the electromagnets on the sensors, the test should be conducted with the electromagnets energized to the bias current level.

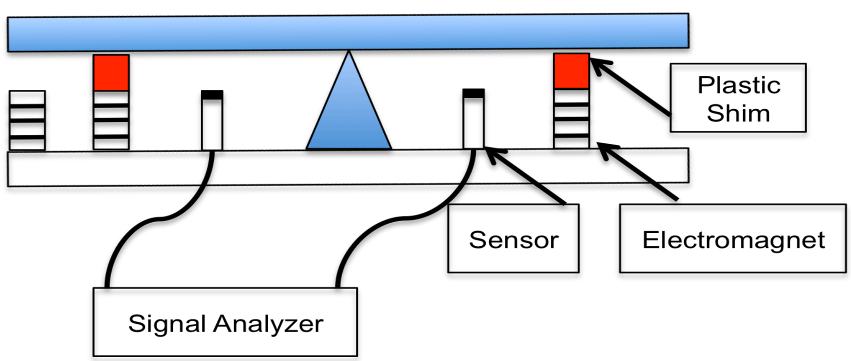

Figure 5-15 Sensor Noise Test

The Frequency Analyzer data (Fig. 5-16) depicts the noise in the sensor output. The smallest significant noise frequency is about 25 kHz. Two LTC1064-1 anti-aliasing Cauer filters are used to filter any noise with frequencies higher than 10kHz, therefore the noise in these higher frequencies are of no practical concern.

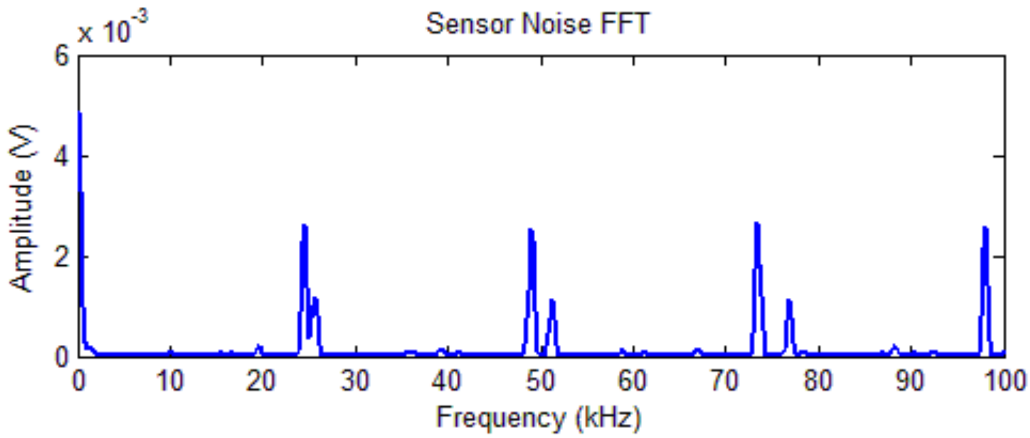

Figure 5-16 Sensor Signal (Electromagnets Are On)

4-Data acquisition cards and the controller software

In order to test these components a sine sweep test should be conducted. For the first test, the derivative portion of the controller (K_d) was set to zero. The input sine wave was fed to the A/D card and the output of the D/A card was fed to the frequency analyzer. In this way the frequency analyzer can capture the dynamics related to the A/D and D/A card as well as the controller software dynamics.

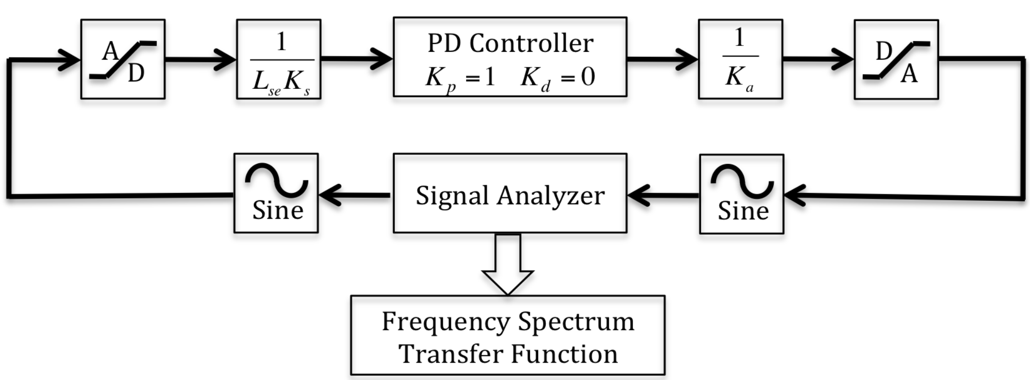

Figure 5-17 Data Acquisition and Software Test

Since the calculated controller values are closer to 1000, Kp is chosen to be 1000 for the Sine swept test. The expected DC gain can be calculated as:

$$\frac{K_p}{K_s K_a L_{se}} = 0.5305$$

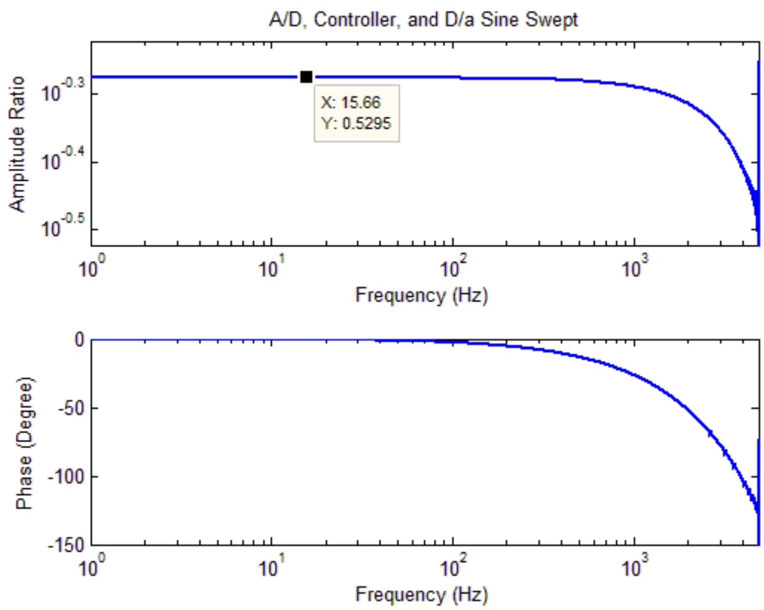

Figure 5-18 The Data Acquisition and Controller Swept Sine (No Beam) Frequency Response

The test was conducted over a frequency range of 1-5000 Hz and the controller and cards exhibit a large cutoff frequency that is more than adequate for our application. To examine the dynamics of the low pass filter, a similar test is conducted, but this time with $K_p = 0$ and $K_d = 1$. The simulated and experimental responses are compared in Figure 5-19.

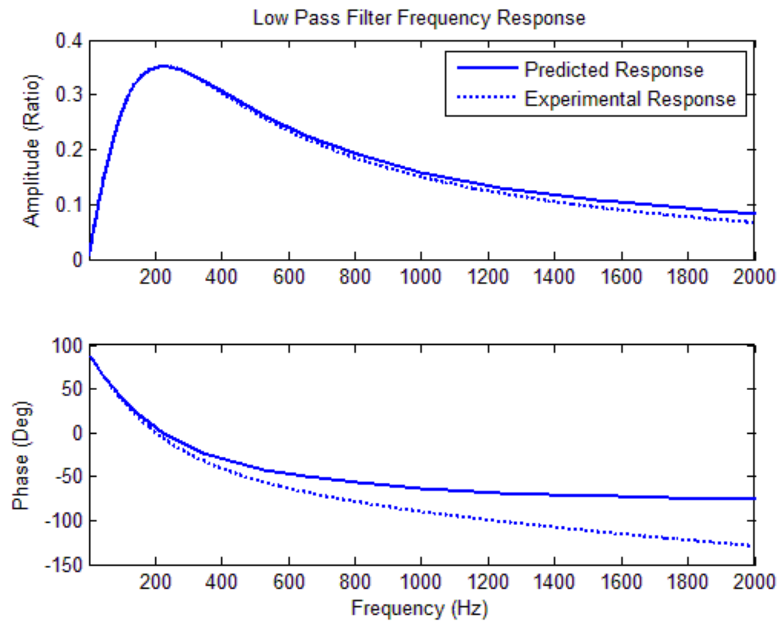

Figure 5-19 The Data Acquisition and Filter Swept Sine

As can be seen the experimental data follows the simulation quite closely. The lag in phase is caused by analog to digital conversion. The sampling frequency of the conversion is 10kHz.

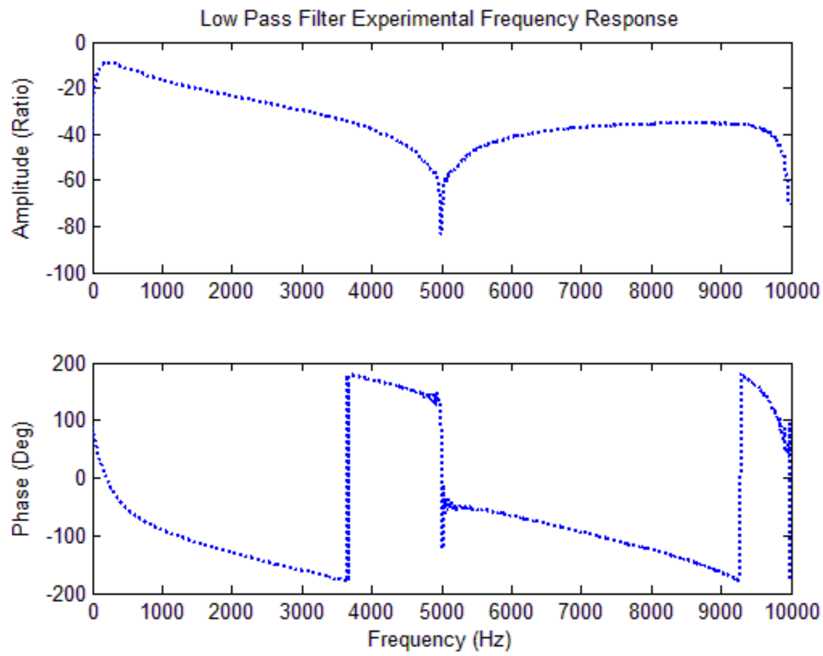

Figure 5-20 The Data Acquisition and Filter Swept Sine Frequency Response

Figure 5-20 Shows the Filter frequency response in a higher frequency range (0-10kHz). The effect of the digital conversion is clearer in this figure.

5-Open Loop Transfer Function

This test examines the frequency response of the mechanical and electrical portions of the system excluding the controller. The signal analyzer input signal is taken right after the controller and the output signal is right before the controller (see Fig. 5-21). The sine-wave excitation can be injected after the controller but this can result in large vibrations. A better place for injecting the sine-wave excitation is just before the controller. By doing this the amplitude of the sine-wave excitation can be adjusted to achieve a desirable displacement level.

Originally the experimental data did not match the model very well, but by accounting for losses and correcting the number of coil turns, the model was made to agree with the experimental results to a high level of accuracy. To account for the losses, and mechanical assembly tolerances, the effective pole face area was reduced to 90% of the original design. In addition the actual number of coils were found to be 95, not 110 as was originally assumed.

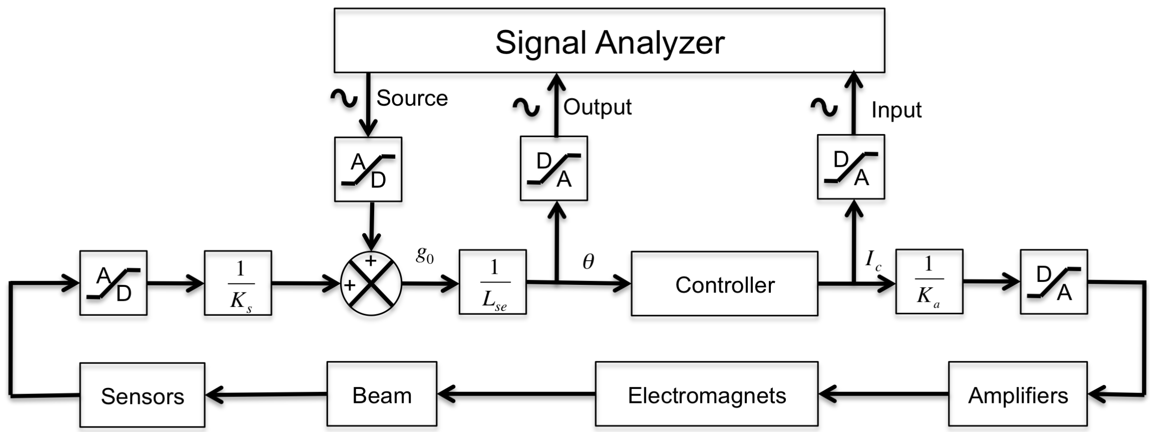

Figure 5-21 Open Loop Test Setup

5-Base

The base’s dynamics can affect the system response. Therefore the base should be rigid enough to avoid this issue. In order to decrease the effect of the base plate even more, it was bolted to a concrete block. To measure the effect of the base on system measurements, a hammer test was conducted. Since the electromagnetic force is exerted on the beam at the actuator location, this was the location chosen for the hammer impact. The accelerometer was placed at the sensor location (see Fig. 5-22)

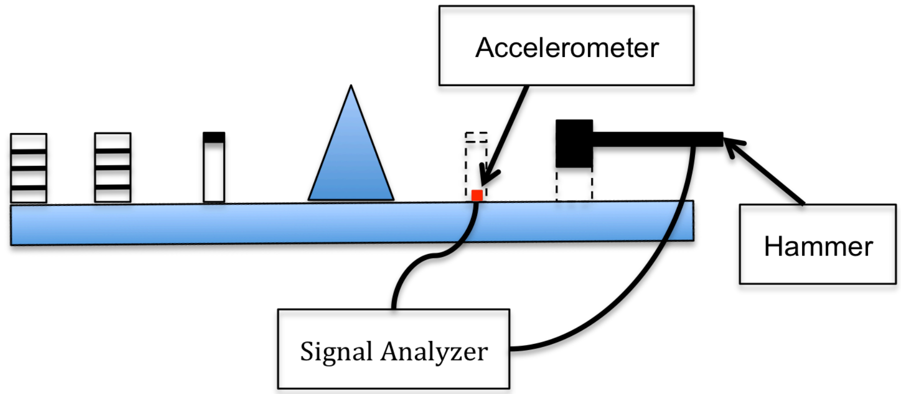

Figure 5-22 Base's Natural Frequency Test

6-Closed loop transfer function

Finally a sine sweep test was conducted on the closed loop system. However since the balance beam is open loop unstable a controller needs to be running to stabilize the system to facilitate the test. For this purpose a PID controller with a low bias current was designed. The design process is explained in the next section.

5.6 PID Controller Design

In order to verify the system model and obtain the system's transfer function experimentally. The beam needs to be levitated and a sine-sweep test with a signal analyzer can be conducted. Initially, a simple controller can be designed to levitate the system since the main goal here is to obtain an experimentally validated system model. For this purpose, a PID controller was designed. Since the integrator portion of the PID controller does not have a significant effect on the system dynamics, a PD controller was designed first and the integrator portion was then added on. The balance beam model used for this control design process is shown in Figure 5-23.

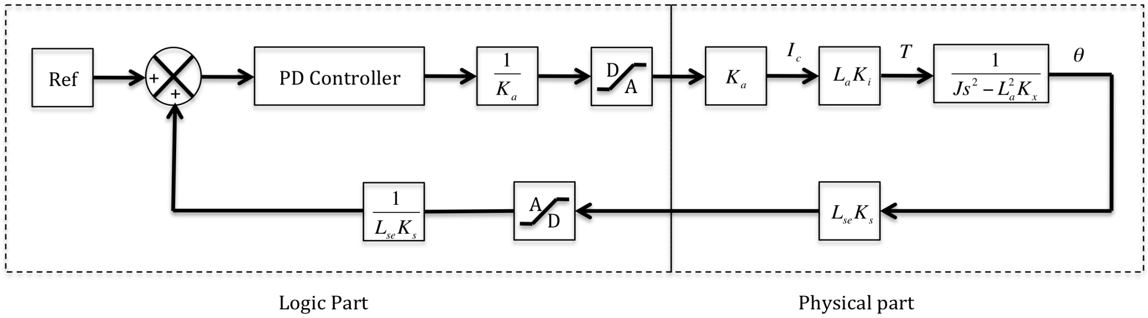

Figure 5-23 The Balance Beam System With a PID Controller

In this system, the D/A and A/D represent the data acquisition cards. Since there is a $\pm 10V$ voltage limit on the D/A card, if currents greater than 10A are required, the amplifier gain needs to be greater than 1.0. For this work, the amplifier gain (K_a) was set to be 2.0. K_I and K_X are the current and displacement force coefficients which are defined in Section 3-6. The force coefficients are multiplied with L_a (the distance between the pivot and the electromagnets) in the block diagram to obtain a torque input to the system. T is the torque exerted on the beam. K_s is the sensor gain and L_{se} is the distance between the sensor and the pivot. For the sensors used in this test rig (MICRO-EPSILON mictoNCDT 100), K_s is equal to 269 V/in (10.6 V/mm). The sensor output should be within $\pm 10V$ to avoid saturating the A/D card. With a nominal airgap of 30 mils for this test rig,this should not be an issue. The PD controller transfer function is:

$$PD(s) = K_d s + K_p \tag{5-3}$$

The beam's transfer function can be expressed as:

$$J\ddot{\theta} = L_a\left(K_x x\right) + T = L_a\left(K_x L_a \theta\right) + T \Rightarrow \frac{T(s)}{\theta(s)} = \frac{1}{Js^2 - L_a^2 K_x} \qquad (5-4)$$

The closed loop transfer function can be calculated as:

$$\frac{\theta(s)}{R(s)} = \frac{G(s)}{1 + H(s)G(s)} = \frac{\dfrac{\left(K_d s + K_p\right)L_a K_i}{Js^2 - L_a^2 K_x}}{1 + \dfrac{\left(K_d s + K_p\right)L_a K_i}{Js^2 - L_a^2 K_x}} = \frac{L_a\left(K_d s + K_p\right)K_i}{Js^2 - L_a^2 K_x + L_a\left(K_d s + K_p\right)K_i}$$

$$\frac{\theta(s)}{R(s)} = \frac{L_a K_i\left(K_d s + K_p\right)}{Js^2 + L_a K_i K_d s + \underbrace{L_a K_i K_p - L_a^2 K_x}_{\overline{K}}} \qquad (5-5)$$

As a rule of thumb, K_p should be chosen such that, $L_a^2 K_x < \overline{K} < 2L_a^2 K_x$. These values are based on experimental experience. Here, the upper limit $\left(2L_a^2 K_x\right)$ was chosen for the balance beam's closed loop stiffness, such that:

$$\overline{K} = 2L_a^2 K_x \Rightarrow L_a K_i K_p - L_a^2 K_x = 2L_a^2 K_x \Rightarrow K_p = \frac{3L_a K_x}{K_i} \qquad (5-6)$$

A bias current of 1A was used for this initial PD controller design. A proportional controller (K_p) value of 612.5 was determined to be suitable for this initial design. With a value for K_p is chosen, an appropriate K_d can be selected to stabilize the system while maintaining an appropriate transient response. To estimate the transient response characteristics of the system, the characteristic equation $\left(Js^2 + L_a K_i K_d s + \overline{K} = 0\right)$ should be written in the standard form $\left(s^2 + 2\zeta\omega_n + \omega_n^2 = 0\right)$. This estimates the system of Equation (5-5) as a standard second order system:

$$\frac{\theta(s)}{R(s)} = \frac{\omega_n^2}{s^2 + 2\zeta\omega_n + \omega_n^2} \qquad (5-7)$$

By writing the characteristic equation in standard form, the system's damping ratio and natural frequency can be estimated as:

$$\omega_n = \sqrt{\frac{\overline{K}}{J}} = L_a\sqrt{\frac{2K_x}{J}} \qquad (5-8)$$

$$2\zeta\omega_n = 2\zeta L_a\sqrt{\frac{2K_x}{J}} = \frac{L_a K_i K_d}{J} \Rightarrow \zeta = \frac{K_i K_d}{2\sqrt{2K_x J}} \qquad (5-9)$$

The important parameters related to transient response are as follows:

$$\text{Settling Time } \left(\mathrm{T_s}\right) \approx \frac{4}{\zeta w_n} \qquad (5-10)$$

$$\text{Rise Time } \left(\mathrm{T_r}\right) \approx \frac{2.5}{w_n} \qquad (5-11)$$

$$\text{Peak Time } \left(\mathrm{T_p}\right) \approx \frac{\pi}{w_d} = \frac{\pi}{w_n\sqrt{1-\zeta^2}} \qquad (5-12)$$

$$\text{Overshoot } \left(\mathrm{M_p}\right) = 100e^{-\frac{5\pi}{\sqrt{1-\zeta^2}}} \qquad (5-13)$$

Based on these equations, an appropriate value for ζ can be selected in order to achieve the designed transient response and K_d can be calculated from Eq. (5-9). Unlike a standard second order system (Eq. (5-7)), the system's transfer function (Eq.

(5-5)) has a zero. This ignored zero affects the calculated transient response characteristics. As an alternative, the system response can be simulated for different values of K_d to find an optimized K_d that provides the system with the best transient response. In order to facilitate this the rise, settling, and peak times were plotted as a function of K_d in Figure 5-24.

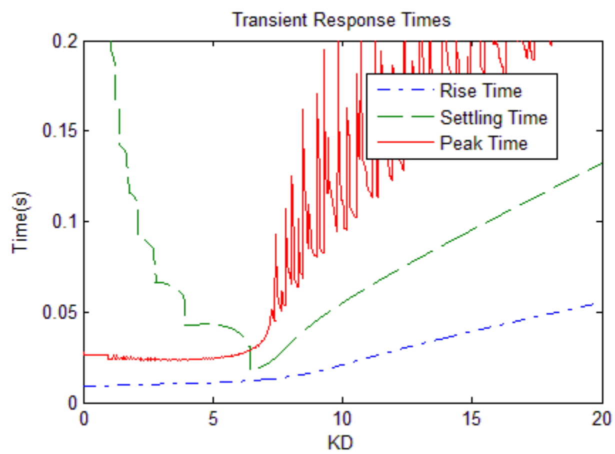

Figure 5-24 The Transient Response Parameters of The Balance Beam

Overshoot as a function of K_d shown in Figure 5-25 and The step response of the system for different K_d values is shown in Figure 5-26. By examining these 3 figures, a suitable value for K_d was chosen to be 7.0.

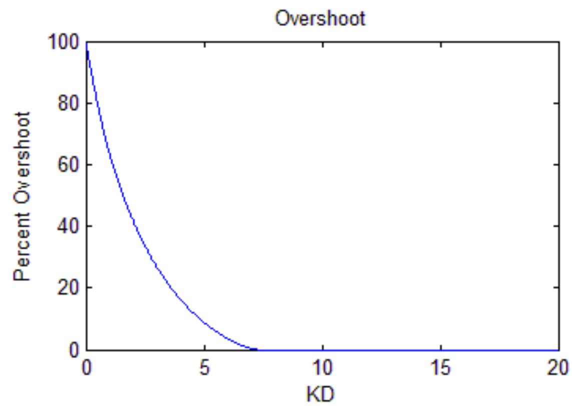

Figure 5-25 The Damping and Overshoot of The Balance Beam

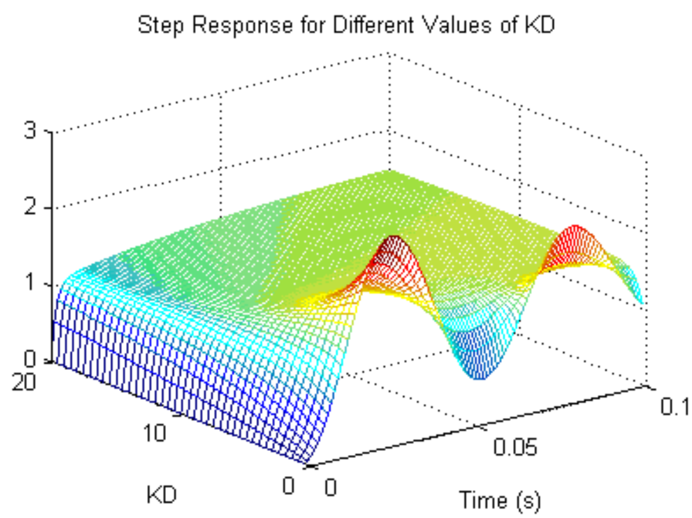

Figure 5-26 The Step Response Plot of The Balance Beam

5.7 Low Pass Filter Design

The controller in this work is a full state controller. Therefore all the states (x and $\dot{x}$) are needed for the controller to function. The eddy current sensors provide the position information, however there is no direct sensor information related to velocity. An observer could be used to estimate the velocity. However to simplify things, the derivative of the position was used instead. The derivative's transfer function (s) has a numerator order of 1, which is larger than the order of the denominator (0). This is not physically realizable. In order to obtain realizable derivative, a low pass filter needs to be added. In other words, a low pass filter is needed in conjunction with the derivative in order to make the order of the denominator greater than or equal to the order of the numerator.

$$\dot{x} \approx \frac{s}{\frac{s}{f_{cut-off}}+1}x \qquad (5-14)$$

The cutoff frequency of the low pass filter should be designed based on the following criteria:

1-Noise level: noise should be minimized as much as possible; therefore the cutoff frequency should be lower than the dominant noise frequencies.

2-Sampling frequency: The cut-off frequency should be lower than half the sampling frequency (Shannon's sampling theorem). As a rule of thumb the cut-off frequency should be at least two times and preferably five times lower than the sampling frequency.

3-Controller bandwidth: The cutoff frequency should be higher than the desired controller bandwidth in order to avoid interfering with the controller. The controller's bandwidth is defined by the frequency of the unstable pole of the open loop system. The controller's bandwidth can be estimated as follows:

$$\text{Controller's Bandwidth} \approx \sqrt{\frac{K_\theta}{J}} \qquad (5-15)$$

Here K_θ and J are the rotational stiffness and mass moment of inertia of the beam. As a rule of thumb the cut-off frequency should be at least two times larger than the controller's bandwidth.

For this experiment the sampling frequency is 10 kHz, therefore a cut-off frequency less than or equal to 2 kHz is desirable. The unstable pole frequency is 45 Hz, therefore the cut-off frequency should be larger than 90 Hz. All things considered, a cut-off frequency of 1 kHz was deemed appropriate. The overall resulting control structure is depicted in Figure 5-27.

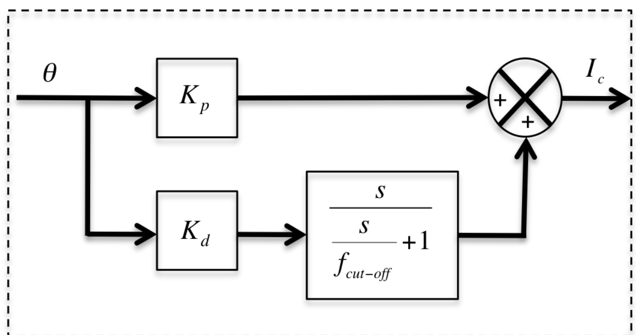

Figure 5-27 The Derivative and The L.P.F Blocks

5.8 Electromagnet Calibration

In order to verify the electromagnet's behavior, a force test was conducted. Different weights were hung from one side of the beam, while the electromagnet on the other side used a PID controller to balance the beam in a horizontal position. When the beam reached the horizontal position (θ=0) the electromagnet's electric current was recorded. This experiment was done for both of the control electromagnets with weights ranging from 1 to 40lb's (see Fig 5-28)

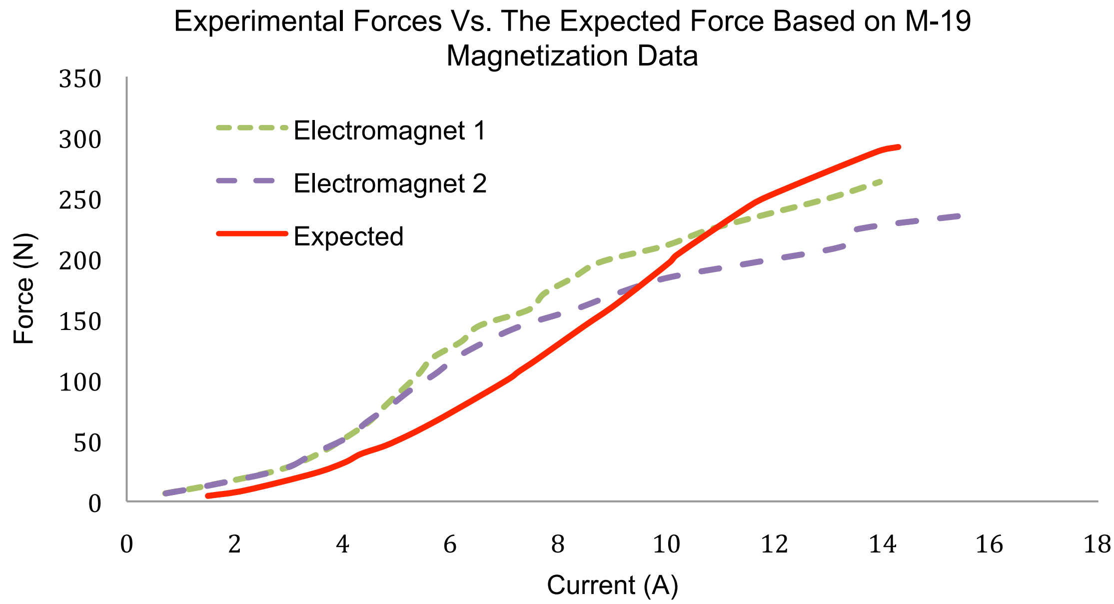

Figure 5-28 Experimental Force vs The Expected Force Based on M19 Magnetization Data

As can be seen in the figure, the electromagnet forces are significantly different from the theoretically predicted force. Therefore, even though the electromagnet cores were made out of M-19 silicon iron, the available M-19 magnetization curve was not accurate enough and could not be used for this work. Therefore, a more suitable B-H curve needed to be generated based on the experimental data. Using Equations 3-4, 3-14, and 3-22, the following equations were used to calculate B and H from the experimental force curves.

$$B = \frac{\sqrt{(\mu_0 W)}}{A} \qquad (5-16)$$

$$H = \frac{\left(\frac{2g_0 B}{\mu_0} - NI\right)}{L_s} \qquad (5-17)$$

Where, W is the weight hung from the beam, A is the electromagnet's pole face area, N is the number of turns in the electromagnet coils, I is the current needed to keep the beam in the horizontal position, L_s is the length of the silicon iron in the magnetic circuit, and g_0 is the airgap. The average of the left and right electromagnet forces were used to determine the experimental B-H curve. The resulting curve can be seen in Fig. 5-29.

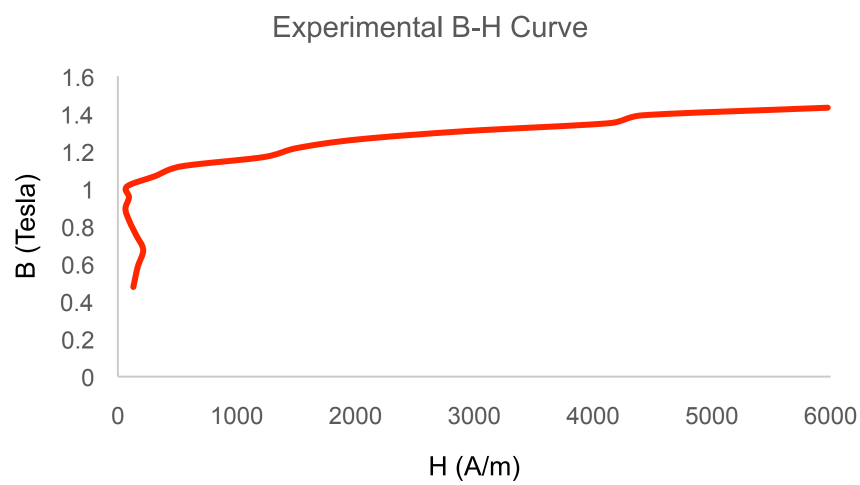

Figure 5-29 Experimental B-H Curve

The method explained in Chapter 3 was used to formulate the nonlinear force. The variable relative permeability for higher flux densities was estimated by curve fitting the data (see Fig 5-31).

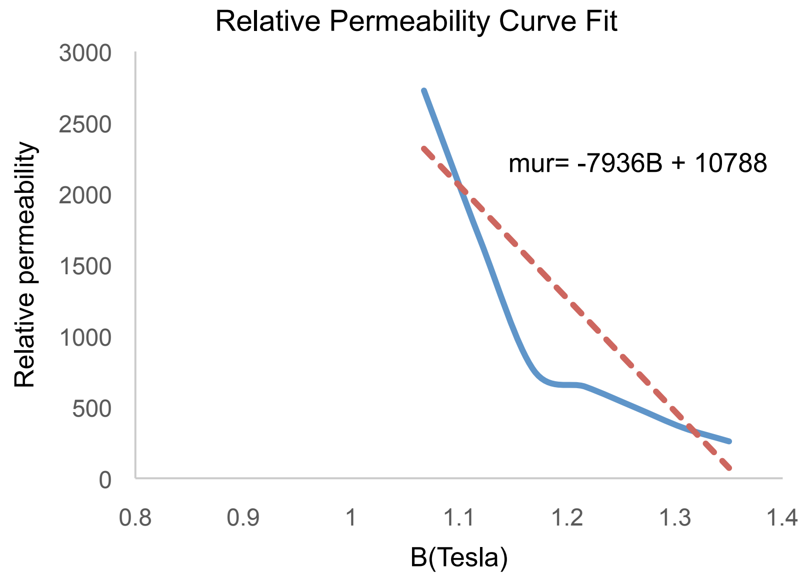

Figure 5-30 Relative Permeability Curve Fit

In order to find the upper and lower bounds for the Lure system used in control synthesis, the experimental force was described by the following equation (see Fig 5-31).

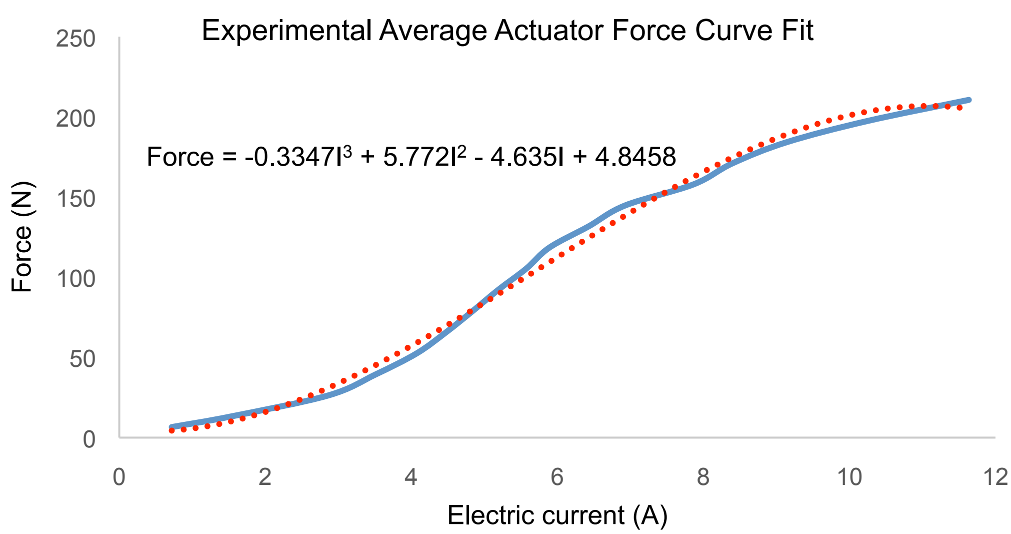

Figure 5-31 Experimental Average Actuator Force Curve Fit

The experimental force equation was used to simulate the total effective force on the electromagnet, while the controller actuates both electromagnets. The sector bounds are shown in Fig. 5-32.

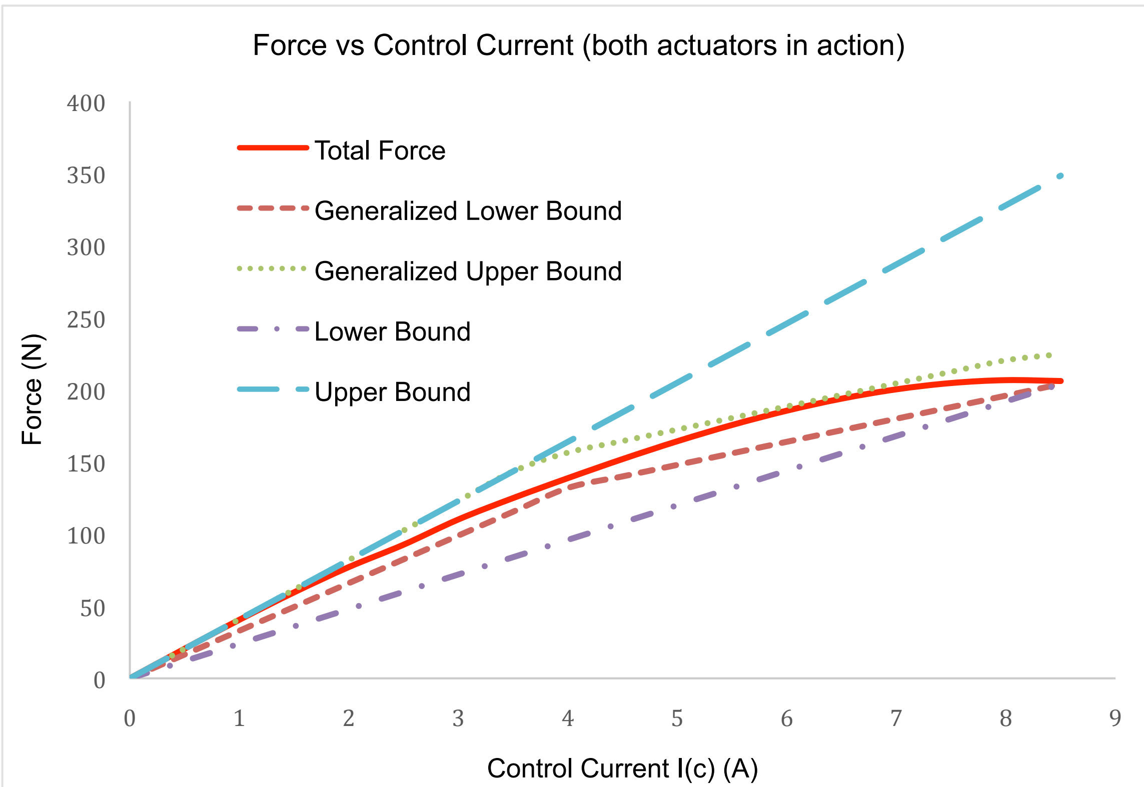

Figure 5-32 Upper and Lower Bounds For The Effective Electromagnet Force

The corresponding sector bound slopes and other constants are as follows:

Lower bound: y=24 I_c

Upper bound: y=41 I_c

Generalized lower bound: k_{01}=33, k_{11}=16, c_{11}=68

Generalized upper bound: k_{02}=41, k_{12}=16, c_{12}=92.5

Based on the new experimental force data and the method introduced in Chapter 4, various control designs were synthesized. The controller values to achieve the best transient response based on linear, nonlinear, and nonlinear with generalized sector conditions system models are listed in Table 5-5:

Table 5-5 CONTROL PARAMETERS FOR THE BEST TRANSIENT RESPONSE

	Linear	Nonlinear	Generalized
Kp	976.4	2752	2651
Kd	5.260	11.90	10.38

The controller values designed for disturbance rejection for both linear and nonlinear models is listed in Table 5-6. Combination of the generalized sector and disturbance tolerance conditions might not be convex to the author's knowledge. Therefore, In the design for disturbance rejection just the regular sector condition is used.

Table 5-6 CONTROL PARAMETERS FOR DISTURBANCE REJECTION

	Linear	Nonlinear
Kp	1108	2712
Kd	7.76	15.26

The Ki value was deliberately chosen to be small (Ki=100) and an anti-windup saturation function with upper and lower values of 10 was used to prevent potential windup. The small Ki guarantees a minimal effect on the dynamics of the system and therefore less variation from the intended control design.

5.9 Transient response Simulation vs Experiment

Using the test rig setup, the 3 different controllers were used to balance the beam. After the beam settled to its new equilibrium position, a reverse step (back to a reference of zero) was conducted. These step response tests were conducted for 5 different step amplitudes (2, 4, 6, 8, and 10mils). And the full set of the step tests were conducted with each of the three controllers (linear, nonlinear, and generalized). The step values correspond to displacements in the sensor location. For instance, the first reference step amplitude of 2 commanded the beam to move +2 mils at the sensor location. After the beam settled to the new position, the reference demand was returned to zero and the beam returned to horizontal position.

In order to improve the simulations accuracy, the difference in the left and right electromagnet forces should have been taken into account. The experimental force data shows that Actuator 1's force is 108% and Actuator 2's force is 93% of the average force that was used for control synthesis.

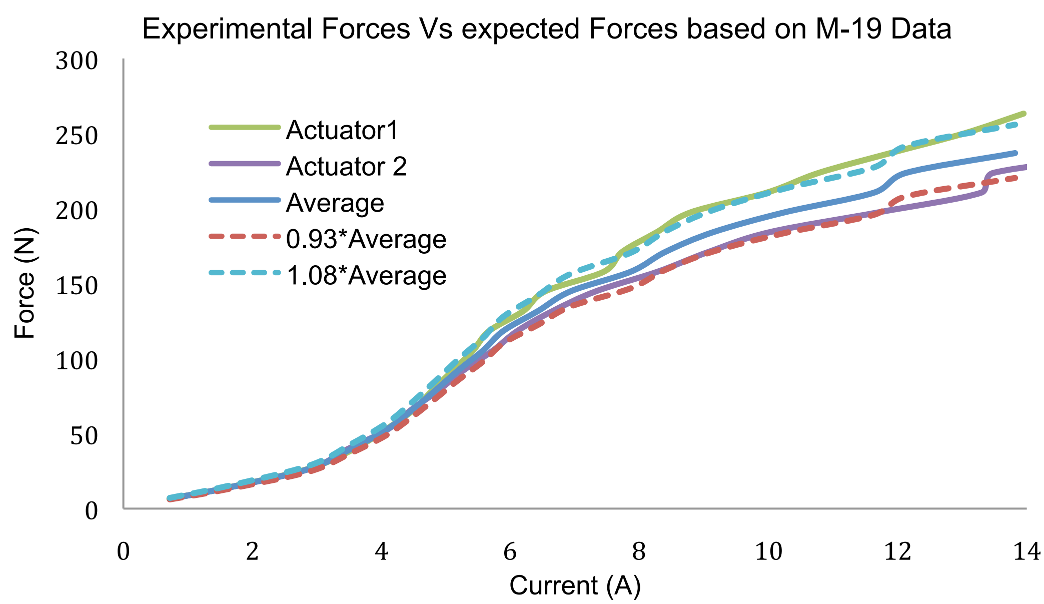

Figure 5-33 Left and Right Electromagnets' Force Deviation From The Average Force

After making this adjustment the experiment, and simulation are in very good agreement. As an example, the simulation and experimental data comparison for a reference step amplitude of 4mils is shown in Figures 5-34 to 5-42. The graphs are shown in different time spans to emphasize both the fast transient behavior and longer-term response. The simulation and experimental comparison for all other step functions can be found in the appendix.

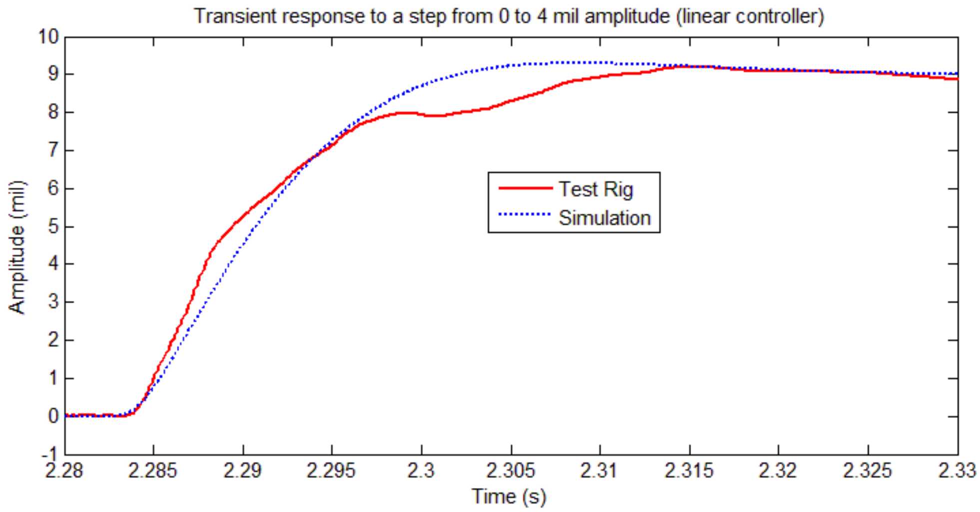

Figure 5-34 Linear Controller Transient Response (Time-span 0.05s)

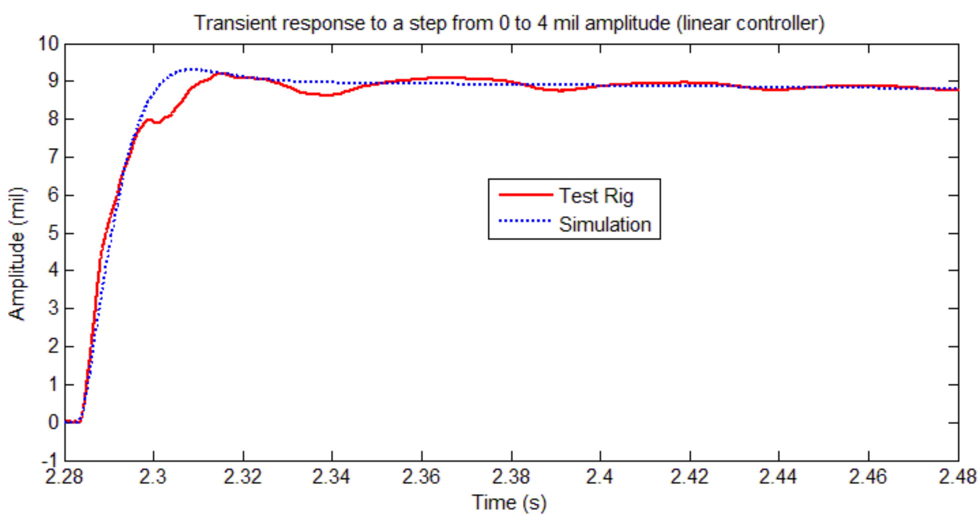

Figure 5-35 Linear Controller Transient Response (Time-span 0.2s)

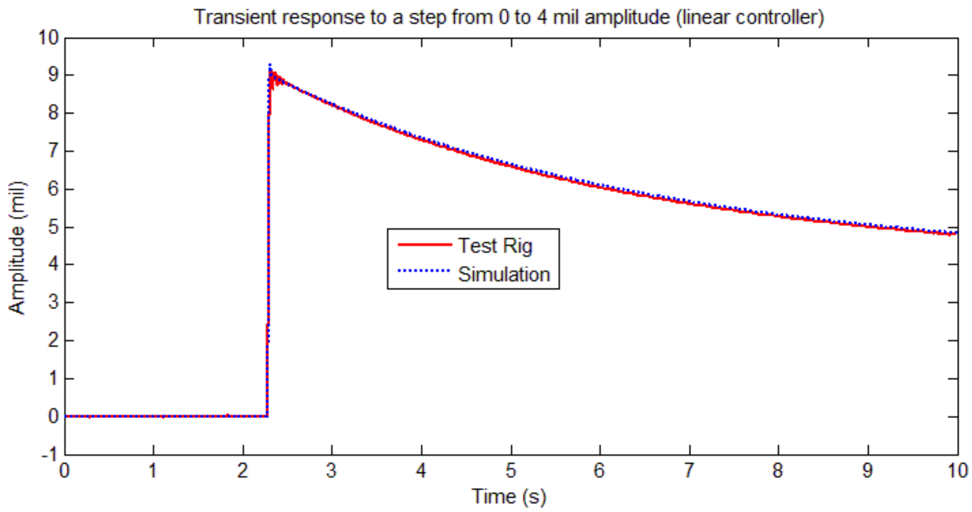

Figure 5-36 Linear Controller Transient Response (Time-span 10s)

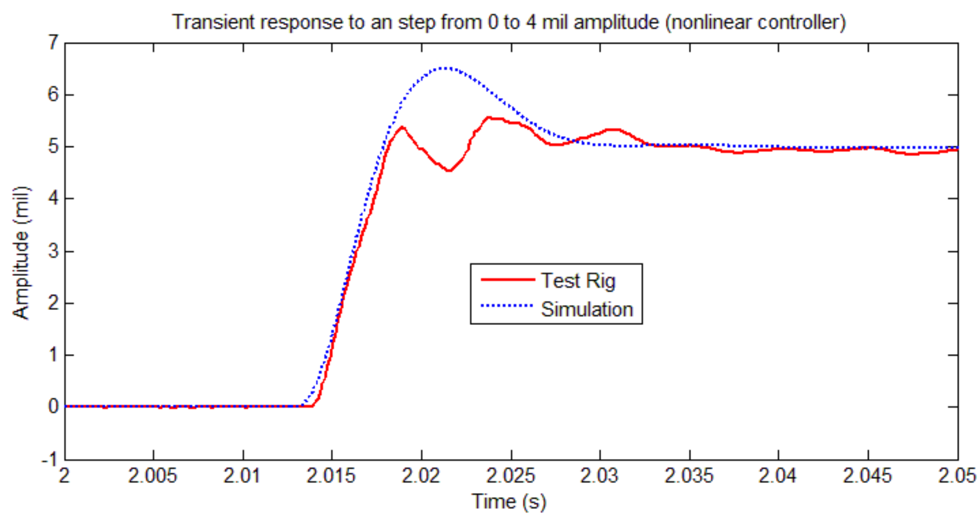

Figure 5-37 Nonlinear Controller Transient Response (Time-span 0.05s)

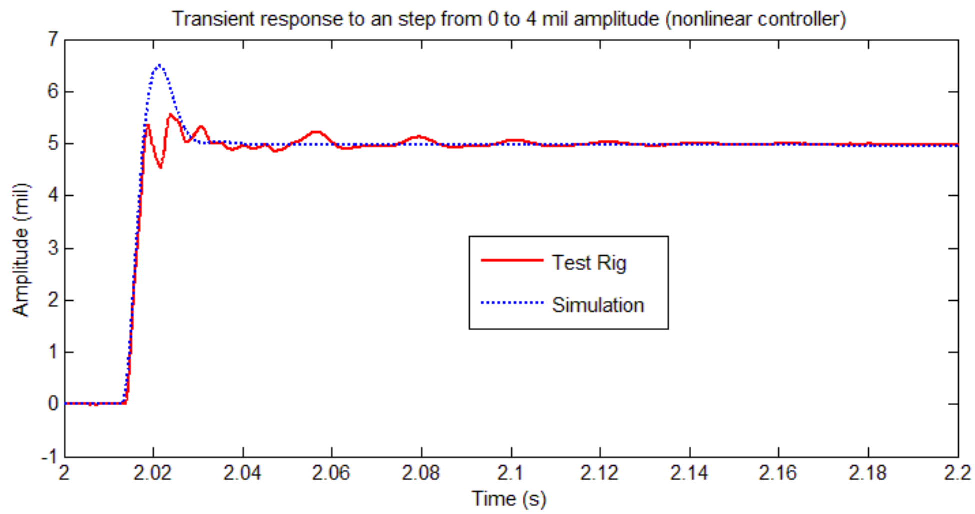

Figure 5-38 Nonlinear Controller Transient Response (Time-span 0.2s)

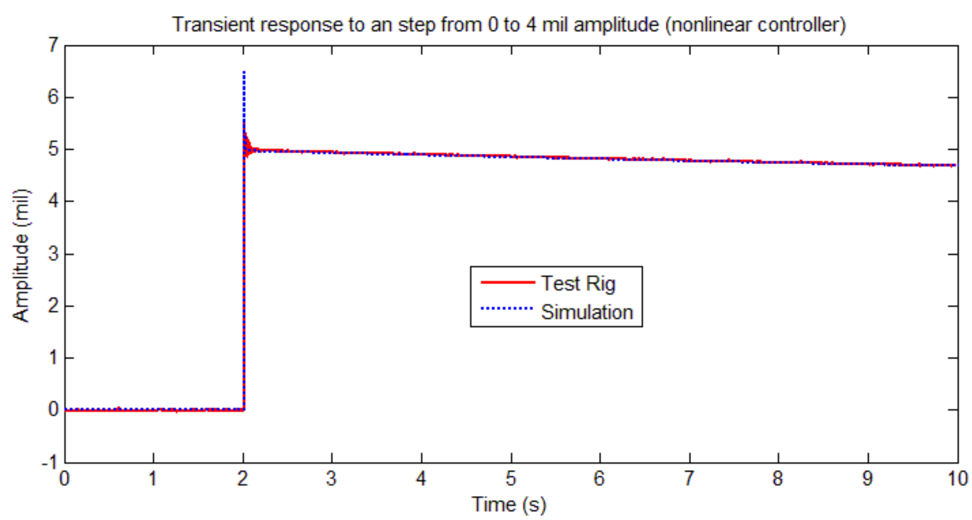

Figure 5-39 Nonlinear Controller Transient Response (Time-span 10s)

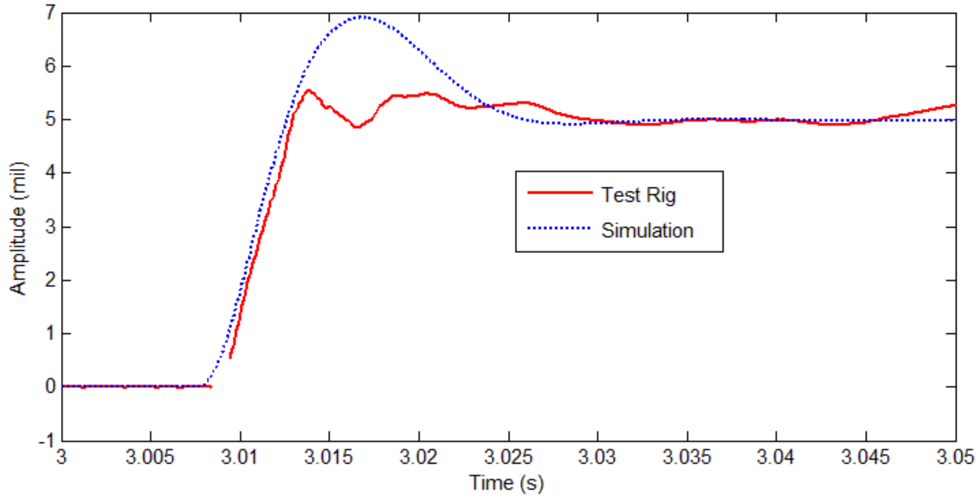

Figure 5-40 Generalized Sector Controller Transient Response (Time-span 0.05s)

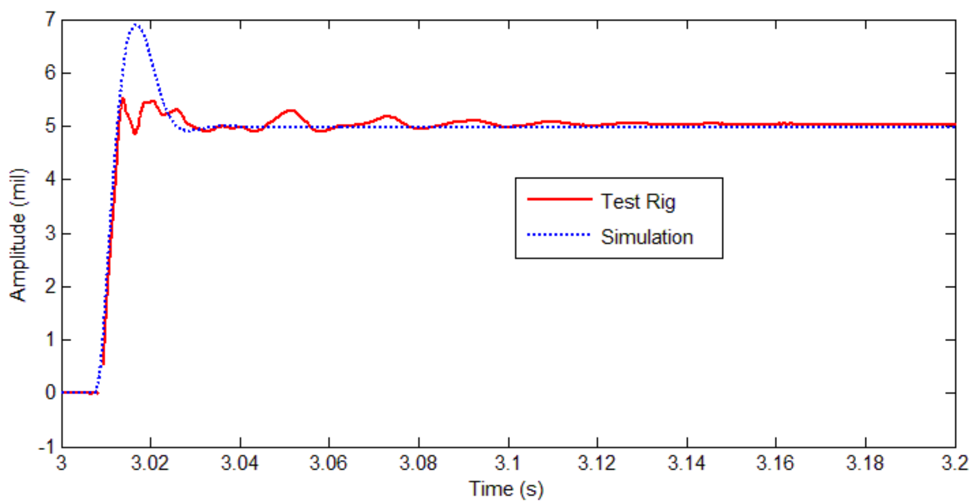

Figure 5-41 Generalized Sector Controller Transient Response (Time-span 0.2s)

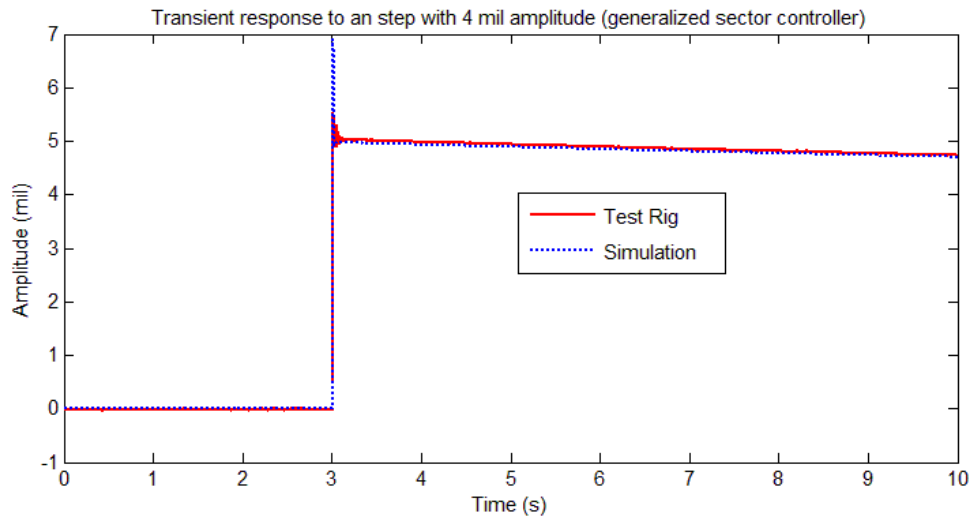

Figure 5-42 Generalized Sector Controller Transient Response (Time-span 10s)

As can be seen from the figures, the controllers designed based on nonlinear and generalized sector models show a significant transient response improvement over the controller designed based on the conventional linear model. Figures 5-44 and 5-45 compare the transient response of the linear, nonlinear, and generalized sector controllers. The nonlinear and generalized sector controllers exhibit identical rise times, which is 17% faster than the linear controller.

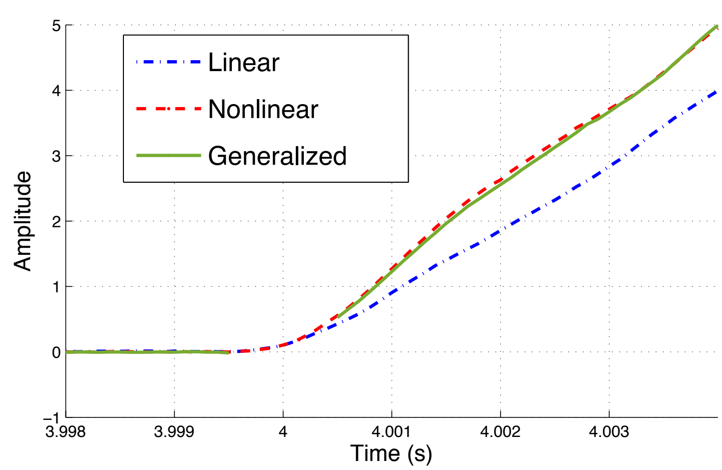

Figure 5-43 Transient Response Comparison (4 mils step)

The linear, nonlinear, and generalized sector controllers' overshoot are 130%, 39%, and 38%, respectively. Using the nonlinear controller dramatically reduces the system's overshoot.

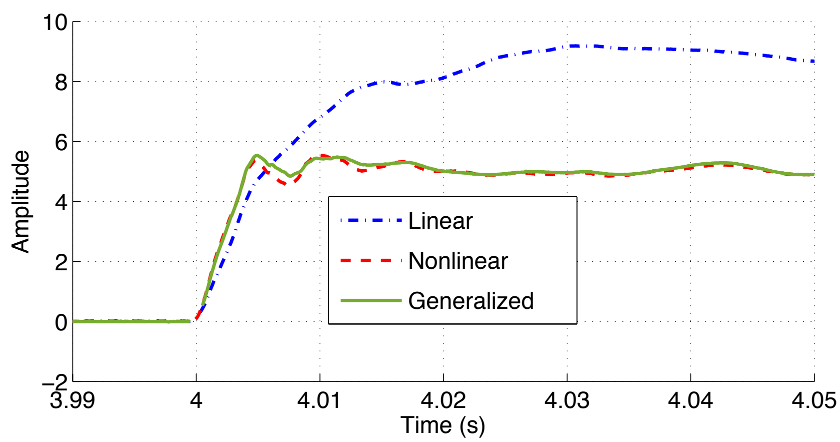

Figure 5-44 Transient Response Comparison (4 mils step)

5.10 Disturbance Rejection Simulation vs. Experiment

Perhaps the most practically important advantage of using the proposed nonlinear controller is in dealing with unexpected external disturbances. A controlled external disturbance was imposed on the beam by using a third electromagnet (disturbance electromagnet). This electromagnet was located closer to the end of the beam than the two control electromagnets.

In order to use the disturbance electromagnet to exert a desired disturbance force, it was first necessary to calibrate this actuator. The calibration procedure was conducted in the following manner. Different weights were hung on the opposite side of the beam and the disturbance electromagnet with a PID controller was used to stabilize the beam at various gaps. At each position the corresponding current was recorded (see Fig 5-45). And from the resulting dataset a lookup table between force and position inputs and current output was developed. The lookup table was then used to deliver a desired disturbance force by looking up the current level required to meet this desired force for the given instantaneous gap measure via the position sensors.

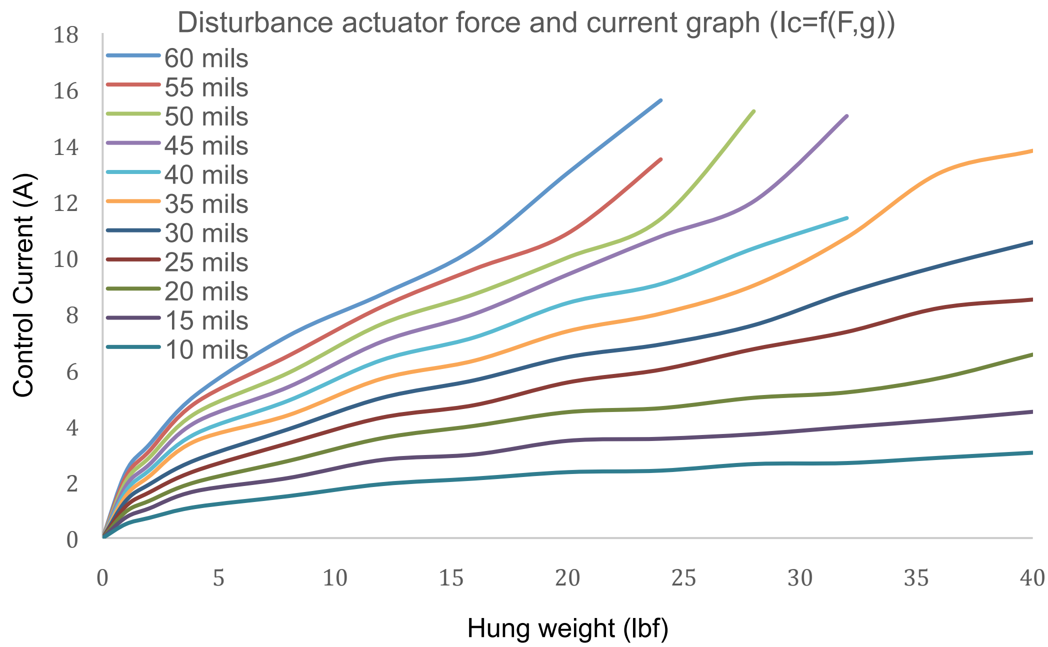

Figure 5-45 The Disturbance Electromagnet’s Experimental Force Data

In Fig. 5-45 each curve represents the force versus control current at one position, and the beam positions were measured from the disturbance electromagnet.

By solving the optimization problem described in Section 4-5, the guaranteed maximum disturbance energy that the linear and nonlinear systems could tolerate, were found to be 10, and 43 consecutively. Therefore, a range of disturbances with the energy of 10 and 43 were imposed on the beam in order to validate each control synthesis method. Six different impulse disturbances with different durations and amplitudes were imposed on the beam by the disturbance electromagnet and the experiments were compared with simulation (see Table 5-7).

Table 5-7 DISTURBANCE ENERGIES, AMPLITUDES, AND DURATIONS

	Duration1 (Sec)	Amplitude1 (N)	Duration2 (Sec)	Amplitude2 (N)	Duration3 (Sec)	Amplitude3 (N)
10 (Energy)	0.01	31.6	0.05	14.1	0.1	10
43 (Energy)	0.01	65.6	0.05	29.3	0.1	20.7

Both linear and nonlinear controllers were tested with all six impulse disturbances listed in Table 5-7, and the experimental data was compared with simulation results. As an example, the linear and nonlinear system's response to an impulse with an energy of 43 and duration of 0.1s is depicted in Figures 3-47 and 3-48. The experimental data and simulation results for other disturbance impulses can be seen in the Appendix B.

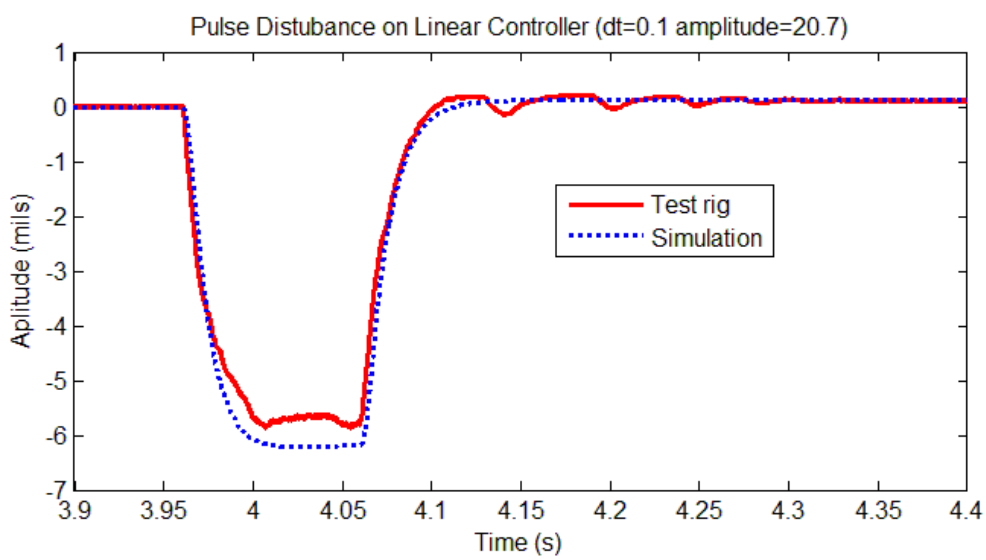

Figure 5-46 The Linear Controller's Response to Disturbance $\left(E = 43,\ \Delta t = 0.1s\right)$

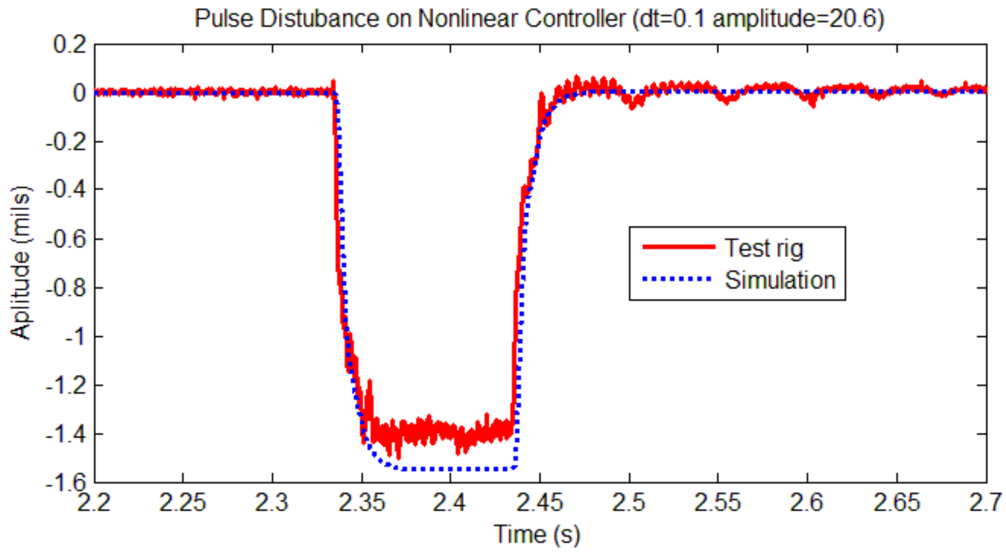

Figure 5-47 The Nonlinear Controller's Response to Disturbance $(E = 43,\ \Delta t = 0.1s)$

As can be seen from these figures, the simulation and experimental data are in very good agreement. The use of the nonlinear controller significantly improves the system's response to an external disturbance. Figure 5-48 shows the beam's response to all three impulses with the energy of 43 and compares the responses of the linear and nonlinear controllers. The displacements were recorded at the sensor location. The gap between the sensor stand and the beam was 15 mils, and as can be seen from the figure, an impulse with the energy of 43 $(\Delta t = 0.01s)$ caused the beam to hit the sensor stand. The same disturbance impulse resulted in the system with the nonlinear controller to move just under 6 mils.

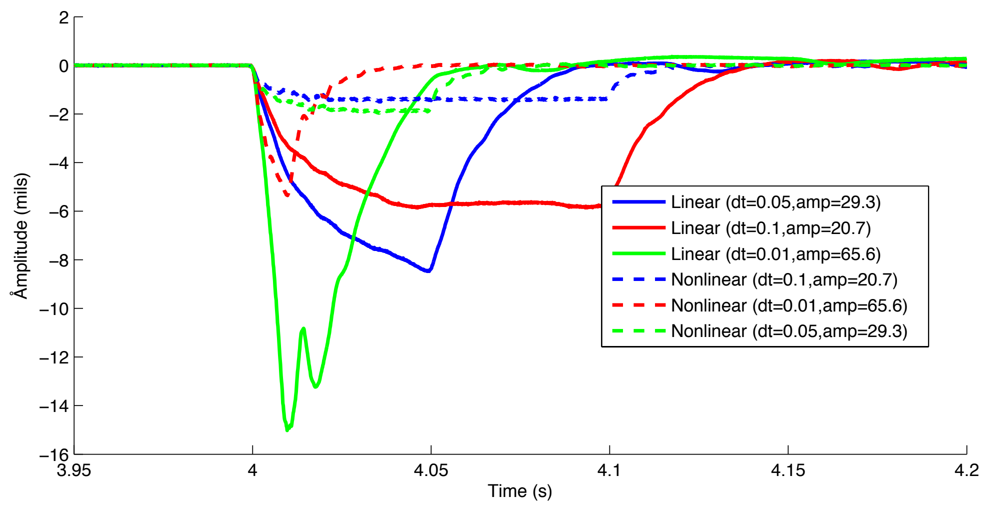

Figure 5-48 System Response to An External Disturbance Energy of 43

The linear and nonlinear controllers were also compared for a disturbance energy of 10 (see Fig. 5-49).

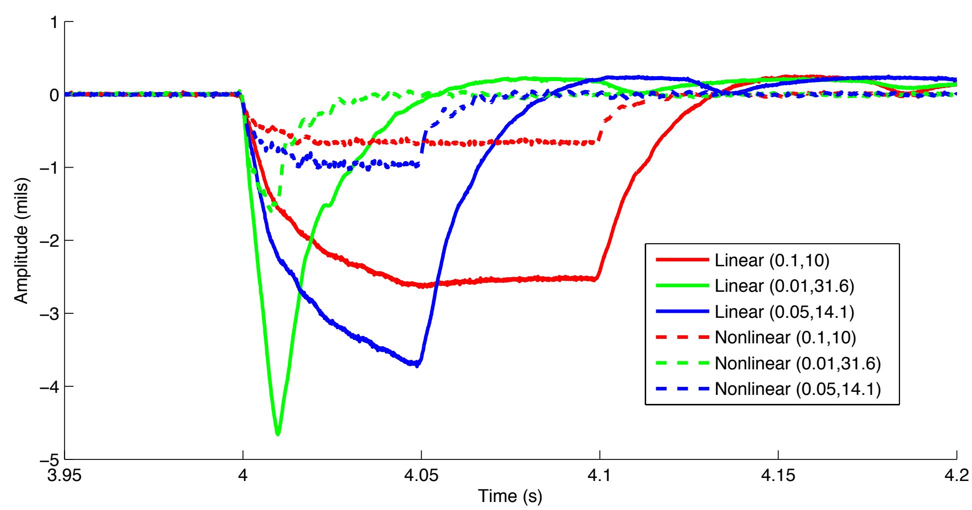

Figure 5-49 System Response to An External Disturbance Energy of 10

As can be seen from this figure, using the controller synthesized based on the nonlinear model, reduced the vibration amplitude by about 3 times compared with the controller designed based on the linear model.

5.11 Set-point weighting

As can be seen, for a number of the test cases the transient response has a very large overshoot. This overshoot is caused by the PID's derivative response to the step change in the reference demand. This large overshoot issue can be resolved by implementing set-point weighting. The conventional form of the PID controller used here for simulation is:

$$u(t) = K_p e(t) + K_i \int_0^t e(\tau)d\tau + K_d \frac{de(t)}{dt} \qquad e(t) = r(t) - y(t) \qquad (5-18)$$

As a solution for the overshoot problem, a widely accepted control structure that includes set-point weighting and derivative weighting can be used [Åström and Hägglund (1995)]:

$$u(t) = K_p \left(br(t) - y(t)\right) + K_i \int_0^t \left(r(t) - y(t)\right)d\tau + K_d \frac{d\left(cr(t) - y(t)\right)}{dt} \qquad (5-19)$$

Here b and c are additional parameters that provide the controller with two extra degrees of freedom. The integral term must be directly based on error feedback without weighting to ensure the desired steady state. Since the weighting is implemented on the reference value, the controllers obtained with different values of b and c respond to disturbances and measurement noise in the same way as a conventional PID controller. While b and c can have any value between 0 and 1 commonly b is chosen to be 0.5 and c is chosen to be zero. Decreasing the value of b reduces the system's overshoot.
As an example a step reference of 4 mills (see Figures 8-10 to 8-12 and 8-35 to 8-37) is chosen to practice the set-point weighting. Figures 1 and 2 compare the linear model controller with and with out set point weighting. Here c is chosen to be 0 and b is chosen to be 0.5 using the set-pint weighting decreases the overshoot from about 137% to just 17%.

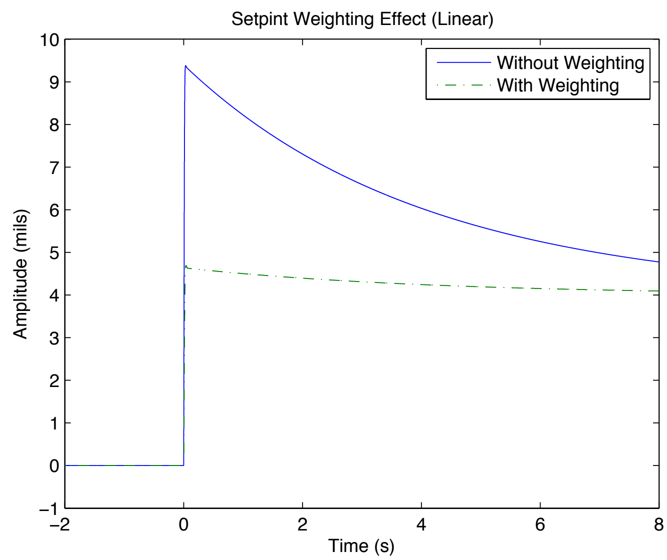

Figure 5-50 Set-point weighting effect on the linear model's transient response

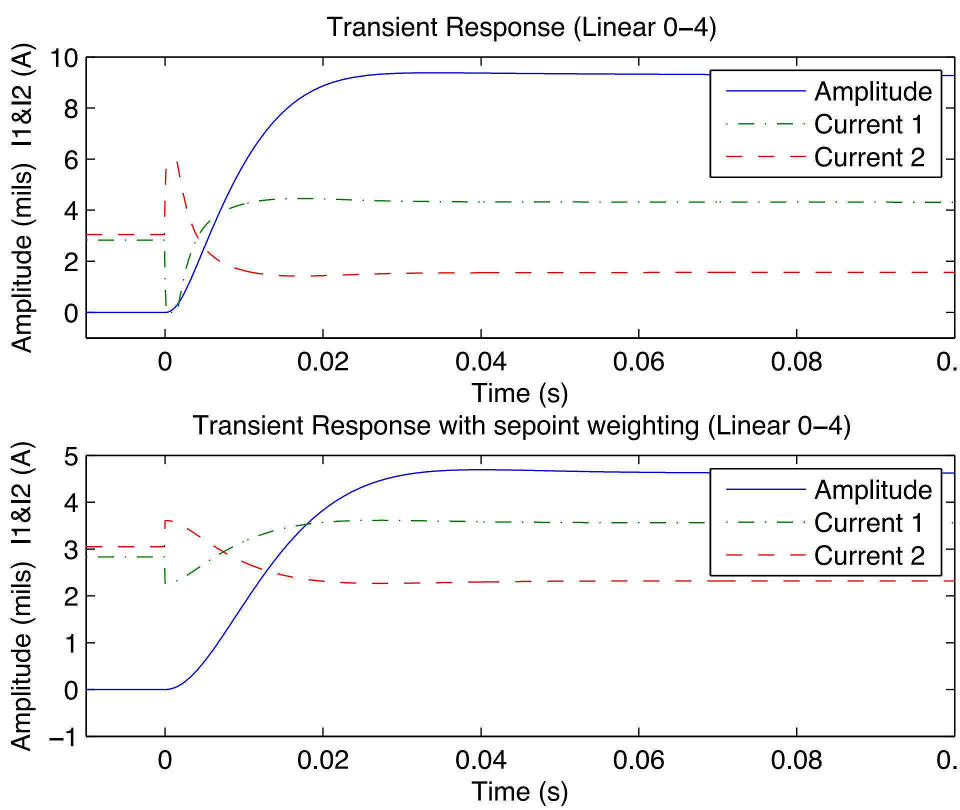

Figure 5-51 Comparing linear systems with and without set-point weighting

Figures 3 and 4 study the effect of set-point weighting on the controller based on the nonlinear model. Here the goal is a combination of fast rise time and small overshoot. Choosing a value of 0.5 for the b parameter results in a significant undershoot. Therefore, while c is chosen to be 0 again, a larger value for b (0.85) was chosen this time. Again set-point weighting reduces the overshoot significantly (from 60% to about 5%.

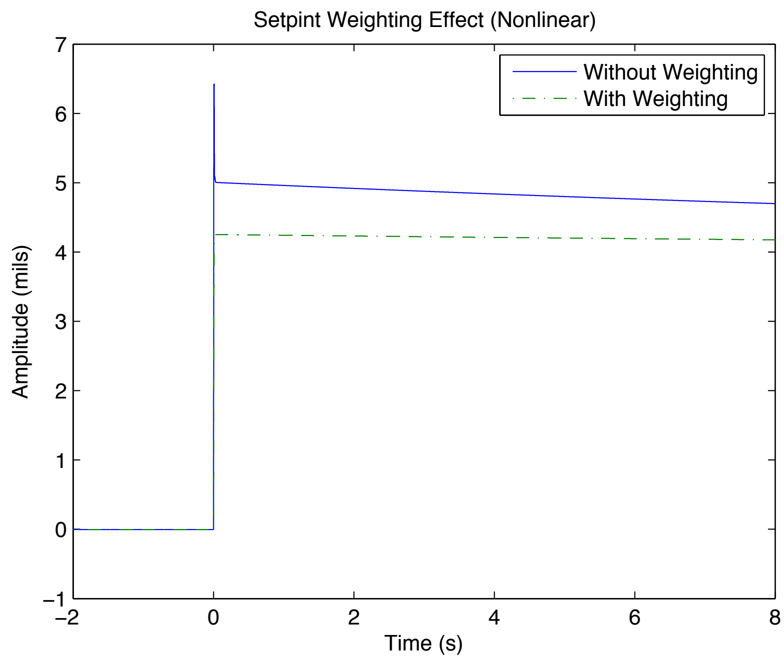

Figure 5-52 Set-point weighting effect on the nonlinear model's transient response

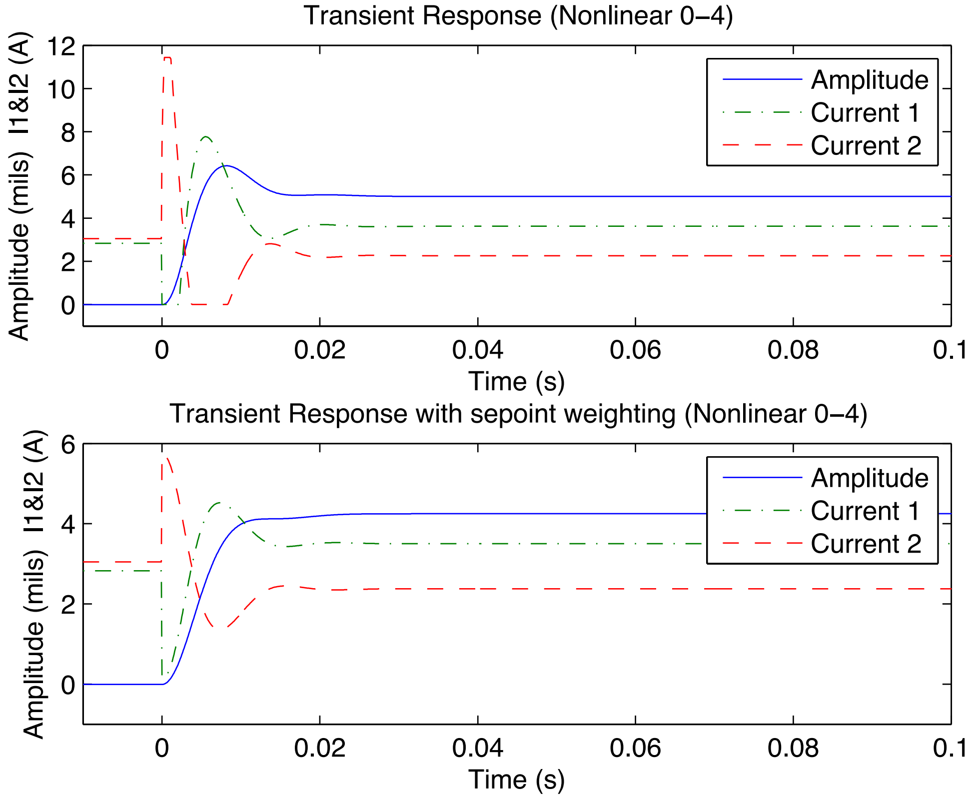

Figure 5-53 Comparing nonlinear systems with and without set-point weighting

6 Conclusion and future work

6.1 Conclusions

Based on the results obtained from the balance beam test rig, a few general conclusions can be drawn:

- Very good correlation was obtained between the experimental data and theoretical predictions. Initial discrepancies were corrected by following a rigorous experimental model and parameter identification procedure.

- In comparison to classical control design, a significantly improved transient response was achieved through the use of the proposed modeling and control design. This was demonstrated by a 17% faster rise time and a more than 90% decrease in overshoot.

- In comparison to classical control design, significant performance improvement in the form of a higher dynamic load capacity was achieved through the use of the proposed nonlinear modeling and LMI method for control synthesis. This was exemplified by the ability of the system to maintain stability and dissipate impulse disturbances with 4 times the energy compared with that achievable by traditional linear control design.

- The proposed method significantly reduces the system's unwanted vibration amplitude compared to classical designs. This can be seen in the system's reaction to a step disturbance. In all cases, the vibration amplitude is reduced by a factor of at least 2.

- The control synthesis based on the nonlinear model with a generalized sector condition offered little or no performance improvement over the control synthesis based on the nonlinear model with a regular sector condition for the problem considered. Despite this fact, using the generalized sector condition was proven to be necessary to guarantee a less conservative design compared to classical control design. This was demonstrated by the analysis of control designs for the balance beam system with different airgaps.

- The uncertainty descriptions developed in this work were appropriate and because of the use of the generalized sector condition, not overly conservative. This was demonstrated by good experimental and theoretical performance correlations and the performance improvements.

- The main contribution of this work can be summarized as: A combined approach for modeling and control of magnetic bearing that optimally uses the extra load capability within the nonlinear magnetization region was proposed in this work for the first time. Various optimized controllers with different objectives were designed using the extra load capability and the designed controllers were experimentally tested and showed almost perfect coloration with the simulation.

6-2 Future work

6-2-1-Modeling and simulation

The individual component models were carefully developed which resulted in a good correlation between simulation and experimental data. Nevertheless, addressing a few uncertainty and simulation issues can ensure higher performance control designs and even better correlation between simulation and experiment.

- The airgap was by far the most influential factor in control synthesis, the measured airgap value varied by 2 mils in the test rig. This variation was due to measurement errors, uneven surface of the target lamination, and slight movement of the target lamination due to a few impacts with the electromagnets during the experiment. Modeling this uncertainty guarantees high performance and better correlation between simulation and test data.

- The base’s dynamic was not modeled in the simulation and slightly affected the experimental data. Using a more rigid base or modeling the base’s dynamics, would yield a slightly better correlation between the experimental and simulation data.

- The disturbance force was generated by using a lookup table. While the lookup table was created based on experimental data and had an acceptable accuracy, using a closed loop controller with flux feedback could possibly yield a more accurate disturbance force and a better correlation between simulation and experimental data.

6-2-2-Performance improvement

In most cases the experiment exhibits similar or better rise time, and peak vibration amplitude compared to the simulation, but almost always it demonstrates a longer settling time. This is caused by the low amplitude vibrations in the system with 20 Hz and 55Hz frequencies. We suspect these vibrations to be caused by the base's dynamics and the noise in the system.

- The substructure modes are due to the balance beam's base design. By stiffening the base, the substructural modes can be pushed up in frequency. This in turn can reduce their effect on the settling time.

- Noise can be a significant deterrent to increased system performance and all possible means of reducing noise should be perused. Using shielded cables and a carefully implemented grounding system were measures taken to perform noise reduction. But further improvements were still possible. A significant source of noise in the system was the amplifier's switching frequency (in this case 25kHz). Using an amplifier with higher switching frequency could yield to a minor improvement in noise. Also the amplifier's electric ground was not isolated from the sensors' grounds, a better isolation could improve the noise. A high order low pass Cauer filter could be considered as another option to reduce the system's noise level, but this decision should be made carefully. Increasing the order of the filter can introduce an unwanted phase lag, which has a negative impact on the control system.

6-2-3-Considering other factors

Integrating other design factors into the current control synthesis can possibly improve the system's performance.

- Due to the nature of the LMI method, just the values for K_p and K_d were optimized in the control synthesis and the K_I value was chosen experimentally. Optimizing K_I

makes the system more complex, but it is possible and may improve the overall performance of the system.

- In this work the nonlinearity in the electromagnets' magnetization and the nonlinearity in the electromagnet force due to electric current is addressed comprehensively. While the nonlinearity in force due to the airgap is only addressed via the sector bound, and was not modeled comprehensively. Modeling this nonlinearity would yield to a more accurate system model and in turn a potentially higher performance capability.

- The proposed experiment mimics the behavior of a thrust magnetic bearing. Similar experiments could be done in the future to improve performance of a radial bearing and prove the effectiveness of the proposed method.

- The balance beam core and target magnetic material was laminated, and therefore the eddy current effect was negligible. However because of lack of laminations in thrust magnetic bearings this effect should be considered in modeling and control synthesis.

- Finally, while the balance beam test rig was ideal for the proof of concept. Future experiments on thrust and radial bearings should be done for practical implementation of the proposed method. Later a small prototype of the energy storage flywheel should be built for proof of concept.

7 References

[1] Yin, Lingbing, and Lei Zhao. "Nonlinear Control for a Large Air-gap Magnetic Bearing System." Proc. of SMiRT 19, Toronto. N.p.: n.p., n.d. N. pag. Web. Aug. 2007.

[2] Inoue, Tsuyoshi, Yukio Ishida, and Shin Murakami. "Theoretical Analysis and Experiments of the Nonlinear Vibration in a Vertical Rigid Rotor Supported by the Magnetic Bearing System." *Ournal of System Design and Dynamics* 1.2 (n.d.): 295-306. Web. 2007.

[3] Abdelfatah, Mohamed M., and Emad P. Fawzi. "Nonlinear Oscillations in Magnetic Bearing Systems." *Ieee* 8th ser. 38 (1993): 1242-245. Print.

[4] Hong, Sung K., and Reza Langari. "Fuzzy Modeling and Control of a Nonlinear Magnetic Bearing System." *Journal of Intelligent & Fuzzy Systems* 7.4 (1999): 335-46. Print.

[5] Smith, R. D., and W. F. Weldon. "Nonlinear Control of a Rigid Rotor Magnetic Bearing System: Modeling and Simulation with Full State Feedback." *Ieee* 31.2 (1995): 973-80. Print.

[6] Walsh, Thomas F. *Nonlinear Dynamic Analysis of a Magnetic Bearing System with Flux Control: The Effects of Coordinate Coupling*. N.p.: DukeUniversity, 1993. Print.

[7] He, Rong, Kang Z. Liu, and Osami Saito. "Nonlinear Output Feedback Control of a 5DOF AMB System." Proc. of 16th IFAC World Congress, Czech Republic. Vol. 16. N.p.: n.p., 2005. N. pag. Print. Ser. 1.

[8] Huang, Shi J., and Lih C. Lin. "Stable Fuzzy Control with Adaptive Rotor Imbalance Compensation For nonlinear Magnetic Bearingsystems." *Journal of the Chinese Institute of Engineers* 4th ser. 28 (2005): 589-603. Print.

[9] Hu, Tingshu, and Zongli Lin. *Control Systems with Actuator Saturation: Analysis and Design*. Boston: Birkhäuser, 2001. Print.

[10] Wang, Yong, James D. Paduano, and Richard M. Murray. "BIFURCATION CONTROL: THEORIES, METHODS, AND APPLICATIONS." *IEEE* (1999): 730-36. Print.

[11] Inoue, Tsuyoshi, Motoki Sugiyama, Yasuhiko Sugawara, and Yukio Ishida. "Nonlinear Vibration in a Vertical Rigid Rotor Supported by the Magnetic Bearing: Case Considering the Delays of Both Electric Current and Magnetic Flux." *21st Biennial Conference on Mechanical Vibration and Noise / Modeling, Vibration and*

Control of Rotor Systems. Proc. of ASME, Nevada, USA, Las Vegas. Vol. 1. N.p.: n.p., 2007. 1195-203. Print.

[12] Zheng, Kai, Heng Liu, and Lie Yu. "Robust Fuzzy Control of A nonlinear Magnetic Bearing system with Computing Time Delay." *IEEE/ASME* (2008): 839-43. Print.

[13] Zheng, Kai, and Lie Yu. "Effects of Time Delay on Resonance of a Nonlinear Magnetic Bearing System with Delayed Feedback." *International Journal of Applied Electromagnetics and Mechanics* 3-4 33 (2010): 1547-554. Print.

[14] Maslen, Eric H., Dominick T. Montie, and Tetsuya Iwasaki. "Robustness Limitations in Self-Sensing Magnetic Bearings." Journal of Dynamic Systems, Measurement, and Control 128.2 (2006): 197–203.

[15] Saket, Fawaz Y., M. Necip Sahinkaya, and Patrick S. Keogh. "Touchdown Bearing Contact Forces in Magnetic Bearing Systems." ASME Turbo Expo. Vol. 7A. San Antonio, Texas, USA: Asme, 2013.

[16] Truong, Nguyen V., Liuping Wang, and Jianming Huang. "Nonlinear Modeling of a Magnetic Bearing System Using SDP Model and Linear Wavelet Parameterization." Proc. of American Control Conference, Marriott Marquis Hotel at Times Square, New York City, USA,. N.p.: n.p., n.d. 2254-259. Print.

[17] Jeng, Jin T. "Nonlinear Adaptive Inverse Control for the Magnetic Bearing System." *Journal of Magnetism and Magnetic Materials* 209.1-3 (2000): 186-88. Print.

[18] Lee, Dong Hwan, Jin Bae Park, Young Hoon Joo, Kuo Chi Lin, and Chan Ho Ham. "Robust H ∞ Control for Uncertain Nonlinear Active Magnetic Bearing Systems via Takagi-Sugeno Fuzzy Models." *International Journal of Control, Automation and Systems* 8.3 (2010): 636-46. Print.

[19] Xu, Youzhi, and Kenzo Nonami. "A Fuzzy Modeling of Active Magnetic Bearing System and Sliding Mode Control with Robust Hyperplane Using .MU.-Synthesis Theory." *JSME International Journal Series C* 46.2 (2003): 409-15. Print.

[20] Yu, Shin S., Shinq J. Wu, and Tsu T. Lee. "Application of Neural-fuzzy Modeling and Optimal Fuzzy Controller for Nonlinear Magnetic Bearing Systems." Proc. of IEEE/ASME Advanced Inteligent Mechanics. N.p.: n.p., 2003. 7-11. Print.

[21] Hsu, Chan-Tang, and Shyh-Leh Chen. "Nonlinear Control of a 3-pole Active Magnetic Bearing System." *Automatica* 39.2 (2003): 291-98. Print.

[22] Hung, J. "Nonlinear Control of a Magnetic Bearing System." *Mechatronics* 13.6 (2003): 621-37. Print.

[23] Fabien, B C. “Observer-Based Feedback Linearizing Control of an Electromagnetic Suspension.” Journal of Dynamic Systems, Measurement, and Control 118.3 (1996): 615–619. Print.

[24] Matsumura, Fumio, Masayuki Fujita, and Masanao Shimizu. Proc. of 2nd Internayional Symposium on Magnetic Bearings, Tokyo, Japan. N.p.: n.p., 1990. 349-356. Print.

[25] Green, Scott A, and Kevin C Craig. “Robust , Digital , Nonlinear Control of Magnetic-Levitation Systems.” Journal of Dynamic Systems, Measurement, and Control 120.4 (1998): 488–495. Print.

[26] Yeh, T.-J., Ying-Jer Chung, and Wei-Chung Wu. “Sliding Control of Magnetic Bearing Systems.” Journal of Dynamic Systems, Measurement, and Control 123.3 (2001): 353–362.

[27] Vidolov, Borislav, Christian Melin, Jerome De Miras, and Ali Charara. "Two- Rules-based Fuzzy Logic Control and Sliding Mode Control of an Active Magnetic Bearing." Proc. of The Fifth IEEE International Conference on Fuzzy Systems. Vol. 2. N.p.: n.p., 1996. 1205-209. Print.

[28] Steffani, H. F., W. Hofmann, and B. Cebulski. "Applying of Bellman's Dynamic Programming to the Control of Magnetic Bearings." Proc. of The 24th Annual Conference of the IEEE. Vol. 3. N.p.: n.p., 1998. 1427-432. Print.

[29] Löwis, Johannes V., and Joachim200 Rudolph. "Flatness-based Trajectory Tracking Control of a Rotating Shaft." Proc. of Seventh International Symp. on Magnetic Bearings, ETH, Zurich, Switzerland. N.p.: n.p., 2000. 299-304. Print.

[30] Grochmal, Thomas R., and Alan F. Lynch. "Nonlinear Control of an Active Magnetic Bearing with Bias Currents: Experimental Study." Proc. of American Control Conference, Minneapolis,Minnesota,Usa. N.p.: n.p., 2006. 4558-563. Print.

[31] Huang, Bin, and Zongli Lin. "Absolute Stability With a Generalized Sector Condition." Automatic Control, IEEE 49.4 (2004): 535-48. Print.

[32] Hu, Tingshu, Zongli Lin, and Ben M. Chen. "An Analysis and Design Method for Linear Systems Subject to Actuator Saturation and Disturbance." IEEE 2 (2000): 725-29 - 729. Print.

[33] Hu, Tingshu, Zongli Lin, Wei Jiang, and Paul Allaire. "Constrained Control Design for Magnetic Bearing Systems." Journal of Dynamic Systems, Measurement, and Control 127 (2005): 601-16. Print.

[34] Polyak, Boris T., Alexander V. Nazin, Michael V. Topunov, and Sergey A. Nazin. "Rejection of Bounded Disturbances via Invariant Ellipsoids Technique." IEEE(2006): n. pag. Print.

[35] Conway, J. H. and Sloane, N. J. A. (1993). Conway, J. H. and Sloane, N. J. A. (2nd ed., p. 1993). Springer-Verlag.

[36] Maslen, E. (2000). Magnetic Bearings.

[37] Thomson, W. T., & Dahleh, M. D. (1997). Theory of Vibration with Applications (5th Editio.). Prentice Hall.

[38] Yeadon, W. H., & Alan W. Yeadon. (2001). HANDBOOKOF SMALLELECTRIC MOTORS (p. Chapter 5). McGraw-Hill.

[39] Boyd, S., Ghaoui, L., Feron, E., & Venkataramanan, B. (1994). Linear Matrix Inequalities in System and Control Theory SIAM Studies in Applied Mathematics. Philadelphia: Siam.

[40] Hu, T., & Lin, Z. (2002). Exact characterization of invariant ellipsoids for single input linear systems subject to actuator saturation. IEEE Transactions on Automatic Control, 47(1), 164–169. doi:10.1109/9.981738

[41] Hu, T., Huang, B., & Lin, Z. (2004). Absolute Stability With a Generalized sector condition. Automatic Control, IEEE Transactions on, 49(4), 535–548. Retrieved from http://ieeexplore.ieee.org/xpls/abs_all.jsp?arnumber=1284716

[42] Hu, T., Lin, Z., Jiang, W., & Allaire, P. (2005). Constrained Control Design for Magnetic Bearing Systems. of Dynamic Systems, Measurement, and Control, 127(December). doi:10.1115/1.2101850

[43] Polyak, B. T., Nazin, A. V., Topunov, M. V., & Nazin, S. a. (2006). Rejection of Bounded Disturbances via Invariant Ellipsoids Technique. Proceedings of the 45th IEEE Conference on Decision and Control, (1), 1429–1434. doi:10.1109/CDC.2006.377785

[44] Hu, T., Lin, Z., & Chen, B. M. (2002). An analysis and design method for linear systems subject to actuator saturation and disturbance. Automatica, 38(2), 351–359. doi:10.1016/S0005-1098(01)00209-6

[45] Fang, H., Lin, Z., & Hu, T. (2004). Analysis of linear systems in the presence of actuator saturation and L2-disturbances. Automatica, 40(7), 1229–1238.

doi:10.1016/j.automatica.2004.02.009

8 Appendix

Appendix A

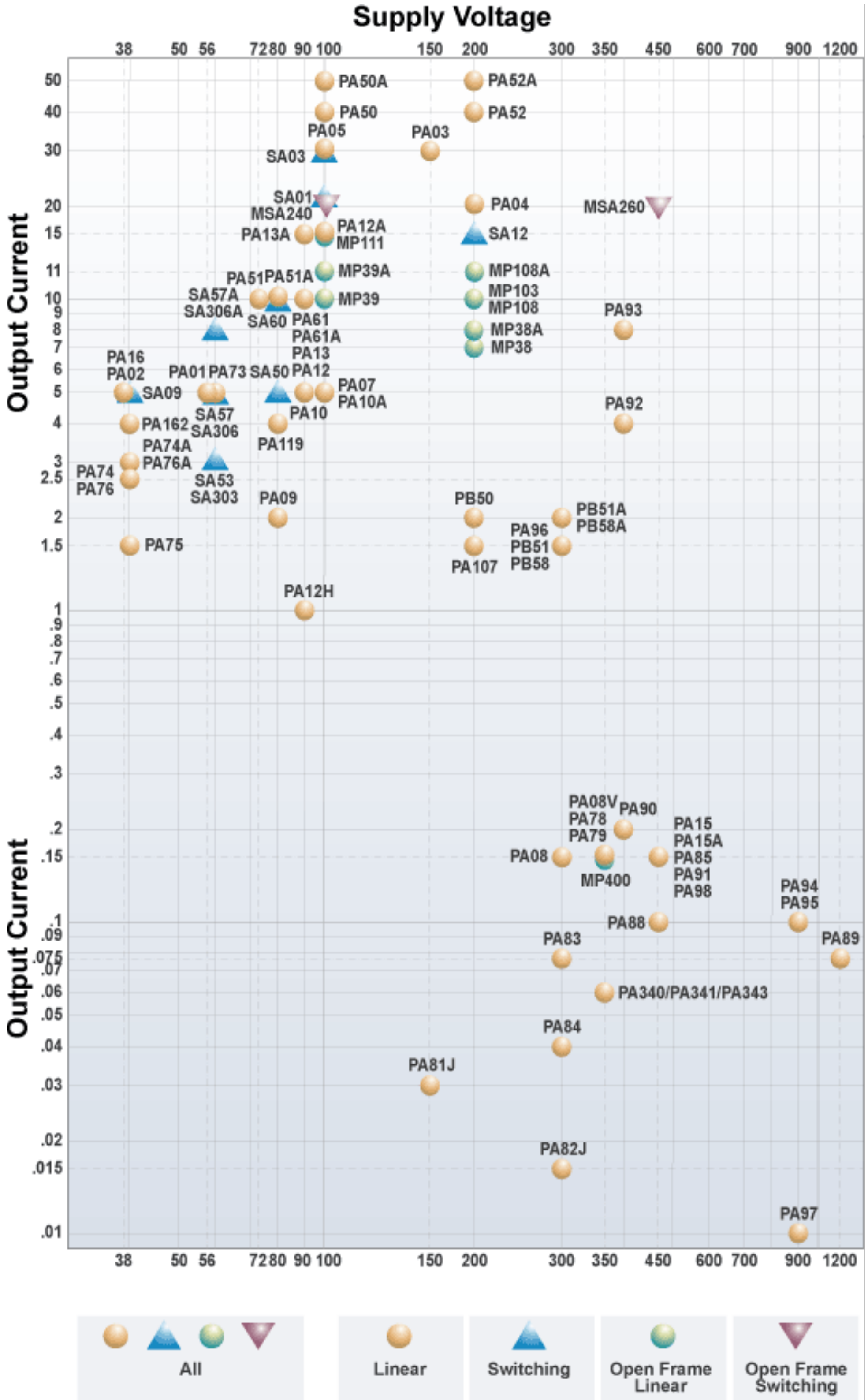

Figure 8-1 Amplifiers Produced by Apex

Appendix B

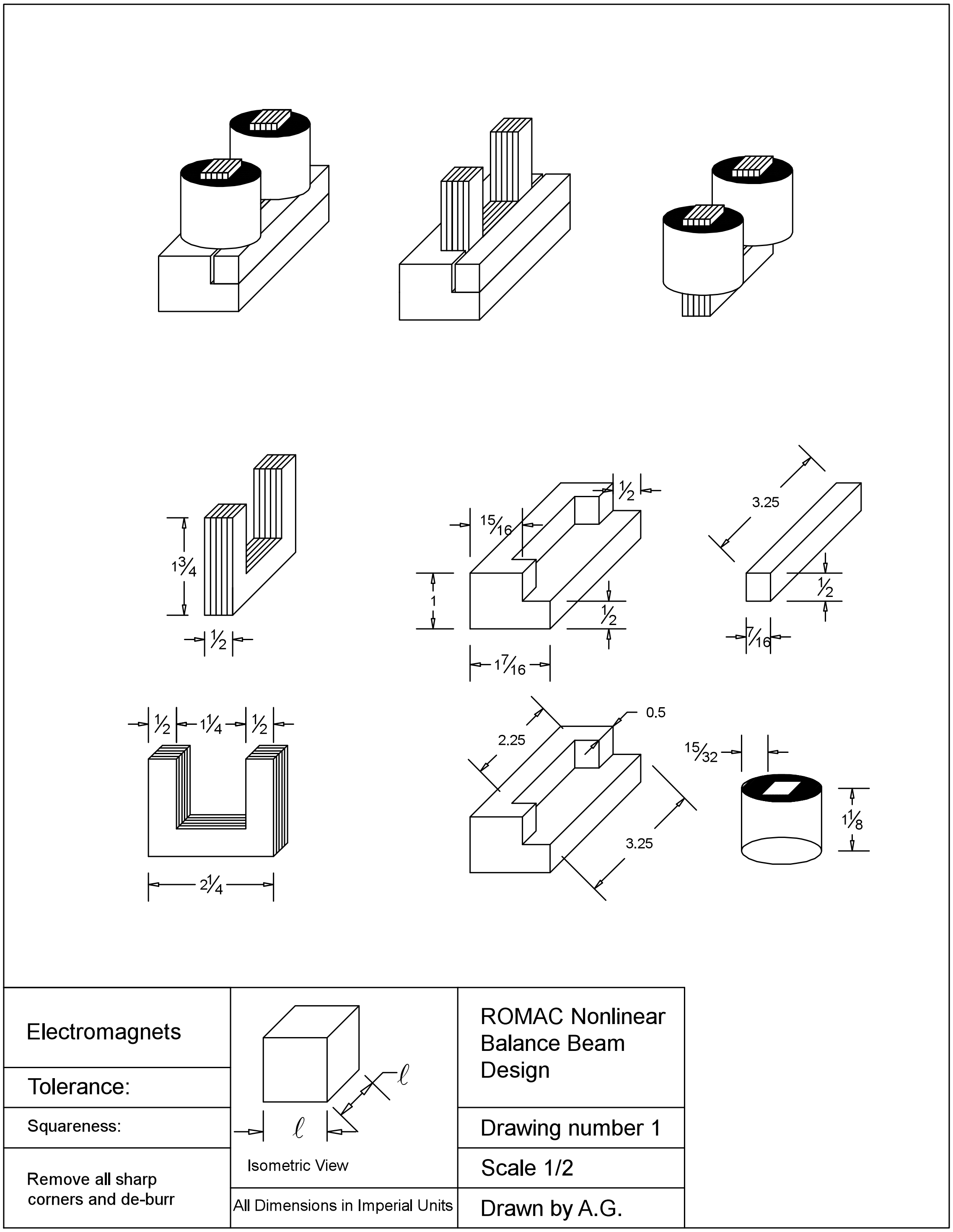

Figure 8-2 Electromagnet Related Dimensions

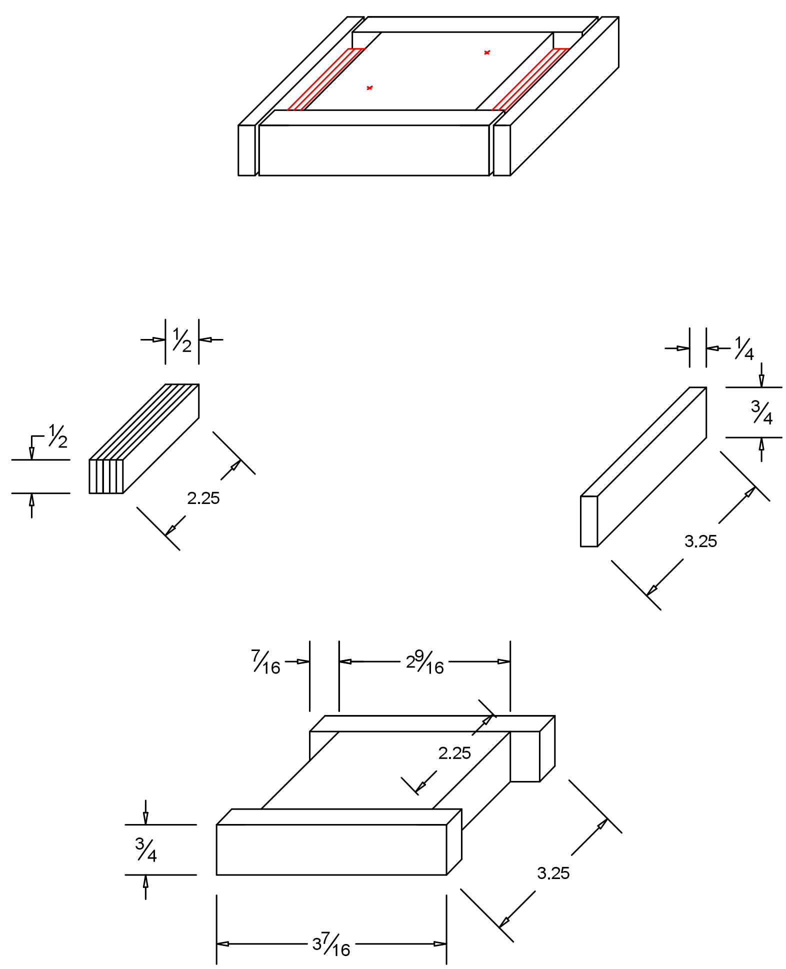

Target lamination, Holder & Clamp	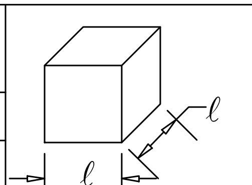	ROMAC Nonlinear Balance Beam Design
Tolerance:		
Squareness:		Drawing number 2
Remove all sharp corners and de-burr	Isometric View	Scale 1/2
	All Dimensions in Imperial Units	Drawn by A.G.

Figure 8-3 Target Lamination and Target Lamination Holder Dimensions

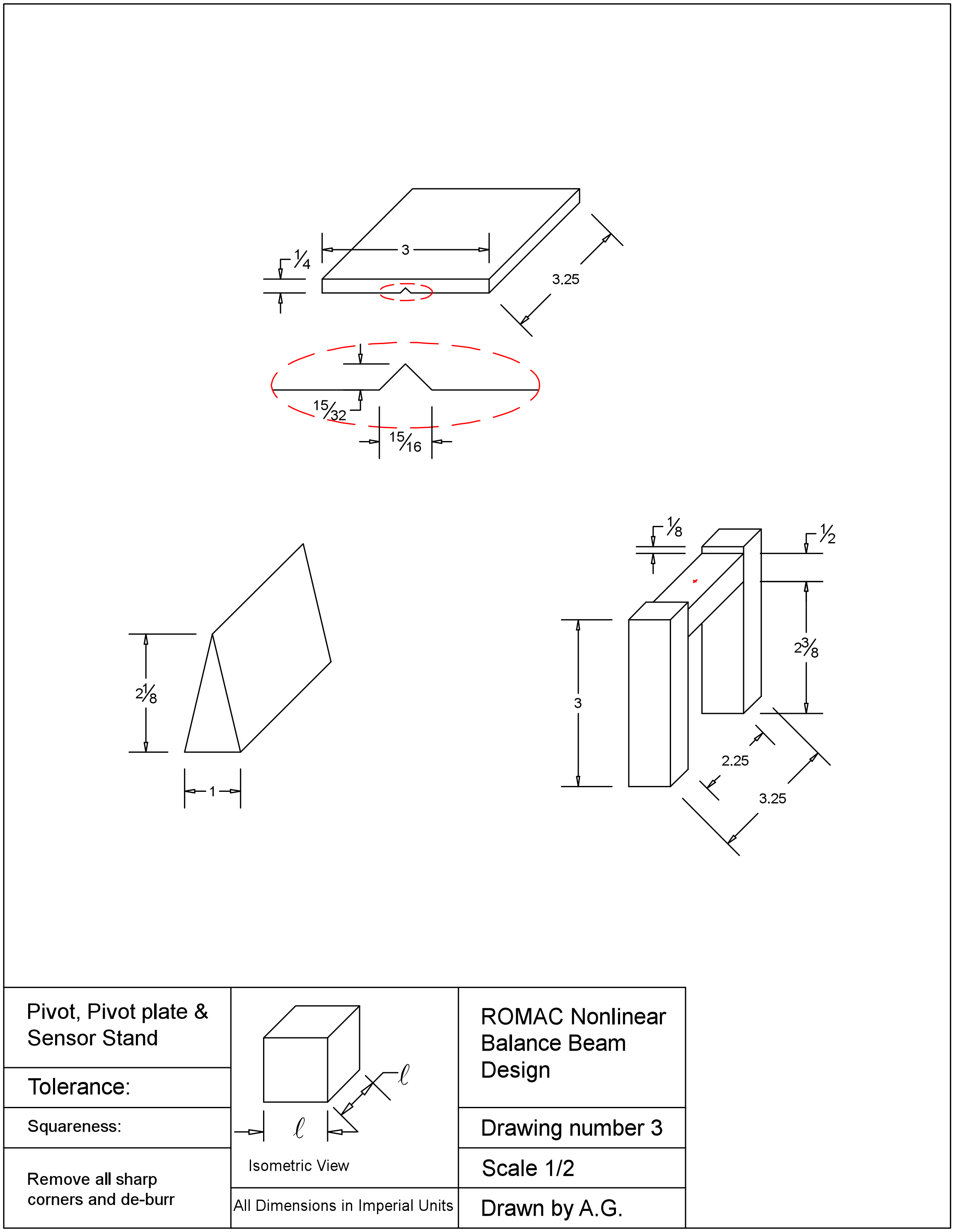

Figure 8-4 Pivot, Pivot Plate and Sensor Stand Dimensions

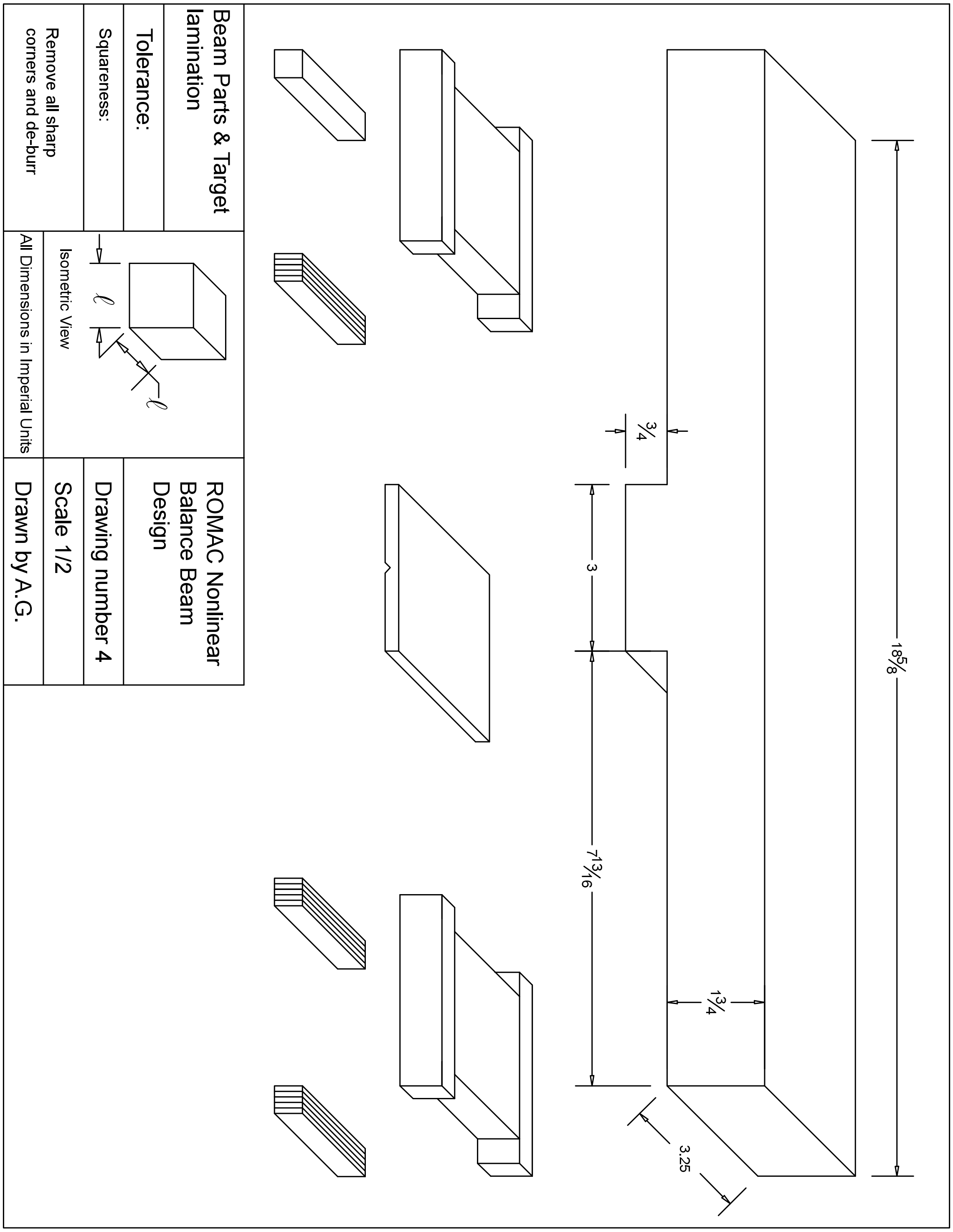

Figure 8-5 Beam Dimensions

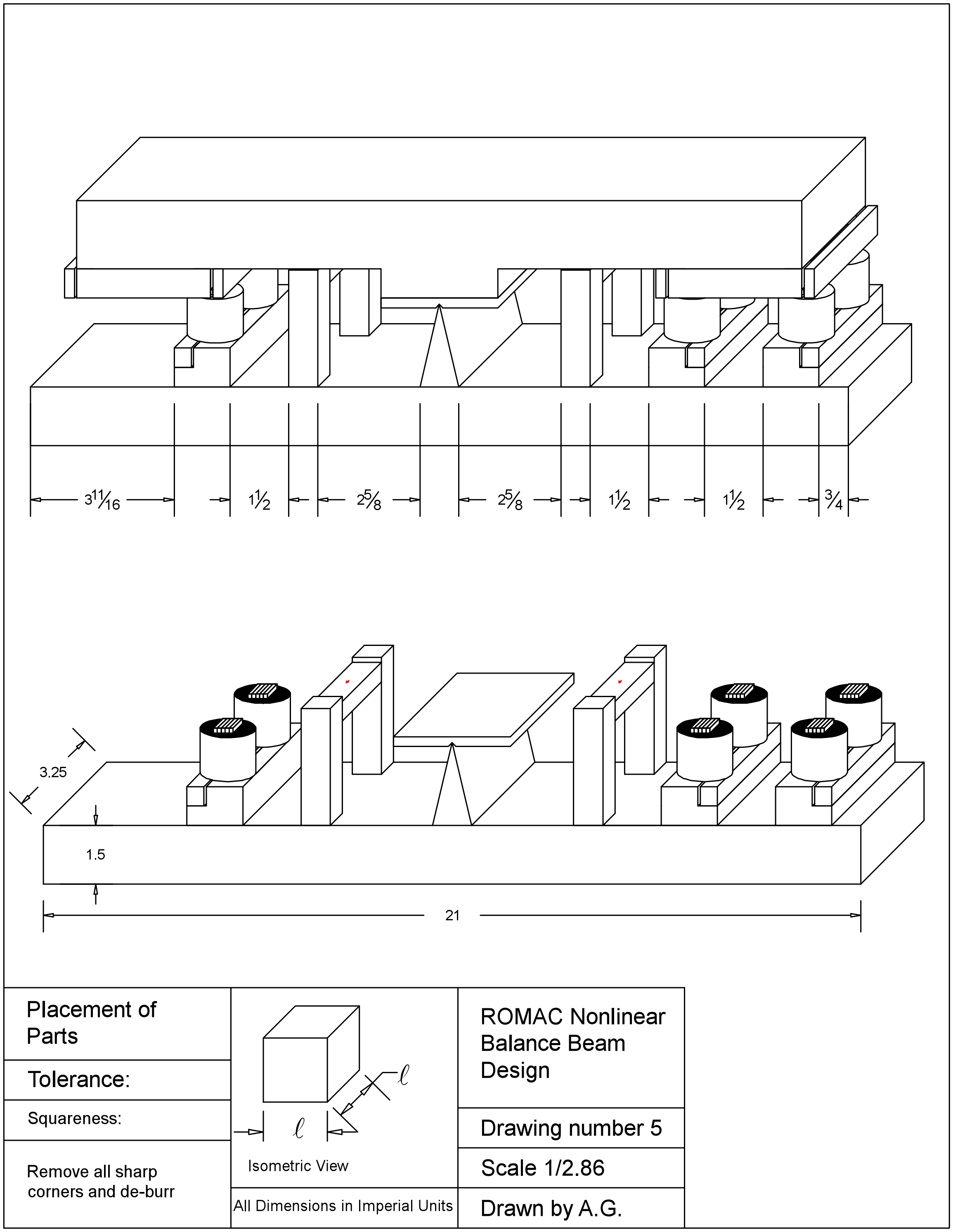

Figure 8-6 Distance Between The Parts

Appendix B

In this section first the balance beam’s transient response to different step functions is compared with simulation. Later the balance beam’s response to various impulse disturbances is compared with simulation as well.

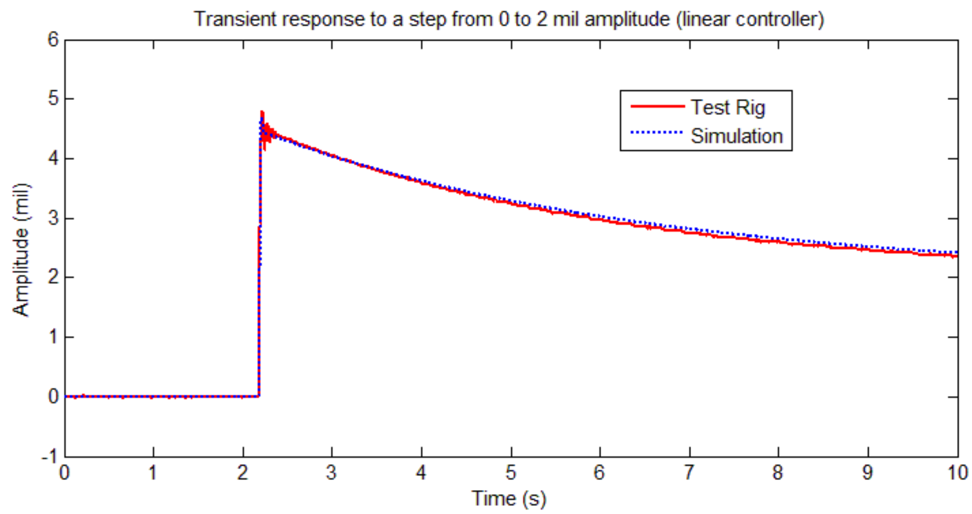

Figure 8-7 Linear Controller Transient Response to Step 0-2 (Time-span 10s)

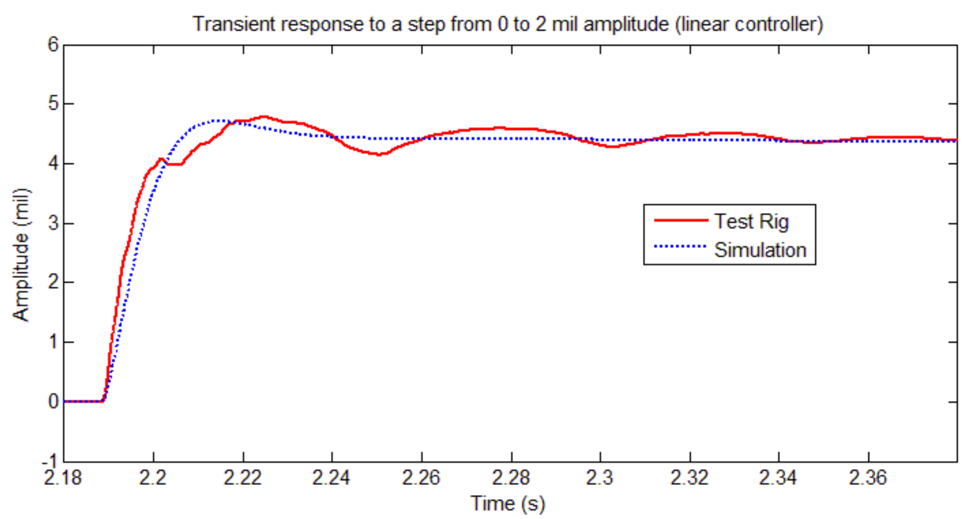

Figure 8-8 Linear Controller Transient Response to Step 0-2 (Time-span 0.2s)

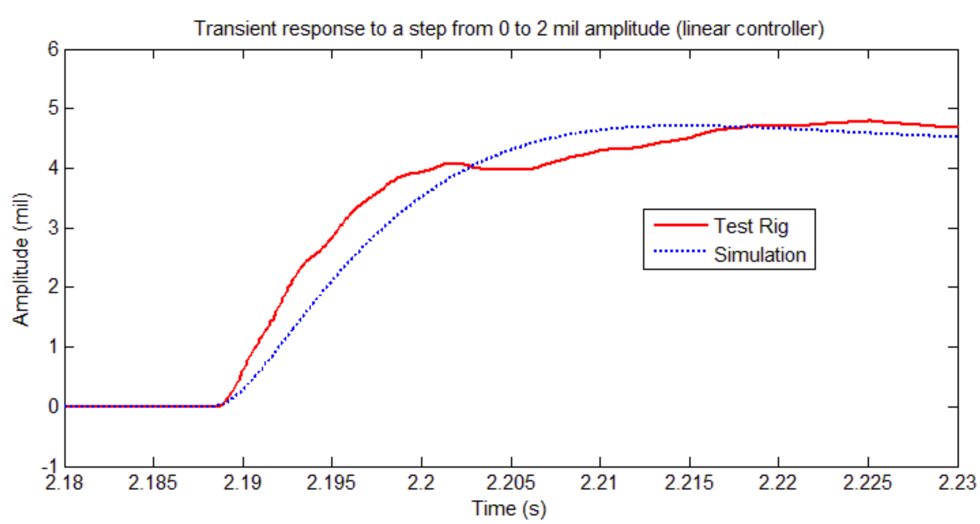

Figure 8-9 Linear Controller Transient Response to Step 0-2 (Time-span 0.05s)

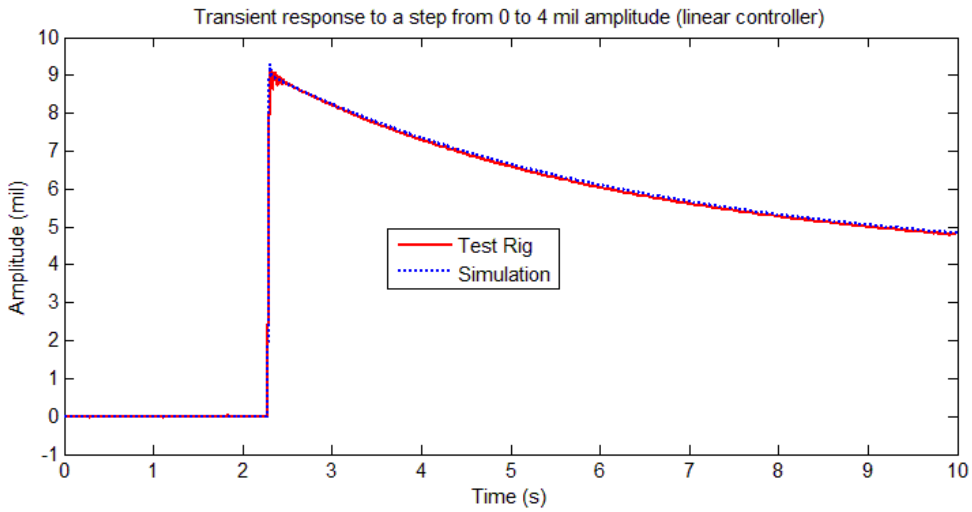

Figure 8-10 Linear Controller Transient Response to Step 0-4 (Time-span 10s)

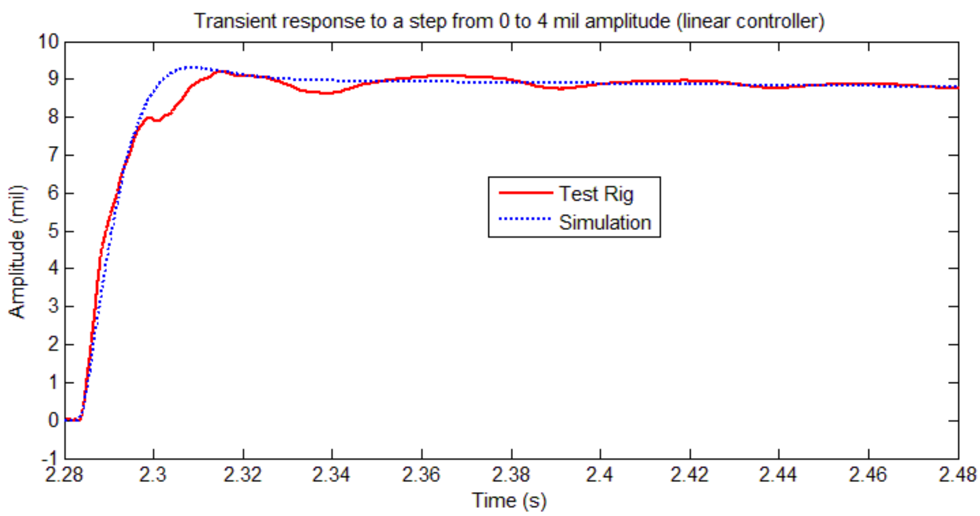

Figure 8-11 Linear Controller Transient Response to Step 0-4 (Time-span 0.2s)

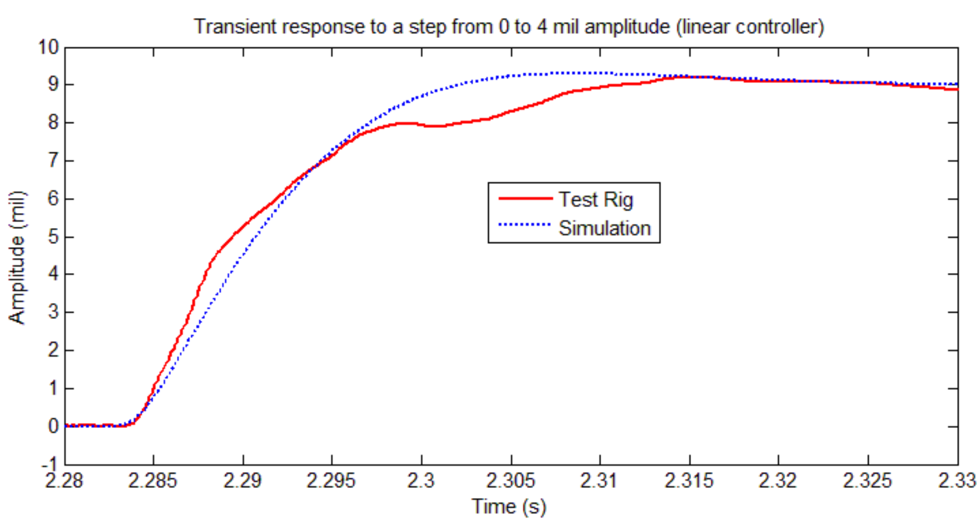

Figure 8-12 Linear Controller Transient Response to Step 0-4 (Time-span 0.05s)

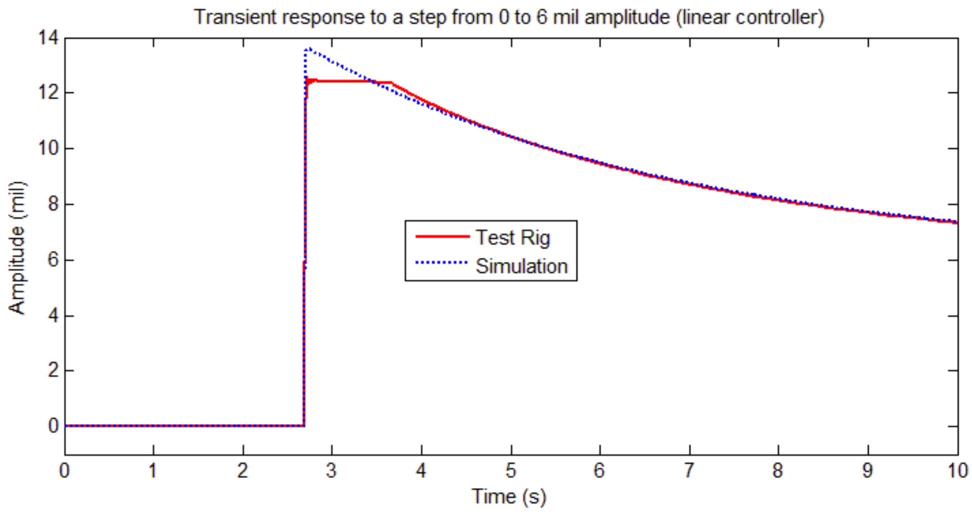

Figure 8-13 Linear Controller Transient Response to Step 0-6 (Time-span 10s)

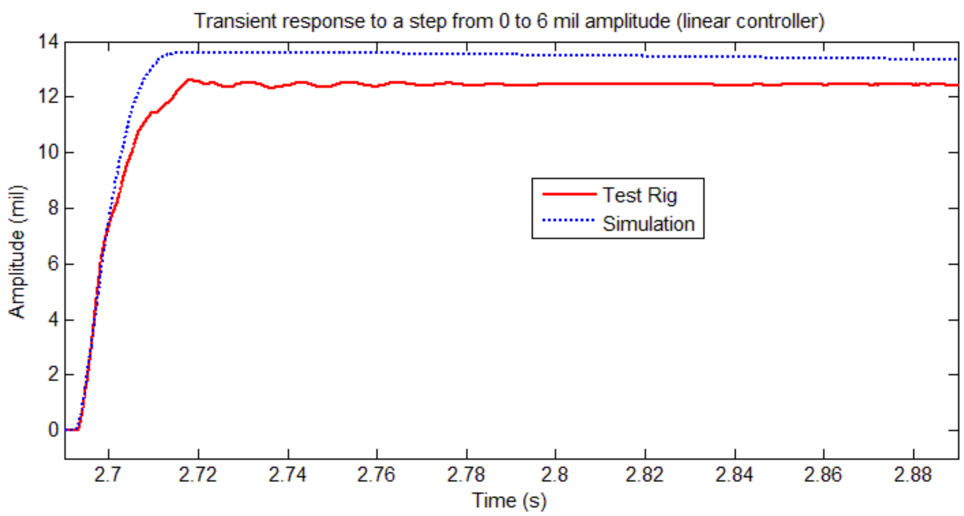

Figure 8-14 Linear Controller Transient Response to Step 0-6 (Time-span 0.2s)

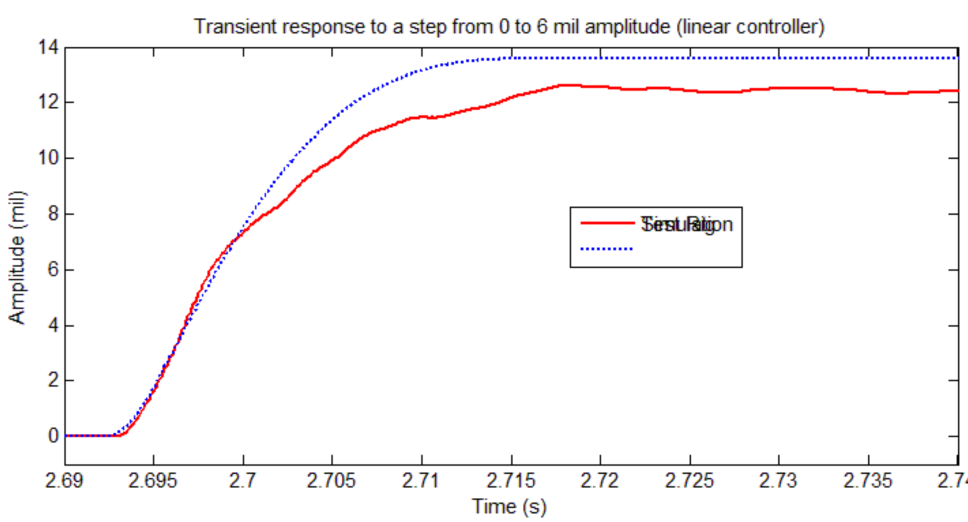

Figure 8-15 Linear Controller Transient Response to Step 0-6 (Time-span 0.05s)

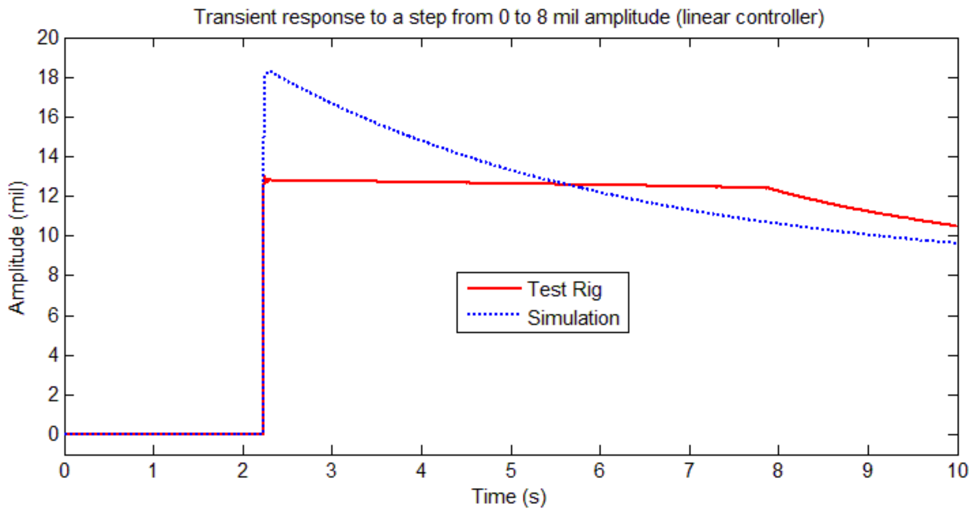

Figure 8-16 Linear Controller Transient Response to Step 0-8 (Time-span 10s)

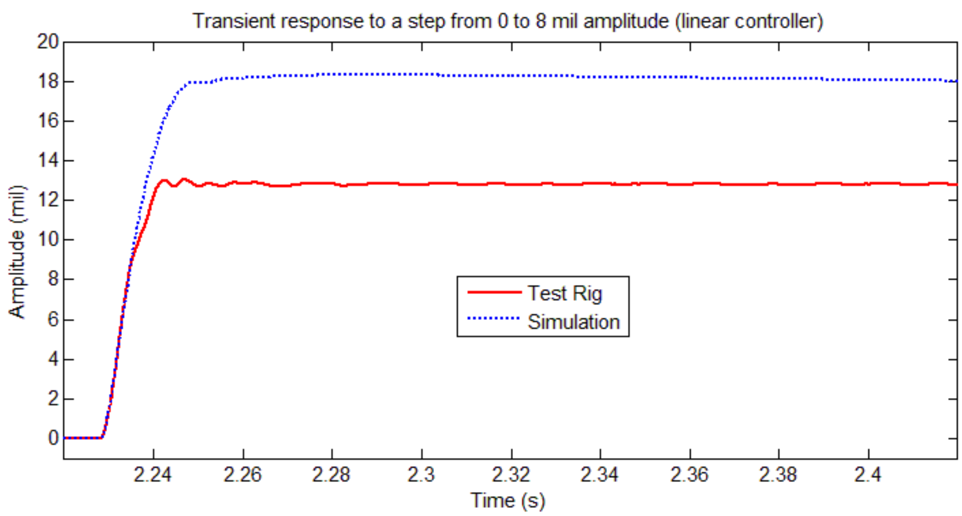

Figure 8-17 Linear Controller Transient Response to Step 0-8 (Time-span 0.2s)

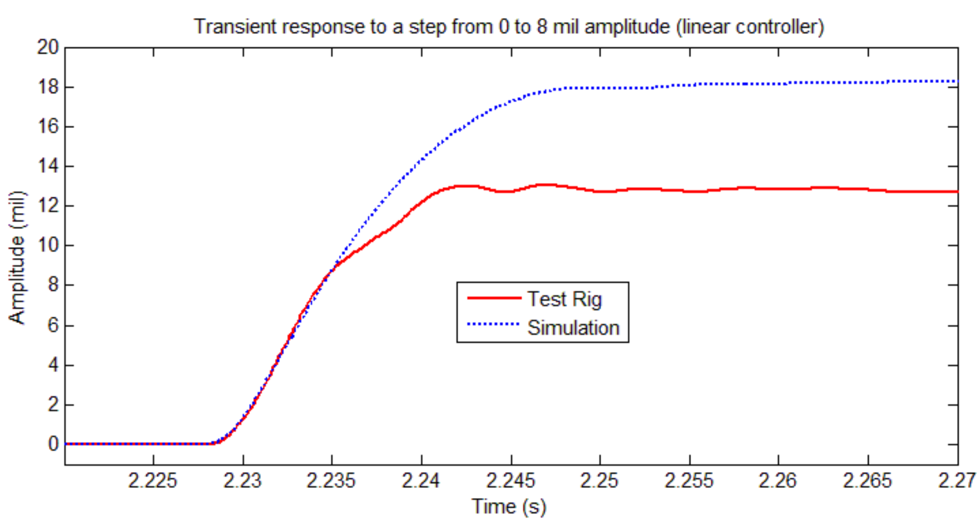

Figure 8-18 Linear Controller Transient Response to Step 0-8 (Time-span 0.05s)

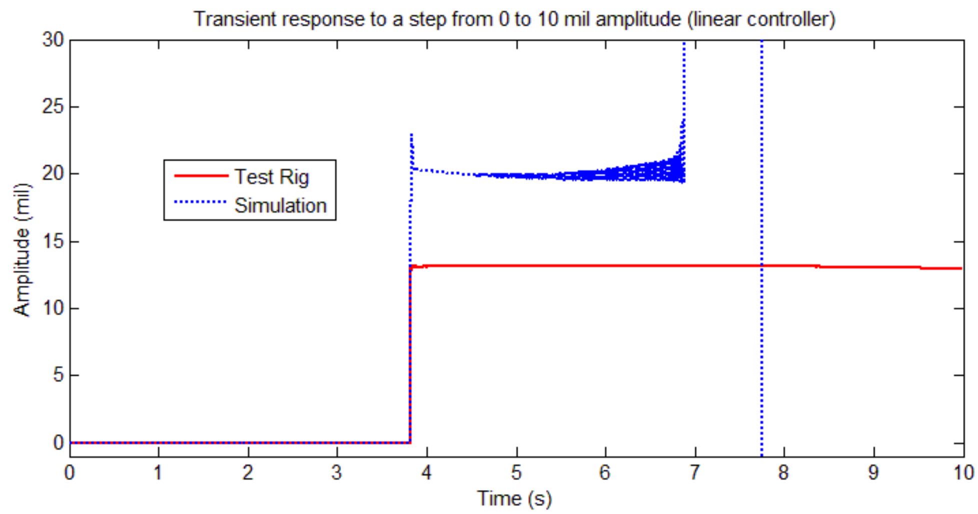

Figure 8-19 Linear Controller Transient Response to Step 0-10 (Time-span 10s)

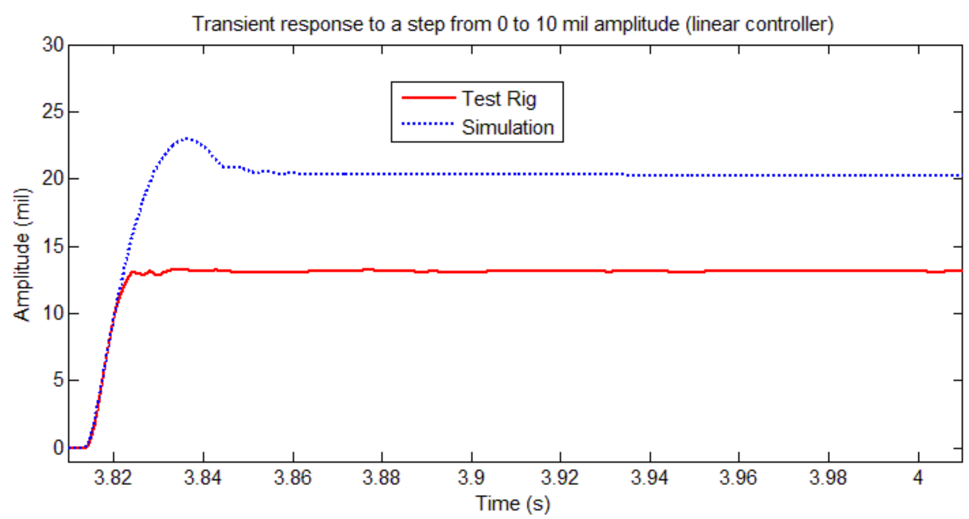

Figure 8-20 Linear Controller Transient Response to Step 0-10 (Time-span 0.2s)

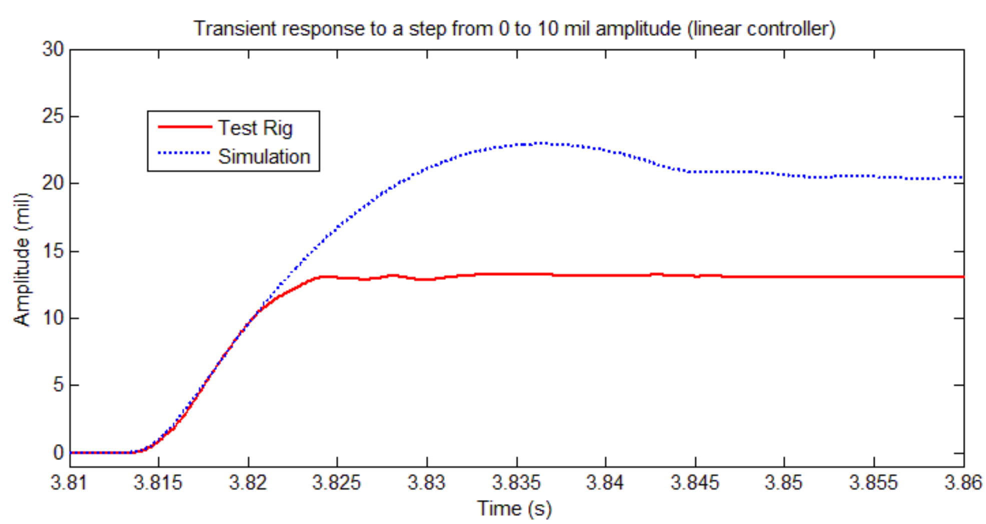

Figure 8-21 Linear Controller Transient Response to Step 0-10 (Time-span 0.05s)

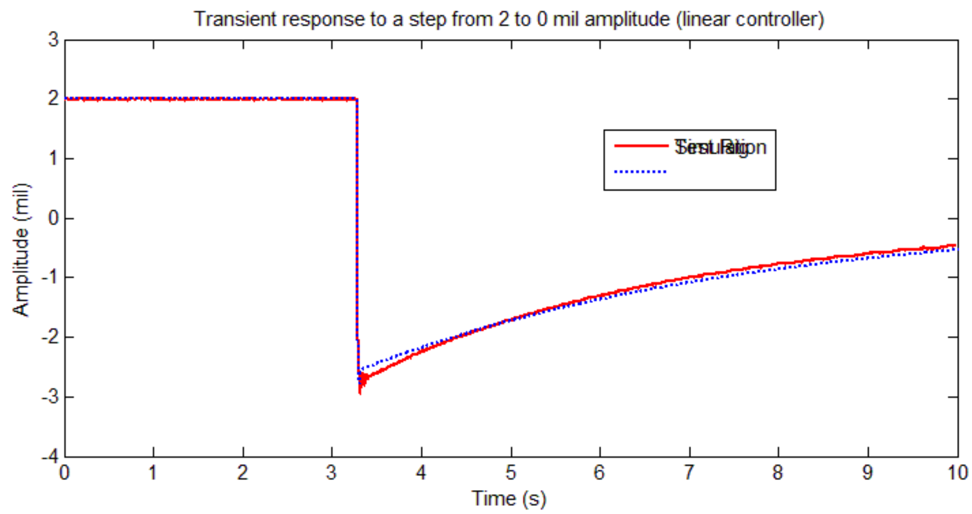

Figure 8-22 Linear Controller Transient Response to Step 2-0 (Time-span 10s)

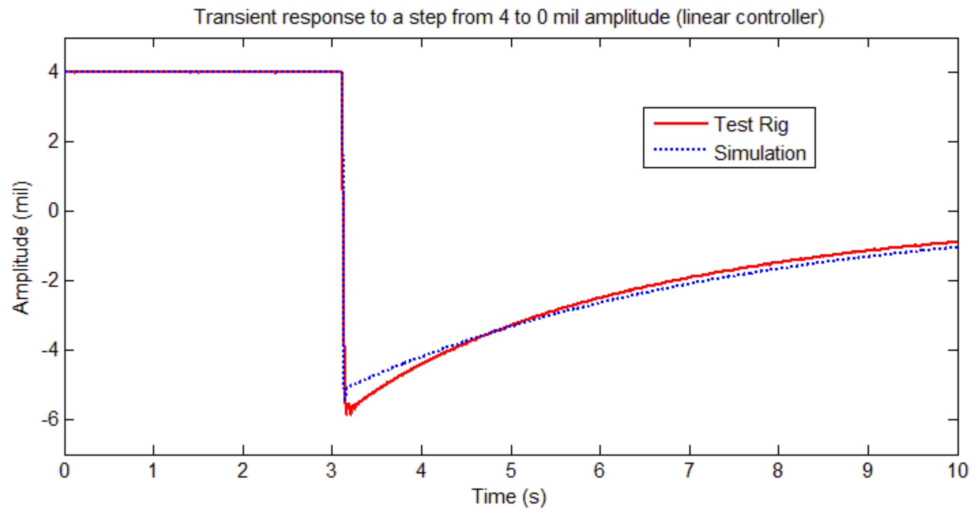

Figure 8-23 Linear Controller Transient Response to Step 4-0 (Time-span 10s)

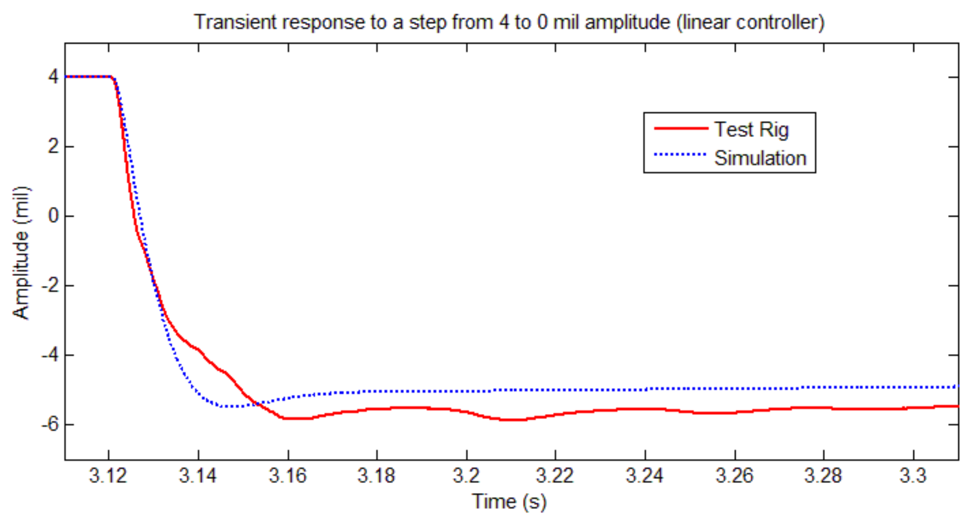

Figure 8-24 Linear Controller Transient Response to Step 4-0 (Time-span 0.2s)

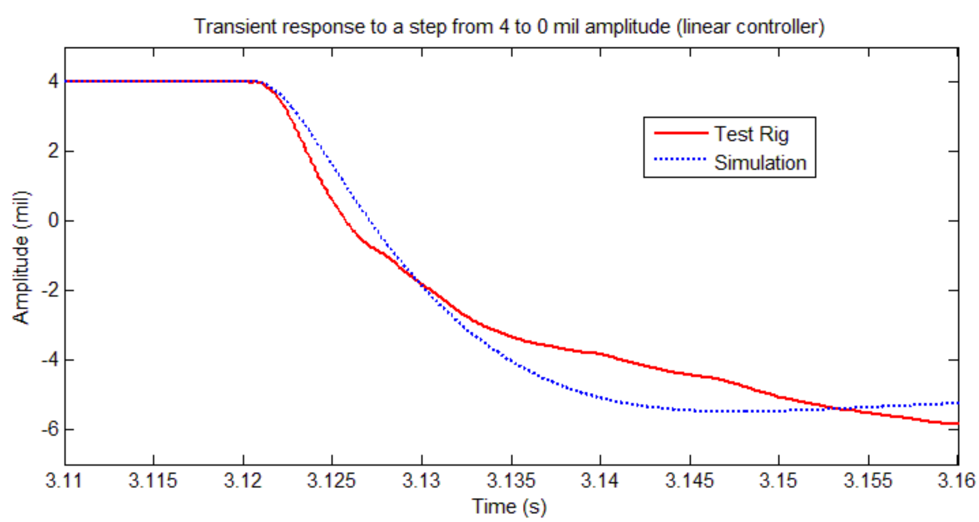

Figure 8-25 Linear Controller Transient Response to Step 4-0 (Time-span 0.05s)

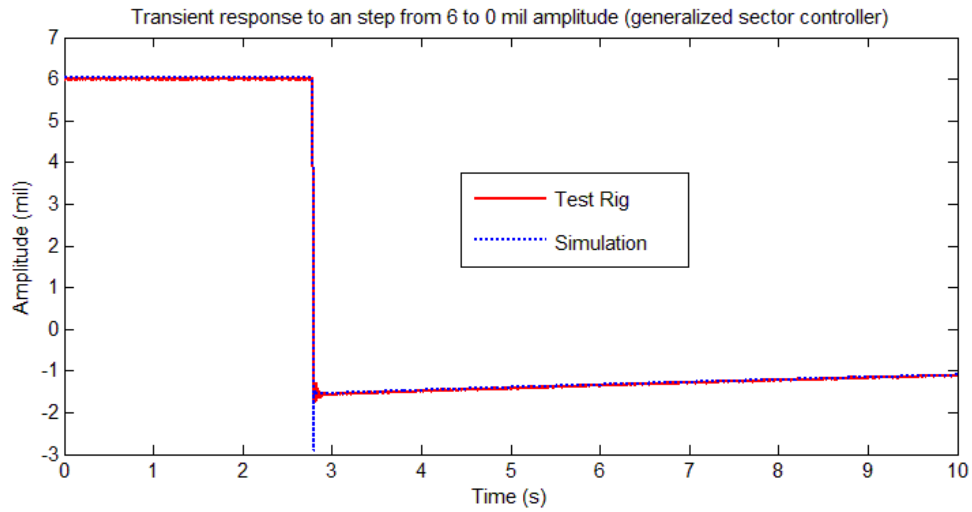

Figure 8-26 Linear Controller Transient Response to Step 6-0 (Time-span 10s)

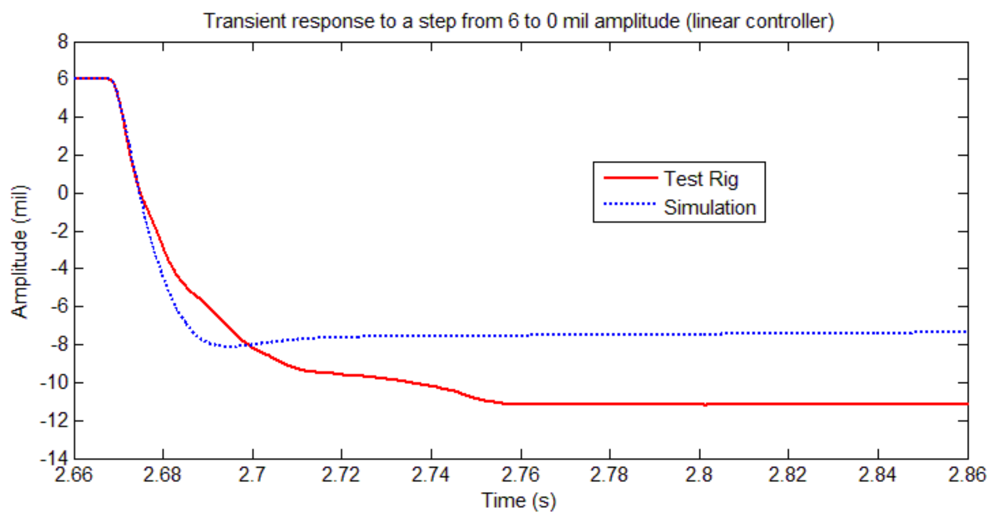

Figure 8-27 Linear Controller Transient Response to Step 6-0 (Time-span 0.2s)

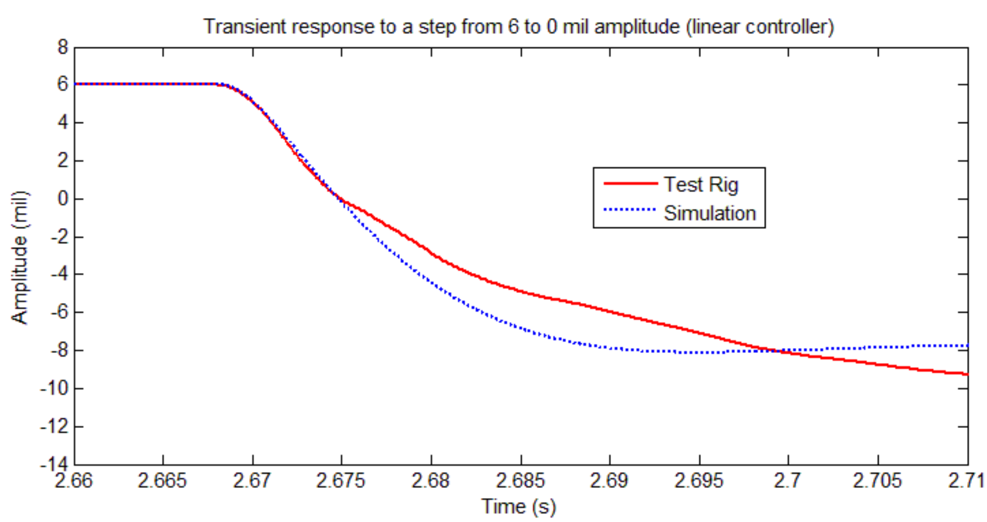

Figure 8-28 Linear Controller Transient Response to Step 6-0 (Time-span 0.05s)

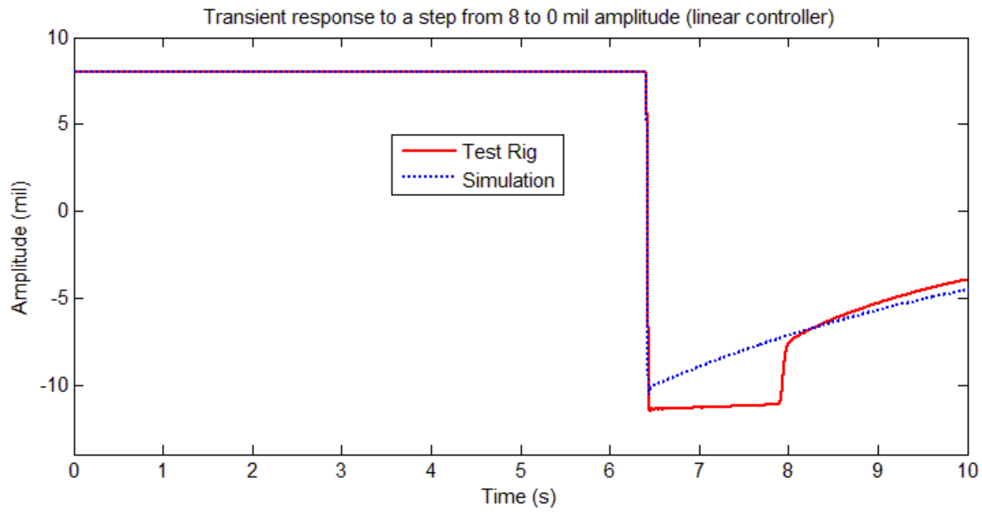

Figure 8-29 Linear Controller Transient Response to Step 8-0 (Time-span 10s)

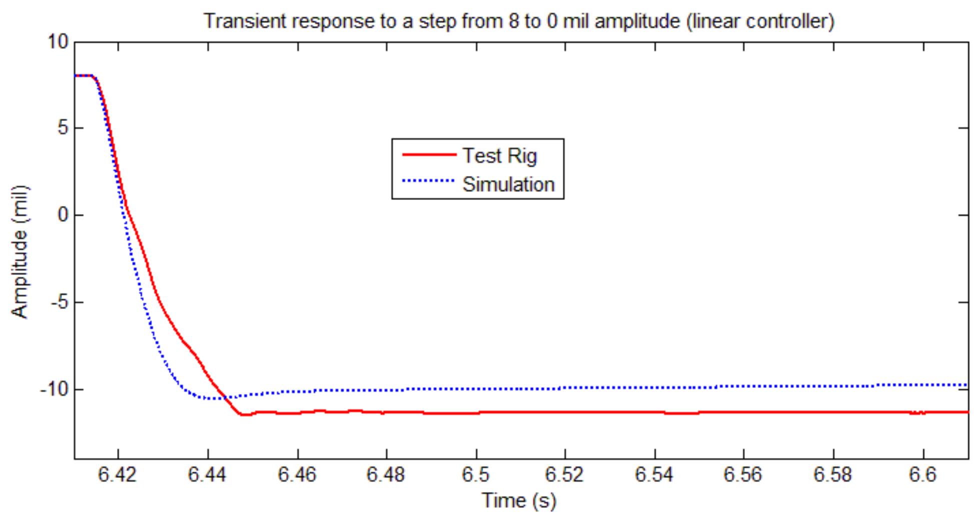

Figure 8-30 Linear Controller Transient Response to Step 8-0 (Time-span 0.2s)

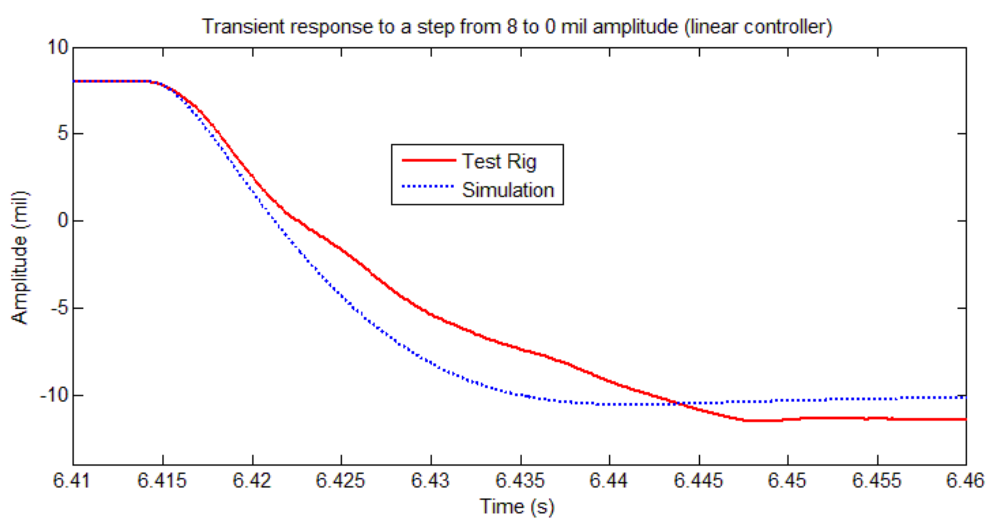

Figure 8-31 Linear Controller Transient Response to Step 8-0 (Time-span 0.05s)

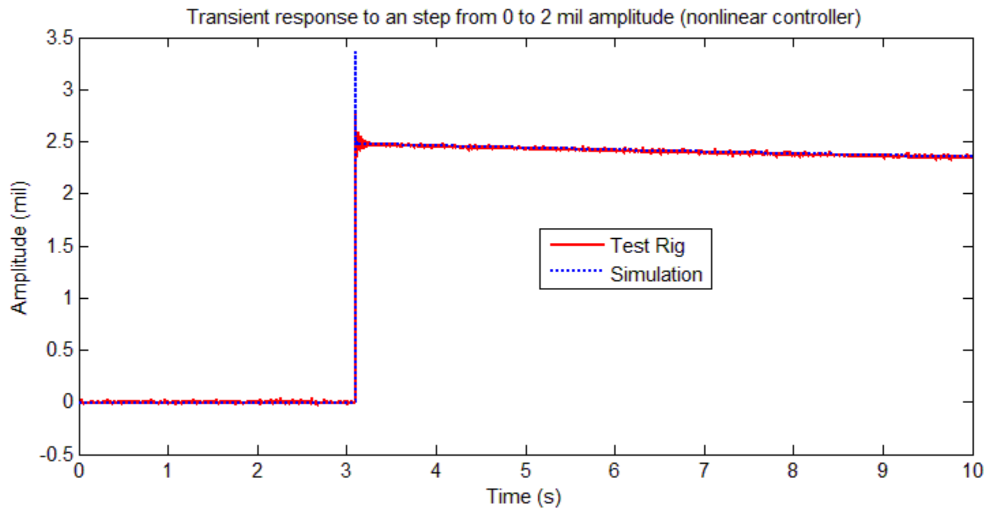

Figure 8-32 Nonlinear Controller Transient Response to Step 0-2 (Time-span 10s)

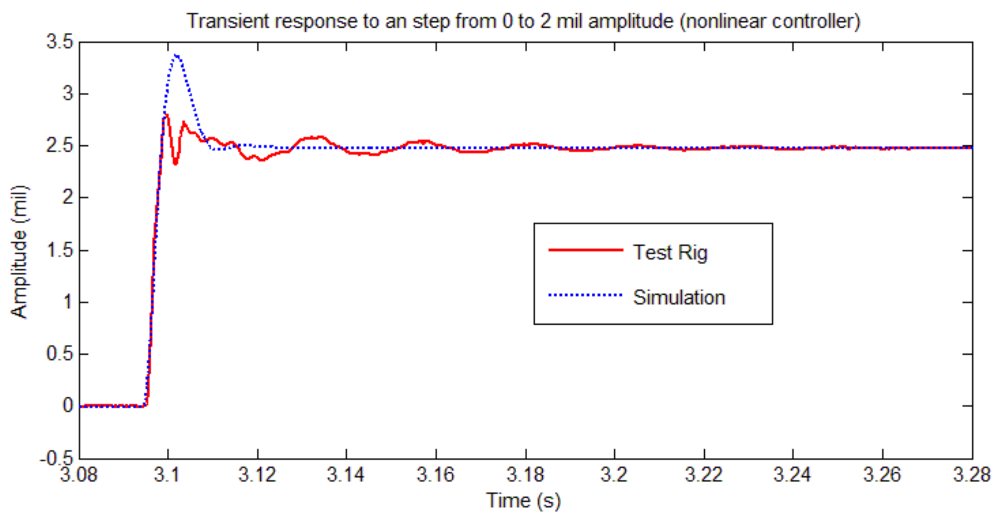

Figure 8-33 Nonlinear Controller Transient Response to Step 0-2 (Time-span 0.2s)

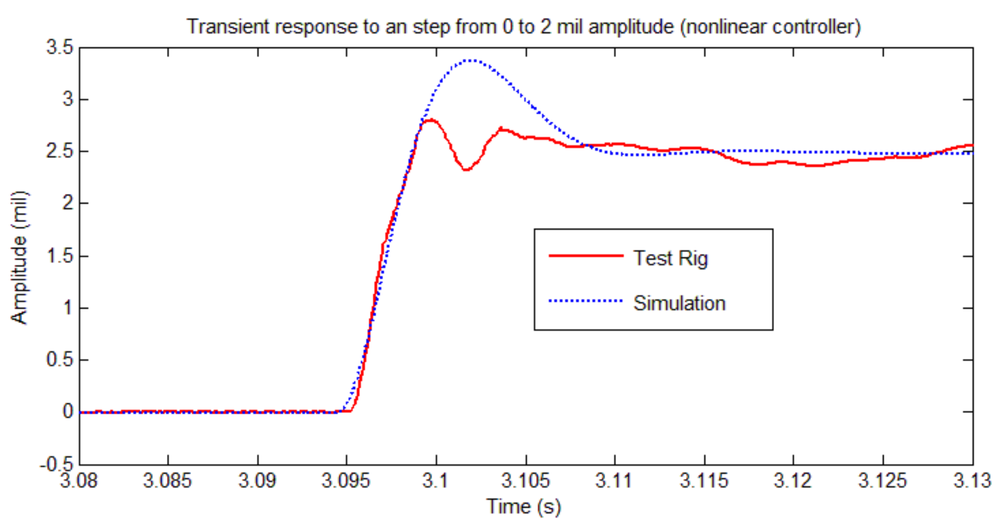

Figure 8-34 Nonlinear Controller Transient Response to Step 0-2 (Time-span 0.05s)

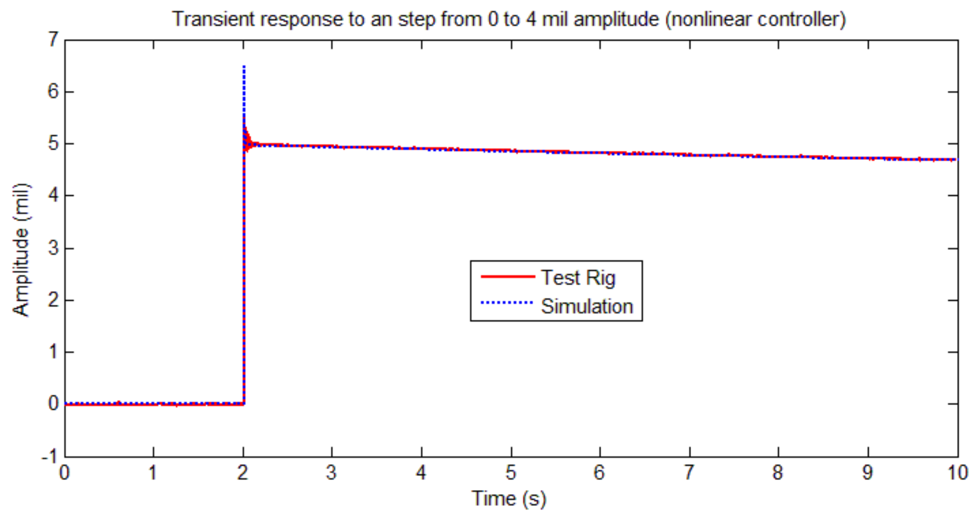

Figure 8-35 Nonlinear Controller Transient Response to Step 0-4 (Time-span 10s)

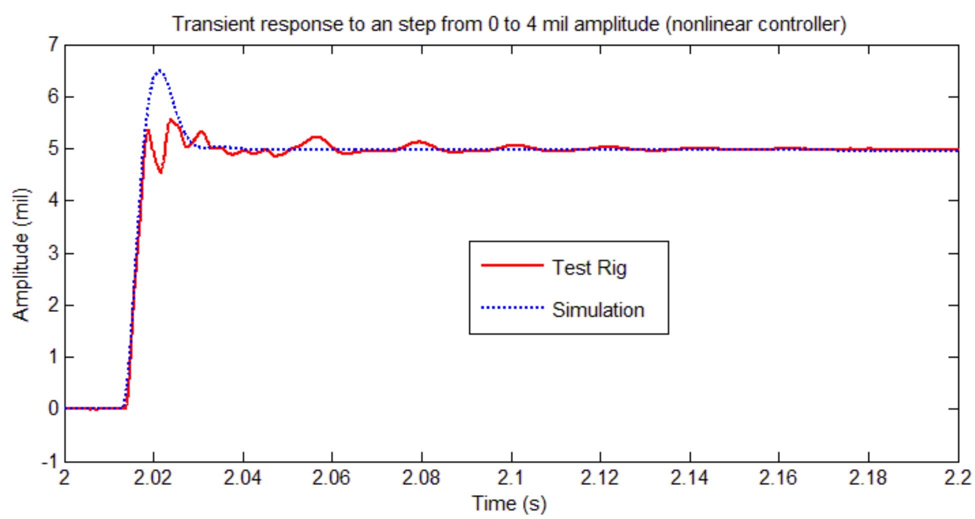

Figure 8-36 Nonlinear Controller Transient Response to Step 0-4 (Time-span 0.2s)

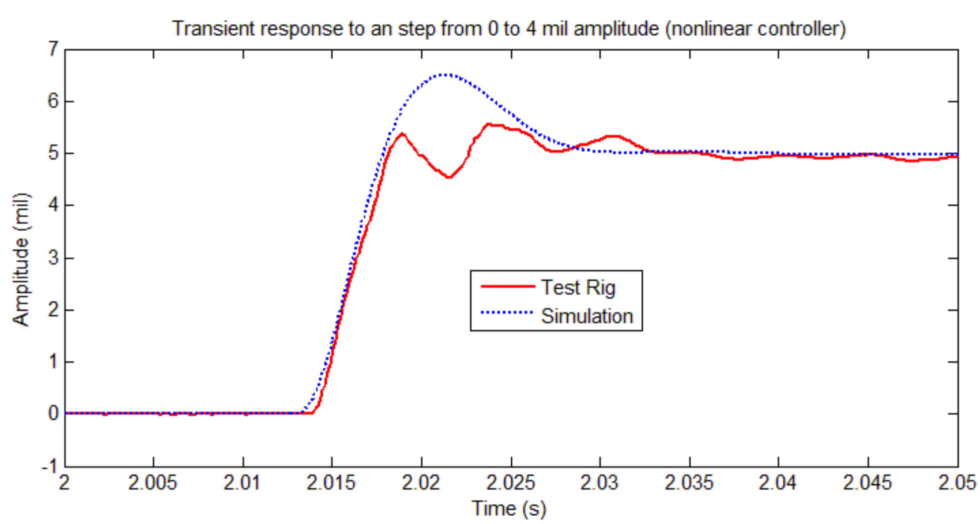

Figure 8-37 Nonlinear Controller Transient Response to Step 0-4 (Time-span 0.05s)

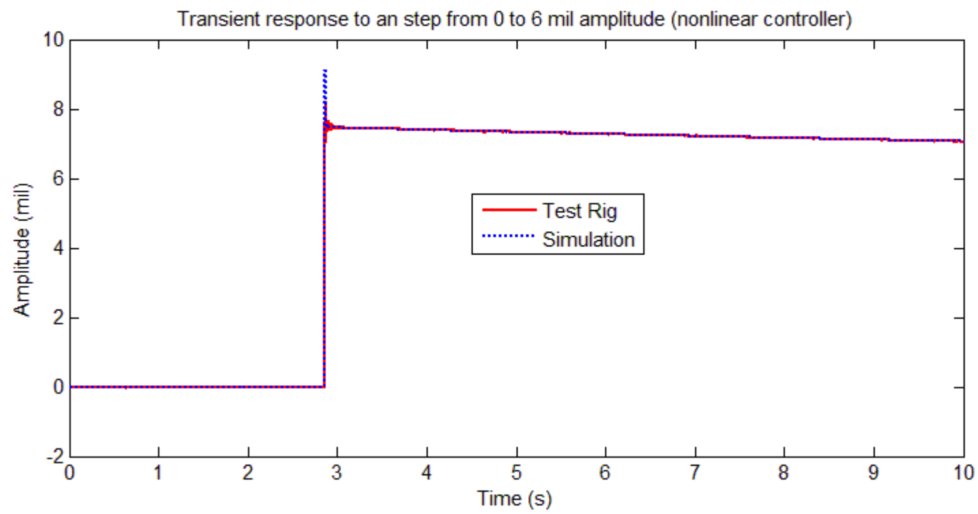

Figure 8-38 Nonlinear Controller Transient Response to Step 0-6 (Time-span 10s)

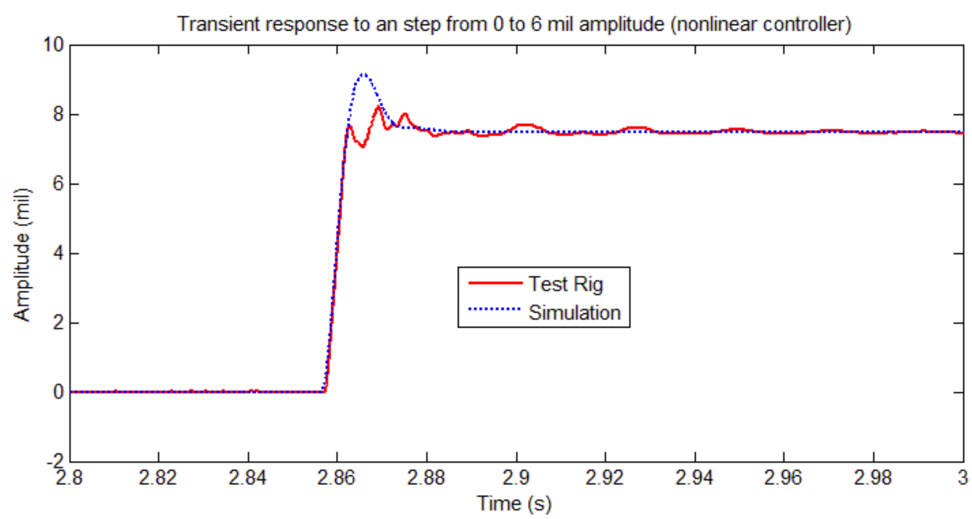

Figure 8-39 Nonlinear Controller Transient Response to Step 0-6 (Time-span 0.2s)

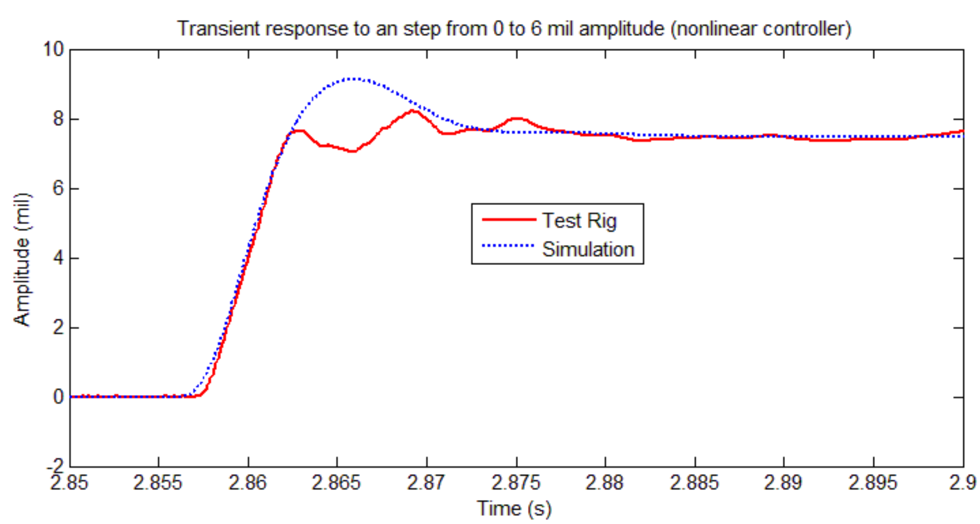

Figure 8-40 Nonlinear Controller Transient Response to Step 0-6 (Time-span 0.05s)

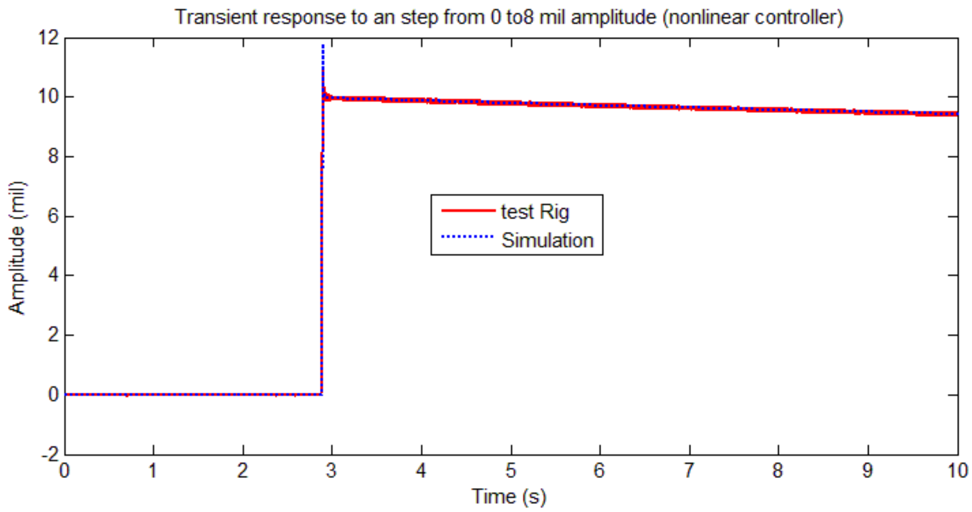

Figure 8-41 Nonlinear Controller Transient Response to Step 0-8 (Time-span 10s)

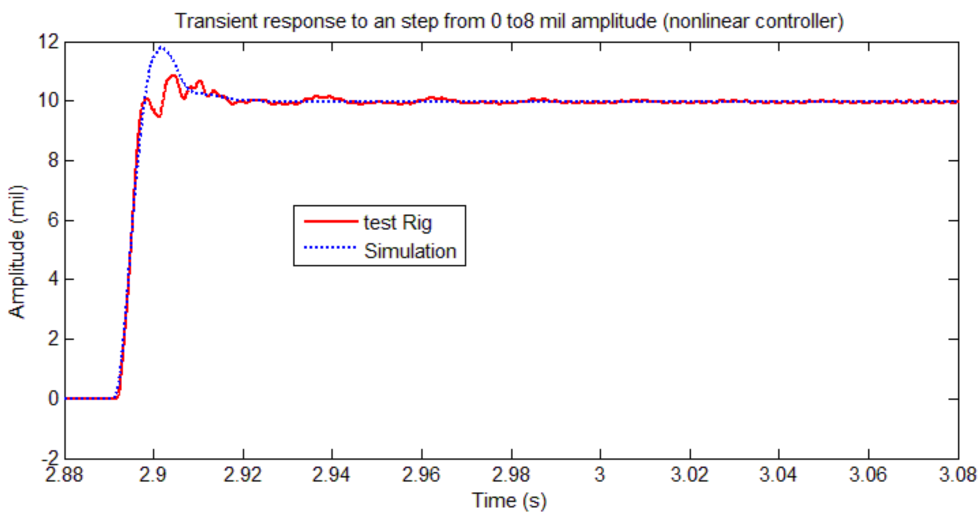

Figure 8-42 Nonlinear Controller Transient Response to Step 0-8 (Time-span 0.2s)

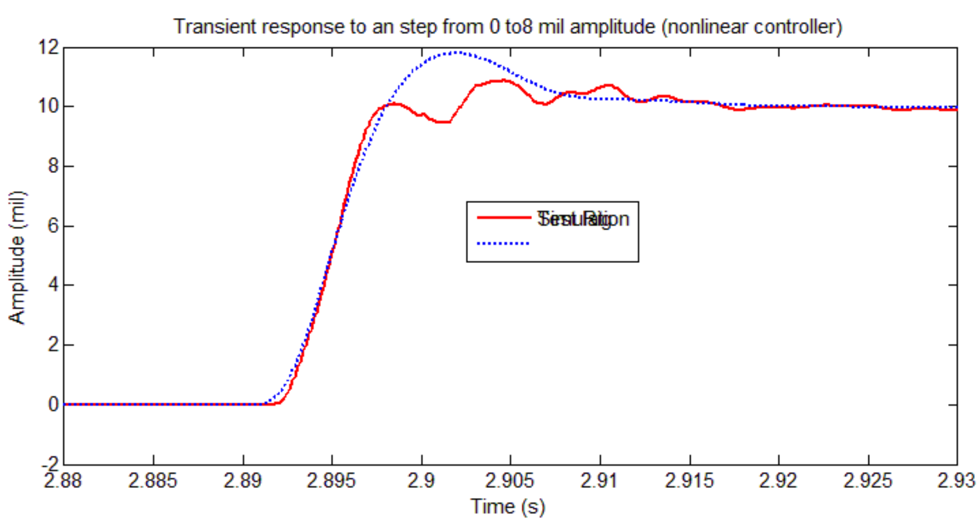

Figure 8-43 Nonlinear Controller Transient Response to Step 0-8 (Time-span 0.05s)

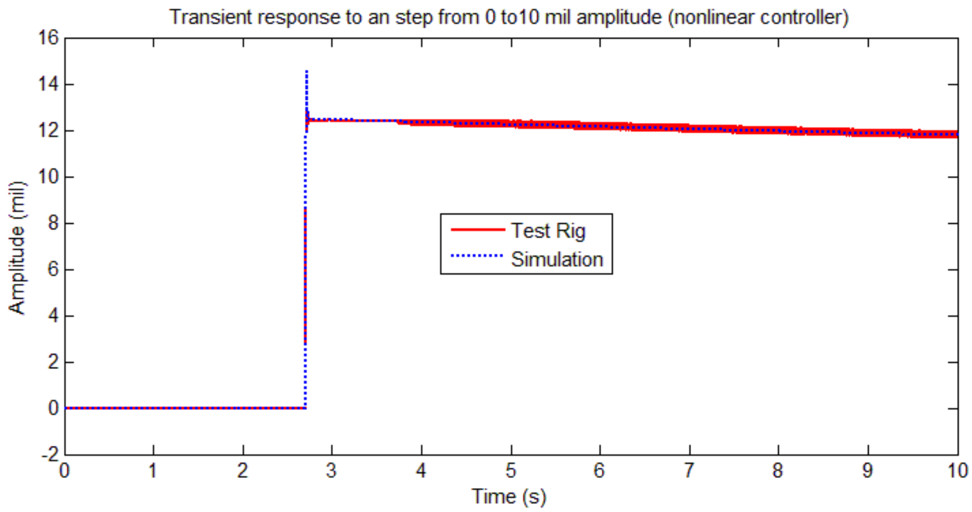

Figure 8-44 Nonlinear Controller Transient Response to Step 0-10 (Time-span 10s)

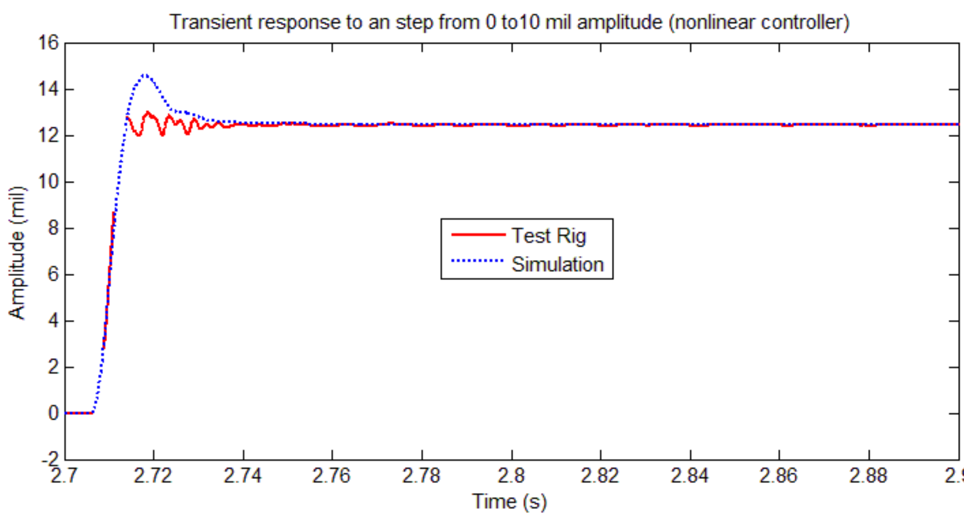

Figure 8-45 Nonlinear Controller Transient Response to Step 0-10 (Time-span 0.2s)

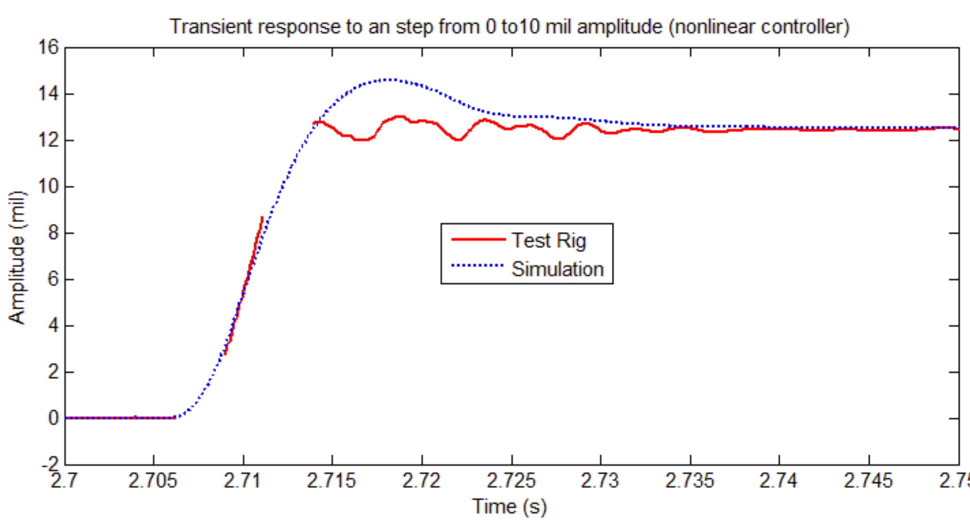

Figure 8-46 Nonlinear Controller Transient Response to Step 0-10 (Time-span 0.05s)

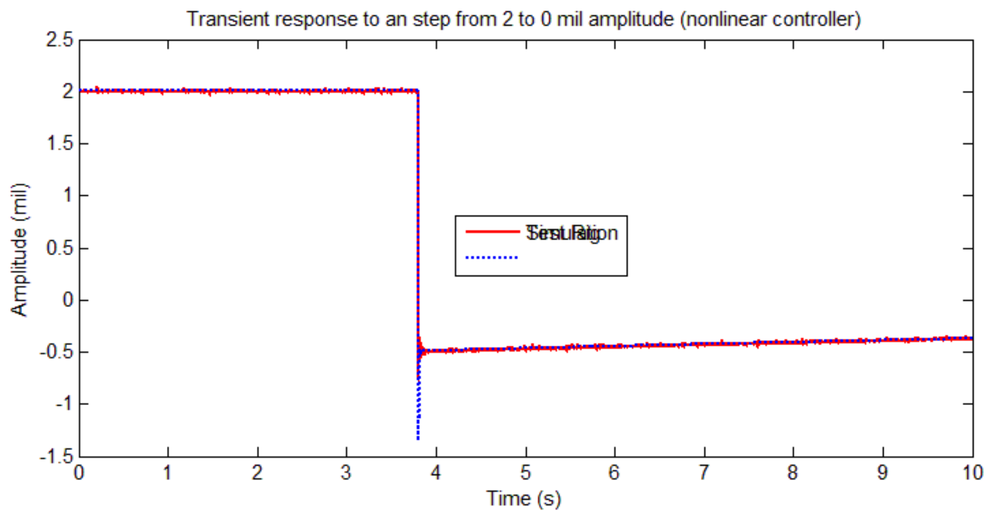

Figure 8-47 Nonlinear Controller Transient Response to Step 2-0 (Time-span 10s)

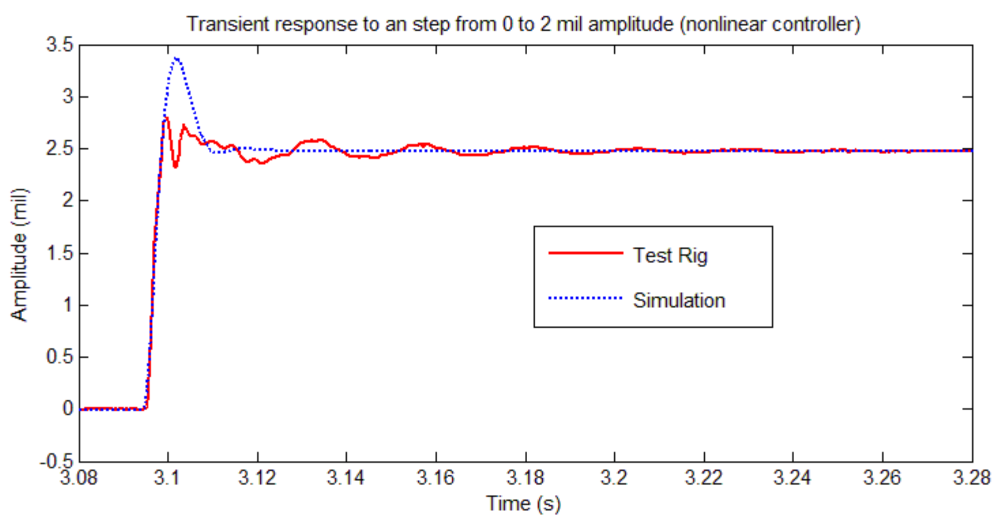

Figure 8-48 Nonlinear Controller Transient Response to Step 2-0 (Time-span 0.2s)

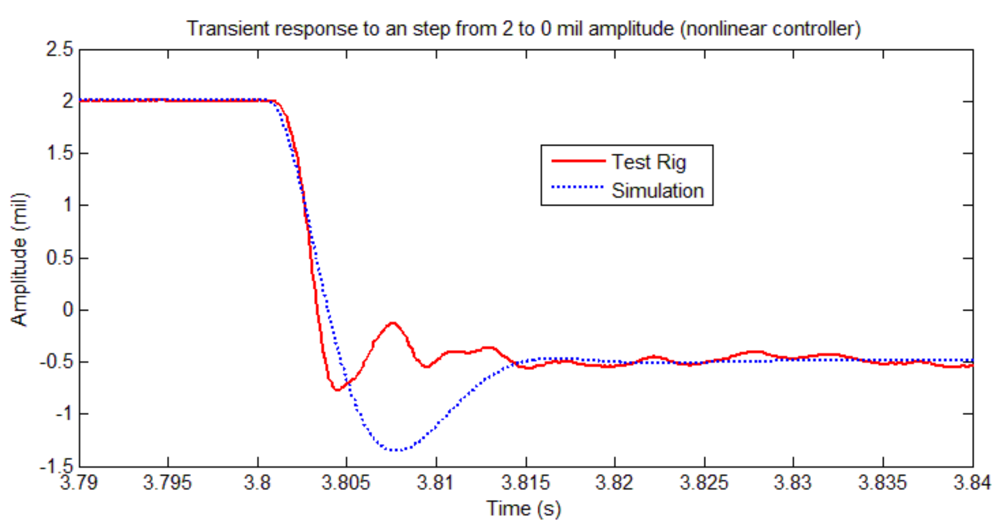

Figure 8-49 Nonlinear Controller Transient Response to Step 2-0 (Time-span 0.05s)

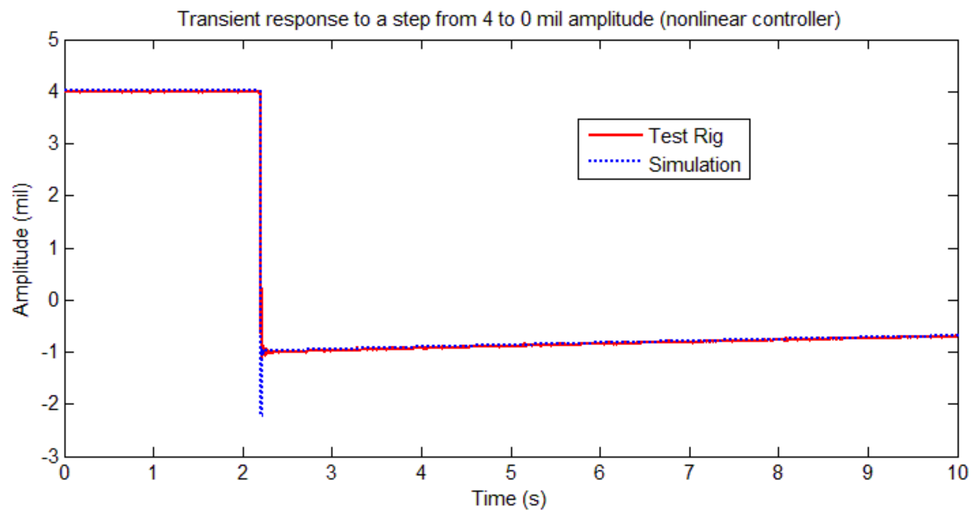

Figure 8-50 Nonlinear Controller Transient Response to Step 4-0 (Time-span 10s)

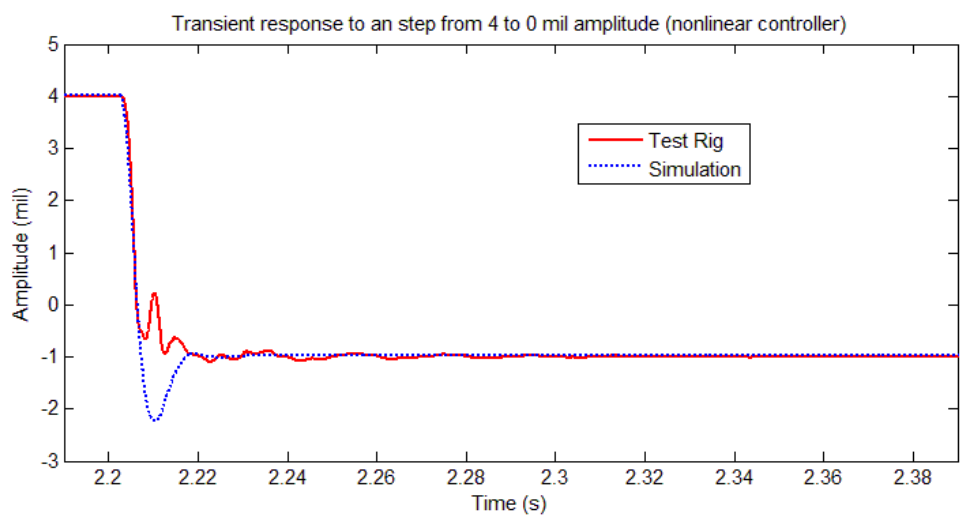

Figure 8-51 Nonlinear Controller Transient Response to Step 4-0 (Time-span 0.2s)

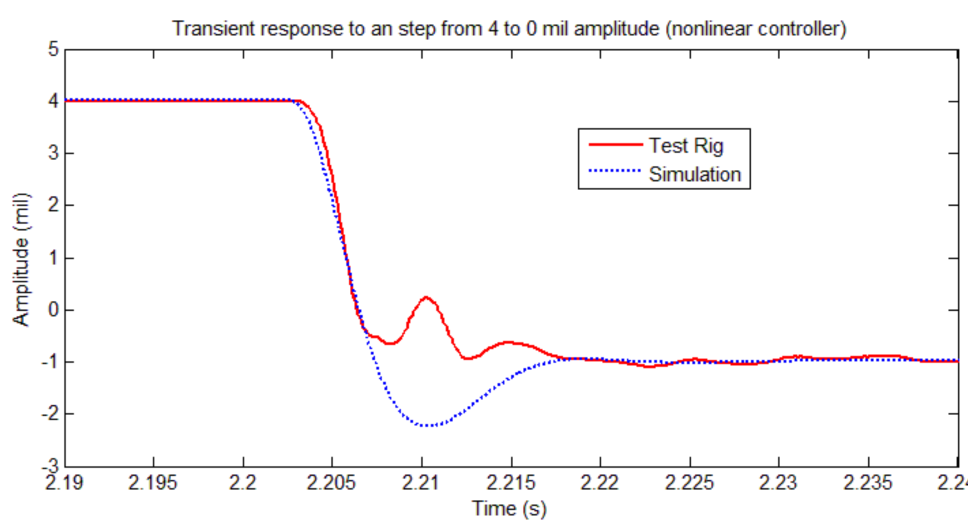

Figure 8-52 Nonlinear Controller Transient Response to Step 4-0 (Time-span 0.05s)

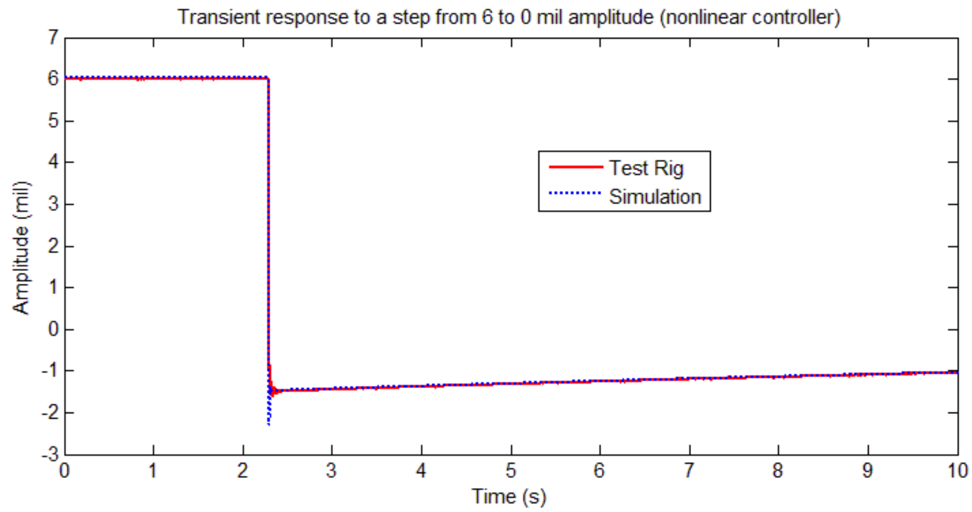

Figure 8-53 Nonlinear Controller Transient Response to Step 6-0 (Time-span 10s)

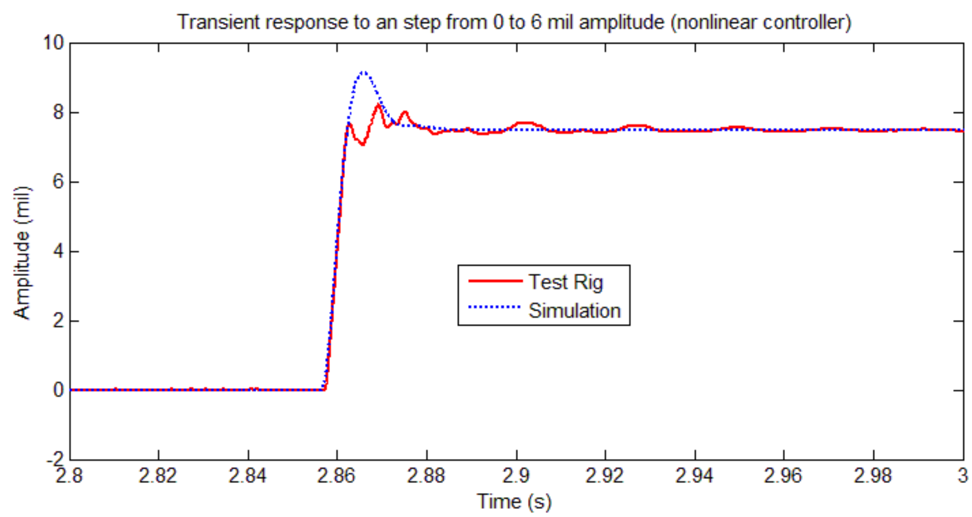

Figure 8-54 Nonlinear Controller Transient Response to Step 6-0 (Time-span 0.2s)

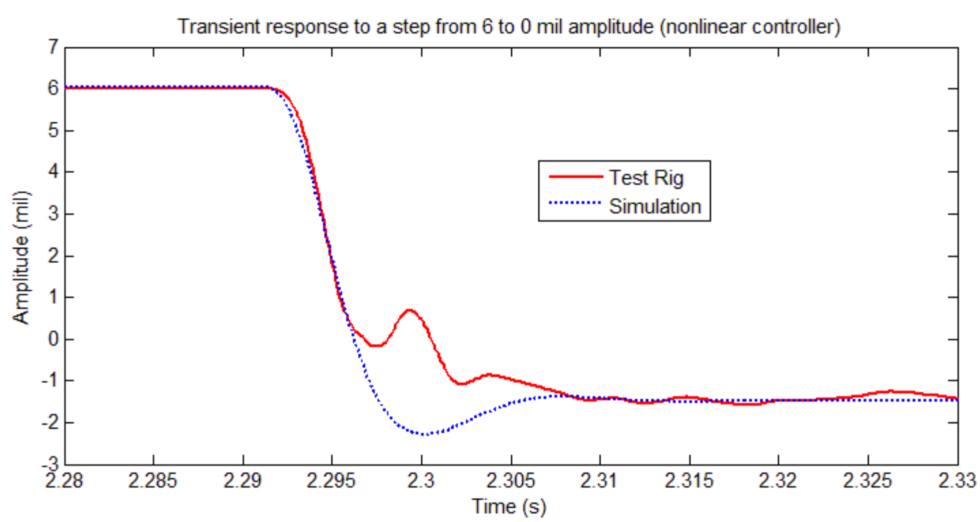

Figure 8-55 Nonlinear Controller Transient Response to Step 6-0 (Time-span 0.05s)

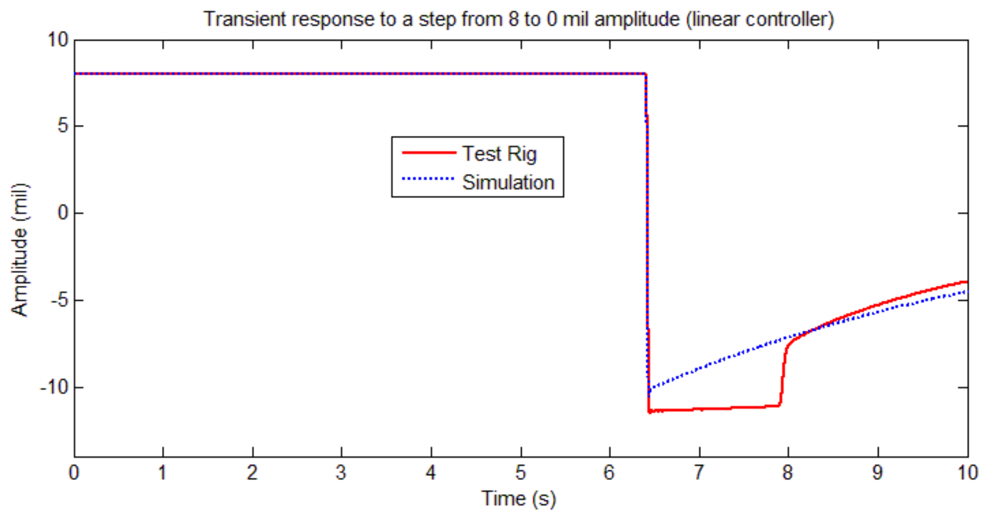

Figure 8-56 Nonlinear Controller Transient Response to Step 8-0 (Time-span 10s)

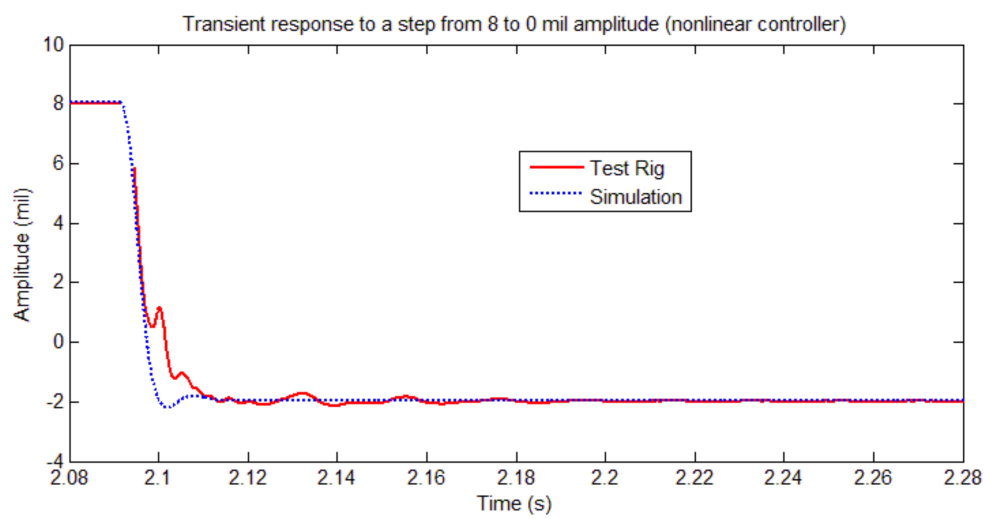

Figure 8-57 Nonlinear Controller Transient Response to Step 8-0 (Time-span 0.2s)

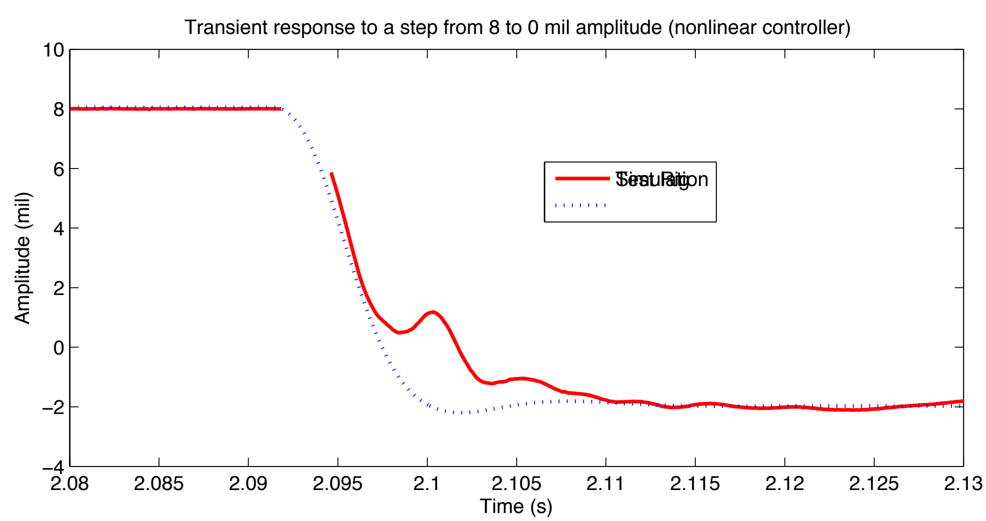

Figure 8-58 Nonlinear Controller Transient Response to Step 8-0 (Time-span 0.05s)

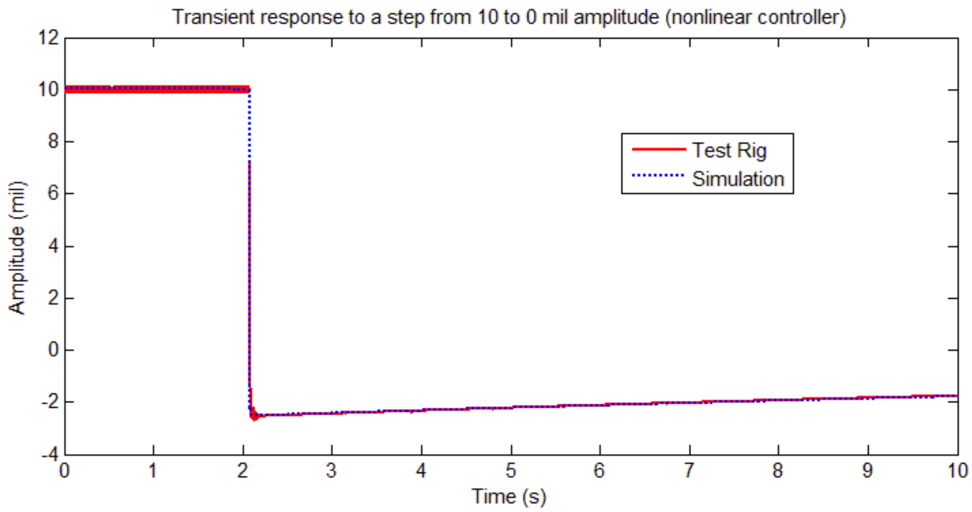

Figure 8-59 Nonlinear Controller Transient Response to Step 10-0 (Time-span 10s)

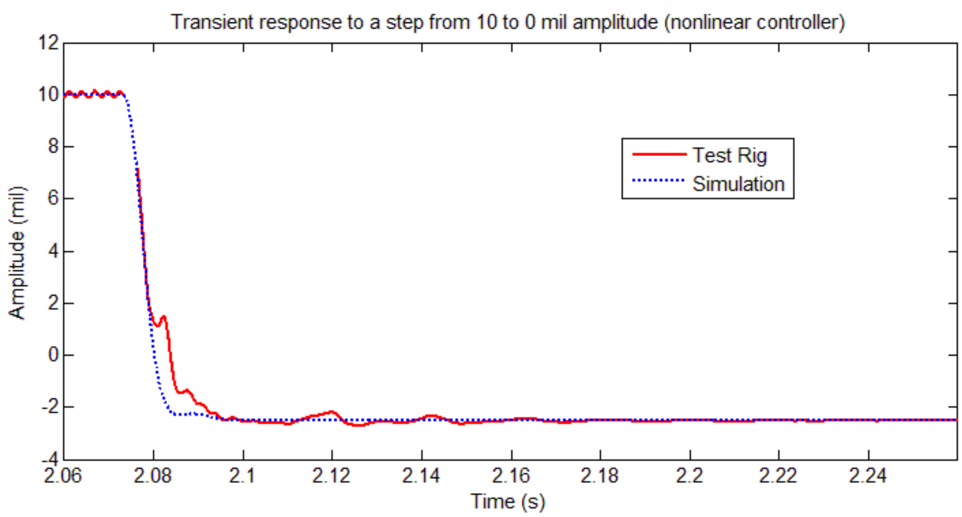

Figure 8-60 Nonlinear Controller Transient Response to Step 10-0 (Time-span 0.2s)

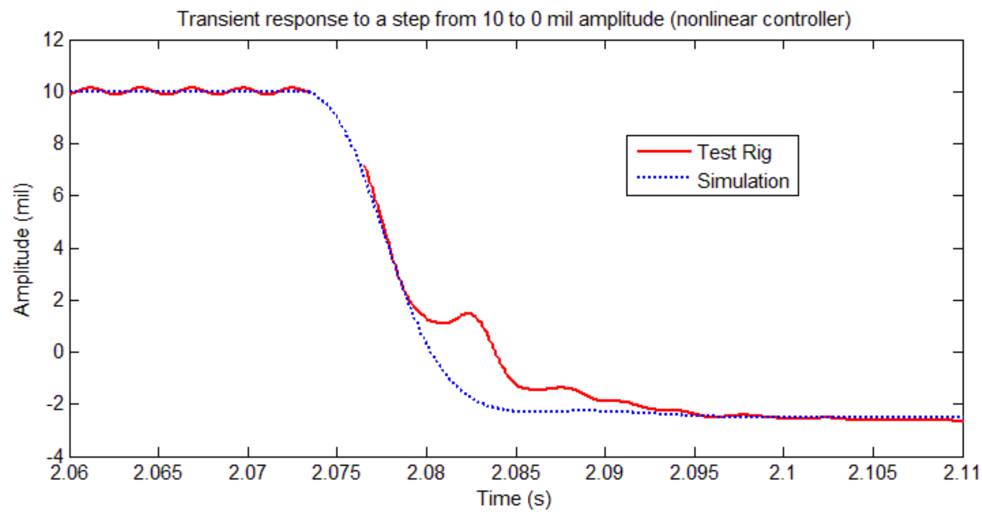

Figure 8-61 Nonlinear Controller Transient Response to Step 10-0 (Time-span 0.05s)

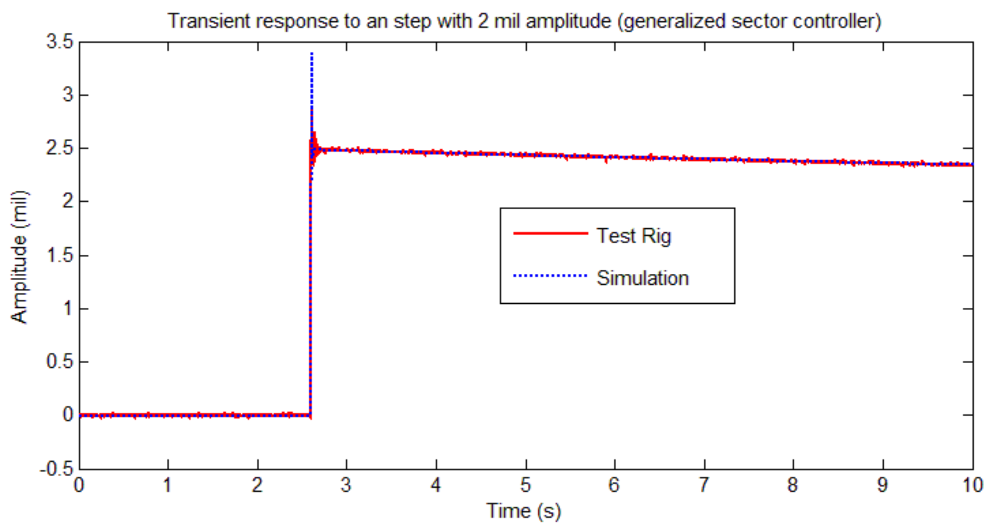

Figure 8-62 Generalized Sector Nonlinear Controller Transient Response to Step 0-2 (Time-span 10s)

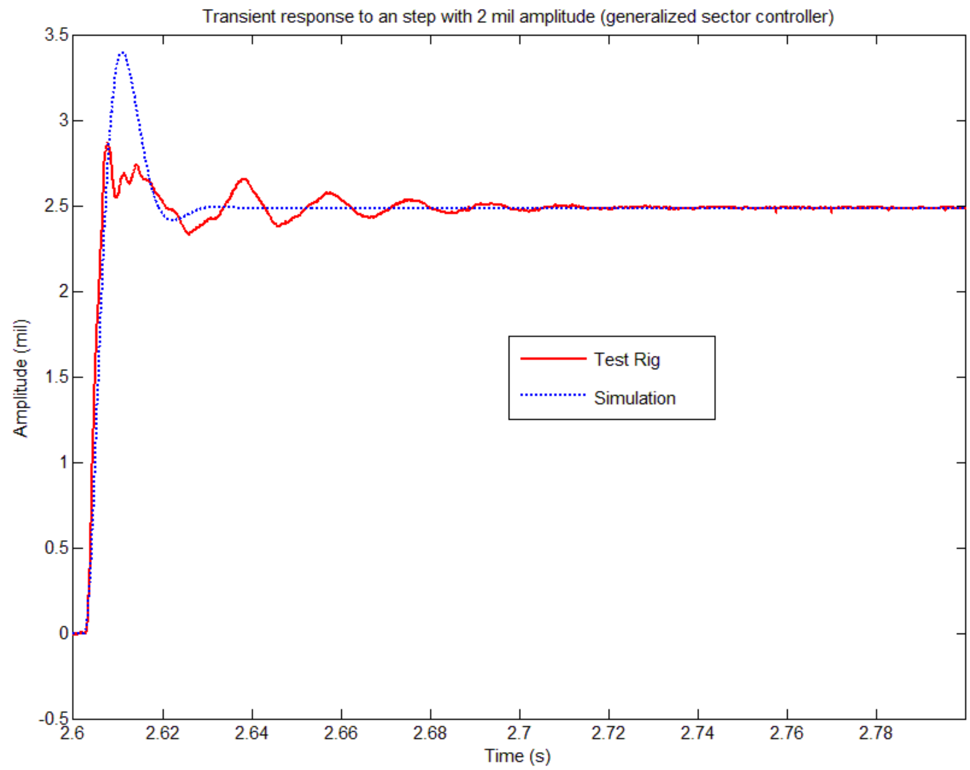

Figure 8-63 Generalized Sector Nonlinear Controller Transient Response to Step 0-2 (Time-span 0.2s)

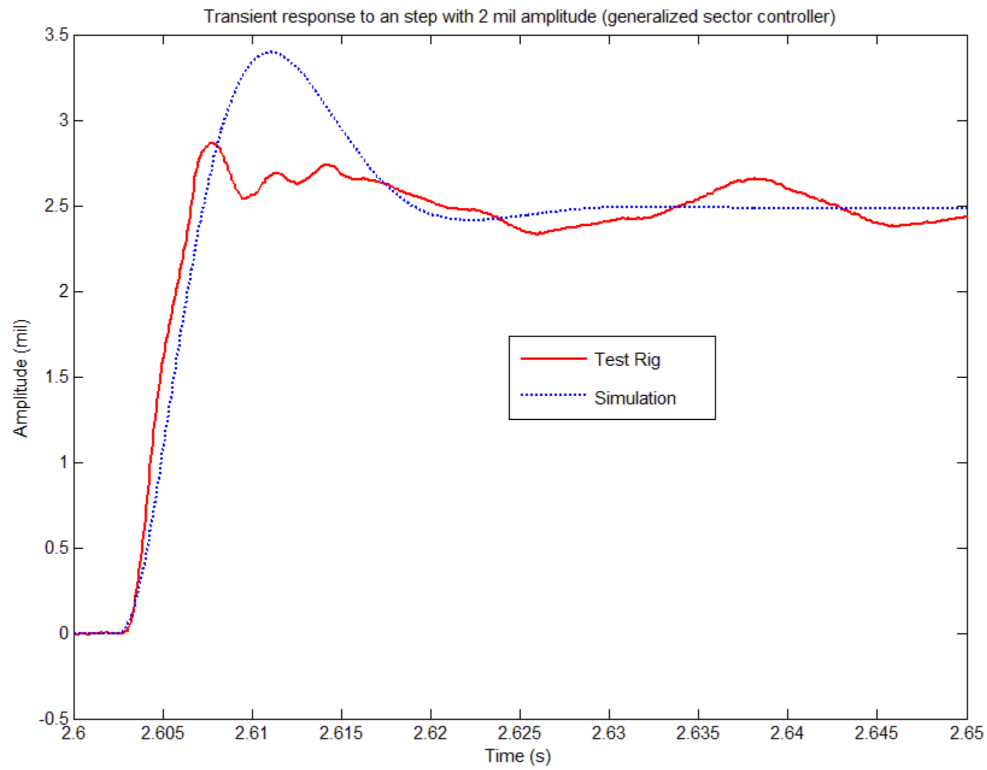

Figure 8-64 Generalized Sector Nonlinear Controller Transient Response to Step 0-2 (Time-span 0.05s)

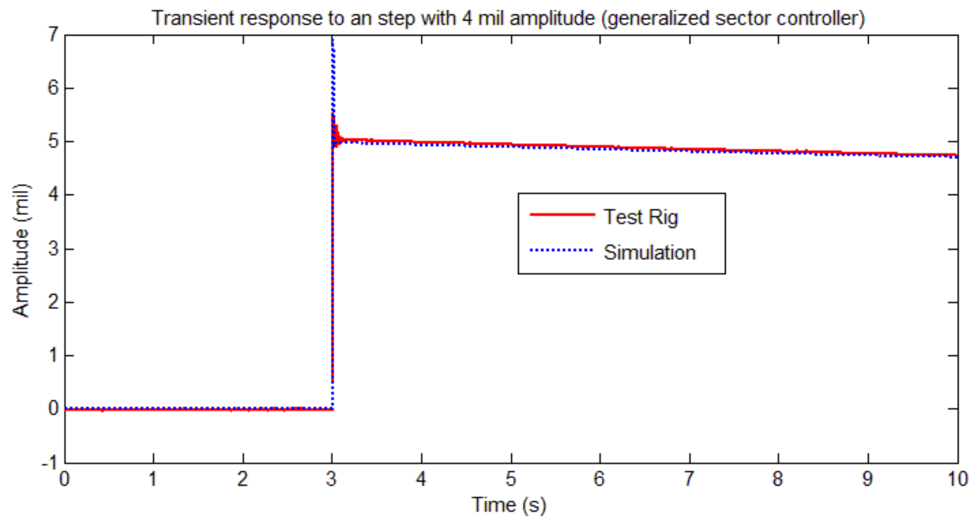

Figure 8-65 Generalized Sector Nonlinear Controller Transient Res.. to Step 0-4 (Time-span 10s)

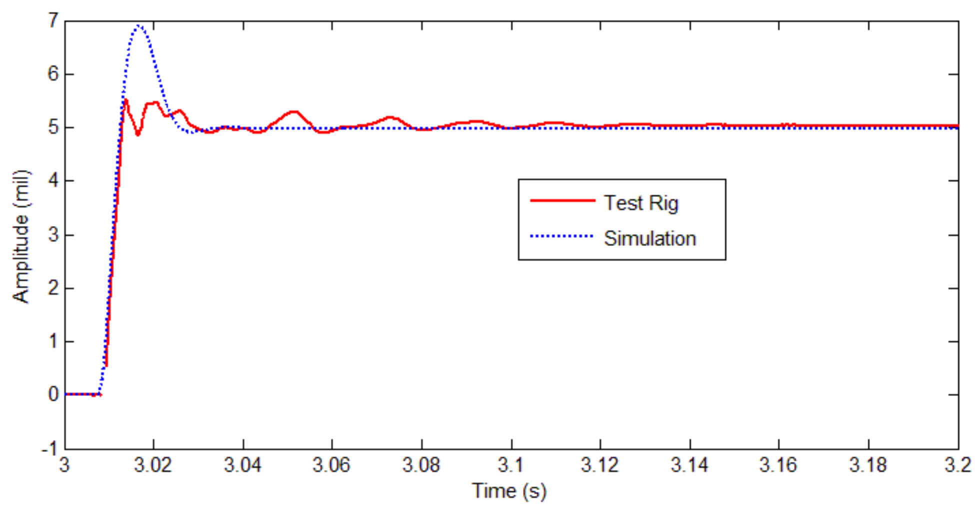

Figure 8-66 Generalized Sector Nonlinear Controller Transient Res. to Step 0-4 (Time-span 0.2s)

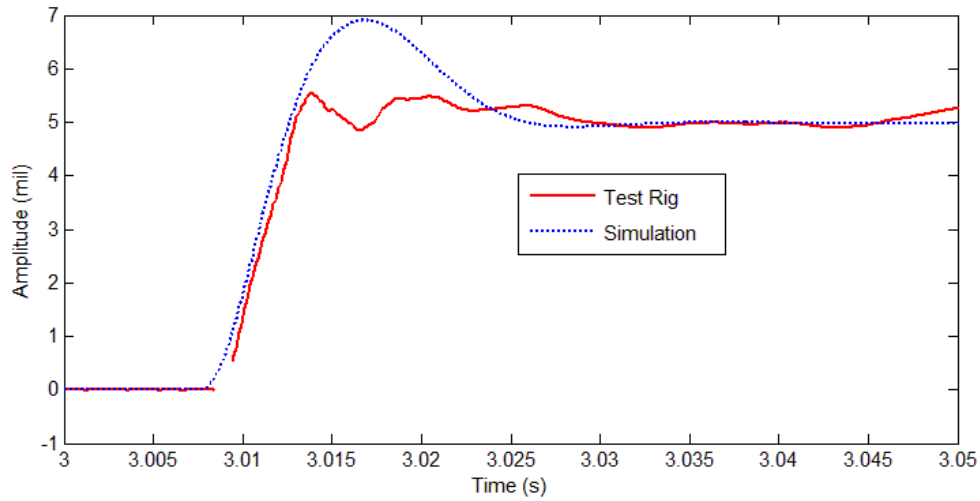

Figure 8-67 Generalized Sector Nonlinear Controller Trans. Res. to Step 0-4 (Time-span 0.05s)

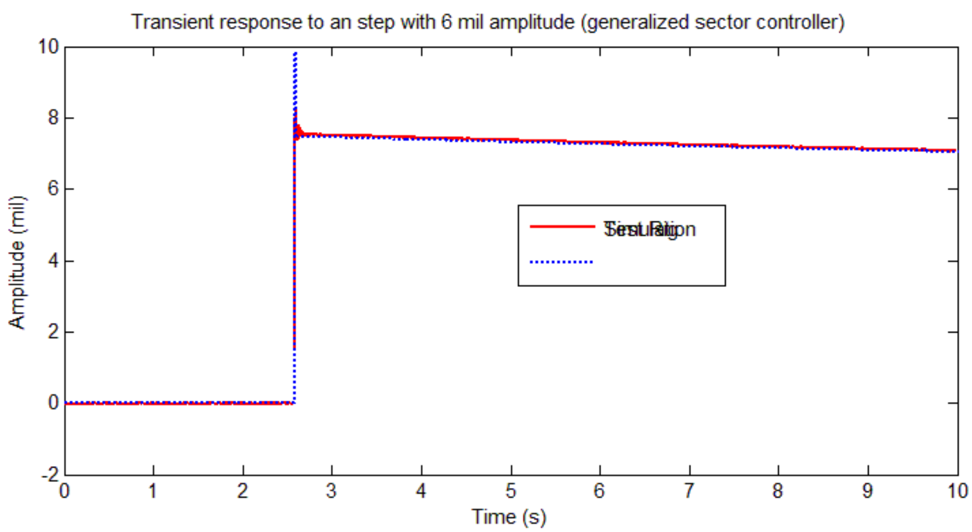

Figure 8-68 Generalized Sector Nonlinear Controller Transient Res. to Step 0-6 (Time-span 10s)

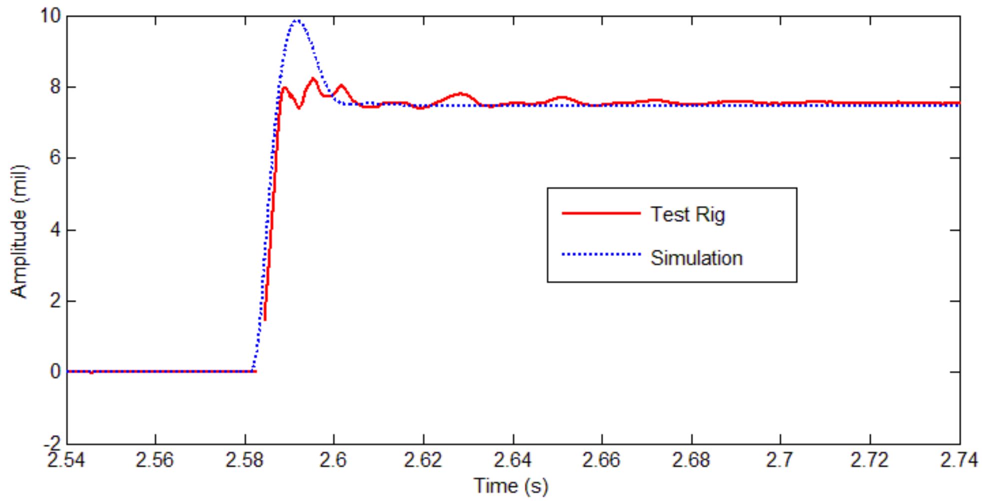

Figure 8-69 Generalized Sector Nonlinear Controller Transient Res. to Step 0-6 (Time-span 0.2s)

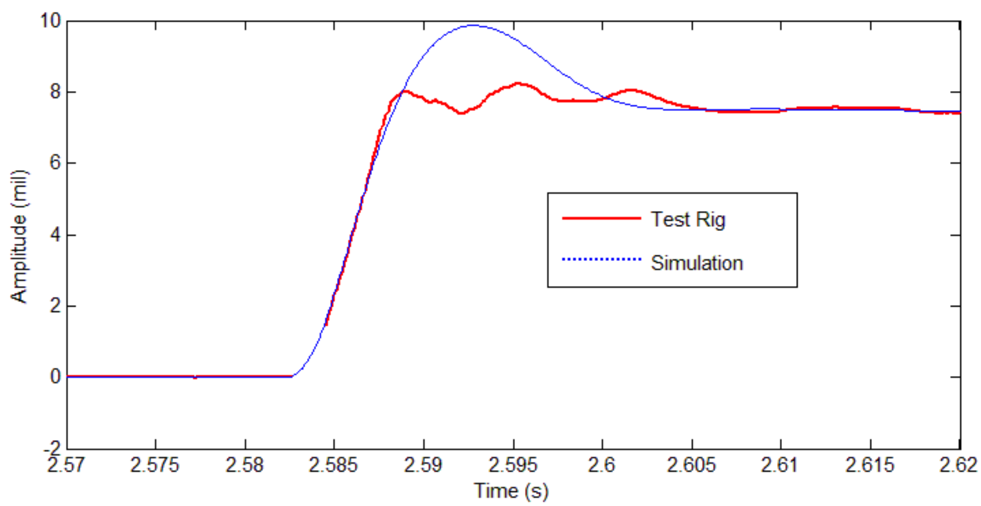

Figure 8-70 Generalized Sector Nonlinear Controller Trans. Res. to Step 0-6 (Time-span 0.05s)

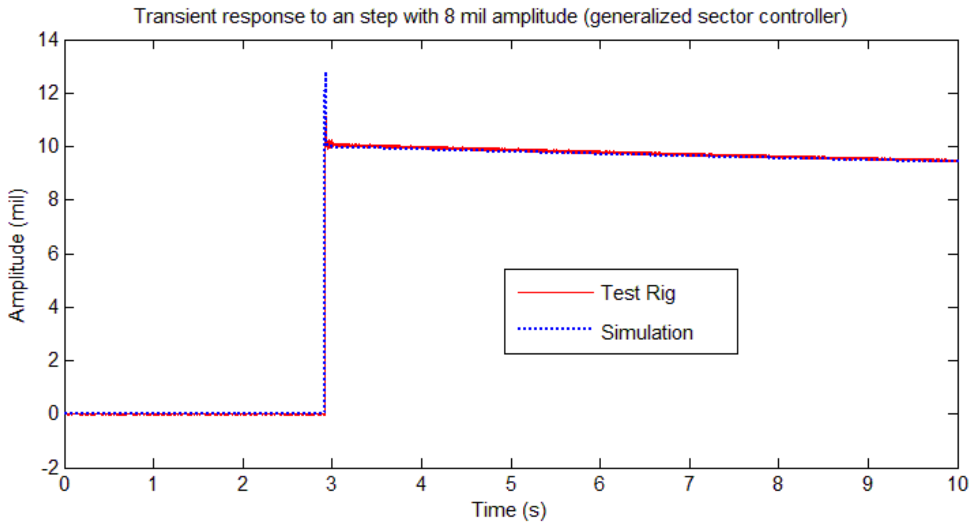

Figure 8-71 Generalized Sector Nonlinear Controller Transient Resp. to Step 0-8 (Time-span 10s)

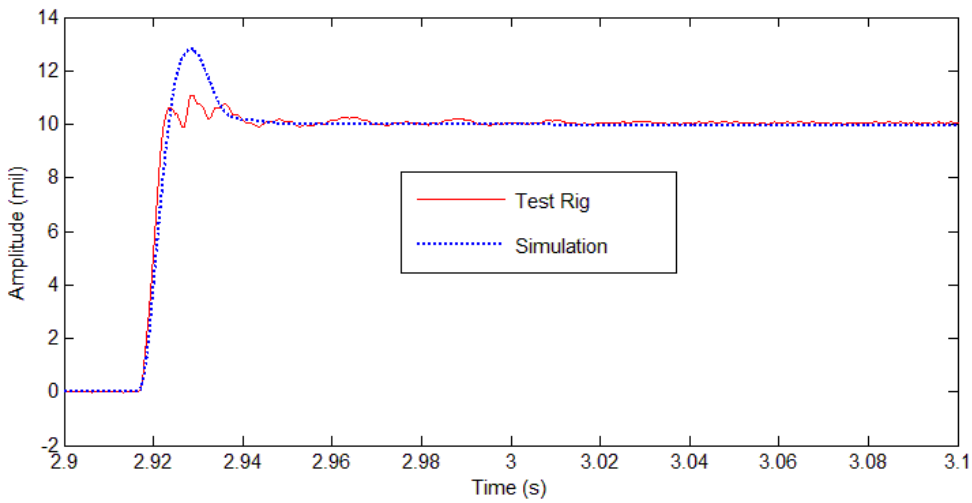

Figure 8-72 Generalized Sector Nonlinear Controller Transient Res. to Step 0-8 (Time-span 0.2s)

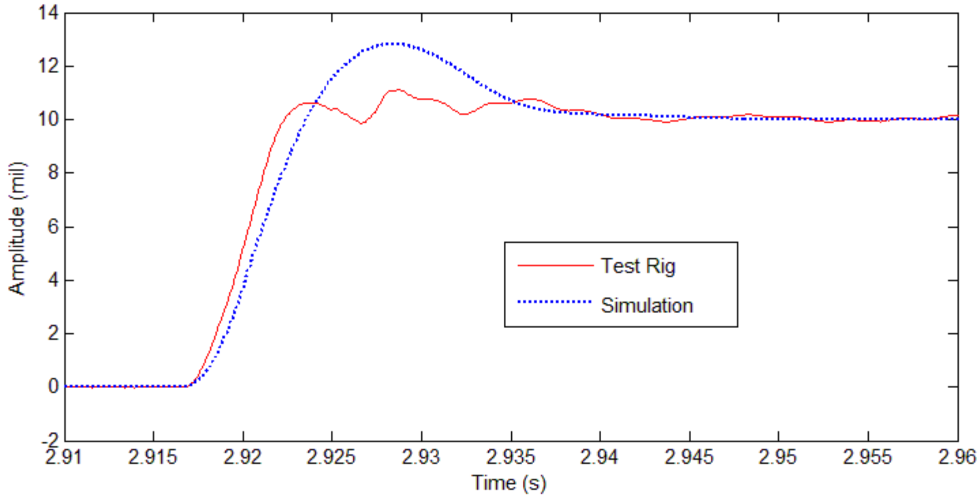

Figure 8-73 Generalized Sector Nonlinear Controller Trans. Res. to Step 0-8 (Time-span 0.05s)

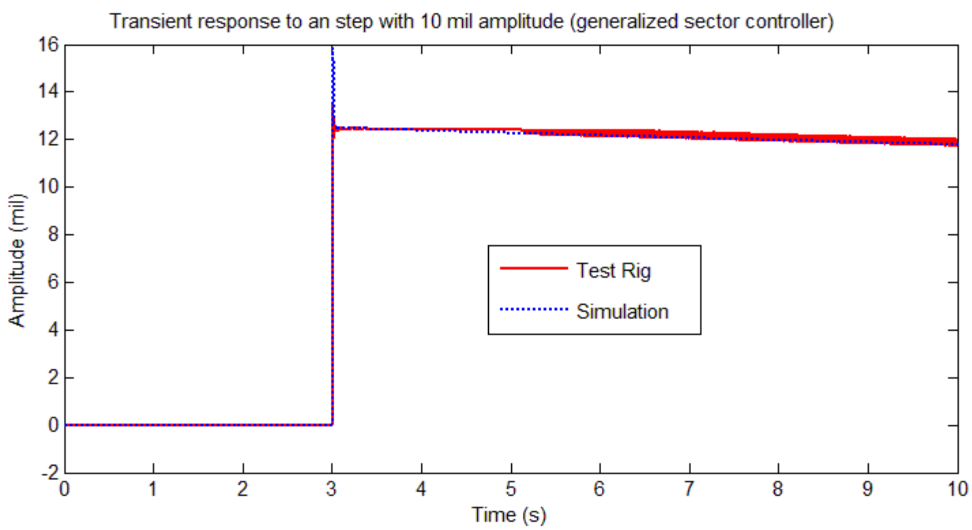

Figure 8-74 Generalized Sector Nonlinear Controller Transient Res. to Step 0-10 (Time-span 10s)

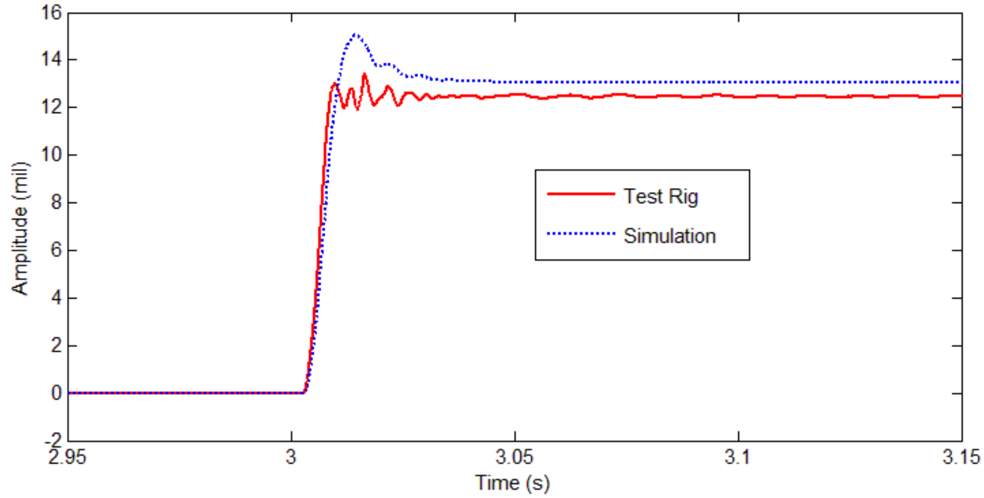

Figure 8-75 Generalized Sector Nonlinear Controller Trans. Res. to Step 0-10 (Time-span 0.2s)

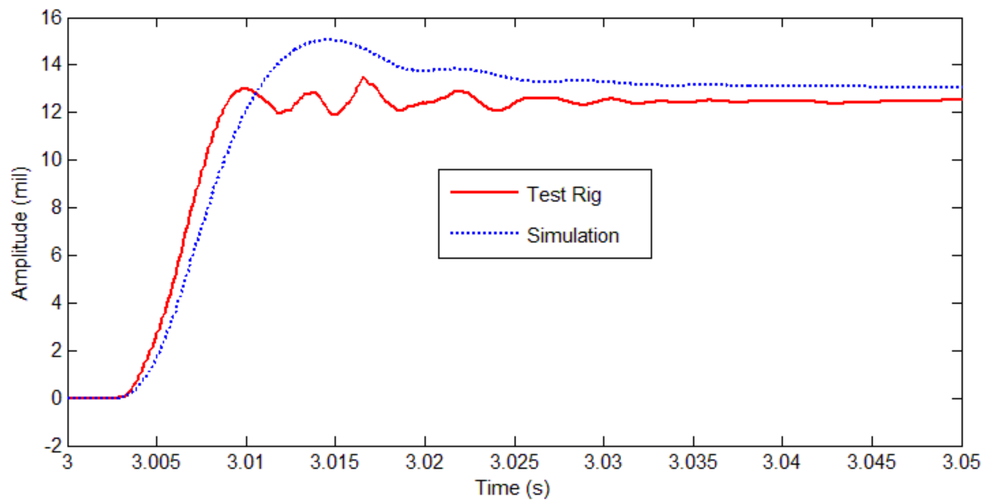

Figure 8-76 Generalized Sector Nonlinear Controller Trans. Res. to Step 0-10 (Time-span 0.05s)

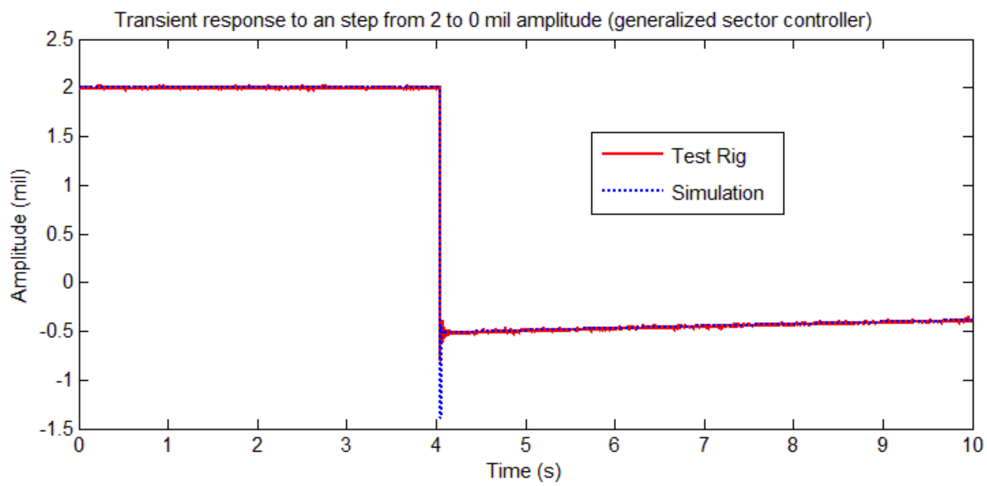

Figure 8-77 Generalized Sector Nonlinear Controller Transient Res. to Step 2-0 (Time-span 10s)

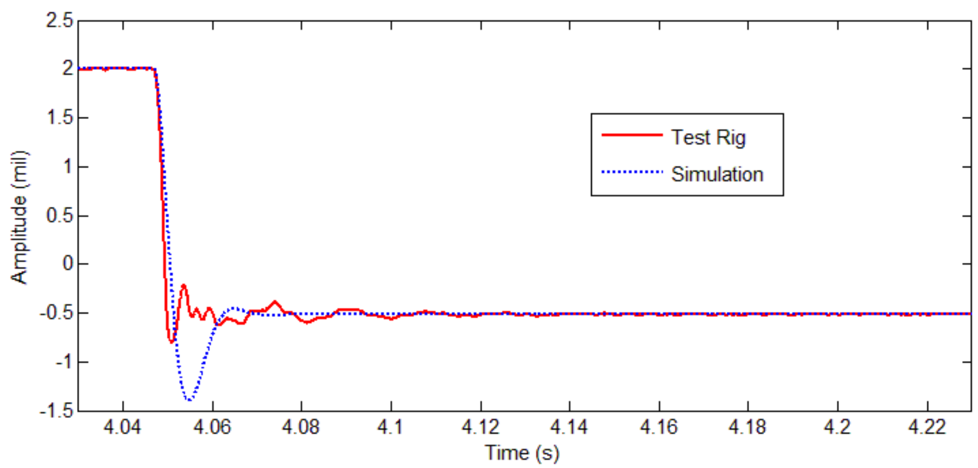

Figure 8-78 Generalized Sector Nonlinear Controller Transient Res. to Step 2-0 (Time-span 0.2s)

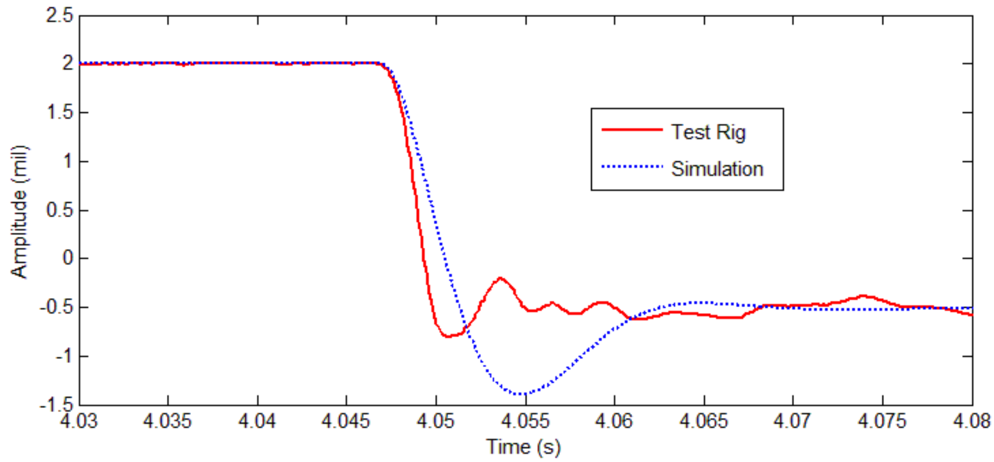

Figure 8-79 Generalized Sector Nonlinear Controller Trans. Res. to Step 2-0 (Time-span 0.05s)

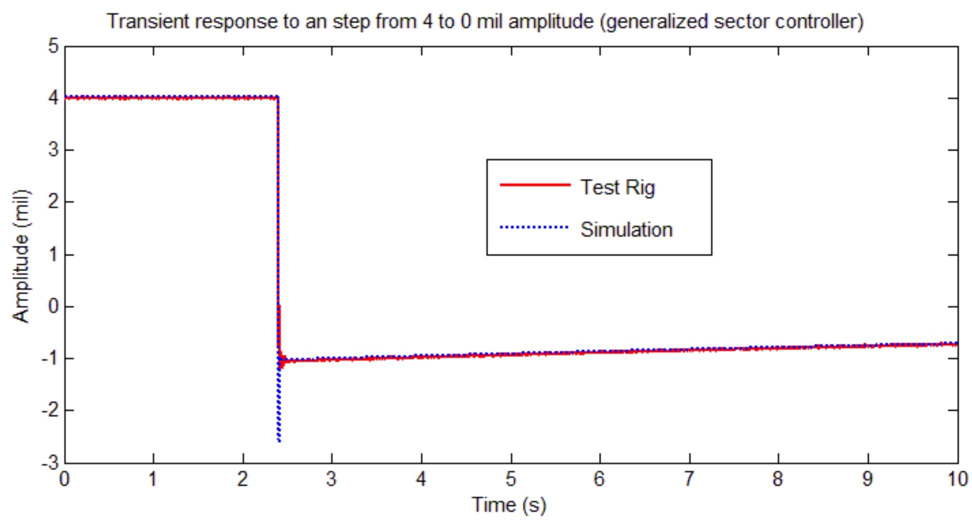

Figure 8-80 Generalized Sector Nonlinear Controller Transient Res. to Step 4-0 (Time-span 10s)

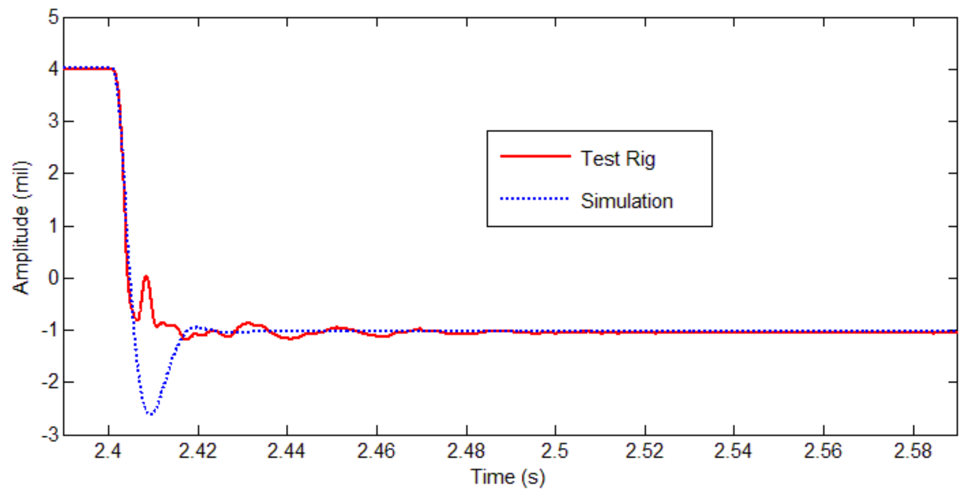

Figure 8-81 Generalized Sector Nonlinear Controller Transient Res. to Step 4-0 (Time-span 0.2s)

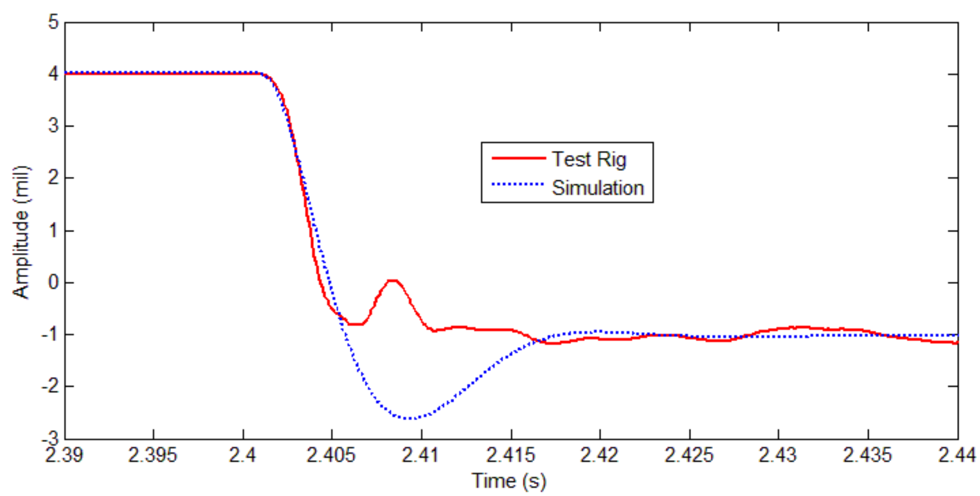

Figure 8-82 Generalized Sector Nonlinear Controller Trans. Res. to Step 4-0 (Time-span 0.05s)

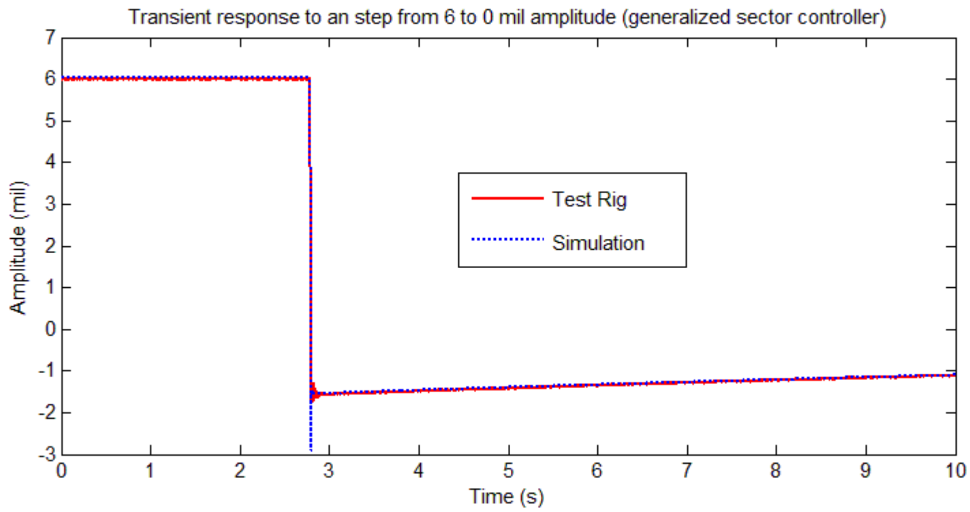

Figure 8-83 Generalized Sector Nonlinear Controller Transient Res. to Step 6-0 (Time-span 10s)

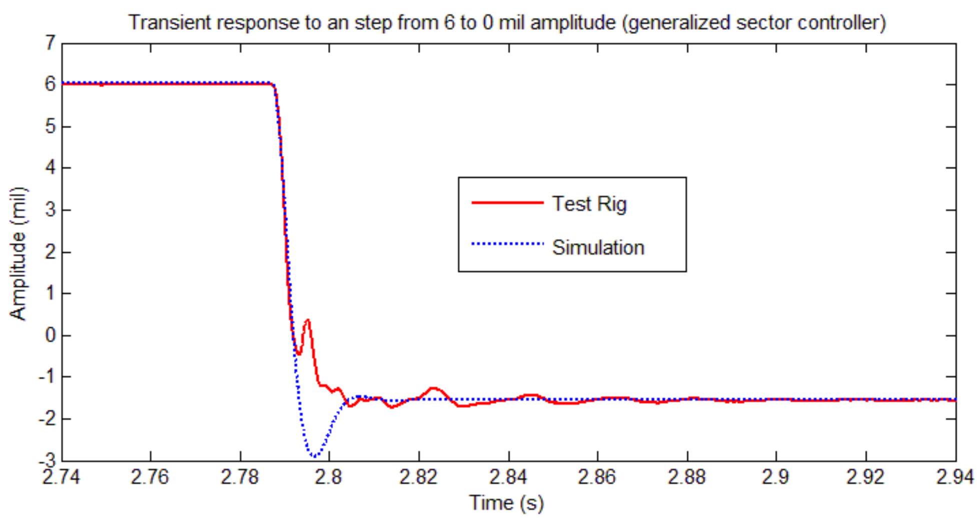

Figure 8-84 Generalized Sector Nonlinear Controller Transient Res. to Step 6-0 (Time-span 0.2s)

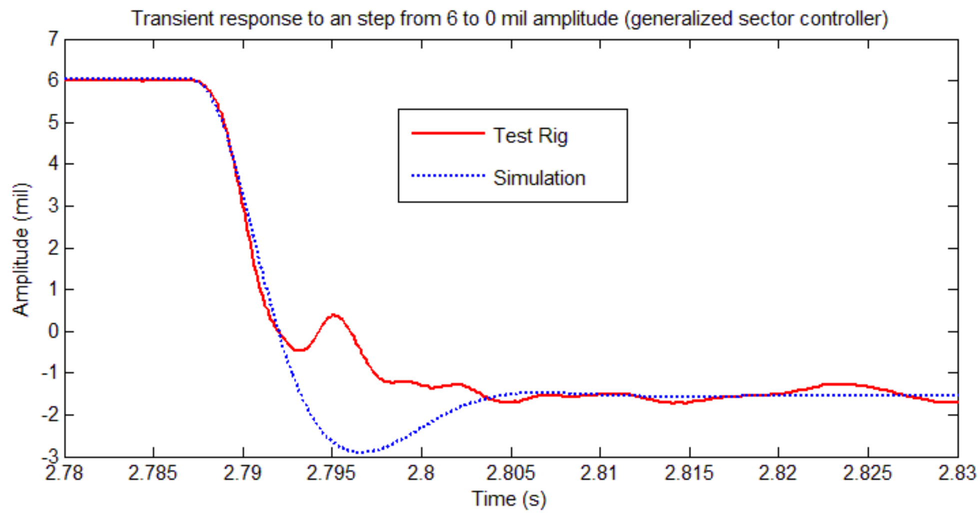

Figure 8-85 Generalized Sector Nonlinear Controller Trans. Res. to Step 6-0 (Time-span 0.05s)

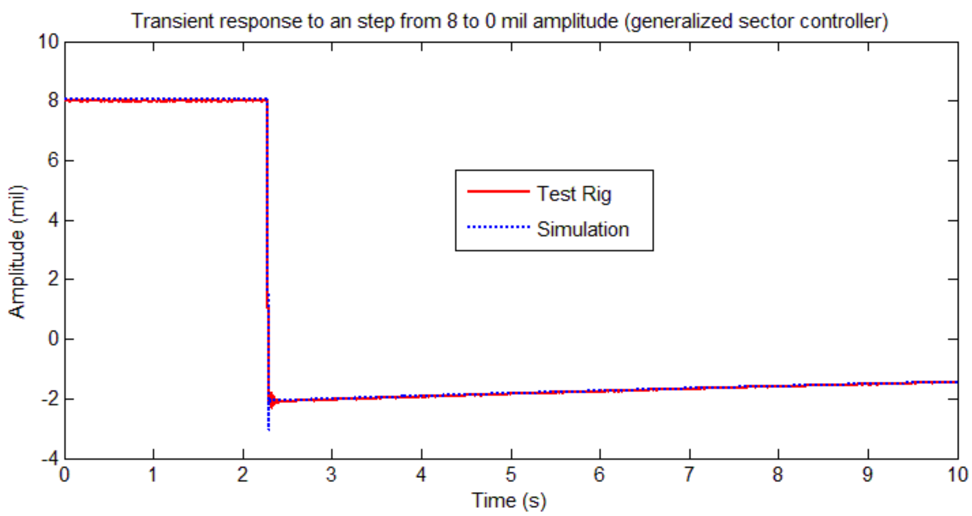

Figure 8-86 Generalized Sector Nonlinear Controller Transient Res. to Step 8-0 (Time-span 10s)

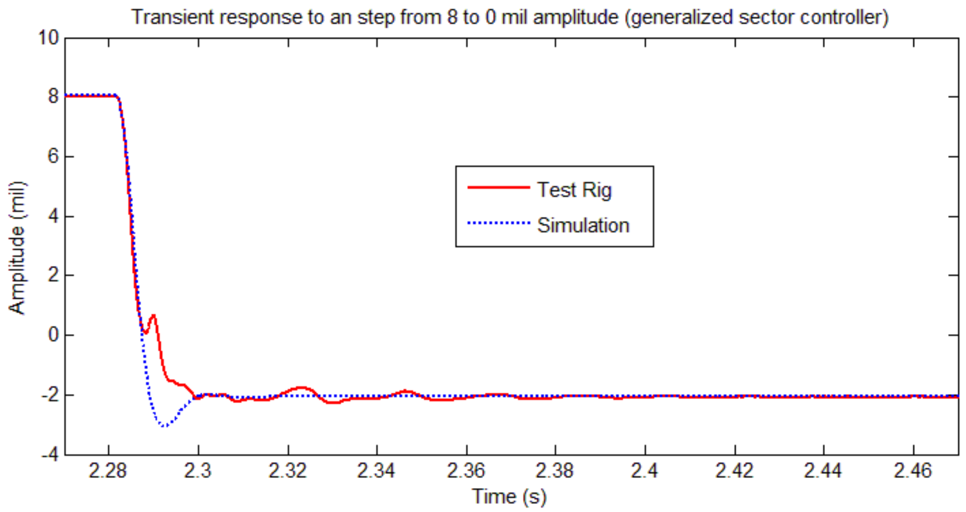

Figure 8-87 Generalized Sector Nonlinear Controller Transient Res. to Step 8-0 (Time-span 0.2s)

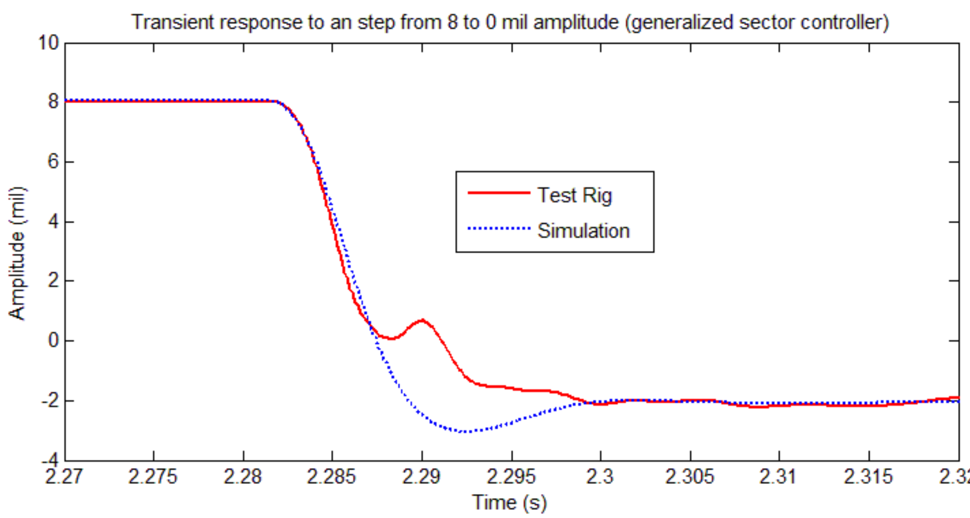

Figure 8-88 Generalized Sector Nonlinear Controller Transi. Res. to Step 8-0 (Time-span 0.05s)

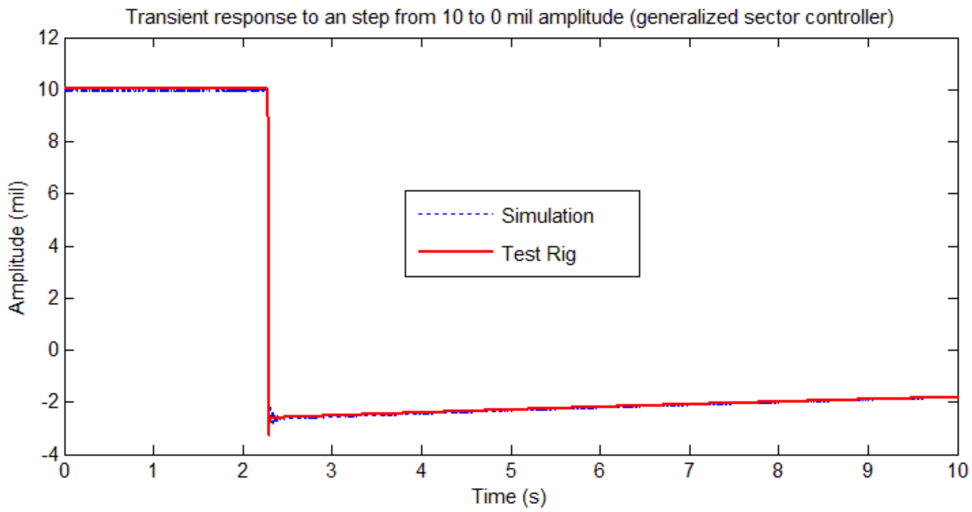

Figure 8-89 Generalized Sector Nonlinear Controller Transient Res. to Step 10-0 (Time-span 10s)

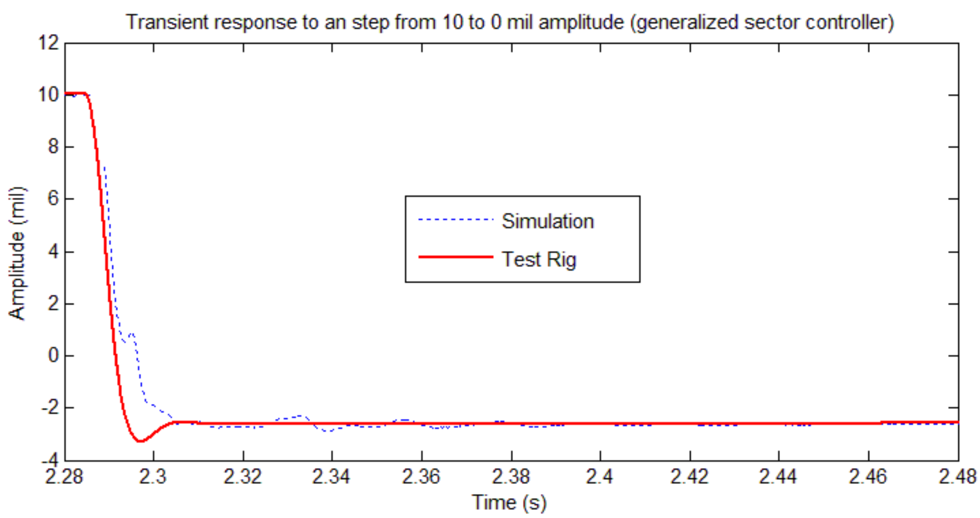

Figure 8-90 Generalized Sector Nonlinear Controller Trans. Res. to Step 10-0 (Time-span 0.2s)

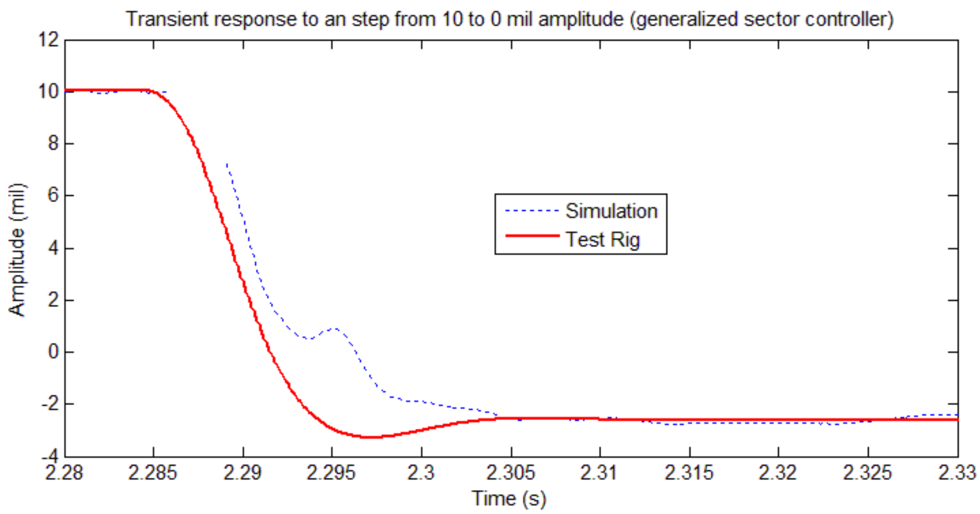

Figure 8-91 Generalized Sector Nonlinear Controller Trans. Res. to Step 10-0 (Time-span 0.05s)

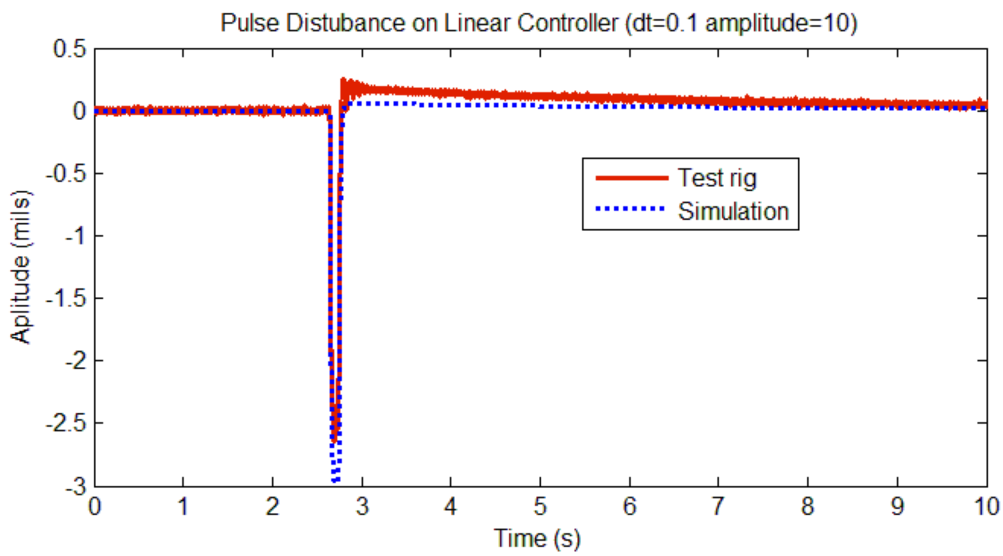

Figure 8-92 The Linear Controller's Disturbance Response (Time Span 10s) $\left(E = 10,\ \Delta t = 0.1s\right)$

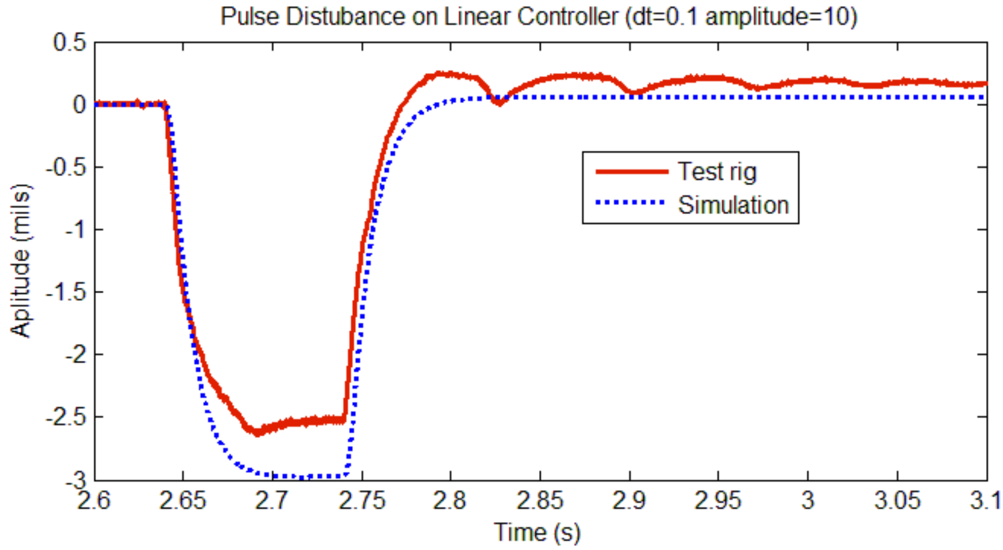

Figure 8-93 The Linear Controller’s Disturbance Response (Time Span 0.5s)
$(E = 10,\ \Delta t = 0.1s)$

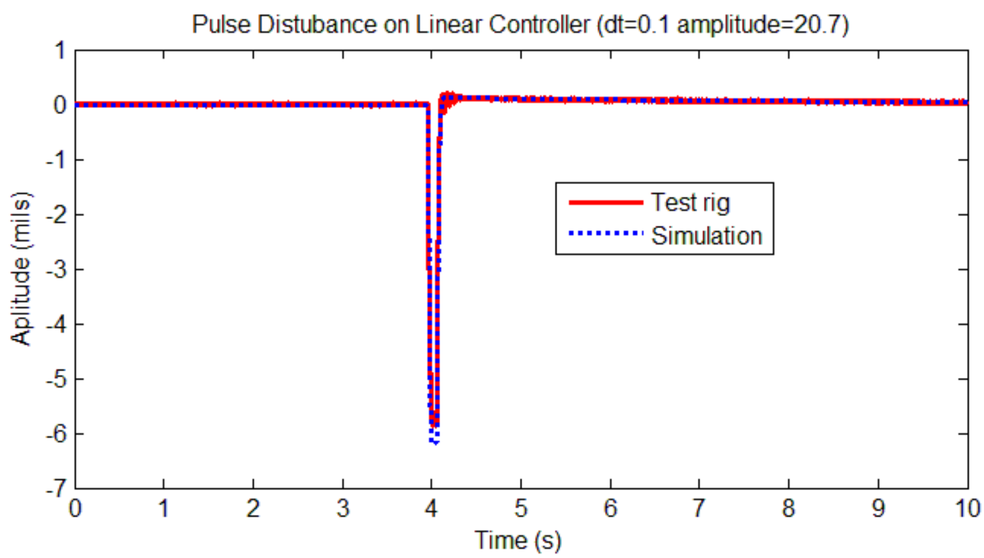

Figure 8-94 The Linear Controller’s Disturbance Response (Time Span 10s)
$(E = 43,\ \Delta t = 0.1s)$

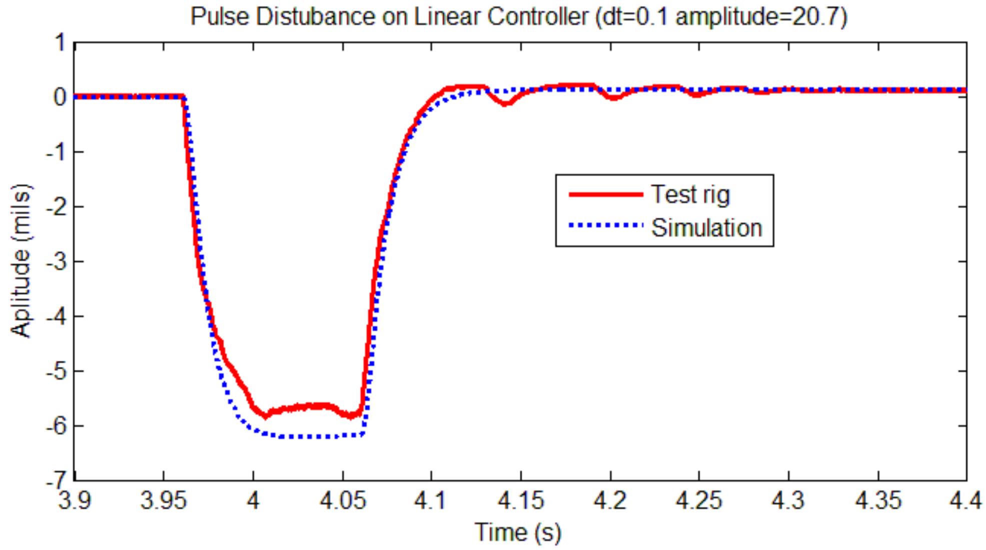

Figure 8-95 The Linear Controller's Disturbance Response (Time Span 0.5s)

$(E = 43,\ \Delta t = 0.1s)$

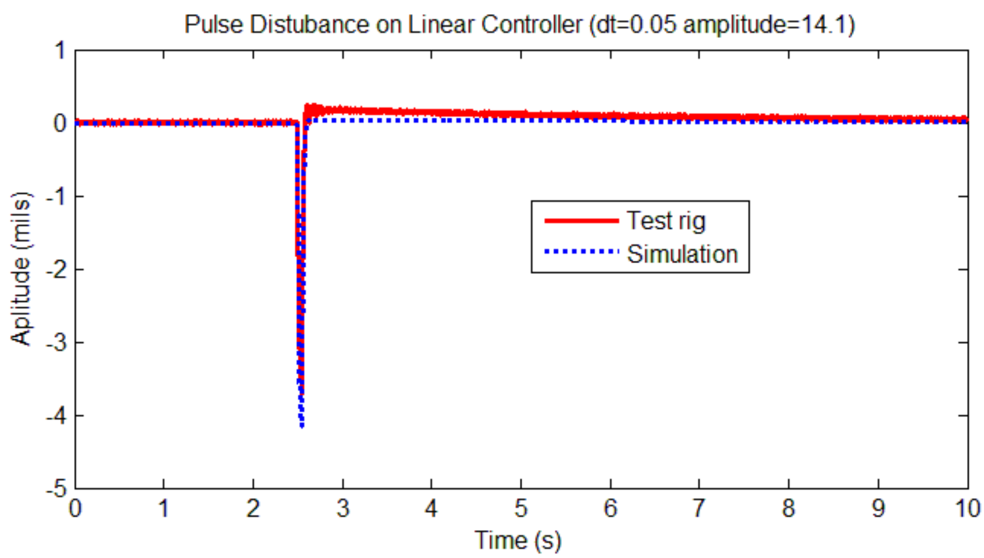

Figure 8-96 The Linear Controller's Disturbance Response (Time Span 10s)

$(E = 10,\ \Delta t = 0.05s)$

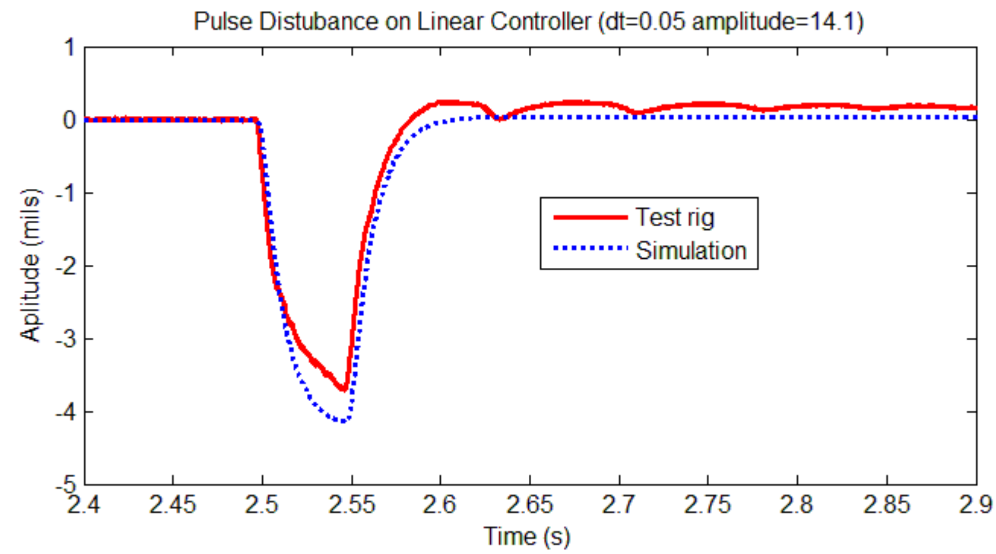

Figure 8-97 The Linear Controller's Disturbance Response (Time Span 0.5s)
$(E = 10,\ \Delta t = 0.05s)$

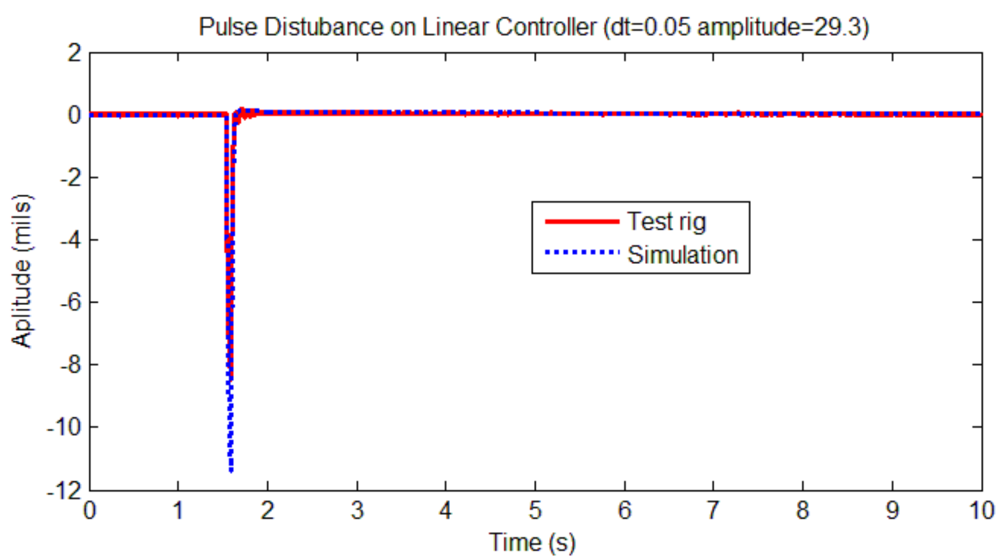

Figure 8-98 The Linear Controller's Disturbance Response (Time Span 10s)
$(E = 43,\ \Delta t = 0.05s)$

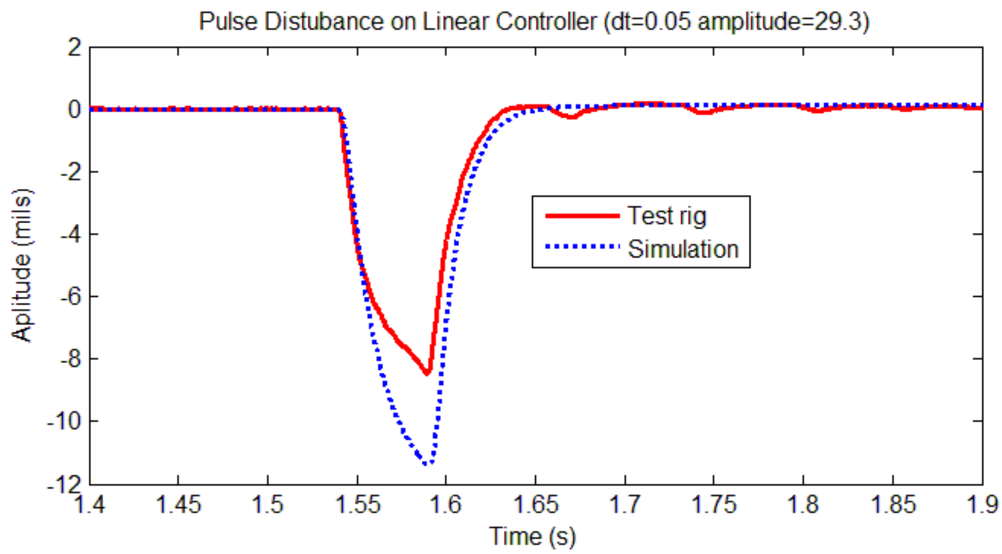

Figure 8-99 The Linear Controller's Disturbance Response (Time Span 0.5s)

$\left(E = 43,\ \Delta t = 0.05s\right)$

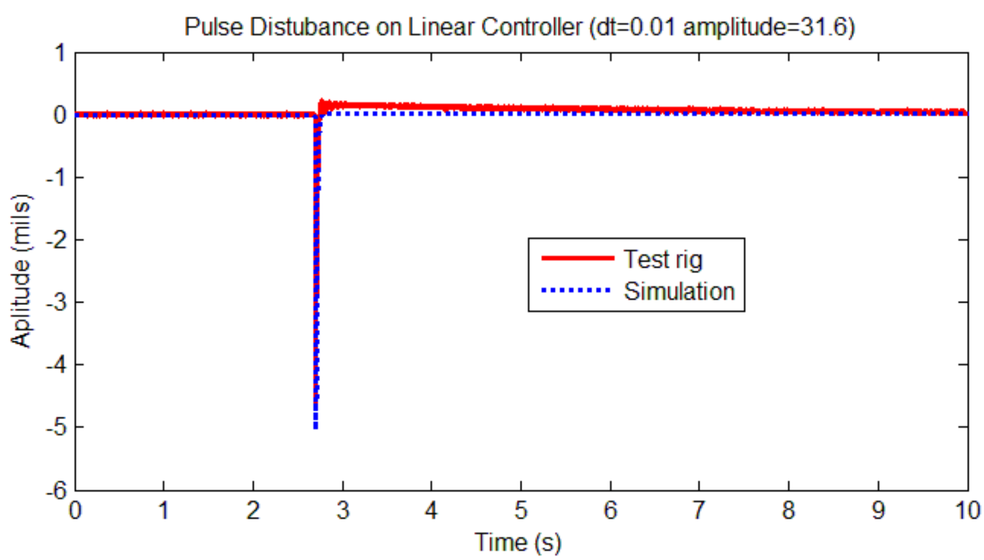

Figure 8-100 The Linear Controller's Disturbance Response (Time Span 10s)

$\left(E = 10,\ \Delta t = 0.01s\right)$

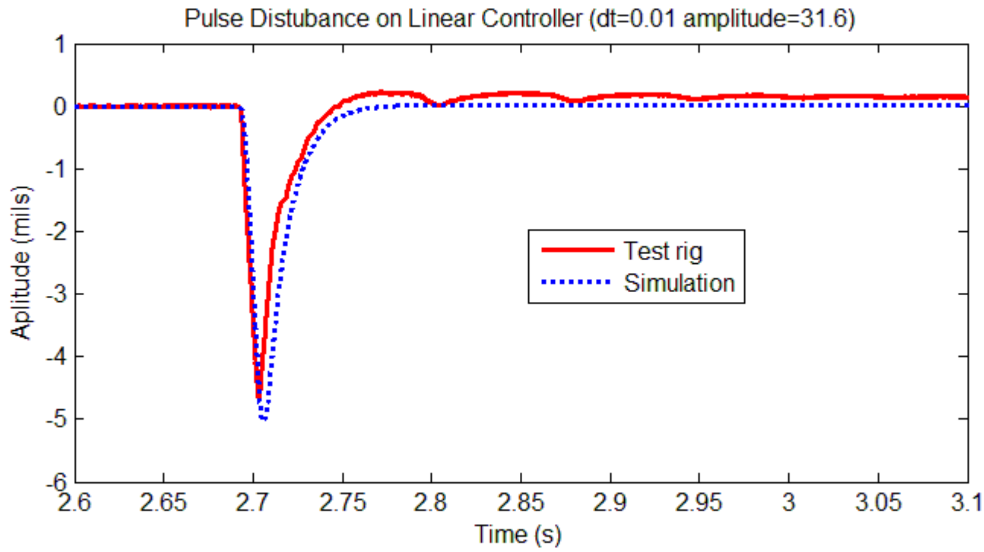

Figure 8-101 The Linear Controller's Disturbance Response (Time Span 0.5s)
$\left(E=10,\ \Delta t=0.01s\right)$

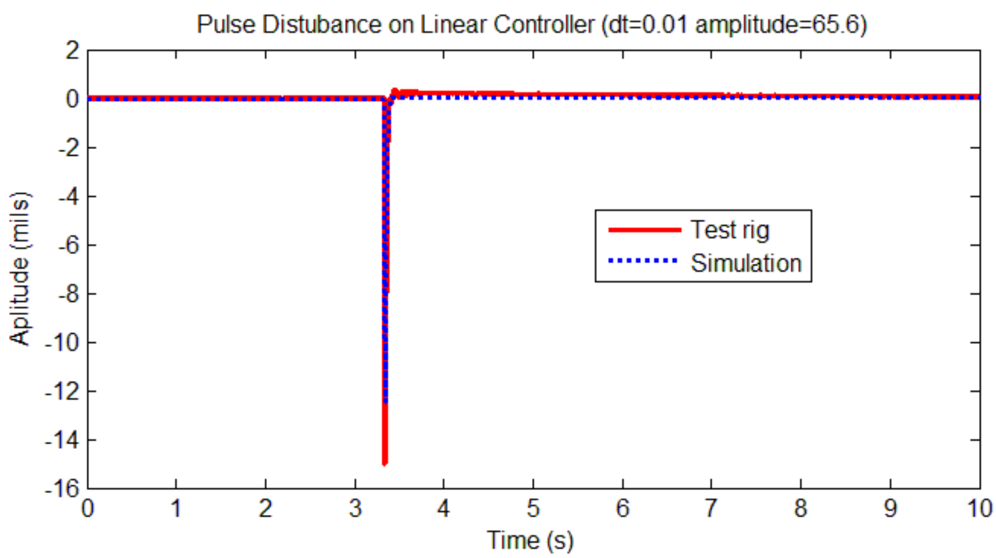

Figure 8-102 The Linear Controller's Disturbance Response (Time Span 10s)
$\left(E=43,\ \Delta t=0.01s\right)$

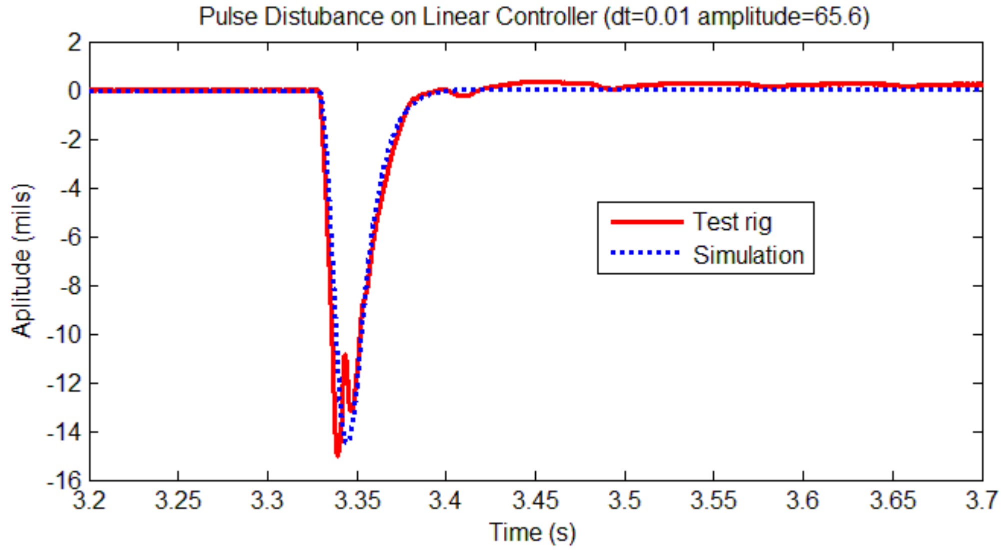

Figure 8-103 The Linear Controller's Disturbance Response (Time Span 0.5s)
$\left(E = 43,\ \Delta t = 0.01s\right)$

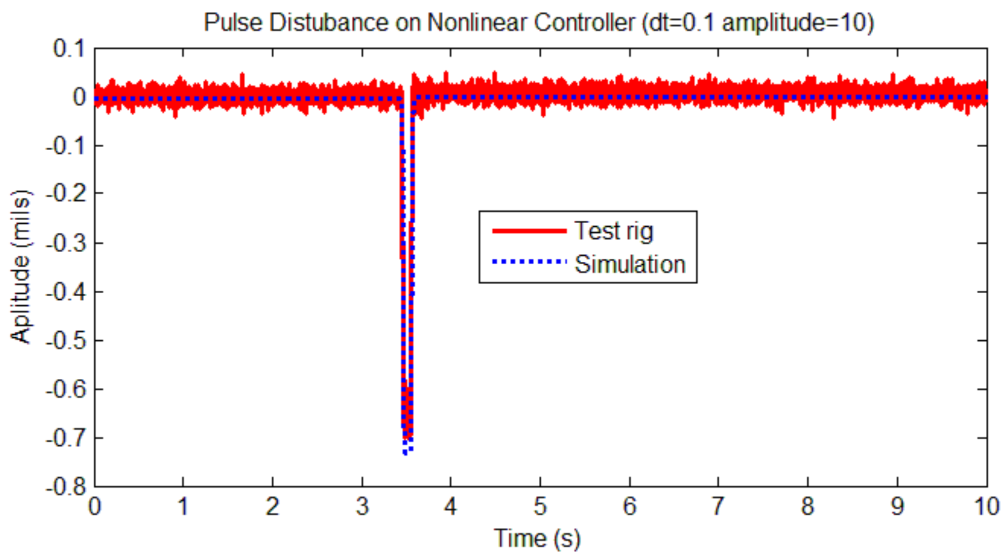

Figure 8-104 The Nonlinear Controller's Disturbance Response (Time Span 10s)
$\left(E = 10,\ \Delta t = 0.1s\right)$

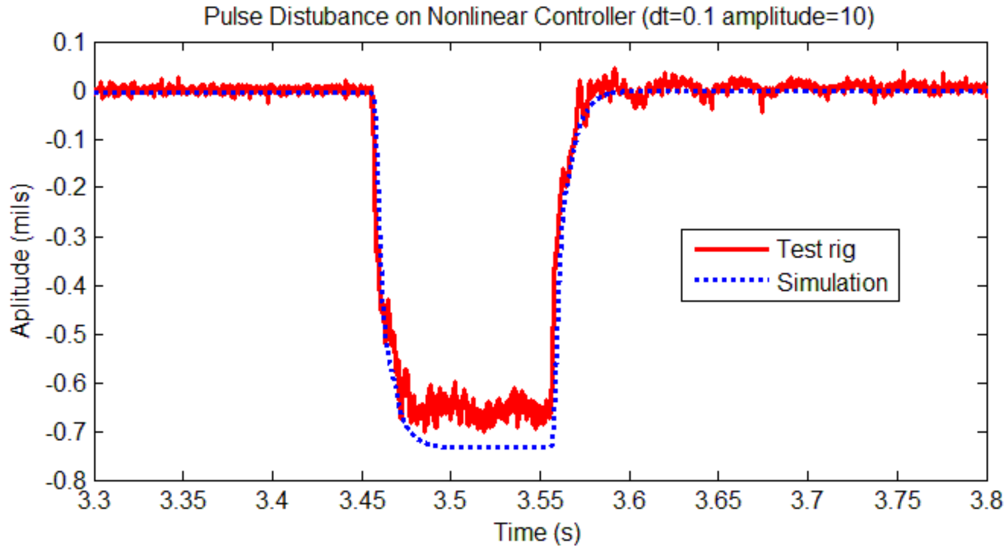

Figure 8-105 The Nonlinear Controller's Disturbance Response (Time Span 0.5s)
$(E = 10,\ \Delta t = 0.1s)$

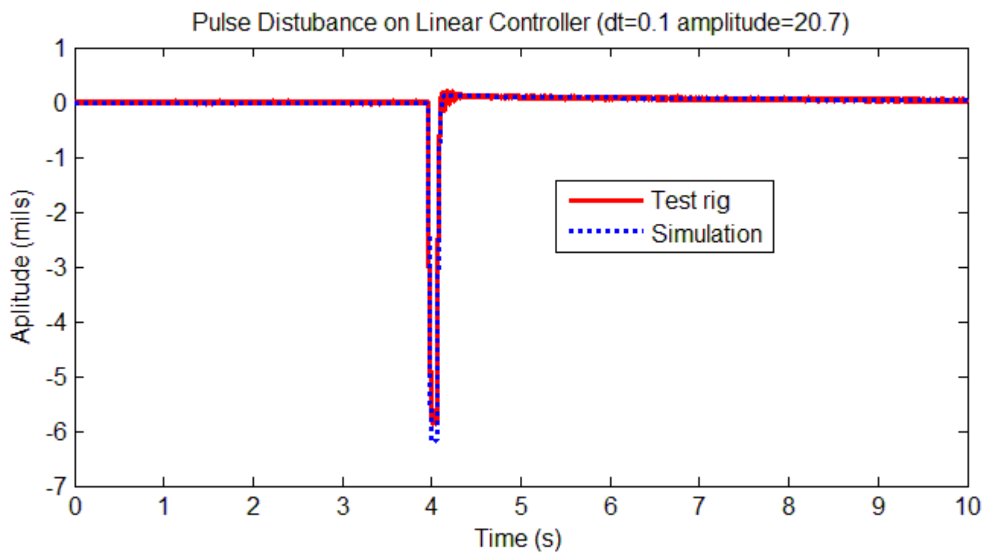

Figure 8-106 The Nonlinear Controller's Disturbance Response (Time Span 10s)
$(E = 43,\ \Delta t = 0.1s)$

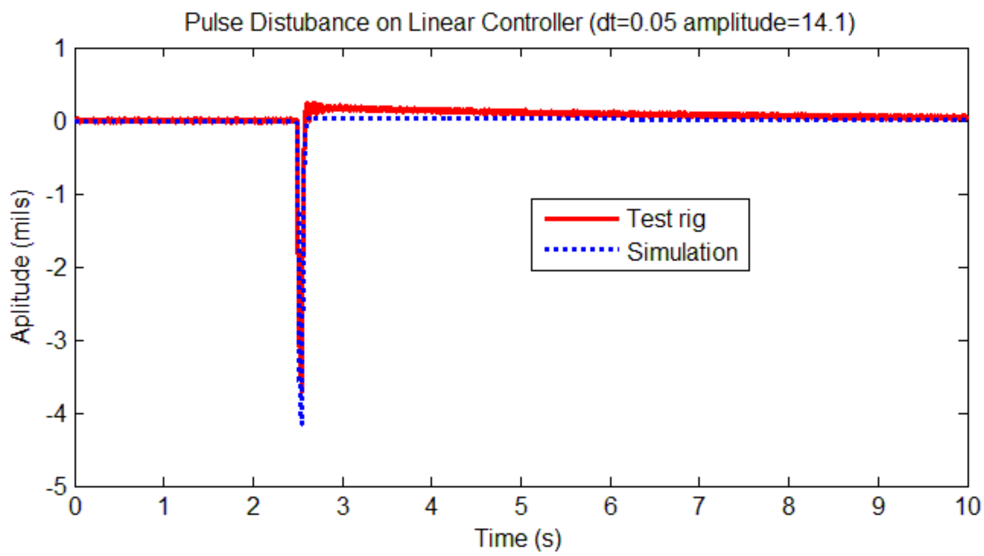

Figure 8-107 The Nonlinear Controller's Disturbance Response (Time Span 10s)
$(E=10,\ \Delta t=0.05s)$

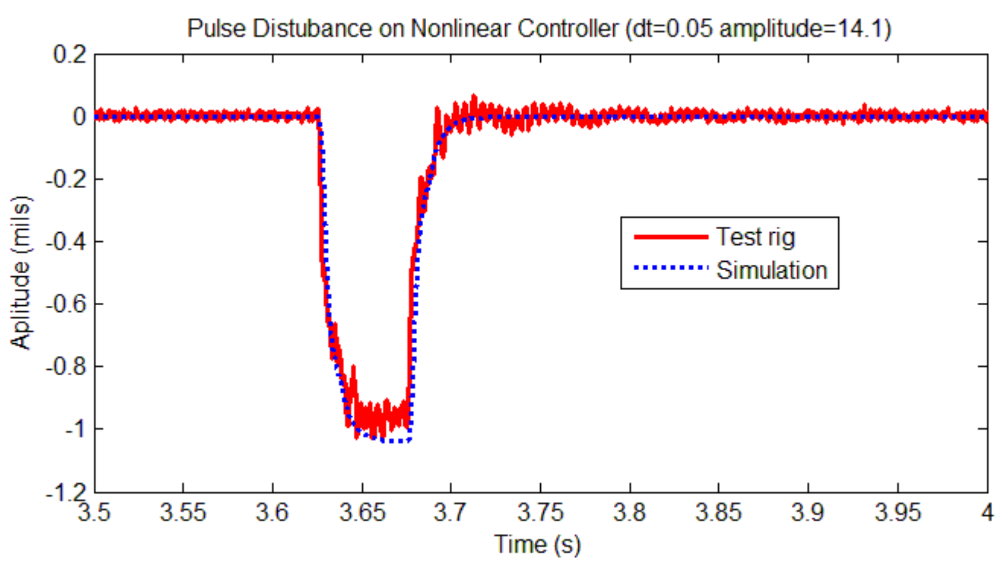

Figure 8-108 The Nonlinear Controller's Disturbance Response (Time Span 0.5s)
$(E=10,\ \Delta t=0.05s)$

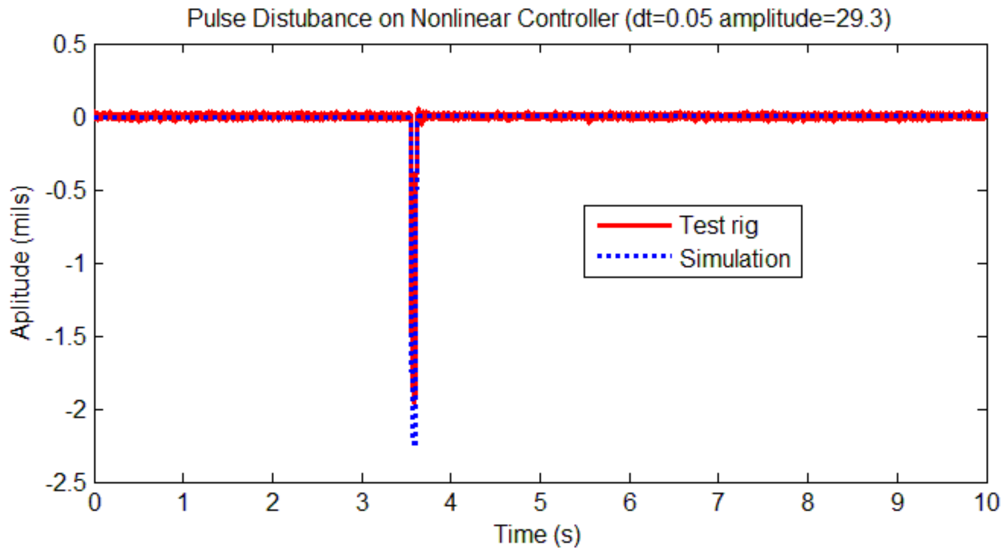

Figure 8-109 The Nonlinear Controller's Disturbance Response (Time Span 10s)
$\left(E = 43,\ \Delta t = 0.05s\right)$

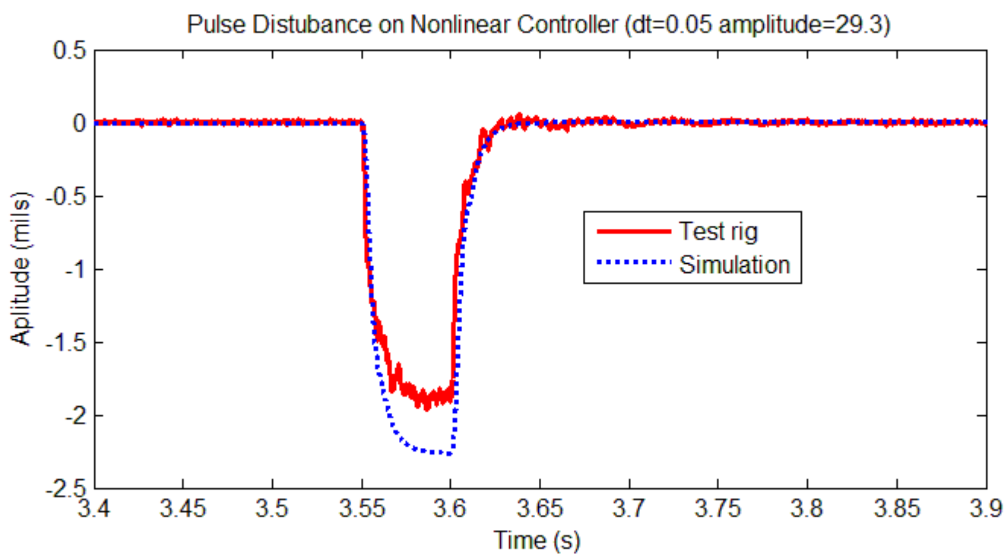

Figure 8-110 The Nonlinear Controller's Disturbance Response (Time Span 0.5s)
$\left(E = 43,\ \Delta t = 0.05s\right)$

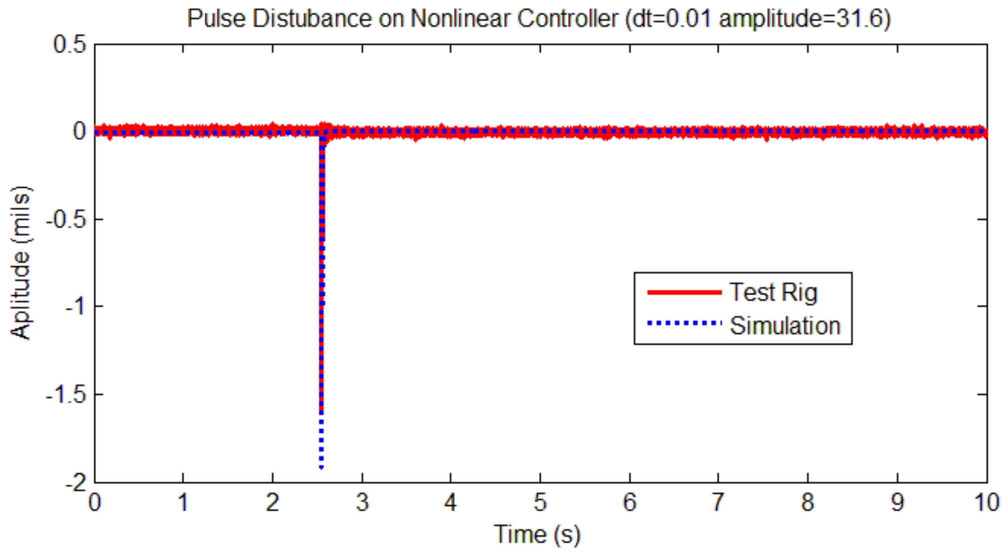

Figure 8-111 The Nonlinear Controller's Disturbance Response (Time Span 10s) $(E = 10,\ \Delta t = 0.01s)$

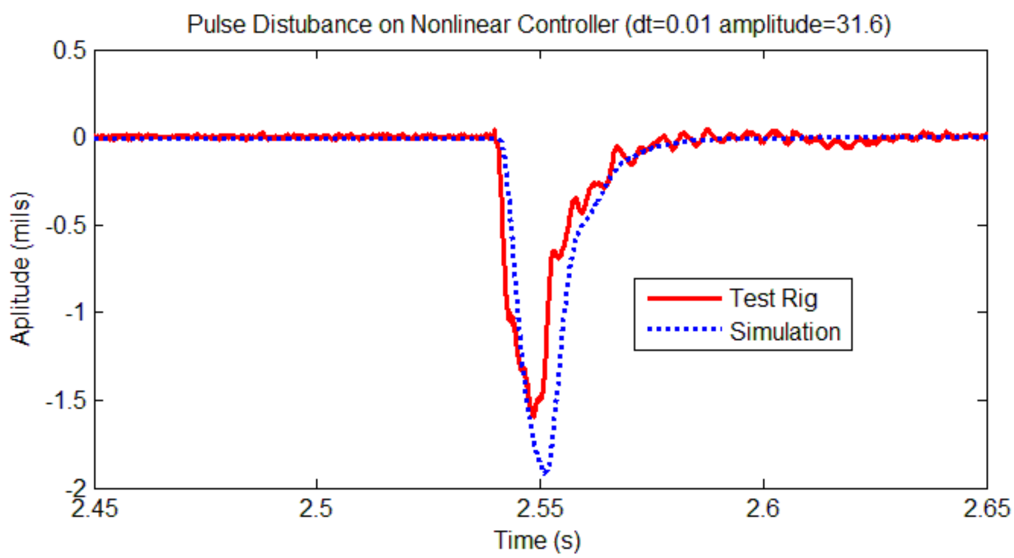

Figure 8-112 The Nonlinear Controller's Disturbance Response (Time Span 0.5s) $(E = 10,\ \Delta t = 0.01s)$

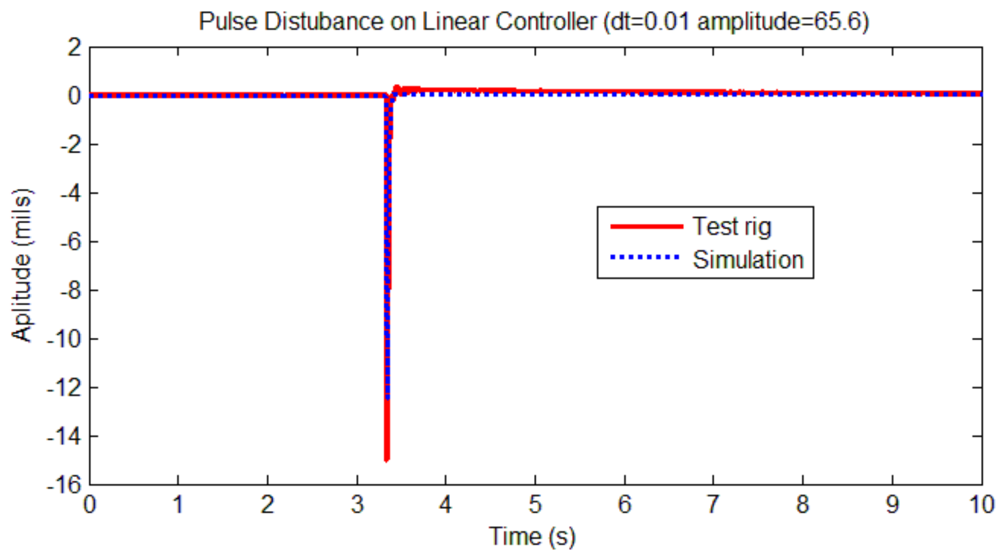

Figure 8-113 The Nonlinear Controller's Disturbance Response (Time Span 10s)
$(E = 43,\ \Delta t = 0.01s)$

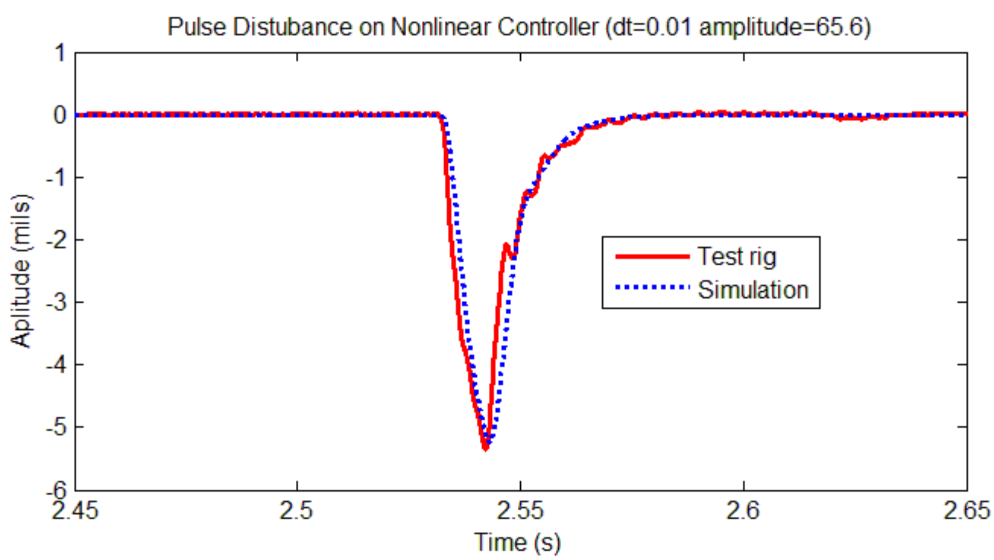

Figure 8-114 The Nonlinear Controller's Disturbance Response (Time Span 0.5s)
$(E = 43,\ \Delta t = 0.01s)$